



## 저작자표시-비영리-변경금지 2.0 대한민국

이용자는 아래의 조건을 따르는 경우에 한하여 자유롭게

- 이 저작물을 복제, 배포, 전송, 전시, 공연 및 방송할 수 있습니다.

다음과 같은 조건을 따라야 합니다:



저작자표시. 귀하는 원저작자를 표시하여야 합니다.



비영리. 귀하는 이 저작물을 영리 목적으로 이용할 수 없습니다.



변경금지. 귀하는 이 저작물을 개작, 변형 또는 가공할 수 없습니다.

- 귀하는, 이 저작물의 재이용이나 배포의 경우, 이 저작물에 적용된 이용허락조건을 명확하게 나타내어야 합니다.
- 저작권자로부터 별도의 허가를 받으면 이러한 조건들은 적용되지 않습니다.

저작권법에 따른 이용자의 권리는 위의 내용에 의하여 영향을 받지 않습니다.

이것은 [이용허락규약\(Legal Code\)](#)을 이해하기 쉽게 요약한 것입니다.

[Disclaimer](#)

MEMBRANE-INTEGRATED AND  
MEMBRANE-FREE MICRO AND  
NANOFLUIDICS FOR ACCURATE  
MOLECULAR TRANSPORT IN  
BIOLOGICAL ASSAYS

Minseok Kim

Department of Mechanical Engineering

Graduate School of UNIST

2015

MEMBRANE-INTEGRATED AND  
MEMBRANE-FREE MICRO AND  
NANOFLUIDICS FOR ACCURATE  
MOLECULAR TRANSPORT IN  
BIOLOGICAL ASSAYS

Minseok Kim

Department of Mechanical Engineering

Graduate School of UNIST

# Membrane-integrated and Membrane-free Micro and Nanofluidics for Accurate Molecular Transport in Biological Assays

A dissertation  
submitted to the Graduate School of UNIST  
in partial fulfillment of the  
requirements for the degree of  
Doctor of Philosophy.

Minseok Kim

7. 15. 2015

Approved by



---

Advisor

Taesung Kim

# Membrane-integrated and Membrane-free Micro and Nanofluidics for Accurate Molecular Transport in Biological Assays

Minseok Kim

This certifies that the dissertation of Minseok Kim is  
approved.

7. 15. 2015



Advisor: Taesung Kim



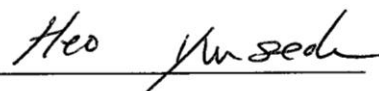
typed name: Heungjoo Shin



typed name: Jaesung Jang



typed name: Sung Kuk Lee



typed name: Yun Seok Heo

## Abstract

Nanofluidics has a comparable characteristic length to the size of ions and biomolecules, so that it can be used as an efficient platform to conduct accurate biochemical assays/analyses. In particular, the nanofluidic elements are often embedded into microfluidics, forming integrated micro/nanofluidic networks for even more complex and systematic applications such as electrokinetic pumps, transistors, and energy converters. Such innovative applications using unique mass-transport phenomena in micro/nanofluidic devices become available with the development of novel and precise nanofabrication techniques. For example, conventional nanolithography techniques such as electron or focused-ion beam lithography are used widely because of high degree of precision and accuracy of patterning. Another general nanofabrication method is micro-electromechanical system (MEMS)-based techniques that include both top-down (e.g., silicon etching) and bottom-up (e.g., thin-film deposition) approaches. However, it has been a challenge to fabricate the mixed-scale micro/nanofluidic devices by using either the conventional nanolithography utilizing the high-energy beams or the conventional MEMS-based nanofabrication because of the cost, time, throughput, and incompatibility issues of the methods. In particular, the limitations become more critical when both the microfabrication and the nanofabrication techniques need to be used in series to make micro/nano multi-scale structures. Therefore, an innovative alternate technique is specifically required to address the current weaknesses of both the conventional nanolithography and the MEMS-based nanofabrications.

This dissertation describes novel and unconventional methods to fabricate mixed-scale micro/nanofluidic devices by integrating nanoporous hydrogels and ion selective membranes (ISMs) into microfluidic devices (membrane-integrated micro/nanofluidics). On the other hand, the micro/nanofluidic devices can be also fabricated by employing microfabricated ratchet structures that perform the same functions of a membrane, and by intentionally creating nanoscale cracks to produce nanochannels (membrane-free micro/nanofluidics). The dissertation's early chapters deal with the development of novel nanomaterial-integrating methods to accurately control mass-transport phenomena at the micro/nanofluidic interfaces. A variety of hydrogel membranes are employed to enable pure diffusive or pure electrophoretic transport for accurate and active controls of chemical environments. In addition, ISMs are used to perform permselective ion transport for electrokinetic applications. The late chapters of this dissertation introduce membrane-free mixed-scale micro/nanofluidic devices that possess enhanced capabilities compared to the membrane-based devices, including higher precision and robustness in mass-transport controls, and higher compatibility with existing microfluidic components. First, an arrowhead-shaped ratchet microstructure in a microfluidic device physically compartmentalizes micron-sized bacterial cells but allows diffusion-controlled chemical environments without convective drag to the cells, which is

commonly performed by a nanoporous membrane or a nanochannel. That is, the microfabricated ratchet structure acts the same function of a nanofluidic element without nanofabrication. Second, nanochannels and microchannels are fabricated simultaneously by an unprecedented cracking-assisted nanofabrication technique (called crack-photolithography) that relies only on a standard photolithography process. The crack-photolithography produces well-controlled micro/nanochannels in any desired shapes and in a variety of geometric dimensions, over large areas and with a high-throughput. Hence, mixed-scale micro/nanofluidic devices can be fabricated by the same technique that is used to fabricate a microchannel without additional nanofabrication processes and expensive equipment.

Basically, the membrane-integrated and membrane-free micro/nanofluidic devices in this dissertation have the same mission, the transport control of biomolecules and chemical species to conduct biological assays in an accurate and high-throughput manner. As practical applications, the mixed-scale micro/nanofluidic devices are used for performing electrokinetic biosample pretreatments such as concentration and separation for ultra-sensitive and ultra-selective detection of target analytes such as proteins, particles and bacterial cells. In addition to the electrokinetic biomolecular/bacterial handling, the devices are also used for accurate characterizations of bacterial behavior such as chemotaxis and gene expression under convection-free and diffusion-controlled chemical stimulations. The role of a nanofluidic element such as a nanoporous membrane and a nanochannel array in microfluidics is essential to enable accurate and permselective transports of ions and molecules in various bioassays. In this context, the proposed membrane-based or membrane-free micro/nanofluidic devices play both microfluidic and nanofluidic functions without complicated nanofabrications, resulting in time-/cost-efficient and high-throughput fabrication. Thus, the research achievements in this dissertation substantially contribute to popularize and revolutionize the micro/nanofluidic systems and technologies, which have been hindered due to expensive and time-consuming conventional nanofabrications.



## Contents

Abstract .....	v
Contents .....	viii
List of Figures .....	ix
List of Tables .....	xii
Nomenclature .....	xiii
<b>Chapter 1. Introduction to Integrated Micro/Nanofluidics .....</b>	<b>1</b>
1.1 The development of microfluidics and nanofluidics .....	1
1.2 Theory: mass transport in micro/nanofluidic devices .....	2
1.3 Conventional and unconventional fabrication of nanofluidic devices .....	6
1.4 Applications of micro/nanofluidics .....	13
1.5 Overview of dissertation .....	18
<b>Chapter 2. Integration of Nanoporous Hydrogel Plugs into Microfluidic Device for Bacterial Chemotaxis Assay in Multiple Chemical Gradients .....</b>	<b>23</b>
<b>Chapter 3. Polydimethylsiloxane-sealed Hydrogel Device for Nonlinear Bacterial Chemotaxis .....</b>	<b>38</b>
<b>Chapter 4. Self-integration of Nanoporous Membranes in Microfluidic Devices: Electrokinetic Preconcentration of Biosamples .....</b>	<b>51</b>
<b>Chapter 5. Continuous Concentration and Separation of Target Analytes by Using Aptamer-Functionalized Microtubules and Hydrogel Sieving Structures .....</b>	<b>64</b>
<b>Chapter 6. Ion Concentration Polarization in A Single and Open Microchannel Induced by A Surface-patterned Perm-selective Film .....</b>	<b>75</b>
<b>Chapter 7. Microfabricated Ratchet Structures for Amplifying Chemotactic Responses of Motile Bacterial Cells .....</b>	<b>87</b>
<b>Chapter 8. Microfluidic Chemostat Device for Sensitive Microbial Biosensor to Detect Heavy Metal Ions .....</b>	<b>95</b>
<b>Chapter 9. Cracking-assisted Photolithography for Mixed-scale Patterning and Nanofluidics .....</b>	<b>105</b>
<b>Chapter 10. Crack-photolithography for Membrane-free Diffusion-based Micro/Nanofluidics .....</b>	<b>116</b>
<b>Chapter 11. Summary and Future Outlook .....</b>	<b>130</b>
References .....	132
Acknowledgements	
Curriculum Vita	

## List of Figures

**Figure 1–1.** Ion distribution and generation of electroosmosis flow in a microchannel under an applied electric field across the channel

**Figure 1–2.** Ion distribution and *Debye*-layer overlapping in micro-/nanochannels

**Figure 1–3.** Ion concentration polarization (ICP) phenomena in a straight micro-nano-micro channel

**Figure 1–4.** Nanochannel fabrication *via* electron beam lithography (EBL)

**Figure 1–5.** Nanochannel fabrication *via* focused ion beam (FIB) and nano imprint lithography (NIL) techniques

**Figure 1–6.** Nanochannel fabrication *via* photolithography followed by silicon etching and bonding processes

**Figure 1–7.** Nanochannel fabrication *via* thin film deposition and sacrificial-layer processes

**Figure 1–8.** Integration of nanoporous materials into microfluidic devices

**Figure 1–9.** Unconventional fabrication of nanofluidic devices using intentional material failures such as cracking and bulking

**Figure 1–10.** Nanofluidic applications to biomolecular handling such as concentration, separation and detection

**Figure 1–11.** Application of nanofluidics to ion and charge selective transport

**Figure 1–12.** Nanofluidic applications combined with microfluidic systems

**Figure 1–13.** Overview of the dissertation structure

**Figure 2–1.** Schematic view of the long-range concentration gradient generator for use with multiple compounds

**Figure 2–2.** Transient concentration gradients obtained using the transport of a fluorescence dye (50  $\mu$ M of FITC) across the H-shaped structure and along the microchannel

**Figure 2–3.** Five reservoirs containing different concentrations of glucose (as a chemoattractant) and one reservoir having only M9 media without glucose (as a control)

**Figure 2–4.** Fluorescent intensity profiles of the bands and flux of cells from the center chamber into the microchannel

**Figure 2–5.** The bacterial population and motility profiles within the bands

**Figure 2–6.** The preferential chemotaxis of bacterial cells toward five different carbon sources

**Figure 3–1.** Concept and fabrication process of the PDMS-sealed concentration gradient generator

**Figure 3–2.** Numerical simulation of diffusion in a PSH device and a CHB device

**Figure 3–3.** Characterization of concentration gradients using fluorescent and food dyes

**Figure 3–4.** Chemotaxis assay using a linear concentration gradient

**Figure 3–5.** Characterization of nonlinear concentration gradients and a chemotaxis assay

**Figure 3–6.** Chemotaxis assays in the convex and concave test channels

**Figure 4–1.** Schematic illustration of bio-sample pre-concentrator integrated with tunable ion-transport membranes

**Figure 4–2.** Fabrication process and various types of nanoporous membranes

**Figure 4–3.** Schematic description of ion concentration polarization (ICP) and time-sequential fluorescent images of biomolecule pre-concentration

**Figure 4–4.** Comparison of electrokinetic properties

**Figure 4–5.** Electrophoretic concentrations of nanobeads and bacterial cells using a non-permeable agarose hydrogel membrane

**Figure 5–1.** Working mechanism of the microfluidic device

**Figure 5–2.** Polymerization and functionalization of MTs

**Figure 5–3.** Time-lapse fluorescent images of functionalized MTs filtered by an NHM

**Figure 5–4.** Characterization of concentration enhancement factors and detection limit

**Figure 5–5.** Selective concentration of target analyte conjugates (Cy3-labeled-aptamer conjugated EGFR) and separation of non-target analytes (FITC-labeled BSA)

**Figure 5–6.** Comparison of the sensitivity of a nanobead-based detection method (TABNB) and of an MT-based detection (TABMT)

**Figure 6–1.** Schematic illustration of an open, SC-ICP device in which a Nafion film is patterned at the center of the microchannel surface

**Figure 6–2.** Characterization of charged molecule transport in an open, SC-ICP device

**Figure 6–3.** Effects of the Nafion film on SC-ICP

**Figure 6–4.** Monitoring of current over time in various electric fields showing a stable and linear relationship between the current and the potential

**Figure 6–5.** Visualization of vortex flows

**Figure 6–6.** Image sequence of 3  $\mu\text{M}$  FITC-labeled BSA pre-concentration over time (25 V/cm)

**Figure 6–7.** Concentration and lysis of bacterial cells using the SC-ICP

**Figure 7–1.** Schematic of the device that can sort and concentrate motile bacterial cells

**Figure 7–2.** Motile cells showing chemotaxis toward a carbon source (glucose) but no chemotactic response toward buffer media containing no carbon sources

**Figure 7–3.** The fluorescent intensity profile obtained from a confocal microscope across the middle channel and concentrators

**Figure 7–4.** Chemotactic responses toward different concentrations and types of carbon sources

**Figure 8–1.** A microfluidic device for microbial biosensors for detecting HMIs ( $\text{Pb}^{2+}$  and  $\text{Cd}^{2+}$ )

**Figure 8–2.** Bacterial cell growth (*E. coli*) in continuous-feed and batch modes

**Figure 8–3.** Detection of HMIs by the microfluidic device and the microbial biosensors

**Figure 8–4.** Comparison between continuous and batch-type induction of microbial biosensors

**Figure 8–5.** High-throughput characterization of the selectivity and cross-talk of the two microbial biosensor cells, HK621 and HK622, respectively, using the microfluidic device

**Figure 9–1.** Cracking-assisted photolithography

**Figure 9–2.** Control of cracking for nanopatterns with arbitrary trajectories

**Figure 9–3.** Characterisation of cracking behaviour and geometry of cracks

**Figure 9–4.** Effect of film thickness on cracking behaviour

**Figure 9–5.** Nanofluidic application of cracking-assisted nanopatterns

**Figure 10–1.** Fabrication processes of crack-photolithography for a diffusion-based micro/nanofluidic device

**Figure 10–2.** Surface morphology and dimension analysis of nanocracks during the replication processes

**Figure 10–3.** Visualization and characterization of the rate of diffusion through nanochannel arrays

**Figure 10–4.** Application of the diffusion-based micro/nanofluidic device to genetic induction assays of synthetic bacterial cells

**Figure 10–5.** High-throughput induction assays of dual-inducible cells (pZBRG) with a concentration gradient of two inducers

## List of Tables

**Table 4–1.** Properties of self-integrated nanoporous membranes

**Table 6–1.** Effects of the Nafion film thickness on the SC-ICP

## Nomenclature

**AA:** acrylic acid

**ASTM:** anion-selective transport membrane

**AFM:** atomic force microscopy

**AFMT:** aptamer-functionalized microtubules

**AHL:** acyl homoserine lactones

**BSA:** bovine serum albumin

**CCD:** charge coupled device

**CHB:** conventional hydrogel based

**CSTM:** cation-selective transport membrane

**DNA:** deoxyribonucleic acid

**DCW:** dry cell weight

**DMAEMA:** 2-(dimethylamino)-ethyl methacrylate

**DMSO:** dimethyl sulfoxide

**DC-ICP:** double channel ion concentration polarization

**EOF:** electroosmosis flow

**EOF:** electroosmosis

**EP:** electrophoresis

**EOF:** electron beam lithography

***E. coli:*** *Escherichia coli*

**EGFR:** epidermal growth factor receptor

**EGDMA:** ethylene glycol dimethacrylate

**FIB:** focused ion beam

**FITC:** fluorescein isothiocyanate

**GFP:** green fluorescent protein

**HEMA:** 2-hydroxyethyl methacrylate

**HMI:** heavy metal ions

**ISM:** ion selective membrane

**ICP:** ion concentration polarization

**IDZ:** ion depletion zone

**LCR:** limit of chemotaxis

**LB:** luria broth

**MEMS:** micro-electromechanical system

**MT:** microtubule

**MCR:** minimum chemotactic response

**M9**: minimal broth

**NEMS**: nano-electromechanical system

**NSE**: *Navier-Stokes* equation

**NIL**: nano imprint lithography

**NPM**: nanoporous membrane

**NHM**: nanoporous hydrogel membrane

**OD600**: optical density at 600 nm wavelength

**PDMS**: polydimethylsiloxane

**PDF**: pressure-driven flow

**PMMA**: polymethylmethacrylate

**PUA**: polyurethane acrylate

**PET**: polyethylene terephthalate

**PSH**: polymethylmethacrylate -sealed hydrogel

**PBS**: phosphate buffered saline

**PEB**: post-exposure baking

**ROI**: region of interests

**RFP**: red florescent protein

**RC**: receiver cells

**SC**: sender cells

**SEM**: scanning electron microscopy

**SCR**: strongest chemotactic response

**STV**: streptavidin

**SFMT**: streptavidin-functionalized microtubule

**SC-ICP**: single channel ion concentration polarization

**TB**: tryptone broth

**TABMTs**: target-analyte-bound-MTs

**TRITC**: tetramethylrhodamine isothiocyanate

**UV**: ultraviolet

**UVO**: ultraviolet/ozone

$z_i$ : valence of species  $i$

$c_i$ : concentration of species  $i$

$D_i$ : diffusivity of species  $i$

**u**: velocity vector

$R$ : molar-gas constant

$F$ : *Faraday* constant

$\phi$ : electrical potential

$\mathbf{j}_i$ : transport flux of a species  $i$

$\mathbf{J}_i$ : transport rate of a species  $i$

$\mu_{EP}$ : electrophoretic mobility

$\mu_{EO}$ : electroosmotic mobility

$\alpha$ : thermal diffusivity

$\nu$ : momentum diffusivity, kinematic viscosity

$\eta$ : dynamic viscosity

$\rho$ : density

$Re$ : *Reynolds* number

$l_c$ : characteristic length

$\zeta$ : zeta-potential

$\mathbf{E}_x$ : electricfield along  $x$ -axis

$\lambda_D$ : *Debye* layer thickness

$\sigma_c$ : concentrated stress

$\sigma_f$ : fracture strength

## Chapter 1. Introduction

### *1.1 The development of microfluidics and nanofluidics*

Microfluidics is a multidisciplinary field dealing with the precise transport of small amounts (e.g., nanoliters or even picoliters) of fluids (liquids or gases) and particles (cells or molecules) at tens to hundreds of micrometer-scale channels for a broad range of biological studies and chemical analyses. The manipulation of fluidic and molecular transports in microchannels can be advantageous to be accurate because of the intrinsic fluid ordering due to low *Reynolds* number (laminar flow) and small quantities of reagents that can be adapted rapidly to the given environmental conditions (e.g., temperature, chemical concentration and *etc.*). Furthermore, the small microfluidic device (about the size of a coin) with highly integrated fluidic networks enables accurate and high-throughput biological/chemical assays through massive parallelization with spatiotemporal controls of reaction/test environments such as chemical concentrations. The beauty of microfluidics not only is utilization of the small quantity of samples, but includes the dominance of surface effects compared to bulkmetric effects, resulting in strong capillary action, stable formation of multi-phase flows, fast heat/mass transports and even active mass transports using an external force (e.g., electric field).

As the fabrication technique develops down to the nanometer scales, nanofluidics of which at least one characteristic length scale is comparable or less than 100 nm has emerged since a few ten years ago. A transition from microfluidics to nanofluidics is analogous to the technical advance from micro-electromechanical system (MEMS) to nano-electromechanical system (NEMS) in solid mechanics. As the characteristic length ( $l_c$ ) reduces, the surface effects getting stronger and even many scientists address the nanometer domain as ‘all surface phenomena’, which is well described by the scaling law ( $S/V = l_c^{-1}$ , where  $S$  is surface area corresponding to  $l^2$ ,  $V$  is volume corresponding to  $l^3$ ). Of course, the surface dominant traits prominently featured in fluidic and ionic transports in nanofluidic systems. For example, ion transports at very near the solid surfaces show preferential migration depending on the surface characteristics such as charge density of the surface; the co-ions that have the same polarity with the surface are repelled and counter-ions that have a different polarity are attracted due to electrostatic interactions between the surface and ions. Such unique features (e.g., permselectivity) at the nanometer scale, which is hardly observed in macroscales, give possibility to develop a variety of unprecedented applications such as transport control of single molecules<sup>1</sup>, diffusion-limited molecular patterning<sup>2</sup>, and anomalously fast ionic transport<sup>3</sup> and even power generation by means of streaming currents<sup>4</sup>.

The Chapter 1 introduces the basic theory that governs mass-transport phenomena in microfluidics and nanofluidics (Ch. 1.2) and show conventional and unconventional approaches to fabricate nanofluidic channels (Ch. 1.3) and their novel applications (Ch. 1.4). The last section (Ch. 1.5) shows a brief overview and the relationship of each chapter in this dissertation.

## 1.2 Theory: mass transport in micro/nanofluidic devices

**Conservation of diluted species.** Assuming a diluted solution without chemical reactions, ions, biomolecules and even small particles are transported along micro/nanofluidic systems *via* diffusion, convection, and electromigration and the driving forces can be linearly superposed as described by the *Nernst-Plank* equation.

$$\frac{\partial c_i}{\partial t} = \nabla \cdot \left[ D_i \nabla c_i + \frac{z_i F}{RT} D_i c_i \nabla \phi \right] - \mathbf{u} \cdot \nabla c_i \quad (\text{Eq. 1-1})$$

where  $z_i$  denotes valence and  $c_i$  and  $D_i$  are concentration and diffusivity of species  $i$ , respectively.  $T$  represents the temperature and  $R$  and  $F$  are the molar-gas constant and *Faraday* constant, respectively.  $\mathbf{u}$  is a bulk fluidic velocity vector and  $\phi$  is the electric potential. By introducing the continuity equation (Eq. 1-2), the *Nernst-Plank* equation can be expressed as a flux format (Eq. 1-3) as follows:

$$\frac{\partial c_i}{\partial t} + \nabla \cdot \mathbf{j}_i = 0 \quad (\text{Eq. 1-2})$$

$$\mathbf{j}_i = \mathbf{j}_{\text{diffusion}, i} + \mathbf{j}_{\text{migration}, i} + \mathbf{j}_{\text{convection}, i} = -D_i \nabla c_i - \frac{z_i F}{RT} D_i c_i \nabla \phi + c_i \mathbf{u} \quad (\text{Eq. 1-3})$$

where  $\mathbf{j}_i$  [ $\text{mol s}^{-1} \text{m}^{-2}$ ] represents net flux of a species  $i$ . The bulkmetric convection term ( $\mathbf{j}_{\text{convection}, i}$ ) is a summation of pressure-driven flow (PDF) and electroosmosis flow (EOF). Given constant thermodynamic conditions ( $D_i$ ,  $F$ ,  $R$  and  $T$  become constant at every space and time step), the electromigration term ( $\mathbf{j}_{\text{migration}, i}$ ) can be simply expressed with the *Nernst-Einstein* equation shown as follows:

$$\frac{|z_i| F}{RT} D_i = \mu_{\text{EP}, i} \quad (\text{Eq. 1-4})$$

where  $\mu_{\text{EP}, i}$  is electrophoretic mobility of species  $i$  that describes the ability to move in response to an applied electricfield.

**Diffusion.** The diffusion is transport of species driven by kinetic energy of molecular random motions to make a thermodynamic balance, so that a species moves from a high-concentration area to a low-concentration area. The *Fick's* law describes the diffusive flux that proportional to the concentration gradient of species and the diffusivity (see  $\mathbf{j}_{\text{diffusion}, i}$  in the Eq. 1-3). Assuming one dimension and steady-state diffusion, which seems to be valid for most microfluidic applications, the diffusion flux can be simply estimated as follows:  $\mathbf{j}_{\text{diffusion}, i} \approx D \Delta c (\Delta L)^{-1}$ . The *Fick's* diffusion law can be analogous to the *Fourier's* law for heat transfer induced by a temperature gradient, and to momentum transfer caused by a velocity gradient, so that the (mass) diffusivity, thermal diffusivity ( $\alpha = k (\rho c_p)^{-1}$ ) and kinematic viscosity (also called momentum diffusivity,  $\nu = \eta \rho^{-1}$ ) have same physical meaning ( $[\text{m}^2 \text{s}^{-1}]$ ).

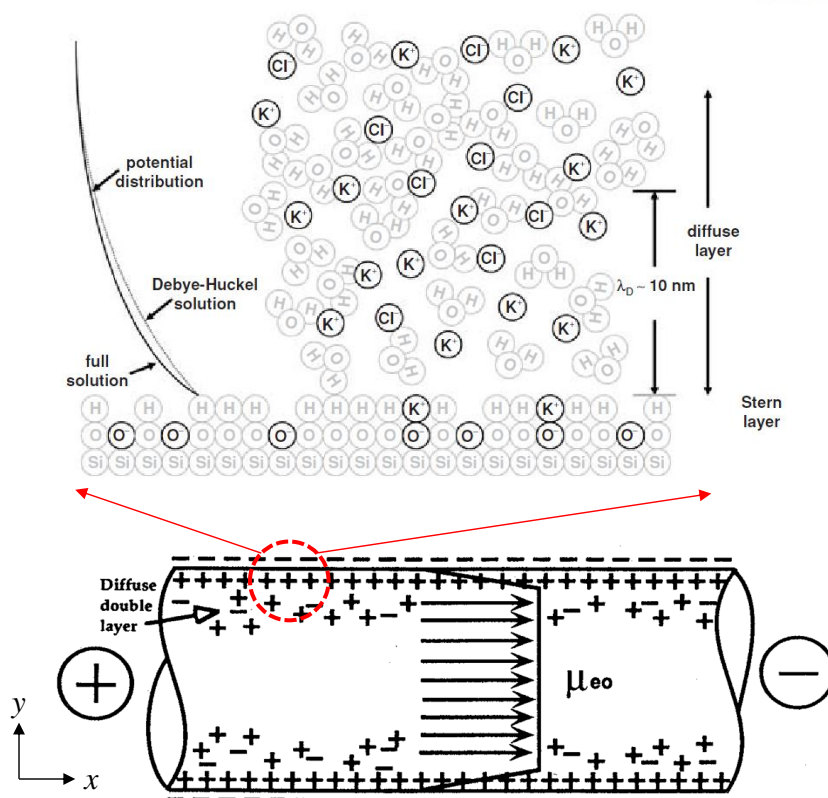


**Figure 1-1.** Ion distribution and generation of electroosmosis flow in a microchannel under an applied electricfield across the channel. The charged surface of the microchannel generates the electrical double layers to satisfy the electrical neutrality near the wall, resulting in that an ionic solution is polarized near the surface with net potentials (zeta potential). This unbalanced ionic distribution induces electrokinetic bulk flow (electroosmosis) in the presence of an applied electricfield across the channel. Figure was adapted from the ALChemE (<http://alcheme.tamu.edu>).

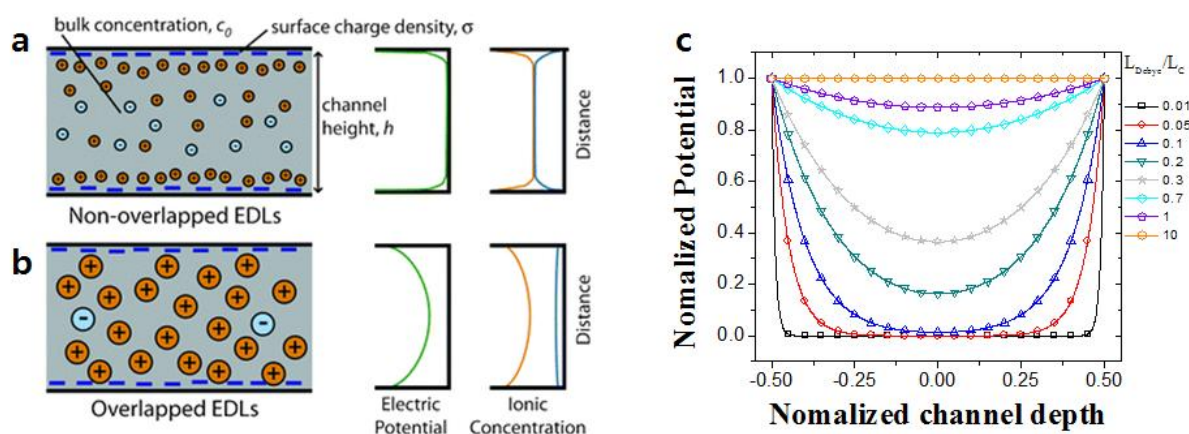


**Figure 1-2.** Ion distribution and *Debye*-layer overlapping in micro-/nanochannels. (a) Ion distribution and charge distribution in microchannel show non-overlapped electric double layer (EDL). (b) Ion and charge distribution in a nanochannel shows overlapped EDL, resulting in counter-ion dominance in the nanochannel, called permselectivity. (c) Normalized potential distribution along the nanochannel height shows significant overlapping phenomena as the characteristic length (height) of the nanochannel is comparable the *Debye*-layer thickness. Figures (a) and (b) were adapted from Karnik *et al.*<sup>5</sup> © 2010 American Chemical Society (ACS). All rights reserved.

**Hydrodynamic convection.** In addition to diffusion, a bulkmetric fluidic motion (convection) leads to a species flux and described by the *Navier-Stokes* equation (NSE) shown as follows:

$$\frac{\partial \mathbf{u}}{\partial t} + (\mathbf{u} \cdot \nabla) \mathbf{u} - \nu \nabla^2 \mathbf{u} + \frac{1}{3} \nu \nabla (\nabla \cdot \mathbf{u}) = -\nabla \frac{w}{\rho} + \mathbf{g} \quad (\text{Eq. 1-5})$$

where  $\nu (= \eta \rho^{-1})$ , where  $\eta$  is the dynamic viscosity,  $\rho$  is the density) is kinematic viscosity,  $w$  and  $\mathbf{g}$  represent internal and external sources, respectively. In the absence of applied external forces ( $\mathbf{g}$ ) such as electric fields, magnetic fields, and acoustic fields, the second term in the right hand side (RHS) becomes zero because the gravity force seems to be negligible in most micro-/nanochannels due to small heights of channels. Also, fluids in micro/nanofluidics are mostly incompressible (e.g., water) so that the fourth term in the left hand side (LHS) of the NSE becomes negligible. Interestingly, the flow regime of most microfluidics is the creeping flow (also called *Stokes* flow or laminar flow) because the small characteristic length ( $l_c \approx 10^{-6}$ – $10^{-4}$  m) keeps *Reynolds* number ( $Re = \nu^{-1} \mathbf{u} l_c$ ) comparable or less than 1, meaning that the nonlinear turbulence term in the NSE (the second term in LHS of Eq. 1–5) becomes negligible. Assuming that the internal source is only pressure ( $w = P$ ) and the flow is fully developed to a steady state, the full NSE can be simplified as follows:

$$\eta \nabla^2 \mathbf{u} - \nabla P = 0 \quad (\text{Eq. 1-6})$$

Therefore, the bulk fluidic velocity in a microchannel becomes a function of a pressure gradient, called hydrodynamic flow or PDF. This PDF is often negligible in a shallow nanofluidic channel due to a high hydraulic resistance.

**Electrokinetic convection (electroosmosis flow).** EOF is bulkmetric fluidic motion induced by an applied electric field across a microfluidic channel having charged surfaces. As shown in Fig. 1 a microchannel made of glass or Polydimethylsiloxane (PDMS) has a negative charge density and this surface charge leads to the creation of an electric double layer. The first layer (surface charge layer) is stuck ions in the wall surface owing to a chemical reaction. The second layer (diffusive layer or *Debye* layer) is composed of movable ions near the surface due to influences of electrostatic interaction and thermal motion. This net charge, called zeta potential, in the *Debye* layer is equal to the surface charge of the wall but the polarity is opposite.

Once an electric field is applied across the microchannel, the counter ions in the *Debye* layer show a collective motion toward an opposite electrode to their polarity (negative electrode in Fig. 1–1). This collective ion movement generates a bulk flow *via* momentum transfer from moving ions to bulk solvent molecules (water); this is referred to EOF. The flow profile of the EOF is uniform in a microchannel as it is generated near the wall as shown in Fig. 1–1. On the other hand, the profile of PDF is parabolic due to the non-slip boundary condition of the surface. In addition, the EOF is linearly proportional to the applied electric field and the zeta potential that can be influenced by the

surface charge density of the wall and concentrations of ions in the bulk solution, which is expressed by *Helmholtz-Smoluchowski* equation:

$$\mathbf{u}_{EOF} = \frac{\varepsilon\zeta}{\eta} \mathbf{E}_x = \mu_{EO} \mathbf{E}_x \quad (\text{Eq. 1-7})$$

where  $\mathbf{E}_x$  is the electricfield across the microchannel,  $\zeta$  is the zeta-potential, and  $\mu_{EO}$  is the electroosmosis mobility.

In nanochannels, a bulk solution can be transported by a longitudinal pressure gradient (PDF) and an electricfield (EOF). The average flow velocity is obtained by superimposing both velocity profiles and averaging across the nanochannel. However, the PDF is often ineffective compare to the EOF due to the high hydraulic resistance in the nanochannel. In addition, *Debye* layer thickness ( $\lambda_D \approx 0.5\text{--}200\text{ nm}$ ) and other physicochemical characteristic lengths become comparable to the dimension of the nanochannel (see Fig. 1-2) so that unique fluidic motions are shown, which is rarely observed in micrometer scales or above. For example, the EOF profile, which is uniform in microfluidics, approaches a parabolic shape in nanochannels with *Debye* layer overlap due to electro-potential gradients near the wall. In addition, there are anomalously rapid fluidic transports<sup>3</sup> due to interactions between charged wall and solute and even between charged wall and solvent such as *Van der Waals* interaction, hydrophobic interaction, and *Debye* layer overlap<sup>6</sup>.

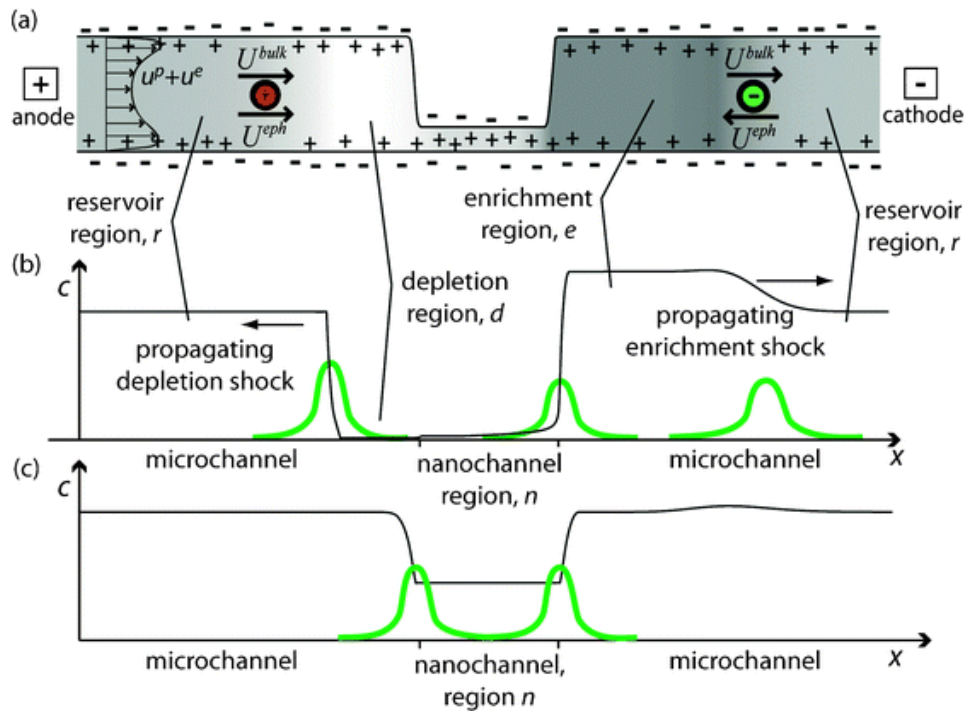


**Figure 1-3.** Ion concentration polarization (ICP) phenomena in a straight micro-nano-micro channel. The permselective ion transport in a nanochannel induces the ion depletion in the anodic microchannel (left) and the ion enrichment in the cathodic microchannel (right). The electricfield gradient in the depletion area keeps charged particles and molecules immobile by balancing bulk and electrophoretic mobilities; the net mobility of the charged particles becomes zero. Figure was adapted from Zangle *et al.*<sup>7</sup> © 2010 Royal Society of Chemistry (RSC). All rights reserved.

**Summary.** The mass-transport phenomena in micro-/nanochannels are attributed to diffusion, convection (PDF and/or EOF) and electromigration (electrophoresis) as described in the flux conversation (Eq. 1–3). In the absence of an applied electricfield, the contribution of the EOF and electromigration is negligible, so that the diffusion and convection governs the transport phenomena. Furthermore, nanochannels and nanopores are often used to prevent the unwanted convective transport caused by a pressure gradient by increasing the hydraulic resistance of the channels; the hydraulic resistance proportional to  $(r)^{-4}$  in circular channel and  $h^3$  in rectangular channel. Therefore, pure diffusion-based transport offers accurate and spatially controllable chemical environments by forming a steady concentration gradient; the concentration of a species is determined by the position of the system. In contrast, the PDF transport can change the concentration of a species rapidly so that it is favorable for temporal control of chemical concentrations.

In the presence of an applied electricfield across micro and/or nanochannels, the diffusive transport can be negligible due to even higher mass flux by electromigration and convection (EOF and PDF). In many cases, the PDF also can be minimized by keeping the balance of hydraulic heads in reservoirs, resulting in that the mass transport is only governed by the electricfield. This electricfield-guided transport enables active control of fluidic and particle motions. Furthermore, the charge density of channel surface is often naturalized to suppress the unwanted EOF effect by functionalizing the surface with non-charged material (c.a., polyimide) or by extremely increasing the buffer concentrations (the increasing buffer strength minimizes formation of *Debye* layer, however it also increases conductivity which can induce side effects such as *Joule* heating). With suppression of the EOF, the mass-transport mechanism is pure electromigration (electrophoresis) which can be an intrinsic material property. Thus, it is possible to conduct an accurate transport and separation of charged particles such as biomolecules and cells, according to the electrophoretic mobilities.

### ***1.3 Conventional and unconventional fabrication of nanofluidic devices***

**Overview.** Most microfluidic devices are fabricated by the well-developed and standardized photolithography and duplicated by the soft lithography. For the nanochannels, however, there is no standardized method so that various methods are used together or in serial depends on the possessing fabrication facilities and environmental conditions. One of the most precise methods to fabricate nanochannel is conventional nanolithography techniques that utilize high-energy-beam sources such as ion and electron. They directly etch or harden a foundation material through sequential exposure of the beams without beam-blocking structures called mask. Another approach uses top-down or bottom-up MEMS/NEMS fabrication techniques such as silicon etching and thin film depositions in conjunction with selective patterning of mask layers *via* photolithography. In addition, the fabricated nanochannel using conventional nanolithography and MEMS-based techniques is often duplicated *via* nanoimprinting/molding and soft lithography to reduce the fabrication cost and time. An alternative

way to fabricate nanofluidic channels is the use of nanomaterials that have nanoporous or nano-clustered structures such as commercial nanoporous membranes, hydrogels, and even self-assembled nanostructures. More recently, designed material failures such as cracking, wrinkling and folding are highlighted as time/cost-efficient methods to create fine patterns at micro-/nanoscale. The nanofabrication using intentional material damages can be done with exquisite control of stress fields over materials and spatiotemporal engineering of material properties, leading to the high-throughput and accurate fabrication of nanopatterns or nanochannels. In this section, I review the current nanofabrication technologies to produce the nanofluidic channels and compare the pros and cons of each method to unveil potential openings for next generation nanofabrication.

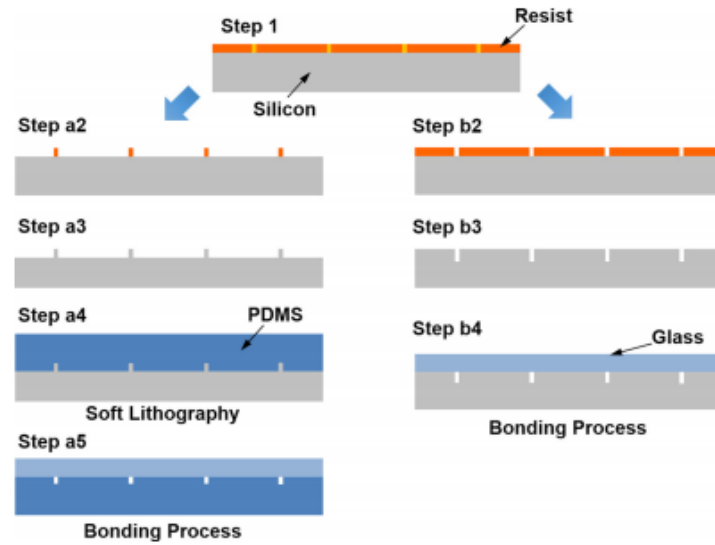


**Figure 1–4.** Nanochannel fabrication *via* electron beam lithography (EBL). The left and right processes show EBL-based nanochannel fabrication using the negative and positive e-beam resists, respectively. Figure was adapted from Duan *et al.*<sup>8</sup> © 2013 American Institute of Physics (AIP). All rights reserved.

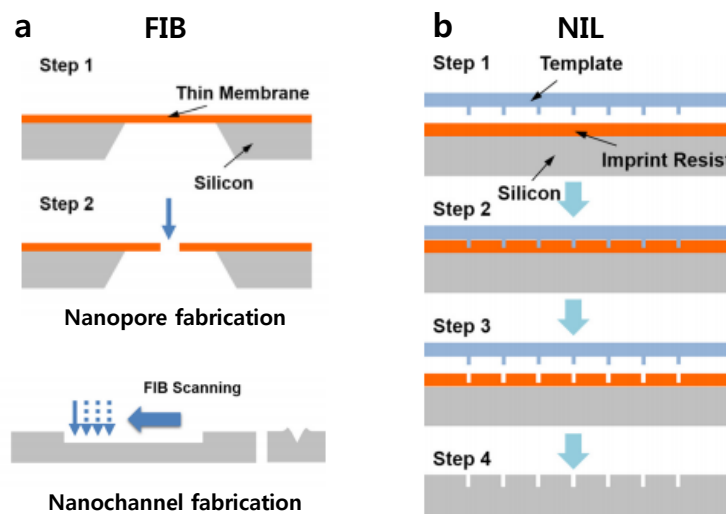


**Figure 1–5.** Nanochannel fabrication *via* focused ion beam (FIB) and nano imprint lithography (NIL)

techniques. The left processes show the FIB technique to fabricate nanopores though drilling thin membrane and nanochannels though directly milling the hard substrate. The right is the NIL method to replicate a nano-patterned template. Figures were adapted from Duan *et al.*<sup>8</sup> © 2013 AIP. All rights reserved.

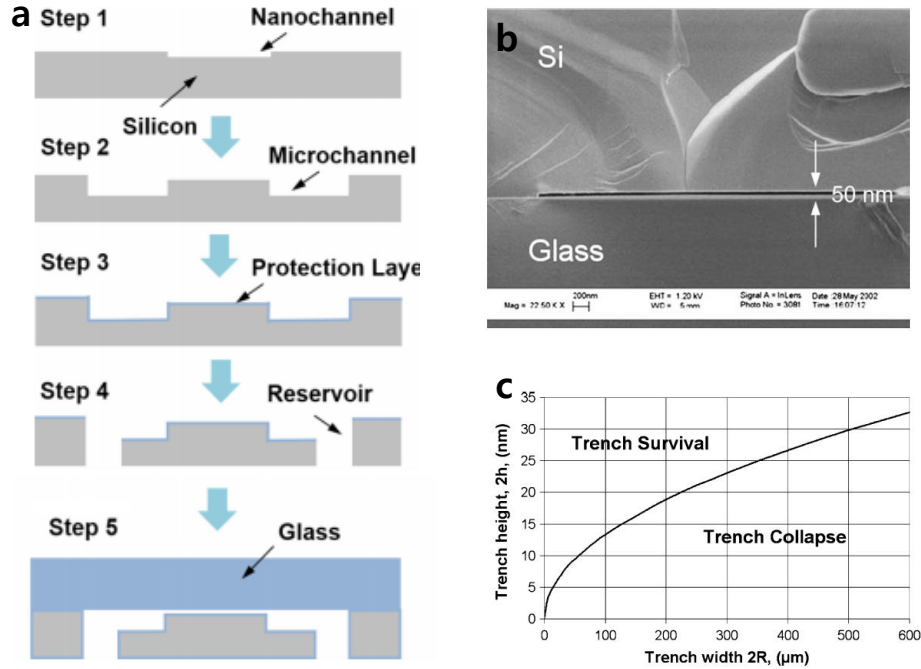


**Figure 1–6.** Nanochannel fabrication *via* photolithography followed by silicon etching and bonding processes. (a) The semantics shows silicon etching and bonding technique to fabricate nanochannels. (b) The scanning electron microscopy (SEM) image shows the produced Si-glass nanochannel. (c) The shallow and wide nanochannels (nanoslit) are susceptible to the roof-collapse. Figures (a) and (b) were adapted from Duan *et al.*<sup>8</sup> © 2013 AIP and Haneveld *et al.*<sup>9</sup> © 2003 *Institute of Physics Publishing*, respectively. Figure (c) was adapted from Kim *et al.*<sup>10</sup> © 2003 *The American Society of Mechanical Engineers*. All rights reserved.

**Conventional nanolithography.** Electron-beam lithography (EBL) is one of the most precise methods to fabricate nanochannels. The EBL employs emitting nano-sized spots of electron beams to electron-sensitive or electron-resistive materials such as polymethylmethacrylate (PMMA) for removing unexposed or exposed resist in a selective manner. The patterning method of the EBL is similar with the photolithography (i.e., resist coating, exposure, and development), but does not require photo-masking structures because the EBL draws patterns directly using the nanoscale e-beam with automated scanning. After patterning the e-beam resist on a silicon wafer, the pattern can be directly used for nanofluidic mold for PDMS-based soft lithography or can be used as a masking layer for substrate etching. Fig. 1–4 shows various nanochannel fabrication processes using the EBL technique.

Another general method is the focused ion beam (FIB) technique (Fig. 1–5 (a)). As similar as the EBL, the FIB technique utilizes sequential exposure of a nanoscale ion-beam spots that can physically damage to a substrate by ion bombardment. Because the ion beam has a much higher power density

than the e-beam, it can directly generate nanoscale scribed patterns on hard substrates without the use of masking structures and resist deposition. Thus, the FIB drilling and milling is used frequently to create nanopores on a thin silicon membrane and to generate nanoscale trenches on a hard substrate (e.g., glass) that become a nanochannel after bonding with a rigid slab.

In addition to the ELB and FIB, which have limitation in fabrication throughput owing to the direct scanning mechanism, the nanoimprint lithography (NIL, Fig 1–5 (b)) is a high-throughput technique of which a large number of nanochannels can be duplicated from a master template. The NIL replicates the pre-defined nanoscale features on a rigid template by mechanically pressing conformal imprint resists. After deforming the imprint resist, photo or thermal energy is applied to harden the resist followed by releasing the master mold. In this manner, an array of nanochannels can be duplicated repeatedly. However, the NIL technique can be cost-ineffective when a template mold is only used for limited replication times, meaning that the master molds should be produced by other expensive nanolithography techniques.

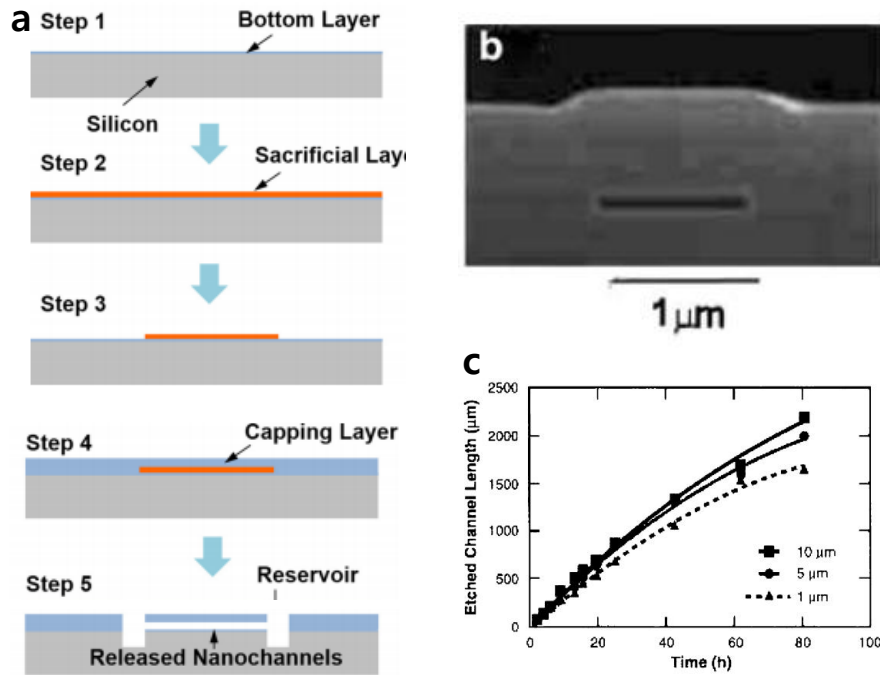


**Figure 1–7.** Nanochannel fabrication *via* thin film deposition and sacrificial-layer processes. (a) The schematics show a fabrication process for a nanochannel using sacrificial-layer releasing. (b) SEM image shows the produced nanochannel using the sequential thin-film deposition and patterning processes. (c) Characterization of the etching rate shows the slow sacrificial-layer releasing process due to the diffusion limitation. Figure (a) was adapted from Duan *et al.*<sup>8</sup> © 2013 AIP. Figures (b) and (c) were adapted from Stern *et al.*<sup>11</sup> © 2013 AIP. All rights reserved.

**Top-down and bottom-up MEMS fabrication.** The standard photolithography technique is used to fabricate not only microchannels but also nanoslit-shaped channels (2-D nanochannel) by combination with bulk machining of an Si wafer and a bonding process. The standard photolithography defines the width and length of the nanochannel by patterning photoresists as a

masking structure during etching process. The elimination of a bulk Si material is usually done by a dry etching (e.g., reactive ion etching) or a wet etching (e.g., KOH solution) (Fig. 1–6 (a)). It means that the critical dimension for nanochannels (height) is controllable according to the etching rate of a Si/glass substrate. After the nanochannel fabrication, similar photoresist patterning and selective Si etching are employed to fabricate microchannels. Then the etched nano-height and micro-height trenches are covered by a glass slab using a thermal or anodic bonding technique to seal the channels. The photolithography technique with silicon etch is relatively simple and cost-effective due to the batch processing throughout a large wafer, but the applications of the nanochannel can be restricted by the 2-D nanochannel shape (nanoslit, see Fig. 1–6 (b)). Furthermore, the bonding process is susceptible to defects and dust on the substrate. Also, the ultra-shallow nanochannel with a low aspect ratio is vulnerable to the collapse of top and bottom surfaces (Fig. 1–6 (c)).

The nanochannels can be also fabricated by surface machining by using the photolithography technique with thin-film deposition for the sacrificial-layer process (SLP, Fig. 1–7 (a)). The SLP is a representative bottom-up approach that utilizes sequential stacking of selectively-patterned thin films. In this process, 2D nanochannels are formed with nanometer-thick sacrificial layers that can be removed through a selective etching process to create the nanochannels (Fig. 1–7 (b)). Although many inorganic and organic materials are employed as the sacrificial material to produce nanochannels, the removal of the sacrificial layer requires a long immersion time in an etchant solution (Fig. 1–7 (c)). For example, it takes up to 80 h of etching time for a 2-mm long nanochannel ( $w = 10 \mu\text{m}$ ,  $h = 50 \text{ nm}$ ).

**Nanomaterial based approach.** Nanoporous materials such as hydrogels and commercial membranes are integrated with microfluidic channels to construct micro and nanofluidic interfaces. The nanoporous material is a cluster of randomly-distributed nanopores and it is analogous to massive arrays of nanochannels (3-D nanoporous matrix). Therefore, the mass-transport flux through a nanoporous membrane is even higher than a conventional nanochannel, which allows rapid and high-throughput analysis. Usually, the integration of nanoporous material has been done by sandwiching a nanoporous membrane between top and bottom microchannels (Fig. 1–8 (a) and (b)). This sandwiching method can produce micro/nanofluidic interfaces without expensive nanofabrication processes and equipment, but often susceptible to fluid leakages due to weak sealing/bonding, leading to high run-to-run variation in controlling mass transports. Furthermore, the observation of the device can be disrupted when the membrane is an opaque.

To overcome the limitations, a nanoporous material is embedded into a microchannel as a short microplug (Fig. 1–8 (c)). The nanoporous microplug is initially introduced as a precursor solution followed by solidification through UV exposure for selectively curing a small region by focusing UV light or using photo-masking structures. On the other hand, when a precursor solution requires temperature treatment or evaporation control for solidification, the precursor should be patterned in a specific region of microchannels to form a microplug. For this, flow guiding structure is used to

control capillary forces and surface tension of the solution. Thus, various nanoporous hydrogels and self-assembled nanoparticle clusters, and even ion selective polymers are integrated with microchannel in a leakage-tight and size-controllable manner. However, the assembling process of the nanoporous materials with microchannels relies on a manual operation, leading to time consumption, incompatibility with other lithography techniques, and difficulty in accurate control of mass transport.

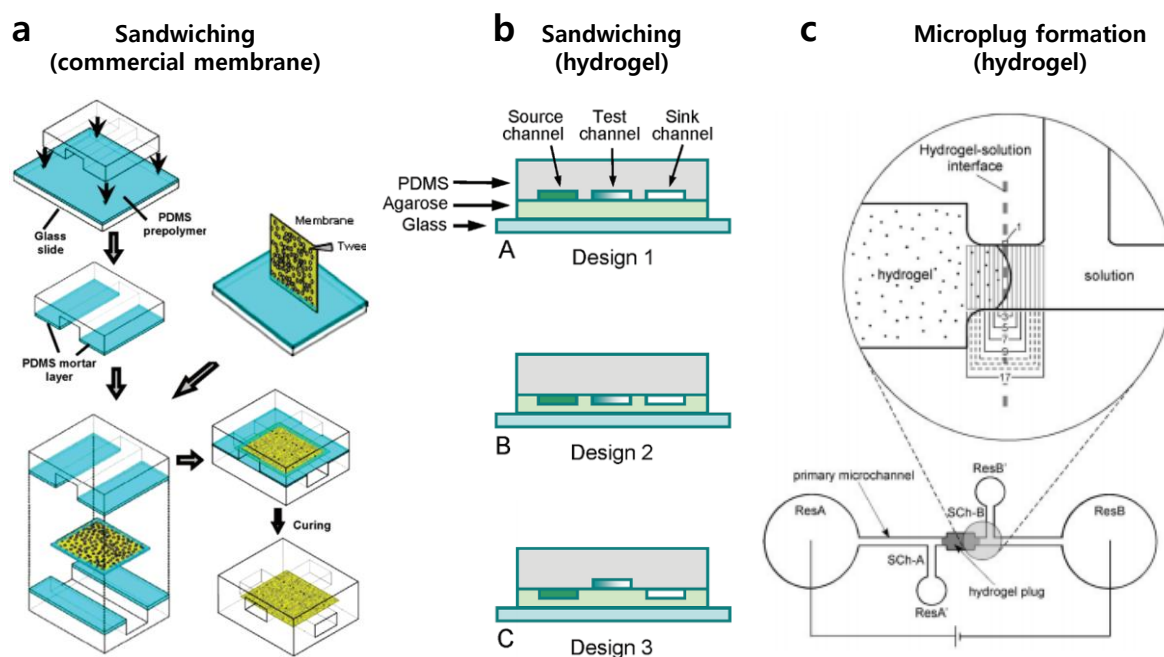


**Figure 1-8.** Integration of nanoporous materials with microfluidic devices. (a) A commercial nanoporous membrane is sandwiched between top and bottom microchannels. (b) A nanoporous hydrogel slab is sandwiched between a microchannel and a glass substrate as a role of the diffusion layer. (c) A hydrogel microplug is integrated into a microchannel using local solidification of a precursor solution. Figure (a) was adapted from Chueh *et al.*<sup>12</sup> © 2007 ACS. Figures (b) and (c) were adapted from Ahmed *et al.*<sup>13</sup> © 2010 ACS and Dhopeswarkar *et al.*<sup>14</sup> © 2005 RSC, respectively. All rights reserved.

**Material-failure-based nanopatterning.** Morphological instabilities of thin films induce surface buckling (wrinkling)<sup>15</sup>, folding, and even cracking<sup>16</sup> and they are rarely welcomed and considered to be avoided in most academic and industry fields. In recent years, however, the failures of thin films have been designed and engineered intentionally because they are expected to serve as a substitute for the conventional, labor and cost intensive nanolithography techniques. Also, the nanopatterns, particularly nanoscale grooves produced by the cracking and buckling have high potential to be developed as a nanofluidic device by bonding the nanopatterns with a rigid slab. For example, the top surface of an elastomeric PDMS substrate is oxidized to form a thin and brittle oxide cluster on top of the PDMS (Fig. 1-9 (a))<sup>17</sup>. Given an applied tensile stress, the oxidized layer is more vulnerable to cracking than the elastic foundation because of brittle nature and low fracture toughness of the oxide layer. It means that the axial tensile stress induces elastic deformation to the PDMS foundation, but

permanent deformation (cracking) to the top oxidized layer. Subsequently, a number of straight cracks are generated in the oxide film, aligned perpendicularly to the direction of the applied tensile stress. Then the crack pattern is replicated by a positive pattern using a UV-curable epoxy which is again used as a master mold for PDMS-based soft lithography. After the soft lithography, the nanopattern (nanochannel) is bonded with a micropatterned PDMS (microchannel) to fabricate a leakage-tight micro-/nanochannel networks. Generally, crack is induced in pinholes or notch structures that concentrate a stress field to a tip point more than atomic bond energy<sup>18</sup>. The initiated crack propagates along the maximum stress field until the concentrated stress at a crack tip is released below a fracture point. Therefore, the precise manipulation of a tensile stressfield is a key factor to design cracks for producing nanochannels in a controllable manner.

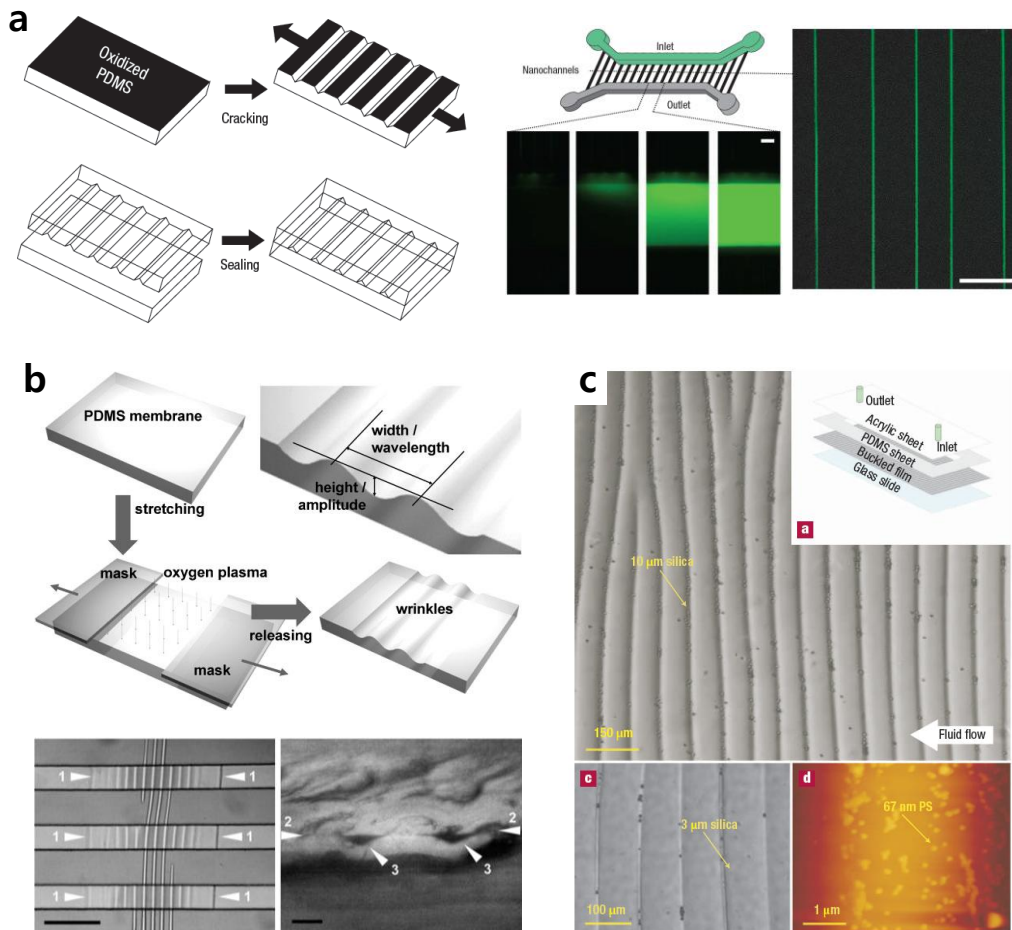


**Figure 1–9.** Unconventional fabrication of nanofluidic devices using intentional material failures such as cracking and bulking. (a) A PDMS slab is uniformly oxidized and then stretched by a tensile stress resulting in generation of straight cracks on the oxide layer. (b) and (c) Pretreated elastic deformation of PDMS slab during an oxidization process induces a compressive stress to generate buckling structures by removing the tensile stress. The cracked and bucked surfaces are covered by a flat slab to make a nanofluidic device. Figures (a) was adapted from Huh *et al.*<sup>17</sup>. © 2007 NPG. Figures (b) and (c) were adapted from Chung *et al.*<sup>19</sup> © 2008 John Wiley & Sons and Efimenko *et al.*<sup>15</sup> © 2005 NPG, respectively. All rights reserved.

On the other hand, buckling (wrinkling) is a failure mode of a thin film subjected to a high compressive stress<sup>15, 20</sup>. As shown in Fig. 1–9 (b), an elastically stretched PDMS substrate is oxidized to form a brittle oxidized film on the top surface of the elastomer<sup>19</sup>, resulting in formation of the similar bi-material structures used in the cracking method. The major difference of the buckling method compared to the cracking is a pretreated elastic deformation of the PDMS, which eventually exerts a compressive stress to the top oxide film because of elastic shape recovery of the PDMS underlayer by removing the stretching force after finishing the oxidization process. That is, the degree of the pretreated elastic deformation in the PDMS controls the magnitude of a compressive stress that determines bulking dimension and density. As shown in Fig. 1–10 (c), the similar shape-recovery phenomena of the elastomer is used after stretching a PDMS slab during thin oxide layer formation using ultraviolet/ozone (UVO) treatment<sup>15</sup>. This UVO treatment generates stiffness oxide film layer on the top surface of the PDMS, which undergoes contraction after removing the stretching force. Depending on the releasing rate of the stretching force, various buckling patterns are created.

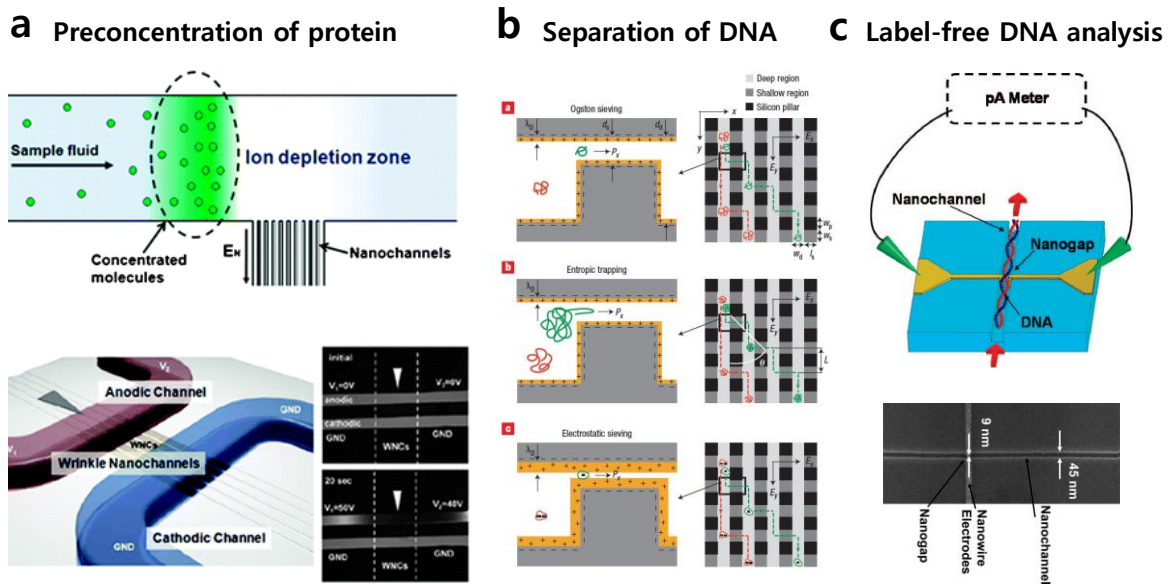


**Figure 1–10.** Nanofluidic applications to biomolecular handling such as concentration, separation and detection. (a) Charged biomolecules are pre-concentrated by using ion concentration polarization in micro/nanofluidic interfaces. (b) The alternating micro-/nanochannel network separates DNA molecules according to their size, mobility and deformability. (c), A DNA detector with a nanogap inside a nanofluidic channel is used to stretch a DNA strand into a linear chain, with a nanogap detector to measure electrical conduction according to the backbone of a DNA strand. Figures (a) and (b) were adapted from Chung *et al.*<sup>19</sup> © 2008 John Wiley & Sons and Fu *et al.*<sup>21</sup> © 2007 NPG, respectively. Figure (c) was adapted from Liang and Chou<sup>22</sup> © 2008 ACS. All rights reserved.

#### 1.4 Applications of micro/nanofluidics

**Overview.** The transport of small particles and biomolecules in nanochannels shows many unprecedented characteristics such *Debye* layer overlapping so that it has high potential for various applications in both science and engineering fields. Particularly, the characteristic length of

nanochannels is comparable to the geometric dimensions with many biomolecules such as protein and DNA, so that the nanofluidic device is widely applied to enrichment, separation and detection of biomolecules. In addition to the biosamples preparation, the mass and charge transport in a nanochannel having a permselective trait is applied to functionalize nanofluidic surface and ion-selective membranes, and even to develop ionic transistors. One of the more efficient strategies of nanofluidics is integration with microfluidic systems, forming integrated micro/nanofluidic interfaces to conduct accurate fluid manipulation and biochemical assays. For example, the fluidic handling was enabled by using an electrokinetic valve, mixer and pump. In this section, I summarize various nanofluidic applications by categorizing into three parts: preparation of biosamples, manipulation of mass and charge transport, and combination with microfluidic technologies.

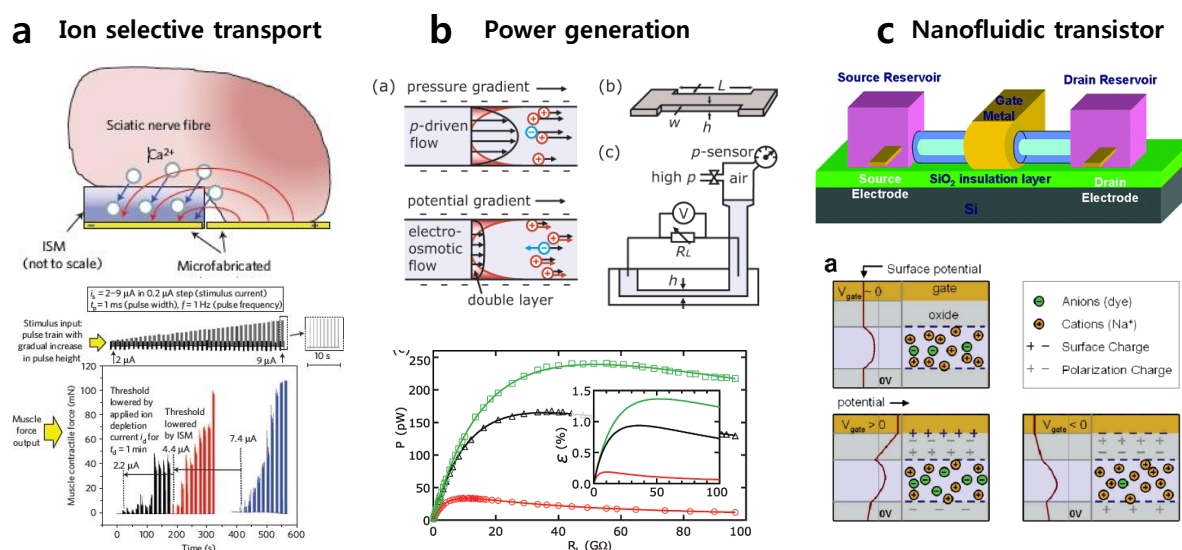


**Figure 1–11.** Application of nanofluidics to ion and charge selective transport. (a) An ion-selective membrane coated on top of a planar microelectrode is applied to a muscular nerve system using transport control of  $\text{Ca}^{2+}$  ions. (b) The permselective trait of a nanochannel is applied to produce electrical power using streaming current that is driven by a pressure gradient. (c) The permselectivity of a nanochannel is tuned actively by applying a gate potential, resulting in a nanofluidic transistor. Figures (a) and (b) were adapted from Song *et al.*<sup>23</sup> © 2011 NPG and Yang *et al.*<sup>4</sup> © 2007 ACS, respectively. Figure (c) was adapted from Karnik *et al.*<sup>5</sup> © 2005 ACS. All rights reserved.

**Preparation of biosamples.** In real biosamples such as a patient's blood, the target analyst often exists with extremely low concentration and is mixed complexly with other biomolecules and cells. For this reason, the enrichment and separation of target biosamples are essential for sensitive and selective detection and accurate bioanalysis. Nanofluidics that has similar dimensions with many biomolecules is advantageous to concentrate and separate biomolecules such as protein and DNA. For example, a local electricfield gradient is applied to concentrate charged biomolecules continuously near micro/nanofluidic interfaces where the electrophoretic mobility and bulk (EOF) mobility are balanced<sup>7, 19</sup>. The electricfield gradient is induced by permselective ion transport of the nanochannel that breaks the electrical neutrality and generates the ICP phenomena (Fig. 1–10(a)). In the ion

depletion zone, the bulk ionic concentration (conductivity) is lower than the average value through the microchannel so that the magnitude of the electric field increases to compensate reduced concentration effects and satisfy the electrical continuity. This electrical barrier prevents passage of charge biomolecules, resulting in continuous concentration and separation of charged particles and molecules depending on their electrophoretic motilities.

As much as preconcentration of biosamples, separation of DNAs and proteins is also important for accurate analysis of a specific target molecule (Fig. 1–10(b)). The nanofluidic trapping device has been well developed for the biomolecule separation<sup>21, 24</sup>. The basic concept of the micro/nanofluidic trapping array is alternating thin nanochannels and thick microchannels. The height of the nanochannels is shallower than the effective radius of target DNA molecules, and thus it acts as a mechanical sieve. In the thick microchannels, DNA molecules are tangled and coiled spontaneously because the spherical rolled shape is the equilibrium states. However, DNA molecules are deformed to travel through the thin nanochannels region as soon as an electric field is applied. This mechanical conformation change makes DNA molecules trapped temporarily at the entrance of the nanochannel. Interestingly, this temporal trapping time in nanochannel is different according to the length of DNAs, which leads to separation of DNAs depending on their length and motilities.

The preconcentration and separation are essential preparation steps for sensitive and selective detection and analysis of biomolecules such as DNAs (Fig. 1–10(c))<sup>22</sup>. Many nanofluidic devices perform stretching a DNA strand into a nanochannel and analyzing the stretched DNA by using a nanogap detector, an electrode pair inside the nanochannel. As the DNA molecules pass through the nanochannels or nanopores, the ionic current (conductivity) between two measuring electrodes in the nanochannel is reduced because the DNAs have lower conductivity than most ionic buffer solutions. Therefore, the current profiles such as the magnitude and bandwidth are changed according to the DNA backbones and DNA lengths. In the similar manner, the frequency of the reduced peaks in the current profile gives the concentration information of the DNAs or nanoparticles in a buffer solution. This nanofluidic detector enables analyzing DNAs in real-time and sequencing without molecular labels such as fluorescents or antibodies that can be a major time delay for the analysis.

**Manipulation of mass and charge transport.** The unique ability of nanofluidic channels and nanopores is the permselective transport of ions and charges, resulting in accurate control of transport phenomena in the presence of an electric field. For example, the ionic selectivity of nanofluidics is applied to the electrochemical activation and inhibition of neural-muscular tissues *via* modulation of  $\text{Ca}^{2+}$  concentrations with permselective Nafion membranes (Fig. 1–11(a))<sup>25</sup>. The Nafion film coated on a micropatterned electrode allows selective transport of small positive ions, but minimizes the other ionic transports to achieve different excitability states of the nervous, depending on the local concentration of  $\text{Ca}^{2+}$ . As a result, the electrode coated by the ion selective Nafion shows a reduced electrical threshold value (4.4  $\mu\text{A}$ ) for the muscular stimulation compared to the electrode without the

Nafion coating (7.4  $\mu\text{A}$ ). This reduction of the threshold is achieved by the contribution of triggered ion depletion with the role of stimulus current simultaneously.

The ion selective transport in nanofluidics are also useful for energy conversion *via* streaming current which originates when an ionic solution is flowed by a pressure gradient through a charged nanochannel or nanopores (Fig. 1–11(b))<sup>4</sup>. Because the electrical neutrality of an electrolyte is broken in a nanochannel due to the *Debye* layer overlapping, the bulkmetric flow driven by a pressure gradient generates net charge transport; the counter ions of the wall charge are transported selectively by the bulk flows. This steaming effect is the reverse process of the bulk EOF driven by an electric potential gradient (electricfield). Although the power density generated by the streaming current is small compared to the required pressure to overcome high hydraulic resistance of a nanochannel, it is often used to measure the zeta potential of surfaces, which is one of the most important properties in nanofluidics and colloidal sciences.

The surface charge condition of the nanochannel can be actively tuned by the induced charge. It means that the nanofluidic channel acts like a gate electrode of a field-effect transistor (FET) in semiconductors, so that this phenomenon is called as nanofluidic FET<sup>5</sup>. As shown in Fig. 1–11(c), it is possible to regulate the zeta potential of the nanochannel by mounting an electrode on a nanochannel as the gate electrode. The nanofluidic FET consisting of three layers as similar as the metal-oxide-semiconductor FET (MOSFET); an oxide layer (dielectric material) is sandwiched between the top metal electrode (gate) and the bottom silica nanofluidic channel. Thus, the ionic current through nanochannel is changed according to the applied potential on the gate electrode. As the MOSFET plays an important role for the solid electronics, the nanofluidic transistor is the fundamental component to build a highly-integrated fluidic circuit for the logical manipulation of mass and ionic transport.

**Combination with microfluidics.** Although the nanofluidics itself shows many unique and interesting phenomena, the integration of nanofluidics into microfluidic systems enables more systematic fluidic manipulation such as valving<sup>26</sup>, pumping<sup>27</sup> and mixing<sup>28</sup> by creating integrated micro/nanofluidic interfaces. For example, Fig. 1–12(a) shows the direct sea water desalination using ICP phenomena that can be formed on a micro/nanofluidic interface<sup>29</sup>. The ion depletion region acts a role of the electrical barriers to repel any charged particles and ions, resulting in continuous filtration of ionic salts and charged particles. The seawater sample was intentionally mixed with fluorescent dyes to visualize the desalinization. As similar as the fluorescent dyes (ions), any charged particles found in the sea water, including most solid particles, microorganisms and biomolecules (proteins, bacteria, viruses, and blood cells), can be separated from the water. The mass/charge transport manipulation at micro/nanofluidic interface also can be used for a fluidic pump<sup>27</sup>.

As shown in Fig. 1–12(b), the two neighboring glass fluidic channels with a nanoscale gap, called nano liquid glass electrode (NLGE), shows new transport phenomena that allows current flows even

along the disconnected glass gap. The NLGE, which is fabricated by the femto-second laser processing, can turn on and turn off the current conduction by controlling the magnitude of external electrical potentials. On the other hand, there is negligible fluid transport through the glass nanogap, because the current conduction happens through the very small area created by an electric breakdown of the glass nanogap. This allows dielectric materials such as glass to serve as conductors, eliminating the need to incorporate metal gate electrodes. As an example application, the NLGE is applied to an electrokinetic pump. When an electric potential is applied along the NLGE, the electric current generates the EOF that induces the pressure build-up near the glass gap. The pressure-driven back flow along the channels is manipulated actively by the magnitude of applied electric potential, which can generate sufficient flows for accurate microfluidic actuators.

As similar to the electrokinetic pump, unique mass-transport phenomena in nanofluidics can be used for fluid mixing in microchannels where the mixing is very slow because the mixing is driven by only diffusion in laminar flows<sup>28</sup>. As shown in Fig. 1–12(c), the two separated flow streams are gathered at the micro/nanofluidic junction where the two flows undergo fast convective mixing because the nonlinear electrokinetic phenomena at the micro-/nanochannel interface generates strong vortex flows. This vortex generated by the ionic permselectivity of the nanochannel shows even faster fluid mixing than the conventional PDF-based mixing that is used in most microfluidic devices.

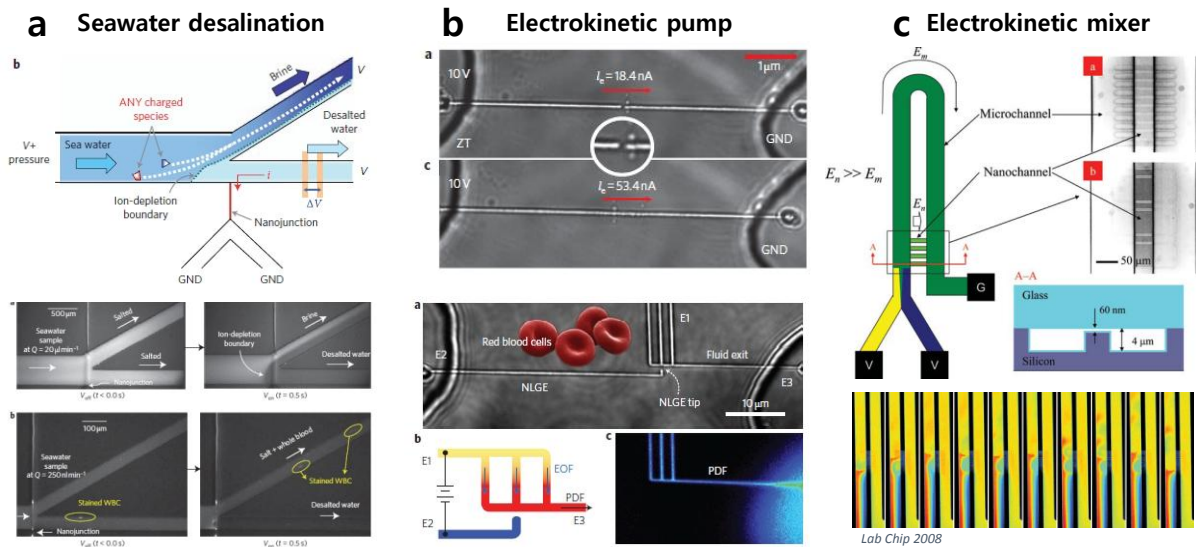


**Figure 1–12.** Nanofluidic applications combined with microfluidic systems. (a) The ion concentration polarization (ICP) created at a micro/nanofluidic junction is applied to desalinate the sea water. The desalination by the ICP phenomena filters any ions and charged particles to produce pure water. (b) Two adjacent glass nanofluidic channels with a nanogap show conductive behavior under an applied electric field that breaks down the glass barrier. The physically separated and electronically connected fluidic channels are used for an electrokinetic pump for transport of fluids in micro-/nanochannels. Nonlinear electrokinetic phenomena such as vortex flows are used for rapid mixing of laminar flows at the micro/nanofluidic junction. Figures (a) and (b) were adapted from Kim *et al.*<sup>29</sup> © 2010 NPG and Lee *et al.*<sup>27</sup> © 2010 NPG, respectively. Figure (c) was adapted from Kim *et al.*<sup>28</sup> © 2008 RSC. All rights reserved.

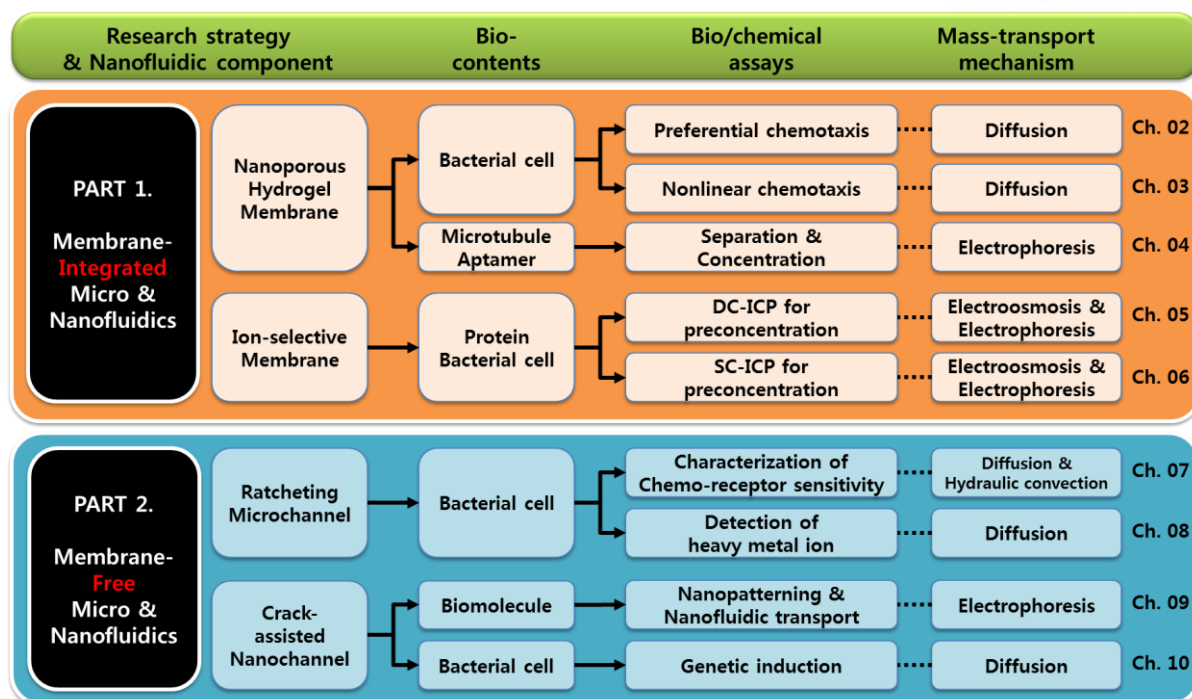


**Figure 1–13.** Overview of the dissertation structure. The dissertation introduces various membrane-integrated or membrane-free micro-nanofluidic devices to accurately manipulate mass transport in bio-/chemical assays.

### 1.5 Overview of dissertation

**Chapter 1: Introduction to Integrated Micro/nanofluidics.** This chapter covers introduction to understand the fundamentals in micro/nanofluidic technologies, including the definition and developmental history of the field of micro/nanofluidics, basic theory governing mass and charge transport in micro/nanofluidic channel networks, conventional and novel alternative techniques for nanochannel fabrication, and applications of the integrated micro/nanofluidic systems to the biology and the chemistry.

**Chapter 2: Integration of Nanoporous Hydrogel Plugs into Microfluidic Device for Bacterial Chemotaxis Assay in Multiple Chemical Gradients.** This chapter presents a diffusion-driven and long-range concentration gradient generator that uses hydrogel as a porous membrane to prevent convection flows but allow the diffusion of cell signaling molecules for the study of bacterial chemotaxis in a microfluidic device. Using this device, we characterized the critical concentrations associated with the chemotactic responses of cells that initially created a population band and then migrated in bands in the presence of multi-concentration gradients. In addition, this device can be used to study the preferential chemotaxis of bacterial cells toward different carbon sources.

\*Note: This chapter is partially or totally adapted from Minseok Kim and Taesung Kim, “Diffusion-based and long-range concentration gradients of multi-chemicals for bacterial chemotaxis assays”, *Anal. Chem.*, 82(22), 9401-9409, Copyright © 2010 American Chemical Society, all right reserved.

### **Chapter 3: Polydimethylsiloxane-sealed Hydrogel Device for Nonlinear Bacterial Chemotaxis.**

This chapter reports a microfluidic device that can rapidly and accurately generate various concentration gradients for the chemotaxis study of motile bacterial cells by integrating hydrogel into PDMS microchannels. We demonstrated that the PDMS-sealed hydrogel device not only produces various linear and nonlinear concentration gradients without flow-induced shear stresses on motile bacterial cells but also exhibits remarkable advantages over conventional hydrogel-based devices. For example, the PDMS-sealed hydrogel device can be used for fast and accurate generation of various concentration gradients; prevents dehydration of hydrogel and evaporation of solutions; directs diffusion of chemicals such as chemoattractants; exhibits long-term durability; and is easy to handle.

\*Note: This chapter is partially or totally adapted from Minseok Kim *et al.*, “Rapid and Accurate Generation of Various Concentration Gradients Using Polydimethylsiloxane-sealed Hydrogel Devices”, *Microfluid. Nanofluid.*, 82(22), 9401-9409, Copyright © 2014 Springer Berlin Heidelberg, all right reserved.

**Chapter 4: Self-integration of Nanoporous Membranes in Microfluidic Devices: Electrokinetic Preconcentration of Biosamples.** This part describes simple and robust methods that can be used for microfabricating four different precursor materials as leakage-tight membranes in a microfluidic channel network. The methods consist of a common self-integration process and individual solidification processes such as solvent evaporation, UV-curing, and temperature treatment. We demonstrate that the fabricated membranes can be used for electrokinetic, nanofluidic pre-concentration of bio-samples such as proteins, cells, and microspheres on either the anodic or cathodic side of the membranes. In addition, we not only characterize the physicochemical properties of the membranes such as conductance of membrane integrated microchannels, relative permselectivity, and pre-concentration ability, but also compare fabrication availability, membrane robustness, surface charge density tunability and biocompatibility with buffer solutions.

\*Note: This chapter is partially or totally adapted from Minseok Kim *et al.*, “Integration of nanoporous membranes into microfluidic devices: electrokinetic bio-sample pre-concentration”, *Analyst*, 138, 6007-6015, Copyright © 2013 Royal Society of Chemistry, all right reserved.

**Chapter 5: Continuous Concentration and Separation of Target Analytes by Using Aptamer-Functionalized Microtubules and Hydrogel Sieving Structures.** This chapter presents a novel biomolecule detection method that enables sensitive and selective detection of target analytes as well as simultaneous separation of non-target analytes by utilizing microtubules (MTs) as a molecular carrier and a nanoporous hydrogel membrane (NHM) as a size-based filter on a microfluidic chip. We functionalized MTs with aptamers, using a streptavidin and biotin linkage, to provide numerous binding sites for specific target analytes. Target analytes captured by the functionalized MTs from a mixture of complex analytes were transported by electrophoresis and then sieved by the NHM, while non-target analytes passed through the NHM because of the size difference between the analytes and nanopores. Subsequently, the concentration and separation of only target analytes was achieved in a

continuous and simultaneous manner.

\*Note: This chapter is partially or totally adapted from Minseok Kim *et al.*, “Aptamer-functionalized microtubules for continuous and selective concentration of target analytes”, *Sensor. Actuat. B-Chem.*, 202, 1229-1236, Copyright © 2014 Elsevier B.V., all right reserved.

**Chapter 6: Ion Concentration Polarization in A Single and Open Microchannel Induced by A Surface-patterned Perm-selective Film.** This chapter describes a novel and simple mechanism for inducing ion concentration polarization (ICP) using a surface-patterned perm-selective nanoporous film like Nafion in single, open microchannels. In this work, we characterize transport phenomena and distributions of ion concentration under various electric fields near the Nafion film and show that single-channel based ICP (SC-ICP) is affected by Nafion film thicknesses, strengths of applied electric fields, and ionic strengths of buffer solutions. We also emphasize that SC-ICP devices have several advantages over previous dual-channel ICP (DC-ICP) devices: easy and simple fabrication processes, inherently leak-tight, simple experimental setup requiring only one pair of electrodes, stable and robust ICP induced rapidly, and low electrical resistances helping to avoid Joule heating, and membrane perm-selectivity breakdown but allowing as high bulk flow as an open, plain microchannel.

\*Note: This chapter is partially or totally adapted from Minseok Kim *et al.*, “Ion concentration polarization in a single and open microchannel induced by a surface-patterned perm-selective film”, *Analyst*, 138, 1370-1378, Copyright © 2013 Royal Society of Chemistry, all right reserved.

**Chapter 7: Microfabricated Ratchet Structures for Amplifying Chemotactic Responses of Motile Bacterial Cells.** This chapter presents a novel microfluidic device that can detect the chemotactic response of motile bacterial cells (*Escherichia coli*) that swim toward a preferred nutrient with high resolution by sorting and concentrating them. The device consists of the typical Y-shaped microchannels that have been widely used in chemotaxis studies to attract cells toward a high concentration and a concentrator array integrated with arrow head-shaped ratchet structures beside the main microchannel to trap and accumulate them. Since the number of accumulated cells in the concentrator array continuously increases with time, the device makes it possible to amplify the chemotactic responses of the cells to 10 times greater than that in the typical Y-shaped channels in 60 min. In addition, the device can characterize the chemotactic sensitivity of chemoreceptors to chemoeffectors by comparing the number of cells in the concentrator array at different distances from the channel junction.

\*Note: This chapter is partially or totally adapted from Minseok Kim *et al.*, “Microfluidic device for analyzing preferential chemotaxis and chemoreceptor sensitivity of bacterial cells toward carbon sources”, *Analyst*, 136, 3238-3243, Copyright © 2011 Royal Society of Chemistry, all right reserved.

**Chapter 8: Microfluidic Chemostat Device for Sensitive Microbial Biosensor to Detect Heavy Metal Ions.** Here, we describe a high-throughput, chemostat-like microfluidic platform that can

continuously supply both nutrients and inducers (heavy metals) using microfabricated ratchet structures and a mixing microchannel network. We demonstrate that the microfluidic platform not only allows microbial biosensors to be highly concentrated in detection microchamber arrays but also enables them to continuously grow and control synthetic genetic circuits in response to heavy metals. We also demonstrate that the combination of the platform and microbial biosensors enhances the sensitivity in detecting divalent lead and cadmium ions approximately three orders of magnitude higher than conventional batch-type methods.

\*Note: This chapter is partially or totally adapted from Minseok Kim *et al.*, “Chemostat-like microfluidic platform for highly sensitive detection of heavy metal ions using microbial biosensors”, *Biosens. Bioelectron.*, 65(15), 257-264, Copyright © 2015 Elsevier B.V., all right reserved.

### **Chapter 9: Cracking-assisted Photolithography for Mixed-scale Patterning and Nanofluidics.**

Here, we describe an innovative cracking-assisted microfabrication technique, which relies only on the standard photolithography process but produces arbitrary-shaped nanopatterns with well-controlled, uniform geometric dimensions in a large-area and high-throughput manner by batch-processing the micropatterns. Hereby, our technique overcomes the crucial limitations that previous cracking-based techniques possess such as limited directions of cracks/patterns, uncontrolled dimensions, the low-throughput in fabrication, and incompatibility with other microfabrication processes. In addition, we show that mixed-scale patterns fabricated using the technique can be used as a master mould for replicating numerous micro/nanofluidic devices via soft lithography, which seems not to be demonstrated in even material-failure-based techniques.

\*Note: This chapter is partially or totally adapted from Minseok Kim *et al.*, “Cracking-assisted photolithography for mixed-scale patterning and nanofluidic applications”, *Nat. Commun.*, 6, 6247, Copyright © 2015 Nature publishing Group, all right reserved.

### **Chapter 10: Crack-photolithography for Membrane-free Diffusion-based Micro/nanofluidics.**

Here, we adopt our previous cracking-assisted nanofabrication technique called the ‘crack-photolithography’ to develop micro/nanofluidic devices with much reduced time and cost. The crack-photolithography makes it possible to not only simultaneously produce micropatterns and nanopatterns with various dimensions but also replicate both the mixed-scale patterns in a high-throughput manner. Therefore, a microfluidic channel network can be easily fabricated with a nanochannel array that can function as a nanoporous membrane wherever necessary and basically play a key role in diffusion-allowed but convection-suppressed microfluidic devices. In addition, the nanochannel array can manipulate the transports of small molecules by adjusting its dimension and/or number at will, so that nanochannel-array-integrated micro/nanofluidic devices proved even more robust and accurate in diffusion control than conventional membrane-integrated microfluidic devices. As an application of such micro/nanofluidic devices, we employed synthetic bacterial cells and found that their genetic induction and expression are dominated by extracellular, diffusive environments that

were completely engineered by using the nanochannel array.

\*Note: This chapter is partially or totally adapted from Minseok Kim and Taesung Kim, “Crack-photolithography for Membrane-free Diffusion-based Micro/nanofluidic Devices”, (submitted).

**Chapter 11: Summary and future outlook.** This chapter describes contribution of this dissertation to the fields of micro/nanofluidic technologies for biological assays; particularly, 1) electrokinetic-based biosamples preparation (concentration and separation) and detection, and 2) diffusion-based accurate and high-throughput characterization of bacterial behavior such as chemotaxis and gene expression. Also, this chapter suggests potential applications and challenging aspects of the proposed membrane-integrated and membrane-free micro/nanofluidic devices.

## Chapter 2. Integration of Nanoporous Hydrogel Plugs in Microfluidic Devices for Bacterial Chemotaxis Assay in Multiple Chemical Gradients

### *Introduction*

In nature, many biological phenomena, such as cell migration<sup>30</sup>, metastasis<sup>31</sup>, angiogenesis<sup>32</sup>, morphogenesis<sup>32</sup> and quorum sensing<sup>33</sup>, take place due to the diffusion of small cell signaling molecules so that microfluidic concentration gradient generators can play a key role in studying cell biology, microbiology and synthetic biology because they hold a high potential to provide biologists with *in vitro* cell culture environments that are similar to *in vivo* environments. To date, a variety of microfluidic gradient generation devices have been developed and can be categorized largely into two groups according to their methods: laminar flow (convection)-based and diffusion-based methods.<sup>34</sup> First of all, laminar flow-based gradient generation methods have been utilized to study biological phenomena within both mammalian and bacterial cells.<sup>35</sup> Even if the laminar flow-based methods show a unique advantage over diffusion-based methods in that they are able to generate controllable and switchable gradients<sup>36</sup>, the effects of the involved convection flows within the microfluidic devices on the cell secreted molecules is unavoidable; the flows can sweep away any secreted biomolecules. In addition, viscous shear stresses produced by these flows interfere with the migration of cells. In particular, for bacterial cells, the range of convection flows in the microfluidic channels is much higher than the average swimming velocity of the cells; the average propulsion force generated by a bacterial cell swimming at the speed of 25  $\mu\text{m/s}$  in a stationary fluid approximately corresponds to 0.5 pN, whereas the convection laminar flows in microchannels ( $>100 \mu\text{m/s}$ ) impose heavier forces on the cell by a factor of four or more ( $> 2.0 \text{ pN}$ ).<sup>37</sup> Therefore, for bacterial chemotaxis studies, diffusion-based gradient generation devices appear more suitable than convection-based devices.

Many efforts have been made to develop microfluidic, diffusion-based gradient generators over the past two decades. Diffusion-based gradient generation methods largely utilize porous membranes, such as polyethylene and polycarbonate, to prevent convection flows but allow diffusion of small molecules.<sup>34, 38</sup> Most of these diffusion-based devices consist of two layers because it is necessary to integrate the membranes into the microfluidic devices. Therefore, making a sandwich device out of thin membranes that are approximately 10  $\mu\text{m}$  in thickness requires a degree of expertise and skills in microfabrication and polymer bonding techniques, which can be inconvenient for biologists. In addition, hydrogels were employed in microfluidic devices because they provide a similar diffusion condition as water is biocompatible and easy to deal with.<sup>39</sup> Nevertheless, current hydrogel methods have some drawbacks in that they not only weakly seal/bond with substrates but also form only loosely fitting tubing connections with external apparatuses.<sup>39b</sup> Furthermore, only short-range concentration gradient generation devices ( $<1 \text{ mm}$ ) have been reported to date, whereas a longer concentration gradient generator ( $>1 \text{ cm}$ ) based entirely on diffusion would be very useful to

investigate both biological and chemotactic responses of cells to small signaling molecules or substrate.

For this reason and to address current weaknesses of both the laminar flow-based devices that generate heavier shear stresses onto bacteria cells and the diffusion-based devices that require elaborate and somewhat complex fabrication procedures, we present a convenient, diffusion-based concentration gradient generation device. The device can produce long-range, multi-concentration gradients of several chemicals simultaneously and in parallel. In addition, the device can be easily fabricated since the membrane structure required for diffusion-based gradients is replaced with a hydrogel (agarose) plug within single layered microfluidic channels.

In this work, we characterize the use of agarose gel as a porous membrane structure in a diffusion-based, long-range concentration gradient device. Using the device, we demonstrate that it is very useful in chemotactic studies of bacterial cells (*E. coli*). This is most clearly demonstrated by its ability to determine and quantify three critical concentrations associated with chemotaxis: the concentration for the minimum (threshold) chemotactic response (MCR), at which the cells start to show chemotaxis, the concentration for the strongest chemotactic response (SCR), at which the cells show the strongest chemotaxis and motility,<sup>40</sup> and the concentration for the upper limit of chemotaxis (LCR), which is defined as the concentration over which cells stop growing or die.<sup>41</sup> We also analyzed the chemotactic responses of bacterial cells in the presence of a long-range concentration gradient and found several interesting phenomena, such as the creation of bacterial population bands and the migration of said cells, which have not been observed previously in the presence of short-range concentration gradients. Lastly, we demonstrate that the device makes it possible to characterize preferential chemotaxis toward various carbon sources (or chemicals). Therefore, we believe that this device will be a very useful tool for both biological scientists to study bacterial chemotaxis as well as microfluidic engineers to easily fabricate porous, biocompatible membranes in single layered microfluidic devices.

## ***Methods and Materials***

**Preparation of bacterial cells.** In this experiment, we used *E. coli* strain MG1655, which is derived from K12 (a wild-type strain). A small colony of *E. coli* grown on a Luria-Broth (LB) agar medium was inoculated into 5 ml of tryptone broth (TB, 1% tryptone and 0.5% NaCl) media. The *E. coli* cells were then grown in a rotary shaking incubator (25°C and 200 rpm) to mid-log phase and required about 12 hours for the OD<sub>600</sub> reading to be about 0.4. TB media was tested and shown to support the best motility compared to other motility buffer solutions (e.g., 10 mM potassium phosphate, 76 mM NaCl, 0.1 mM Na-EDTA, pH=7).<sup>42</sup> Hence, TB was mainly used in all experiments unless otherwise noted. Before the cell motility was observed, the cells were centrifuged at 5000 rpm for 2 min, the supernatant poured off, and the pelleted cells were resuspended in fresh M9 minimal

media without a carbon source. We also used the expression of the green fluorescent protein (GFP) as a reporter by transforming competent cells of *E. coli* strain MG1655 with a plasmid (pLtetO-1 with GFP) that constitutively expresses GFP. GFP-expressing cells are very useful for quantifying the accumulation rates of the cells in the microchannels and for evaluating the chemotactical responses to chemoattractants. The GFP-expressing cells were cultured in the same manner as described above.

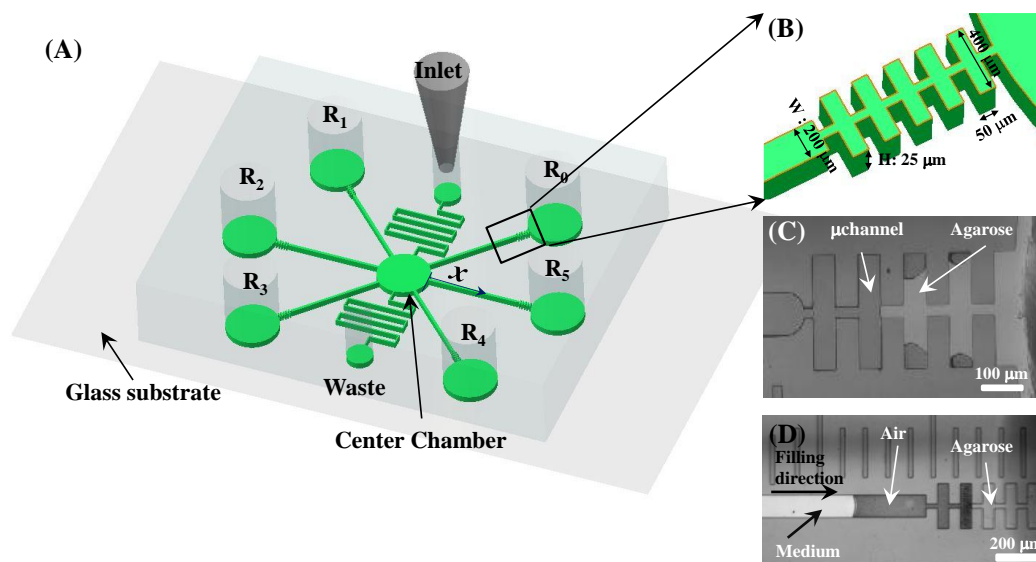


**Figure 2-1.** (A) Schematic view of the long-range concentration gradient generator for use with multiple compounds. Each channel is 8 mm long from the center chamber to the reservoir and a constant flow is used to provide fresh media to the center chamber, in which the cells are introduced after generation of the chemical gradients. (B) The H-shaped microfluidic channel structure was designed to integrate the agarose gel into the microchannel near the reservoirs. (C) The microimage shows a hydrogel plug mixed with fluorescent dye which prevents convection flows in the microchannel but allows diffusion of small molecules from the reservoir to the center chamber. (D) After a hydrogel plug was made, the channel was filled with a medium by removing the air trapped within the channel through PDMS. The medium contains 50  $\mu$ M of FITC for demonstration.

**Design and fabrication of the microfluidic devices.** As shown in Figure 2-1, we designed a microfluidic channel network consisting of a microfluidic chamber at the center and six reservoirs around the chamber that are connected with microchannels (200  $\mu$ m wide and 25  $\mu$ m high). Two microchannels, indicated as “Inlet” and “Waste”, were additionally designed in order to provide and drain media at the central chamber. At the entrance of the microchannels, *i.e.*, from the reservoirs, we used H-shaped microfluidic structures to integrate agarose plugs, which function as a membrane, so that it was possible to completely prevent convection flow but allow diffusion of small molecules from the reservoirs to the chamber at the center. The circular chamber in the middle of the device functioned as a sink to maintain all chemical concentrations to be zero in order to ideally block the cross-talk of chemicals which diffused from the reservoirs into the center chamber along channels. In addition, the center chamber enabled cells to be exposed and then attracted to the sugar sources with

the same opportunity to increase the experimental accuracy and used for producing lower concentration gradients at the upstream while higher concentration gradients at the downstream of the center chamber to minimize unnecessary contamination of chemicals in all experiments.

The microfluidic devices were fabricated using standard soft-lithography.<sup>34</sup> Briefly, an SU-8 (Microchem 2025, Newton, MA, USA) master approximately 25  $\mu\text{m}$  thick was fabricated using standard photolithographic procedures. The surface was silanized using trichloro(3,3,3-trifluoropropyl)silane (Sigma Aldrich, Korea) in a vacuum jar for an hour. Polydimethylsiloxane (PDMS) was then cast, cured, and peeled off. After punch holes were made the microfluidic devices were prepared. The PDMS devices were directly bonded to a glass substrate without any surface treatment and then they were treated with oxygen plasma under 50 sccm of  $\text{O}_2$  and 70 W for 90 sec (Cute-MP, Femto Science, Korea). This treatment was done to make the surfaces of the PDMS channel hydrophilic so that solutions flowed along the channel easily. All microchannels were coated with Pluronic surfactant (F-68, 0.01%, Sigma Aldrich) to minimize any nonspecific binding between the cells and the glass surface by flowing 50  $\mu\text{l}$  of the Pluronic surfactant over 2 hours. After the residue was subsequently rinsed with culture medium or the motility buffer solution, the microchannels were dried using a vacuum pump.

**Construction of hydrogel plugs in microchannels.** As seen in Figure 2–1(B), H-shaped microchannels were designed at the reservoir sides to construct a hydrogel membrane (agarose gel, 1%). For this, 5  $\mu\text{l}$  of an agarose solution at 65 $^{\circ}\text{C}$  was loaded at the entrance of the H-shaped channel and the solution was allowed to flow along the channel. However, the flow stopped at the middle of the H-shaped channel because the repeated narrow and wide channels retarded the flow and reduced the flow rate so that the agarose cooled down to room temperature (24  $^{\circ}\text{C}$ ) and solidified before it reached the main channel. Since flow velocity is a function of hydrostatic pressure, 5  $\mu\text{l}$  of the agarose solution into reservoirs in 4 mm diameter produced the hydraulic head as about 400  $\mu\text{m}$ , limiting to about a few tens  $\mu\text{m/s}$  of flow. In addition, since the surface to volume ratio of the H-shaped channel was a high value as most microfluidic channels are, the solution lost heat very fast and turned into the gel in a couple of seconds (<5 seconds). Within this period of time, the solution flows less than 1 mm. This was why we used 1 mm long H-shaped channel. The H-shaped channel reduced the flow rate toward the main channel by irrigating/filling the side chambers (see Figure 2–1(C)). And some amount of the gel was stacked in wells and the amount does not differ much at each experiment. In addition, since the diffusivity of 1% agarose is almost the same as water and the variation of the length of the agarose plugs was quite small (< 200  $\mu\text{m}$ ) compared to the length of the main channels (8 mm long) the diffusion profiles were not affected by the agarose plugs. After an agarose hydrogel plug was made, the channel was filled with a medium. Since PDMS is a gas permeable material so that the air trapped within the channel was compressed and then removed by the pressure built by the flow (Figure 2–1(D)). After each reservoir was filled with a fluorescent solution containing 50  $\mu\text{M}$

fluorescein isothiocyanate (FITC), diffusion-driven concentration gradients resulting from the agarose plugs were measured and characterized by quantifying fluorescent intensity signals.

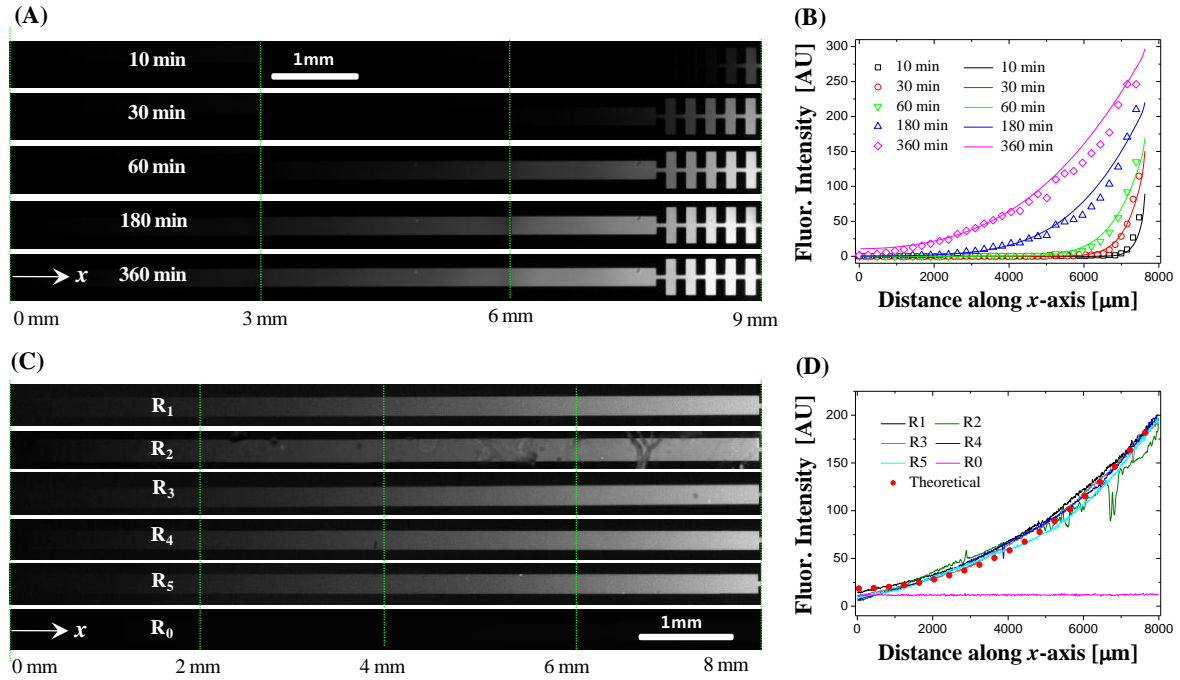


**Figure 2–2.** (A) Transient concentration gradients were obtained using the transport of a fluorescence dye (50 μM of FITC) across the H-shaped structure and along the microchannel. (B) Quantification of the fluorescent signals (symbols) shows good agreement with the theoretical results (line). (C) The concentration gradients with six microchannels after 10 hours of diffusion (at steady state). (D) Quantification of the fluorescent signals show good agreement with the theoretical results, confirming that this device generates stable and robust concentration gradients of small molecules simultaneously and in parallel.

**Theoretical analyses.** The transient convection-diffusion is governed by the following equation:

$$\frac{\partial c}{\partial t} = \mathbf{u} \cdot \nabla c + D \nabla^2 c \quad (\text{Eq. 2-1})$$

where  $c$  is the concentration,  $\mathbf{u}$  is the velocity of a fluid and  $D$  is the diffusivity of molecules in a water solution. In the absence of convection flow ( $\mathbf{u}=0$ ) and in a long microchannel, diffusion is assumed to be one-dimensional and the solution of the concentration gradient is given in a complementary error function as follows:

$$c_i(x, t) = c_{i0} \left( 1 - \text{erf} \left( \frac{L-x}{2\sqrt{Dt}} \right) \right) \quad (\text{Eq. 2-2})$$

where the initial conditions of the reservoirs ( $i=1, 2, 3, \dots$ ) are  $c_i(x, 0)=0$  and the boundary conditions are  $c_i(0, t)=0$  (the center chamber) and  $c_i(L, t)=c_{i0}$  (reservoirs).<sup>43</sup> Therefore, the concentration gradients are theoretically asymptotic with time and the gradients of small molecules gradually become linear. Hence, every device was stored in a 100 % humidity box (to prevent

evaporation) for about 10 hours before we started the chemotaxis experiments. This was done to obtain linear gradients in the channel because carbon sources have slightly different molecular weights (glucose=180.16, galactose=180.16, mannose=180.16, arabinose=150.13, and xylose=150.13, Sigma Aldrich). It should be noted that during this long storage time, the chamber at the center was continuously flushed using a flow between the inlet and outlet, but not within the microchannels because of the hydrogel plugs (membranes). Eq. 2–2 was also used to compare experimental concentration gradients with the theoretical results. The H-shaped structure can affect diffusion so that COMSOL simulations (COMSOL Multiphysics 4.0) were performed and compared with experimental results for additional confirmation. All plots of concentration gradients versus distance from the center chamber to each reservoir were drawn with Origin 7.1 (OriginLab, Northampton).

**Experimental procedure and data analysis.** After the hydrogel plugs were fabricated in each channel and the reservoirs were filled with the hydrogel solution (about 300  $\mu\text{m}$  high theoretically), the channels were filled with culture medium (see Figure 2–1(D)) and the reservoirs were filled with solutions with different sugar concentrations. And then the device was put into a humidity box for 10 hours for the sugar molecules in the reservoirs to diffuse to the center chamber. And then, cells were loaded into the inlet channel and observed. All bright-field and fluorescent micro-images were obtained with an inverted epi-fluorescent microscope (Nikon, Ti-S, Japan) and a CCD camera (Nikon, DS-Qi1, Japan) equipped with a digital image recorder (Digital Sight DS-U2, Nikon, Japan). To quantify the cell densities, GFP-expressing cells at different concentrations ( $\text{OD}_{600}=0.2, 0.4, 0.6, 0.8$  and  $1.0$ ) were loaded into the device and the fluorescent signals were used to calibrate the cell densities. Images were recorded at 15 fps using 4X and 10X objective lenses. The motility of the bacterial cells was analyzed using Image J when they traveled in run mode (not in tumble mode).<sup>44</sup>

## ***Results and Discussion***

**Device characterization.** Initially we characterized the concentration gradients of the device integrated with agarose gel membranes. As shown in Figure 2–2, 100  $\mu\text{l}$  of 50  $\mu\text{M}$  FITC was loaded in the reservoirs and then the fluorescence signals within the channels were measured with time. The H-shaped channel filled with agarose gel showed the similar diffusivity as the main channel filled with a buffer solution since the agarose gel is comprised of 99% water. Although it has been reported that diffusivity slightly decreases in high hydrogel concentrations ( $<\sim 10\%$ ),<sup>45</sup> we neglected the difference in simulations. After 6 hours, the fluorescent signals reach the center of the channel across the H-shaped structure and along the long microchannel, implying that long-range concentration gradients are well generated. As shown in Figure 2–2(B), the quantified fluorescent signals show good agreement with the theoretical results obtained from the simulations. For these calculations, the diffusivity of FITC ( $D_{\text{FITC}}$ ) was assumed to be  $D_{\text{FITC}}=0.49\times 10^{-9} \text{ m}^2/\text{s}$ .<sup>46</sup> We also measured the

fluorescent signals within all six of the microchannels after a 10 hour diffusion (at steady state) and confirmed that concentration gradients produced are nearly identical as shown in Figures 2–2(C) and (D). Since the inlet reservoir maintained the highest pressure, while the outlet reservoir had the lowest, for the extent of the experiment, the concentration within the center chamber remained zero ( $c(0,t)=0$ ). We found that the hydrogel plugs were stable enough to last longer than the entire period of experiments ( $> 20$  hours) and concentration gradients were maintained as well.

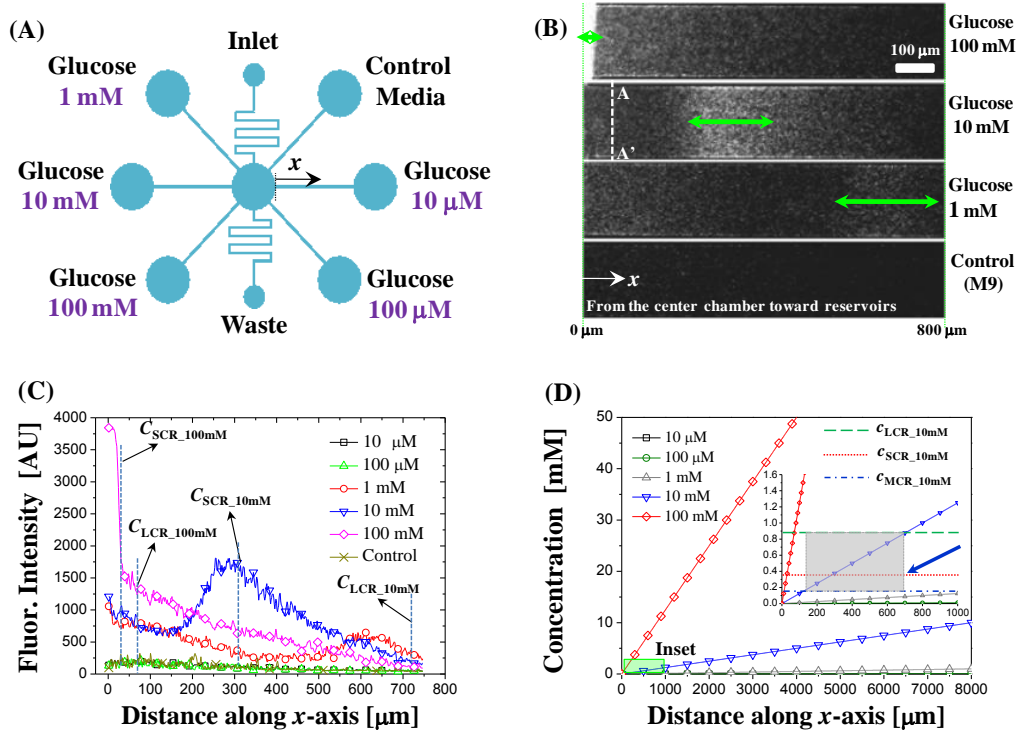


**Figure 2–3.** (A) Schematic showing the experimental conditions. Five reservoirs contain different concentrations of glucose (as a chemoattractant) and one reservoir has only M9 media without glucose (as a control). Cells were loaded into the center chamber. The distances were measured from the entrance of each channel. (B) Micrographs taken 30 minutes after cell loading, during which time the cells showed chemotaxis towards the glucose. In contrast, no chemotaxis was observed in the absence of glucose (no fluorescent signals in the control channel). As the cells migrated from the center chamber toward the reservoirs, they created population bands located at the different distances along the microchannels and according to the concentration gradients. (C) Profiles of the population bands quantified using the fluorescent signals. The profile of the band in 100 mM is narrow but very close to the center chamber whereas that in 10 mM is wide and ranges from  $x=0$  to  $x=700$  μm. (D) Concentration gradients produced in each of the microchannels. The creation of bands can be described by the critical concentrations such as  $c_{MCR}$ ,  $c_{SCR}$  and  $c_{LCR}$  (not to scale).

**Chemotaxis of bacterial cells in multi-concentration gradients.** We investigated the chemotaxis of bacterial cells (strain MG1655 expressing GFP) by generating long-range, multi-concentration gradients of glucose, which was selected since it is a well-known chemoattractant. M9 media samples (200 μL) containing 0 μM ( $R_0$ ), 10 μM ( $R_5$ ), 100 μM ( $R_4$ ), 1 mM ( $R_1$ ), 10 mM ( $R_2$ ) and 100 mM ( $R_3$ )

glucose were added to the reservoirs, respectively, as shown in Figure 2–3(A). This configuration and the continuous flow between the inlet and the outlet minimized the cross-contamination of both the center chamber and the entrance of the low concentration channels from high concentration channels via diffusion.

As shown in Figure 2–3(B), no bacterial cells (no fluorescent signals) were observed in the M9 control channel while the bacterial cells showed chemotatic responses toward the glucose-containing media (strong fluorescent signals). For 100 mM, 10 mM and 1 mM, the cells traveled from the center chamber up the microchannel and created population bands at different locations within the channels as indicated with arrows. The bands observed 30 minutes after cell loading showed two distinct features according to the glucose concentration. The bands seen from the higher glucose concentrations formed closer to the center chamber and were narrower than the bands seen from the lower concentrations. Furthermore, the narrowing of the bands led to increased fluorescence intensity from these bands. For instance, the band in the 100 mM channel was about 50  $\mu\text{m}$  wide and ranged from  $x=0$  to  $x=50$   $\mu\text{m}$  whereas that in the 10 mM is much wider and ranges from  $x=0$  to  $x=700$   $\mu\text{m}$ .

Figure 2–3(C) shows quantitative results for the fluorescent signals along the length of the microchannels from the center to the reservoirs. No clear bands were created in the 10  $\mu\text{M}$  and 100  $\mu\text{M}$  channels; the profiles of fluorescent signals are almost the same as control. These results can be explained by the fact that, in general, bacterial cells show chemotactic behavior at a certain threshold concentration. It was reported that the chemotactic threshold concentration ( $c_{\text{MCR}}$ ) for glucose is about 1  $\mu\text{M}$  and the strongest chemotactic response takes place at 1 mM, which is defined as the  $c_{\text{SCR}}$  in this work.<sup>47</sup> In addition, a higher concentration may exist over which the cells cannot grow or may not survive. This concentration was defined as the  $c_{\text{LCR}}$  in this work, and is the concentration at which cells show a very weak chemotactic response because of an excess of a carbon source. Hence, in the presence of concentration gradients of a chemoattractant, cells tend to migrate and stay at a range of proper concentrations at which they typically show good motility.<sup>40</sup>

In contrast, for 10  $\mu\text{M}$  and 100  $\mu\text{M}$  glucose, the bacterial cells showed no chemotactic responses, as shown in Figure 2–3(C). This is because both the concentration at the entrance of the channels was too low to attract cells ( $c_i(x, t) < c_{\text{MCR}}$ ) and the concentration gradients were lower than the required threshold value (see Figure 2–3(D)).<sup>39b, 41</sup> Therefore, we concluded that the  $c_{\text{MCR}}/L$  should be greater than or equal to  $1/8$  mM mm<sup>-1</sup> (1 mM over a 8 mm long channel). On the other hand, the concentration gradient for the 10 mM glucose microchannel is very steep so that it easily extends from the  $c_{\text{MCR}}$  to  $c_{\text{LCR}}$  (refer to the rectangle indicated with an arrow). Therefore, bacterial cells at the entrance of the 10 mM channel will show a strong chemotaxis up the microchannel and gathered at a range where the proper concentrations are achieved, between which the band is created. As illustrated in Figure 2–3(D), for 100 mM, the range of proper concentrations was much more narrow when compared with that seen in the 10mM microchannel, while, for 1 mM, it was extended. It is clear,

therefore, that the width of the population band varies inversely with the concentration gradients because the range of proper concentrations depends on the slope of the concentration gradients that were produced on a chip in order to easily characterize critical concentrations related with chemotaxis at a time.

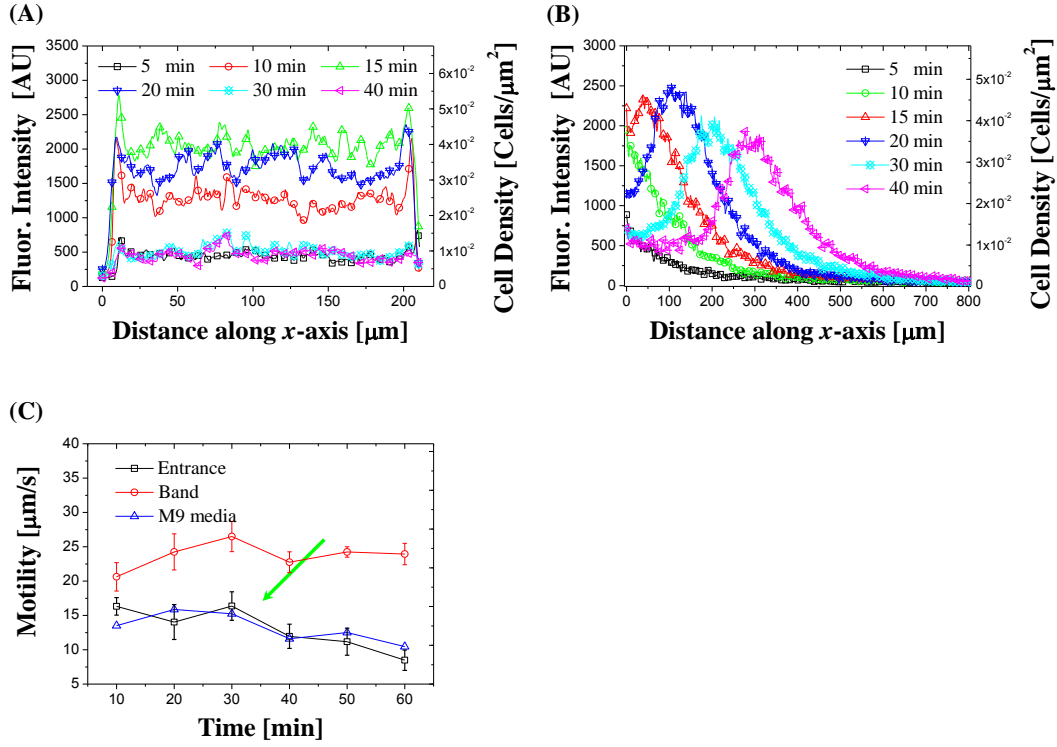


**Figure 2–4.** (A) Flux of cells from the center chamber into the microchannel and across the dashed line A–A' (shown in Figure 2–3(B)). The flux gradually increases up to a time of 15 minutes, decreases with time and, after 40 minutes, no cell migration is apparent. (B) Fluorescent intensity profiles of the bands. The average velocity of the peaks is about 7.5 μm/min along the microchannel. (C) The cells within the bands show stronger motility (20–25 μm/s), meaning that they are more active due to sufficient carbon sources (metabolism). On the other hand, cells outside of the bands show relatively weak motility (10–15 μm/s) because of insufficient carbon sources. Error bars are the standard deviation (N=25).

**Critical concentrations associated with chemotaxis.** We attempted to relate the range of proper concentrations with the chemotactic responses of the cells by employing the values of  $c_{LCR}$ ,  $c_{SCR}$  and  $c_{LCR}$  and the theoretical solution of concentration gradients in the microchannels. Since it takes about 10 hours for small molecules to completely diffuse through the microchannels, the concentration profile of Eq. 2–2 can be linearized as:

$$c_i(x, t) \approx c_i(0) + \frac{x}{L} \frac{dc_i}{dx} \quad (\text{Eq. 2–3})$$

where  $x$  is the distance from the entrance of each channel and  $L$  is the channel length ( $L=8$  mm).

Therefore, the range of proper concentrations for which the cells aggregate (*i.e.* the bands) can be subsequently approximated to be  $c_{MCR} < c_i(x) < c_{LCR}$ , where  $x$  can be obtained from the fluorescent signals of the bands in Figure 2–3(C). Again, for 10  $\mu\text{M}$  and 100  $\mu\text{M}$ , no chemotactic behavior was seen because the threshold concentration gradient, which is defined as  $c_{io} L^{-1}$ , too low. However, cells showed chemotaxis in the 1 mM, 10 mM and 100 mM channels. Therefore, we are able to conclude that  $c_{io} L^{-1}$  should be greater than or equal to  $1/8 \text{ mM mm}^{-1}$  for a chemotactic response to be seen. In addition, the  $c_{SCR}$  value can be derived from the fluorescent profile of the band created in the 10 and 100 mM channels; the peaks of the bands are located at  $x=30 \mu\text{m}$  and  $x=300 \mu\text{m}$ , respectively, as indicated by  $C_{SRC\_100\text{mM}}$  and  $C_{SRC\_10\text{mM}}$  in Figure 2–3(C). Therefore, the  $c_{SCR}$  is calculated to be about 0.375 mM, which is slightly smaller than the literature value (1 mM).<sup>47</sup> In the same manner, the  $c_{LCR}$  value was calculated to be 0.875 mM from the right-hand boundaries of the bands, which are located at about  $x=70 \mu\text{m}$  and  $x=700 \mu\text{m}$ , respectively, as indicated by  $C_{LRC\_100\text{mM}}$  and  $C_{SRC\_10\text{mM}}$ . It is noted that these values were measured for the first time to our best knowledge.

Based upon these results, this device can produce multiple concentration gradients simultaneously so that the concentration range of a chemoattractant can be determined reliably. Furthermore, our device can significantly reduce the number of experiments required since the range of concentrations leading to chemotaxis of bacterial cells can be measured on a chip and the parameter values, *i.e.*,  $c_{MCR}$ ,  $c_{SCR}$  and  $c_{LCR}$ , can be calculated using the location and width of the resulting population bands.

**Mechanism of creating a band.** We expanded on the mechanism of creating a population band by measuring the flux of the cells over time, as shown in Figure 2–4(A). As the cells migrated from the center chamber toward the higher concentrations in the 10 mM glucose microchannel the fluorescent signals along the dashed line A–A', in Figure 2–3(B), were quantified and then converted into the number of cells per unit  $\mu\text{m}^2$  using the calibration data. These values ( $\text{cells}/\mu\text{m}^2$ ) were then integrated with respect to the distance along the line A–A' and multiplied by the velocity of cells to determine the flux of cells ( $\text{cells/s}$ ). The flux initially increased with time, because the cells were attracted to the glucose, but gradually decreased after 15 minutes as the peak of the band grew higher and wider (Figure 2–4(A) and (B)). We hypothesize that this was because the concentration gradients between the entrance of the channel and the middle of the band ( $x=0$  and  $x=x_{SCR}$ ) may decrease due to the consumption of glucose by the cells located within the band, resulting in a collapse of concentration gradient. The band was saturated with cells after about 30 minutes, based upon the flux results in Figure 2–4(A), and the band started to move along the channel (Figure 2–4(B) and 5(A)).

To verify our hypothesis, samples of cells located at the entrance of the channel, inside the bands and at the M9 control channel were taken to measure and compare their motility. As shown in Figure 2–4(C), the cells taken from the band have the highest motility, presumably because these cells are provided with sufficient glucose for an active metabolism. On the other hand, the cells taken from the entrance of the channel (between  $x=0$  and  $x=x_{SCR}$ ) show a relatively weaker motility which was on

the same scale as the control channel, suggesting that this lower motility is due to both groups lacking a sufficient carbon source. It is obvious that the time when the cell motility rapidly decreased coincided with a decrease in the flux ( $t=30$  min as indicated with an arrow in Figure 2–4(C)). Hence, we confirmed that the band is created by the chemotactic migration of cells within 30 min of cell loading and that the cells within band consume all of the glucose, causing the band to migrate up the microchannel to obtain more glucose. Therefore, the most accurate critical concentrations associated with chemotaxis should be calculated from the band at  $t=30$  min. Furthermore, we confirmed the motility difference between the upper and lower regions of the microchannel by tracing two individual groups (30 cells each) swimming at left- and right-hand sides of a moving band for eight seconds. The cells at the left-hand side (*i.e.*, high glucose concentration) showed much shorter swimming distances than those at the right-hand side because of the insufficient provision of a carbon source and the collapse of concentration gradients.

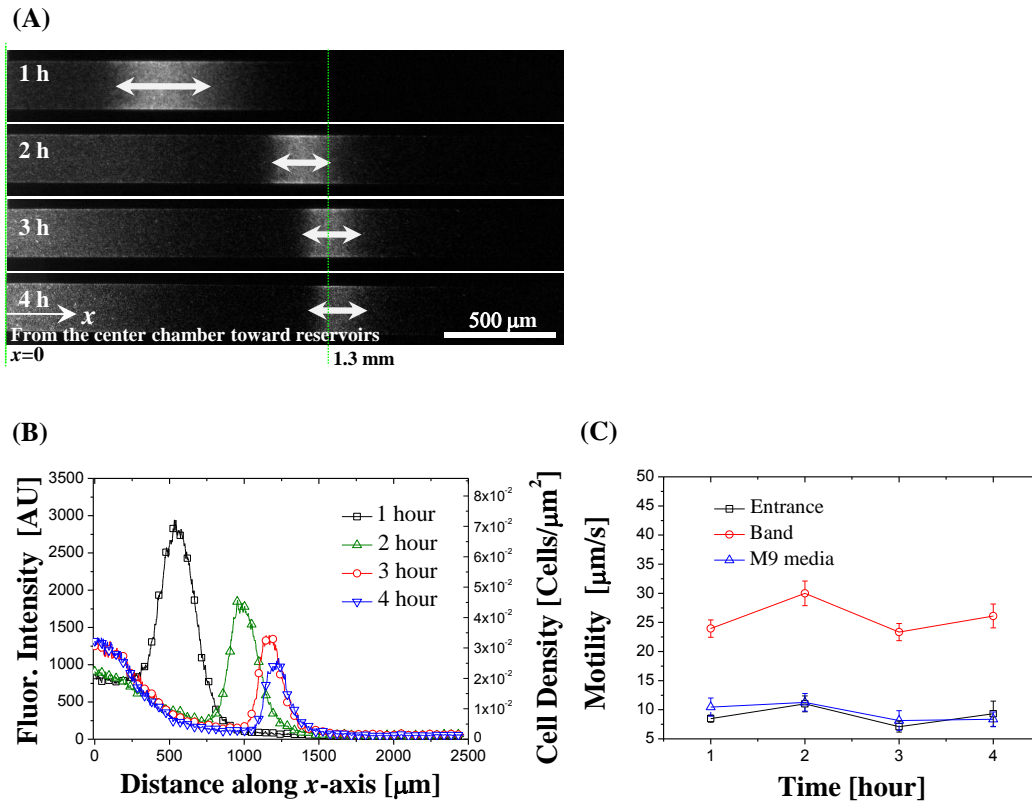


**Figure 2–5.** The band continued to migrate and then stopped at  $x=1.3$  mm, likely because the consumption rate of a carbon source by the cell population and the diffusion rate from the reservoir is in equilibrium. (B) The fluorescent intensity profiles of the bands. The average velocity of the peaks is about 5–10  $\mu\text{m/min}$  along the microchannel. (C) The cells within the bands show stronger motility (25–30  $\mu\text{m/s}$ ), meaning that they are more active due to sufficient carbon sources (metabolism). On the other hand, cells outside of the bands show relatively weak motility (5–15  $\mu\text{m/s}$ ) because of an insufficient carbon source. Error bars are standard deviation ( $N=25$ ).

**The movement of bacteria in bands.** After the chemotactic migration of cells from the entrance

of the channel to the band was completed, we observed the band move for more than four hours. As shown in Figure 2–5(A), the population band in the 10 mM channel continued to move at a velocity of about 5–10  $\mu\text{m}/\text{min}$  for up to two hours and then slowed down and eventually stopped at  $x=1.3$  mm. Since some cells observed in the left-hand side of the moving band were too inactive to follow the band, the width of the band decreased with time. The fluorescent signals of the bands were also quantified, and the results are shown in Figure 2–5(B). In fact, it was previously demonstrated that bacterial cells in a silica capillary tube migrated in bands while consuming the oxygen dissolved in the media.<sup>48</sup> In that study, it was found that the band migrated slightly to find more oxygen to digest the carbon sources, even though enough carbon sources were left in the capillary. In our experiment, however, the PDMS is gas-permeable and, therefore, the band movement is more likely caused by the depletion of carbon source. To verify that the oxygen concentration was not the reason for the migration, the oxygen concentration along the microchannel was measured and found to be similar along the length of the microchannel. Accordingly, it appears likely that the movement of bands was not caused by the depletion of oxygen but the depletion of a carbon source. This idea is also supported by the band stopping at  $x=1.3$  mm, where the flux of carbon sources is approximated to be

$$J_i = D_{glu} A_x \frac{\partial c_i(x, t)}{\partial x} \approx D_{glu} A_x \frac{c_{i0}}{L - x} \quad (\text{Eq. 2-4})$$

where  $D_{glu}$  is the diffusivity of glucose ( $D_{glu}=7 \times 10^{-10} \text{ m}^2/\text{s}$ ),<sup>49</sup>  $J_i(x)$  is the flux ( $\text{mol}/\text{s}$ ) and  $A_x$  is the cross-sectional area (200  $\mu\text{m}$  by 25  $\mu\text{m}$ ), so that  $J_i = 9.33 \times 10^{-13} \text{ g/s}$ .<sup>50</sup> At the same time, the number of cells in the band ( $L_{\text{band}}=100 \text{ }\mu\text{m}$  long,  $V_{\text{band}}=A_x \times L_{\text{band}}$ ) was calculated to be  $N_{\text{cell}}=1054$  from the microscope calibration results so that the cell density in dry cell weight unit (DCW) would be

$$DCW_{\text{band}} = \frac{N_{\text{cell}}}{V_{\text{band}}} \cdot \frac{0.6042 \text{ g}}{L} \cdot \frac{1}{1OD_{600}} \quad (\text{Eq. 2-5})$$

where 1  $OD_{600}$  was assumed to be 0.6042  $\text{g/L}$ .<sup>51</sup> Since glucose consumption rate and its molecular weight were reported to be  $Q_{glu}=5 \times 10^{-3} \text{ mol/g-cells/hour}$  and  $MW_{glu}=180 \text{ g/mol}$ , the glucose consumption rate by the cells in the band was estimated using the following equation

$$R_i = DCW_{\text{band}} \cdot Q_{glu} \cdot MW_{glu} \quad (\text{Eq. 2-6})$$

to be  $R_i=5.31 \times 10^{-12} \text{ g/s}$ .<sup>52</sup> Hence, it was confirmed that the diffusion rate was consistent with the consumption rate, proving that these two parameters were in equilibrium and explains why the band stopped migrating. The motility of the cells in the band was also checked and it was found that they were still active during the band migration, as shown in Figure 2–5(C).

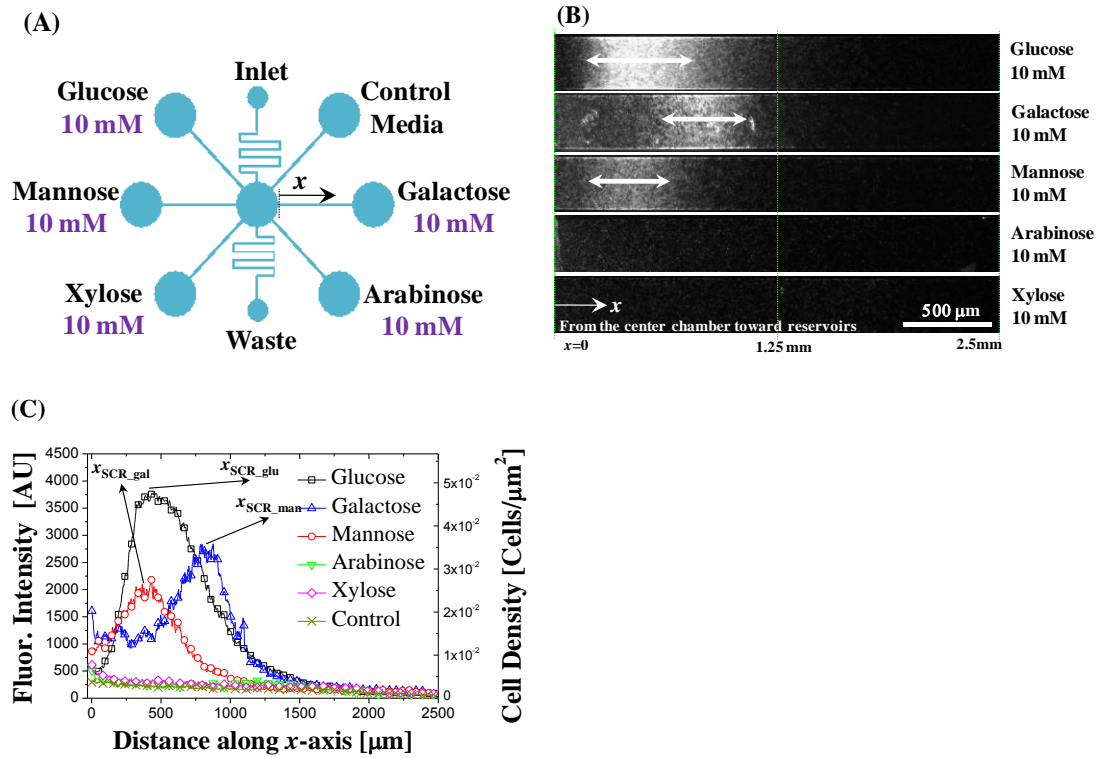


**Figure 2–6.** Schematic showing the experimental conditions used to the study the preferential chemotaxis of bacterial cells toward five different carbon sources. Each reservoir has a different carbon source, respectively, but at the same concentration of 10 mM. (B) The bands formed within 30 minutes but differed both in their locations and the density/number of cells. (C) Quantification of the fluorescent signals implies that the preferential chemotaxis of cells is toward glucose, galactose and then mannose, in this order. No chemotaxis was observed in the arabinose and xylose channels.

**Preferential chemotaxis of bacterial cells toward carbon sources.** We extended the application of the device to investigating the preferential chemotactic response of bacterial cells toward various chemicals because concentration gradients of multiple chemicals can be easily produced on a chip by loading the test chemicals in different reservoirs. In the same manner, we employed the wild type *E. coli* cells engineered with GFP because they are known to digest many different carbon sources, such as glucose, arabinose, galactose, mannose and xylose. As illustrated in Figure 2–6, all these carbon sources were loaded at the same concentration (10 mM) and produced a linear concentration gradient which could be used to find out the preferential chemotaxis of cells for the carbon sources. As shown in Figure 2–6(B), cells showed a positive chemotaxis toward glucose, galactose and mannose (for both glucose and galactose,  $c_{\text{MCR}}=1 \mu\text{M}$ , and for mannose,  $c_{\text{MCR}}=10 \mu\text{M}$ ) but no chemotactic responses (no fluorescent signals) were observed in the arabinose and xylose channels because they have relatively higher threshold concentration values (for both arabinose and xylose,  $c_{\text{MCR}}=100 \mu\text{M}$ ).<sup>47</sup> In addition, 30 minutes after loading the cells, cells were observed to migrate and create population bands at different locations in a similar fashion as seen in Figure 2–3(B). Furthermore, difference between the diffusion coefficients for these sugars would be negligible because their molecular

weights are similar.

Consequently, by quantifying the number of cells, we can conclude that *E. coli* prefers glucose, galactose and mannose, in this order, to arabinose and xylose. This conclusion is supported by the fact that cells not only have various chemoreceptors on their membranes, with most being more sensitive to glucose than other carbon sources, but *E. coli* is also known to express the enzymes for glucose metabolism constantly.<sup>53</sup>

A similar study was performed using capillary tube chemotaxis by Adler *et al.* who dipped a solution of a carbon source in the end of a capillary tube into a suspension of motile bacterial cells and then quantified the number of colonies the next day that were obtained by plating the accumulated bacterial cells in the capillary tube.<sup>53</sup> To determine the preferential chemotaxis of *E. coli* toward various chemicals, they repeatedly performed their experiments with a number of concentrations and type of chemicals. Based upon their study, they concluded that *E. coli* prefer glucose, galactose and mannose to arabinose and xylose, in this order. Although our finding was the same, our device was capable of determining the preferential chemotaxis on a chip and showed that glucose is the preferential carbon source and that both arabinose and xylose have a relatively high concentration threshold value. For this reason, bands were not observed in the channels for these two sugars. Although the  $c_{SCR}$  values of glucose, galactose and mannose were reported to have the same value (1 mM), we were able to estimate more accurate  $c_{SCR}$  values from the experimental results (the locations of peaks) as shown in Figure 2–6(C). For glucose, since  $x_{SCR\_glu}$  was 300  $\mu\text{m}$ , the  $c_{SCR\_glu}$  would be 0.375 mM using Eq. 2–3. In turn, we find that for galatose  $x_{SCR\_gal} = 800 \mu\text{m}$  leads to  $c_{SCR\_gal} = 1 \text{ mM}$  and for mannose  $x_{SCR\_man} = 300 \mu\text{m}$  gives an  $c_{SCR\_man} = 0.375 \text{ mM}$ . While galactose has the same  $c_{SCR}$  value as in the literature, we found that glucose and mannose have smaller  $c_{SCR}$  values.<sup>47</sup>

**Summary and additional applications of the device.** The device presented in this study has the potential to further bacterial chemotaxis studies since it can significantly reduce the amount of time and effort needed and makes determining the critical concentrations and chemotactic preference of bacterial cells toward various carbon sources within a single system possible. In addition, our device also successfully demonstrated the creation of population bands, which, to the best of our knowledge, is the first time it has been demonstrated in a miniaturized gradient generation device. This is possible since this device produces long-range concentration gradients within the microchannels. Lastly, the device would be applied to the screening and sorting of different motile microbes based upon their chemotactic natures, because this device enables one to find chemoattractants as well as chemorepellants on a chip and the number of chemicals tested with a single device can be increased.

## Conclusions

We developed a diffusion-based microfluidic gradient generator using hydrogel plugs as a porous membrane in the microchannel to prevent convection flows but allow the diffusion of small molecules

with a similar diffusivity. Since hydrogels can be easily integrated into a microfluidic channel, it was possible to develop long-range, linear concentration gradients of various chemicals on a single chip. The hydrogel membrane was shown to be very stable and robust so that we were able to produce long-range concentration gradients of small molecules to study the chemotaxis of bacterial cells. Using the device, the threshold (minimum) concentration in which bacterial cells start to show chemotaxis, the maximum concentration values over which cells do not show chemotaxis and the most preferred concentration, at which the strongest chemotactic responses are observed, were all determined. In the presence of long-range concentration gradients, we demonstrated that, initially, bacterial cells created population bands and then these bands migrated toward higher concentrations of the sugar until the consumption rate by the cells and the diffusion rate of a carbon source were in equilibrium. In addition, using this device, it was possible to determine the preferential chemotaxis of cells toward different carbon sources. The results of this study were that *E. coli* prefers glucose, mannose and galactose to arabinose and xylose, in this order. Hence, we believe that our device can be widely used in studying chemotaxis of numerous microorganisms and help accelerate the development of microbiology and synthetic biology because it permits parallel experimentation and reduces the time and effort needed in characterizing bacterial responses to various chemicals.

## Chapter 3. Polydimethylsiloxane-sealed Hydrogel Device for Nonlinear Bacterial Chemotaxis

### *Introduction*

Bacterial chemotaxis is a model that clarifies how cells and microorganisms sense and respond to concentration gradients in chemical environments<sup>48, 54</sup>. Apart from studies on the chemotaxis of surface-adherent cells such as neutrophils<sup>35b, 55</sup>, it is more challenging to study the chemotaxis of motile bacterial cells because they are highly susceptible to convection flow. As a result, direct application of convection-flow-based microfluidic devices to study the chemotaxis of motile bacteria is limited and diffusion-based devices have conventionally been preferred to study bacterial chemotaxis<sup>13, 39b, 56</sup>. The diffusion of small chemoattractant molecules is controlled by using nanoporous, biocompatible materials such as agarose hydrogel<sup>13, 39b, 56-57</sup>, polyethylene, polycarbonate, nitrocellulose membranes<sup>12, 34, 39c</sup>, and self-assembled nanoparticles<sup>58</sup>. However, using such materials is an obstacle to producing various concentration profiles for different chemoattractants. Although laminar-flow-based devices have previously been used to quickly generate and tune concentration gradients<sup>35b, 59</sup>, convection flow can significantly bias the chemotactic responses of bacterial cells<sup>60</sup>. For example, *Escherichia coli* (*E. coli*) swim at the speed of approximately 25  $\mu\text{m/s}$  in a static fluid<sup>56</sup> while convection flow seems to be typically  $>100 \mu\text{m/s}$ <sup>59a, 61</sup>, which may limit the use of convection-flow-based devices that can produce nonlinear complex concentration profiles across microchannels in bacterial chemotaxis studies.

Although conventional hydrogel-based (CHB) microfluidic devices<sup>13, 39b, 62</sup> effectively eliminate convection flow, they show some limitations. For example, they produce simple (mostly linear) concentration profiles, they exhibit low durability, and (most importantly) the chemoattractants used in CHBs diffuse out in all directions in the hydrogel regardless of the design of the microchannels. Further, it is difficult to produce complex patterns on hydrogels such as agarose because hydrogels are amorphous, soft materials that mostly consist of water ( $\sim 99\%$ ). In addition, hydrogels easily become dehydrated and the transport of molecules through hydrogels is not well guided in a desired direction. To overcome these limitations, we sealed a hydrogel with PDMS to develop a diffusion-based microfluidic device that generates linear and nonlinear concentration gradients on a chip for bacterial chemotaxis assays. Typically, nonlinear concentration gradients are important to understand the chemical sensing mechanism of motile cells because they are known to sense both an ambient concentration and a concentration gradient simultaneously<sup>13, 41, 63</sup>.

Here, we describe a PDMS-sealed hydrogel (PSH) device that encapsulates a thin agarose hydrogel layer (15  $\mu\text{m}$ ) between a source and a sink channel with patterned test microchannels in it. We use numerical simulation to compare the PSH device with a representative CHB device and characterize the concentration gradients across the test microchannels to prove the usefulness of the

PSH device. Lastly, we also demonstrate that the PSH device can be used to rapidly produce and accurately control various, robust, and stable concentration gradients, facilitating the chemotaxis assays of motile bacterial cells.

### ***Methods and Materials***

**Chemicals and reagents.** Green and red food dyes were used to visualize the microfluidic device and diffusion profiles. Fluorescein isothiocyanate (FITC, No. 3326-32-7) of 50  $\mu$ M in M9 buffer (No. 248510, BD Biosciences) was used to measure the concentration gradient, 1 mM  $\alpha$ -methyl aspartate (No. 2792-66-7) was used as a chemoattractant, and Pluronic® F-127 (0.02%) was done as a surfactant. Agarose power (No. 9012-36-6) was dissolved in M9 buffer (1%) to generate the hydrogel layer. Tryptone-Broth (TB, 1% tryptone and 0.5% NaCl, No. 211705, BD Biosciences) and Luria-Broth (LB, L3022, BD Biosciences) media were used for cell cultures. A mineral oil (No. M5904) was used to seal the reservoirs in order to prevent dehydration of the hydrogel and evaporation of the fluid. All the chemicals and reagents were purchased from Sigma-Aldrich Corporation unless otherwise noted.

**Preparation of bacterial cells.** We used *E. coli*, a motile bacterium, to measure the chemotactic responses in the presence of concentration gradients. The MG1655 strain was transformed with plasmids that contain a constitutive promoter (pLtetO-1) and green fluorescent protein (GFP) genes to quantitatively analyze the chemotactic responses of *E. coli* and determine whether our device was suitable for studying bacterial chemotaxis or not. A single colony of *E. coli* grown on an LB agar plate was inoculated into 5 mL of the motility buffer solution (TB), which was subsequently shaken at 180 rpm and incubated at 32 °C for 12 h in a rotary incubator. The cells were then centrifuged at 5000 rpm for 2 min, the supernatant liquid was poured off, and the pelleted cells were resuspended in M9 media. A final optical density at 600 nm wavelength was gauged to  $\sim$ 0.4. Chemotaxis assays were then performed. More detailed information about how the bacterial cells were prepared is described in our previous work<sup>56, 59a</sup>.

**Design and operation of microfluidic device.** Standard photolithography was used to fabricate the multi-depth microfluidic device<sup>64</sup>. SU-8 (Microchem 2025, Newton, MA, USA) was first spin-coated onto a Si wafer as thick as 15  $\mu$ m, baked, and then exposed to UV light using the first photomask for a shallow microfluidic channel network (MA6, Sussmicrotec, Germany). And then, the same fabrication process such as spin-coating, baking and exposure was repeated for a deep microfluidic channel network (30  $\mu$ m) by using the second photomask. The exposure dose for the first and second photomasks was 150 mJ/cm<sup>2</sup>, respectively. The processed Si wafer was subsequently developed, resulting in a dual-level master, which was silanized using trichloro(3,3,3-trifluoropropyl)silane (Sigma-Aldrich, Republic of Korea). PDMS devices were then replicated in the

same manner as in our previous work<sup>56, 65</sup>. In parallel with the preparation of PDMS devices, PDMS prepolymer was uniformly spin-coated (spin-1200D, MIDAS SYSTEM, Republic of Korea) at 500 rpm onto a glass substrate. The PDMS-prepolymer-coated substrate was then cured in a convection oven at 65 °C for over 1 h to produce a 1-mm-thick PDMS slab, which was then directly bonded to the PDMS devices through oxygen plasma treatment (50 sccm O<sub>2</sub>, 50 W for 3 s, Cute-MP, FemtoScience, Republic of Korea). This process was performed to confer a homogeneous surface property on all the microchannels and very important to facilitate load the agarose hydrogel into the microchannels.

As shown in Fig. 3–1(A), the microfluidic channel network mainly consisted of three parts: chemical-loading (*i.e.*, source and sink) channels, a cell-loading (*i.e.*, test) channel, and hydrogel-loading channels. The “source” channel is the chemical-loading channel that is flushed with a buffer medium containing a chemoattractant. The “sink” channel is the chemical-loading channel that is flushed only with the buffer medium. Therefore, the source and sink channels are used to maintain the fixed boundary conditions of the chemoattractant, resulting in a linear concentration gradient that is perpendicular to the chemical-loading channels (A–A’). The cell-loading channel was designed as a test channel in which various linear and nonlinear concentration profiles could be generated. The fluid flow was stopped after the cell-loading channel was filled with bacterial cells and a stationary state was maintained to completely eliminate any effects of convection flow on the generated concentration profiles and the chemotaxis of the bacterial cells.

As shown in Fig. 3–1(B), the deep (30 μm) and shallow (15 μm) microchannels were fabricated using PDMS. That is, the hydrogel-filling (test) channel was designed to be shallow while the other channels (including the test channel) were designed to be deep in order to selectively fill the hydrogel layer with a hydrogel precursor solution. The device was heated on a hotplate at 55 °C and a hydrogel solution that had been maintained in a hot water bath (65 °C) was then loaded through the inlets of the middle chamber to fabricate a hydrogel diffusion layer between the source and sink channels. As shown in Fig. 3–1(C), a fluorescein-containing hydrogel solution was gradually squeezed into the middle (test) channel and the solution completely penetrated through the test channel except for the dark areas still showing after 25 s. The device was then removed to a work bench at a room temperature for gelation. The hydrogel solution continued flowing along the shallow channels but did not cross the deep channels because of the effect of the surface tension of the oxygen-plasma-treated PDMS surface on the hydrogel solution despite the complex, patterned microchannels across the filling layer. After gelation, the surfaces of all the microchannels were subsequently treated with a surfactant solution to minimize any nonspecific binding between chemoattractants and the surfaces by flushing the microchannels with 200 μL of the surfactant solution. The residue was rinsed with the M9 buffer solution prior to cell-loading.

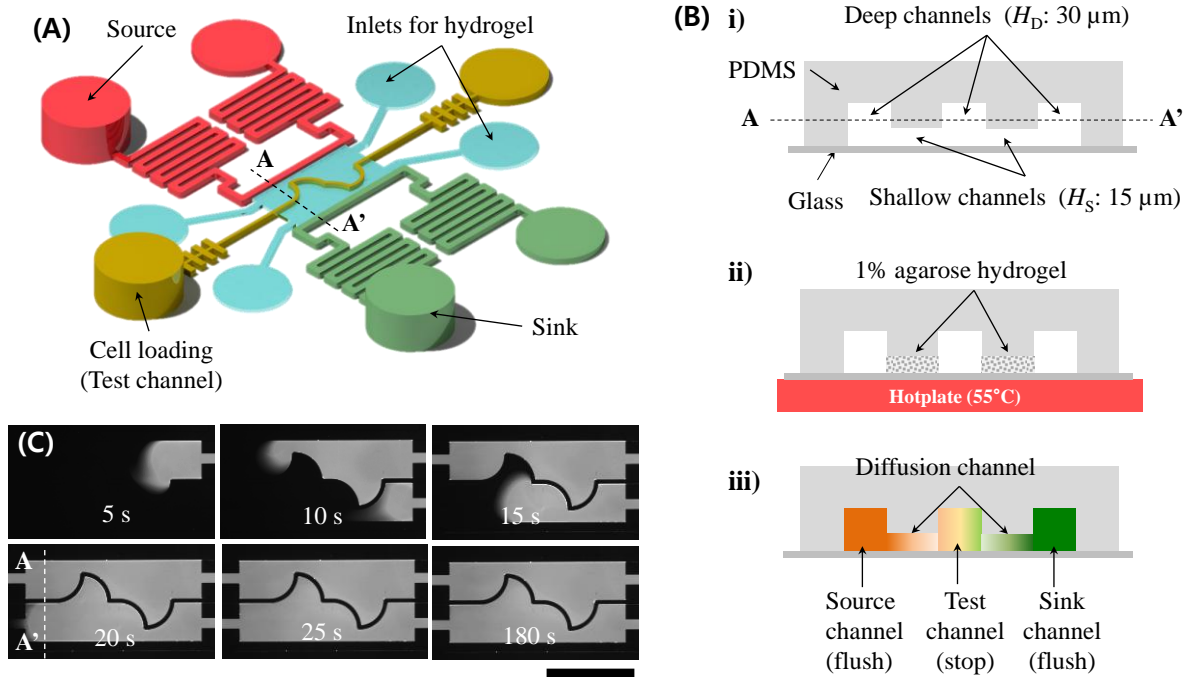


**Figure 3–1.** Concept and fabrication process of the PDMS-sealed concentration gradient generator. (A) Schematic drawing shows that the device consists of an arbitrary test channel in the middle which is used for cell loading, two hydrogel-filling channels, and chemical source and sink channels. (B) Generating the concentration gradient in three steps: i) dual-level, interconnected PDMS microchannels are fabricated; ii) a hydrogel solution is patterned by using capillary forces to integrate nanoporous hydrogel into the microchannel; iii) the source and sink channels are then filled with a chemoattractant and a buffer solution, respectively. (C) Time-lapse fluorescent images show the construction of a hydrogel layer (scale bar = 3 mm). This process corresponds to the patterning of hydrogel in (B) and the cross-sectional view of the line A–A' in (A) and (C) is illustrated in (B).

**Experimental setup and data analysis.** An epi-fluorescence microscope (Ti-U, Nikon, Japan) was equipped with a charge-coupled-device (CCD) camera (ORCA R2, Hamamatsu, Japan), 10× lenses (focal depth 8.5 μm), and a filter cube (B-2E/C, Nikon) to detect GFP. A confocal microscope (LSM700, Zeiss, Germany) was also used to measure the fluorescence intensities that determined whether a linear concentration gradient was formed along the line A–A' in Fig. 3–1 that crosses the source channel, the hydrogel layer, the test channel, the hydrogel layer, and the sink channel. Image J (NIH, USA) and Origin 7.1 (OriginLab, Northampton, NC, USA) were used wherever necessary to process images and analyze data, respectively.

**Numerical simulation of diffusion.** The transport of small chemoattractant molecules in both hydrogel and buffer solutions can be governed by the transient convection-diffusion equation as follows:

$$\frac{\partial c}{\partial t} + (\mathbf{u} \cdot \nabla)c = D\nabla^2 c \quad (\text{Eq. 3–1})$$

where  $c$  represents the concentration of the chemoattractant,  $\mathbf{u}$  represents the velocity of the fluid, and  $D$  represents the diffusivity of the chemoattractant in the hydrogel or a buffer solution. To study the chemotaxis of the bacterial cells, we forced the convection flow to stop in the test channel so that the flow was negligible across the hydrogels because of the high degree of hydraulic resistance of the nanoporous hydrogel and membrane<sup>39c</sup>. From the experimental conditions and theoretical assumption,  $\mathbf{u}$  was neglected and an initial condition ( $c(x, 0) = 0$ ) and boundary conditions (*i.e.*, source:  $c(x = 0, t) = c_0$  and sink:  $c(x = L, t) = 0$ ) were used for the finite-element-method-based simulations using COMSOL Multiphysics (Ver. 4.3a, COMSOL, USA). To quantitatively characterize and compare the PSH device (Fig. 3–2(A)) and the CHB device (Fig. 3–2(B)), we fixed the source-, sink-, test-channel, ( $h_c = 30 \mu\text{m}$  deep,  $w_c = 300 \mu\text{m}$  wide) and hydrogel diffusion layer geometries ( $h_h = 15 \mu\text{m}$  deep and  $w_h = 500 \mu\text{m}$  wide), as depicted in Fig. 3–2(A). The source channel (left) was filled with a chemoattractant solution ( $\alpha$ -methyl aspartate 1 mM,  $D = 1.4 \times 10^{-9} \text{ m}^2/\text{s}$  in water<sup>66</sup>) while the sink (right) channel was only filled with water. The same diffusivity, which was assumed to be uniform across the test channel, was used for both models. The PSH model reached a steady state in 10 min because of the thin, confined PDMS geometry while the CHB model took several hours to reach a steady state. As expected, the chemoattractant molecules diffused much faster in the PSH device than they did in the CHB device. For the PSH model, the concentration of the chemoattractant in the test channel seems to be linear for the entire range of the  $x$ -axis and the concentration profile at  $t = 10 \text{ min}$  was very close to that when  $t$  approached an infinite value. However, for the CHB model, it was almost impossible to produce a linear concentration gradient although we let the chemoattractant diffuse in this model for a very long time. This can be attributed to the semi-infinite diffusion boundary condition at the source channel. This finding means that the PSH device generates much more accurate linear concentration gradients in the test channel across the hydrogel layer than the CHB device.

Eq. 2–1 is typically simplified as a complementary error function for a transient 1-D model as follows:

$$c(x, t) = c_0 \left( \text{erfc} \left( \frac{x}{2\sqrt{Dt}} \right) \right) \quad (\text{Eq. 3–2})$$

Therefore, the concentration gradients are theoretically asymptotic with time and the gradients of small molecules gradually become linear when the concentration of the chemoattractant in the sink channel becomes zero as follows:

$$c(x) = c_0 \left( 1 - \frac{x}{w_t + 2w_h} \right) \quad (\text{Eq. 3–3})$$

Although this approximation has been used for many CHB devices, according to the simulation result, more attention needs to be paid for minimizing errors mainly caused by the diffusion time and

boundary effects. In addition to rapidly generating concentration gradients, it is important to consider the linearity of a concentration gradient at the interfaces between the test channel and the hydrogel layer. As shown in Fig. 3–2(C), the PSH model generated a highly accurate linear concentration gradient because the transport of small chemoattractant molecules was well directed and controlled to diffuse across the test channel. In contrast, the CHB model generated a linear concentration gradient only for a narrow region at the center because isotropic diffusion could not be avoided and resulted in the inaccurate formation of concentration gradients. The slope of the concentration gradient in the test channel was twice as mild as that of the concentration gradient in the diffusion channel. This is straightforward because the cross-sectional area of the diffusion layer (shallow, middle channel) was fabricated to be twice as shallow as that of the test channel (deep). Because the diffusion mass of the chemoattractant should be conserved, the concentration of the chemoattractant was halved at the test channel, resulting in a concentration gradient that was twice milder.

It is important to consider whether the concentration gradient in the test channel changes when the test channel is relocated from the center (*e.g.*, from  $x = 500$  to  $800\ \mu\text{m}$ ) to the left side (*e.g.*, from  $x = 100$  to  $400\ \mu\text{m}$ ) of the device. When the test channel was at the center of the device, the slope of the concentration gradient ( $\phi_1$ ) was calculated from Fig. 3–2(C) ( $1\ \text{mM} + \phi_1 \times 500\ \mu\text{m} + \phi_1/2 \times 300\ \mu\text{m} + \phi_1 \times 500\ \mu\text{m} = 0$ , therefore  $\phi_1 = -1/1150\ \text{mM}/\mu\text{m}$ ); the same result was obtained when the test channel was on the left side of the device and the slope of the concentration gradient was calculated ( $1\ \text{mM} + \phi_2 \times 100\ \mu\text{m} + \phi_2/2 \times 300\ \mu\text{m} + \phi_2 \times 900\ \mu\text{m} = 0$ , therefore  $\phi_2 = -1/1150\ \text{mM}/\mu\text{m}$ ). This is because the diffusion mass along the  $x$ -axis should be conserved between the source and sink channel. In fact, this result suggests that the test channel can be relocated anywhere in the hydrogel layer (middle chamber), which enabled us to design an arbitrary test channel to accurately produce nonlinear concentration profiles. Again, the slope of the concentration gradient in the test channel is identical wherever it is located, so nonlinear, arbitrary concentration gradient profiles can be generated as designed. Hence, it is straightforward that diffusion differences along the  $y$ -axis in the test channel can be neglected because of the source and sink boundary conditions.

## Results

**Formation of concentration gradients in PSH devices.** We used food dyes and a  $50\ \mu\text{M}$  FITC solution to test the PSH device. We first injected solutions containing red and green food dyes into the source and sink channels, respectively, and found that fluid does not leak between the hydrogel layer and the PDMS microchannel. As shown in Fig. 3–3(A), the food dyes diffused from the source to the sink channel across the test channel that was filled with only a buffer solution at the center of the device. We performed a similar experiment by replacing the food dye solutions with an FITC solution to quantitatively measure the concentration gradient of the chemoattractant. A regular fluorescence microscope was unsuitable for accurately quantifying the concentration gradient across the hydrogel

layer and the test channel because the latter was twice deeper than the former. The fluorescence intensities are typically proportional to the depth of a microchannel when the focal depth is deeper than the microchannel. To resolve this limitation, we used a confocal microscope to measure the fluorescence intensities. This method provided the real concentration of the chemoattractant across the test channel, as shown in Fig. 3–3(B). The test channel did not show a brighter stripe because the focal depth of the confocal microscope was approximately 2  $\mu\text{m}$  while both the hydrogel layer and test channels were much deeper ( $>15 \mu\text{m}$ ) than the focal depth. Fig. 3–3(C) shows the normalized fluorescence intensities along the  $x$ -axis from the source channel across the hydrogel layer to the sink channel. The fluorescence intensities show an almost linear concentration gradient regardless of the position along the  $y$ -axis, which is consistent with the theoretical simulation result. Fig. 3–3(B)) shows a fluorescence image taken from the same PSH device using a fluorescence microscope. The fluorescence intensities quantitatively measured at various positions along the  $y$ -axis are also very consistent with each other. Furthermore, the concentration gradient was measured daily for a week, demonstrating the long-term durability and stability of the linear concentration gradient. Because the device rapidly generated various stable, durable concentration gradients, we used the concentration gradients to study the chemotaxis of *E. coli*.

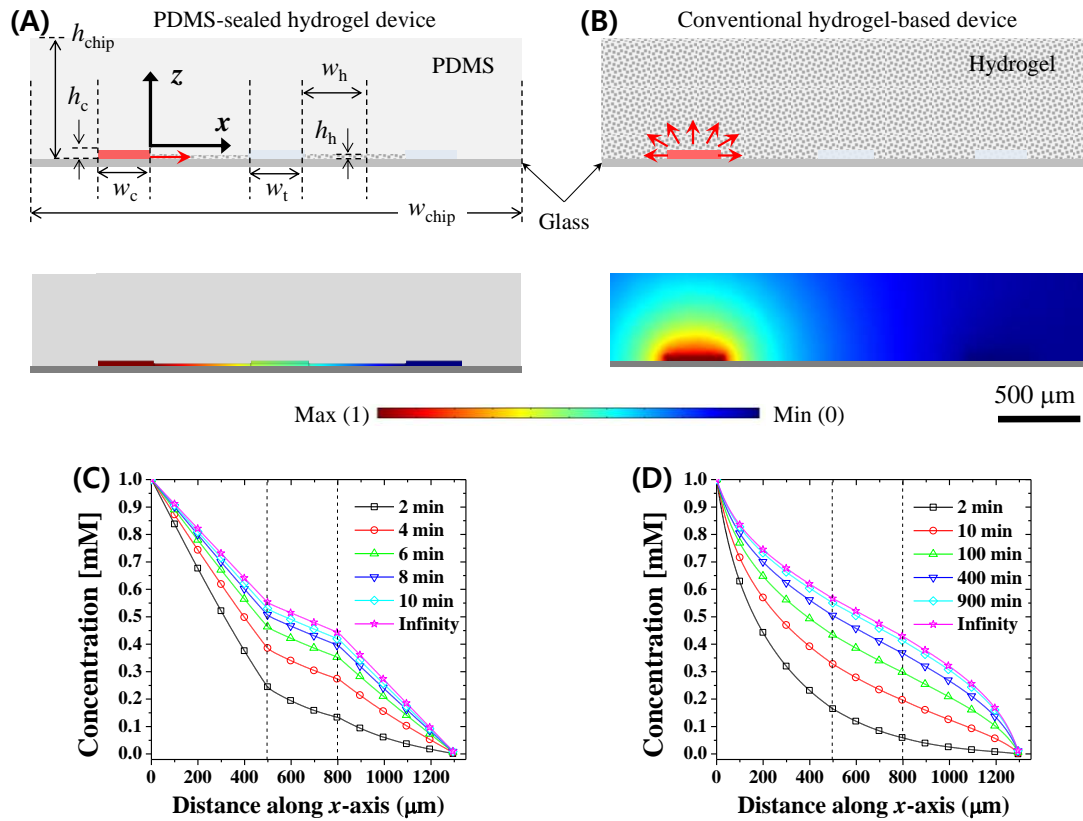


**Figure 3–2.** Numerical simulation of diffusion in a PSH device and a CHB device. (A) The PSH device (1-D diffusion model) shows directed diffusion of small molecules. (B) The CHB device (2-D diffusion model) shows isotropic diffusion including molecular transport in undesired directions (illustrations are not to scale). (C)–(D) The transient concentration distribution profiles computed

from the numerical simulations for (A) and (B), respectively. The PSH device generates a much more linear concentration gradient and reaches a steady state much more rapidly than the CHB device does. The dimensions of the model are  $h_h = 15 \mu\text{m}$ ,  $h_c = 30 \mu\text{m}$ ,  $w_h = 500 \mu\text{m}$ , and  $w_t = w_c = 300 \mu\text{m}$ , and  $h_{\text{chip}} = 3 \text{ mm}$ .

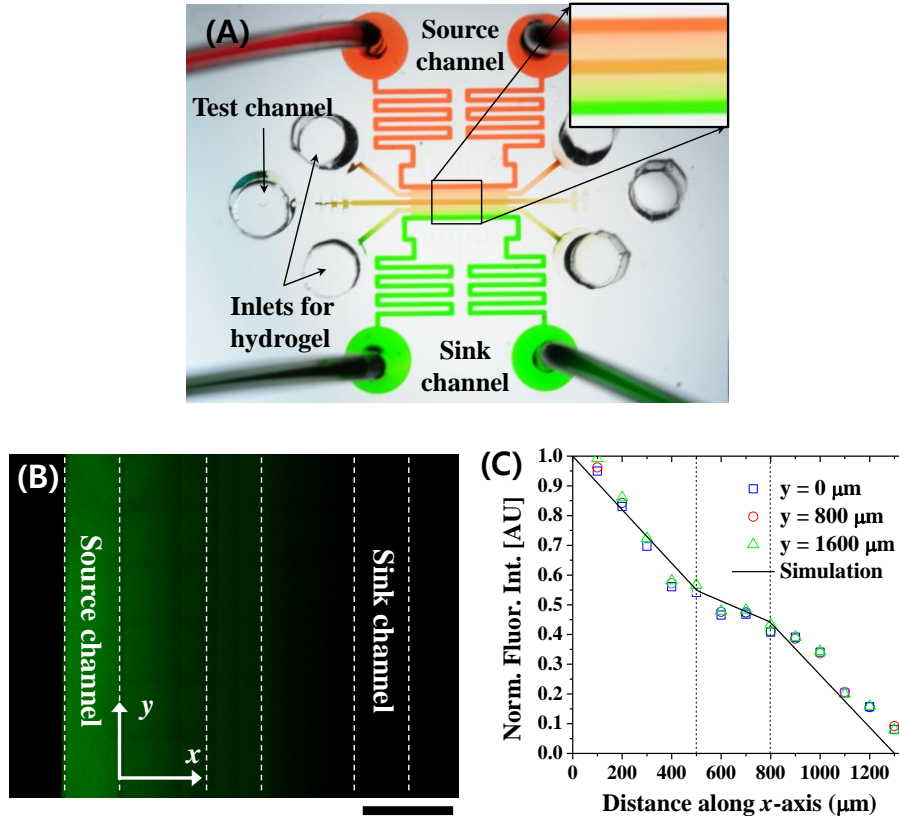


**Figure 3–3.** Characterization of concentration gradients using fluorescent and food dyes. (A) Colorful image shows that the PSH device generates linear concentration gradients of red and green food dyes, respectively. (B) Confocal microscope image visualizes a linear concentration gradient formed by using a FITC solution. The scale bar is  $500 \mu\text{m}$ . (C) Quantification of the fluorescence intensities of the image in (B) along the  $x$ -axis for  $y = 0 \mu\text{m}$ ,  $800 \mu\text{m}$  and  $1600 \mu\text{m}$ , respectively, which is consistent with simulation results.

**Chemotaxis assays performed using a linear concentration gradient.** We used the PSH device to study the chemotaxis of *E. coli*. We fabricated a straight test channel in the middle of the hydrogel layer, as shown in Fig. 3–4. We loaded an 1-mM  $\alpha$ -methyl aspartate solution as a chemoattractant into the source channel and only a buffer solution into the sink channel (Fig. 3–4(A)). Subsequently, we waited approximately 20 min for the chemoattractants to diffuse and form a linear concentration gradient and then loaded *E. coli* cells into the test channel (Fig. 3–4(C)). Next, we sealed the inlet and outlet reservoirs of the device with mineral oil to balance the hydrostatic pressure, which resulted in the prevention of convection flow in the test channel. Most of the *E. coli* migrated toward the high concentration of chemoattractants in the linear concentration gradient. We photographed the fluorescence intensities of the cells and measured the biased chemotactic responses of the cells after 1

min and 20 min, respectively, as shown in Fig. 3–4(C)–(D). Three regions of interest (ROIs) were arbitrarily determined in the images and the fluorescence intensities of the cells in the three ROIs were analyzed. Since the chemotactic responses were distinctly revealed and close to each other, we came to a conclusion that the PSH device is suitable for conducting bacterial chemotaxis assays as shown in Fig. 3–4(B).

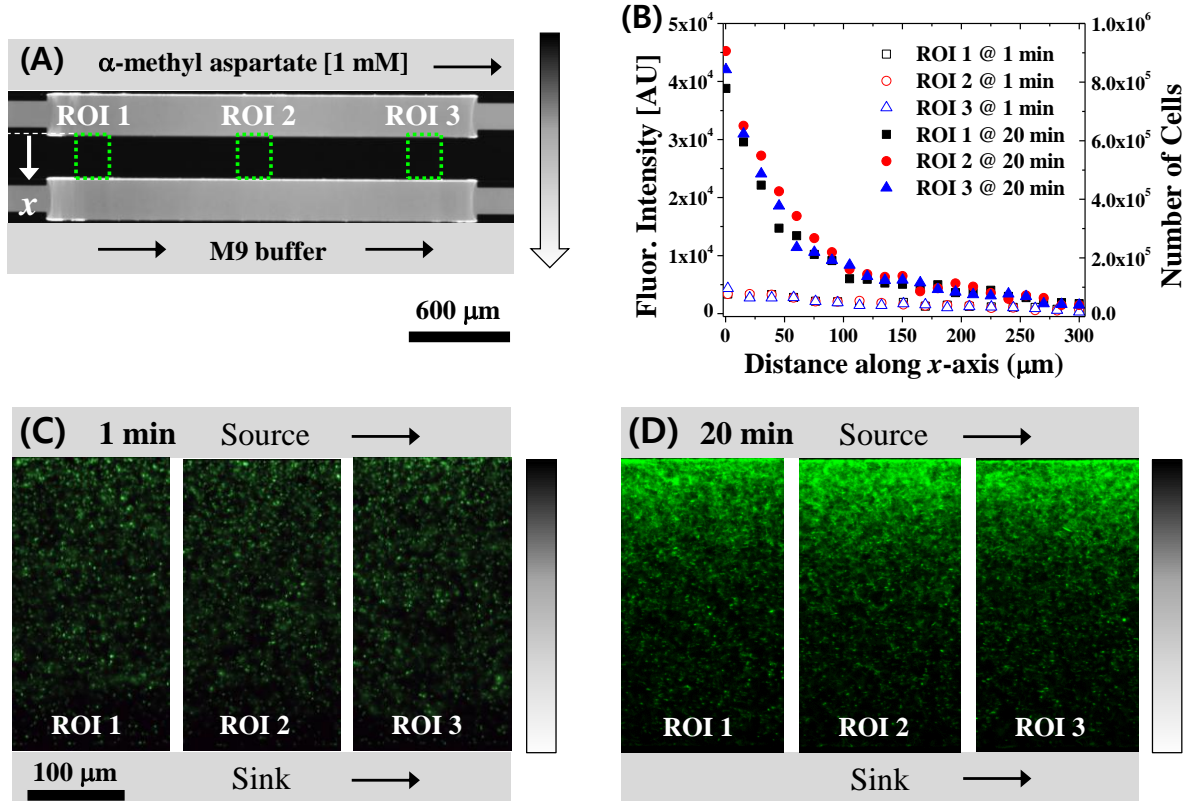


**Figure 3–4.** Chemotaxis assay using a linear concentration gradient. (A) Microimage shows experimental conditions generating a linear concentration gradient between the source and the sink channel, two hydrogel layers that contain FITC for visualization, and a straight test channel where cells are loaded and observation was made. (B) Quantification of the fluorescence intensities of the cells migrating toward the high concentrations. (C)–(D) Fluorescence images taken at 1 min and 20 min show the migration of the cells toward the high concentrations.

**Bacterial chemotaxis assays performed using various nonlinear concentration gradients.** We also produced various nonlinear concentration gradients. As shown in Fig. 3–5(A), a linear concentration gradient was produced from the source to the sink channel in the same manner as before. At the same time, various test channels were fabricated in the hydrogel layer. This configuration produced a global, linear concentration gradient while the local concentration gradient depended on the profile of the microchannels. For example, the fluorescence intensities of the FITC solution along line 1, as plotted in Fig. 3–5(B), indicate the formation of a linear concentration gradient. In addition, the concave and convex microchannels produced nonlinear concentration gradients along line 2 and line 3, respectively, and the magnitude of the concentration gradient in line 4 was different from that

of the concentration gradients in line 1.

After generating concentration gradients with the chemoattractant in the same manner, we loaded *E. coli* into the test channel and then completely stopped the convection flows to observe the chemotactic responses of the cells. Fig. 3–5(C) shows the various fluorescence intensities of the cells along the concave and convex channels when a global, linear concentration gradient was maintained throughout the entire period of the assay. For example, the dashed line in yellow in the middle of the image may indicate half the concentration of the chemoattractant in the source channel ( $c_0/2$ ) at a steady state according to Eq. 3-3. However, the local concentration gradient varies along the channel; that is, the incremental concentrations of the chemoattractant along  $S_1$  continuously increase while they continuously decrease along  $S_2$  (*i.e.*,  $|\Delta c/\Delta S_1| > |\Delta c/\Delta S_2|$  for  $x$  when  $c(x) > c_0/2$ ). As a result, the cells showed different chemotactic responses; that is, the cells showed stronger positive chemotactic responses in the steep concentration gradient ( $|\Delta c/\Delta S_1|$ ) than in the mild one ( $|\Delta c/\Delta S_2|$ ). The cells in the concave channel (along  $S_1$ ) shows stronger chemotactic responses so that most cells moved to the highest local concentration region in the hydrogel layer. This is why cells are rarely observed in the concave (along  $S_1$ ) channel compared to the convex channel (along  $S_2$ ) even though the global concentration of the chemoattractant remains constant. Fig. 3–5(D) shows the number of the cells along the concave and convex channels. The cells in the concave channel clearly migrated toward the region containing the highest local concentration of the chemoattractant. To confirm this observation, we repeatedly compared the chemotactic responses of the cells to the concentration gradients in the convex and concave channels. Fig. 3–6(A) shows a wide population band while Fig. 3–6(C) shows a narrow, focused one because the steeper concentration gradients in the concave channel attract more cells than the milder ones in the convex channel. Figs. 3–6(B) and (D) show the fluorescence intensities of the cells along the curvilinear channels, demonstrating a potential of highly concentrating a bacterial cell population at a desired location.

## Discussion

The PSH device completely resolved the dehydration problem of hydrogels because it encapsulated the hydrogels in the microchannel. From experimental perspective, hydrogels easily dehydrate in CHB devices unless a humidity controller is integrated with them. In addition, the PSH device used a low-density hydrogel (1%) while CHB devices seem to depend on a high-density hydrogel (3%). This is because the CHB devices need to handle hydrogel layers without significant deformation. However, the high-density hydrogel decreases the size of the pores in it, dramatically decreasing the effective diffusivity of the hydrogel to less than that of water. For example, the diffusivity of glucose in 1% agarose is  $9.8 \times 10^{-8} \text{ m}^2/\text{s}$ , which is very close to the diffusivity of that in pure water, as used in this work. However, the diffusivity of that in 2% hydrogel significantly decreases to  $5.0 \times 10^{-9} \text{ m}^2/\text{s}$ <sup>67</sup>. We note that the PSH device makes it possible to much more accurately

produce and control concentration gradients, which are more suitable for various bacterial chemotaxis assays. Of course, the low-density hydrogel in the PSH device seems to be susceptible to degradation and infiltration by motile cells. This may alter potentially diffusivity and permeability of chemoattractant molecules over time but we found no defect during the bacterial chemotaxis assays that can be done within several hours.

The motility and density of the cells used for chemotaxis assays in the presence of various nonlinear concentration gradients were at the exactly same condition. This was possible because the hydrogel layer in the PSH device provided enough room to simultaneously produce various concentration gradients by fabricating the concave and convex microchannels. Herein, it would be worth to mention the downside of the test channel. This would be negligible but high motility of bacterial cells may affect the concentration gradient in the test channel by disturbing stationary fluid (swimming). The higher the cell density and motility, the greater errors may be caused. However, the errors can be further minimized once the width of the test channel reduces but is long enough to investigate the chemotactic responses of motile bacterial cells.

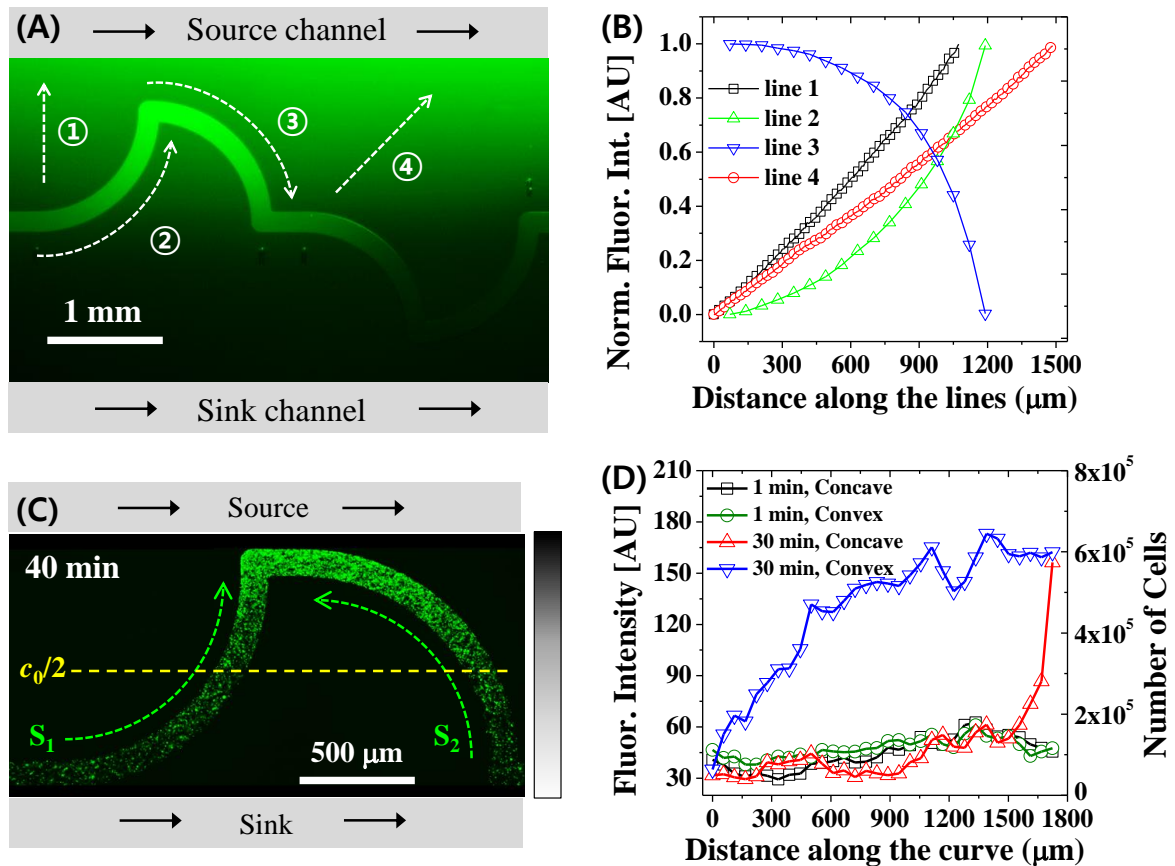


**Figure 3-5.** Characterization of nonlinear concentration gradients and a chemotaxis assay. (A) The microscopic image shows the linear and nonlinear profiles of the concentration gradients of the FITC solution in the test channel. A global, linear concentration gradient is present between the source and the sink channel. (B) Quantification of the fluorescence intensities along the test channels shows various, nonlinear concentration gradients which depend on the shape of the test channel in the

hydrogel layer. (C) The chemotactic responses of the cells in the presence of nonlinear concentration gradients reveal that more cells are attracted to the high concentration region along  $S_1$  than along  $S_2$  because the local concentration gradient increased more steeply along  $S_1$  than that along  $S_2$ . (D) Quantification of the fluorescence intensities of the cells measured 1 min and 30 min after the assay along  $S_1$  and  $S_2$ .

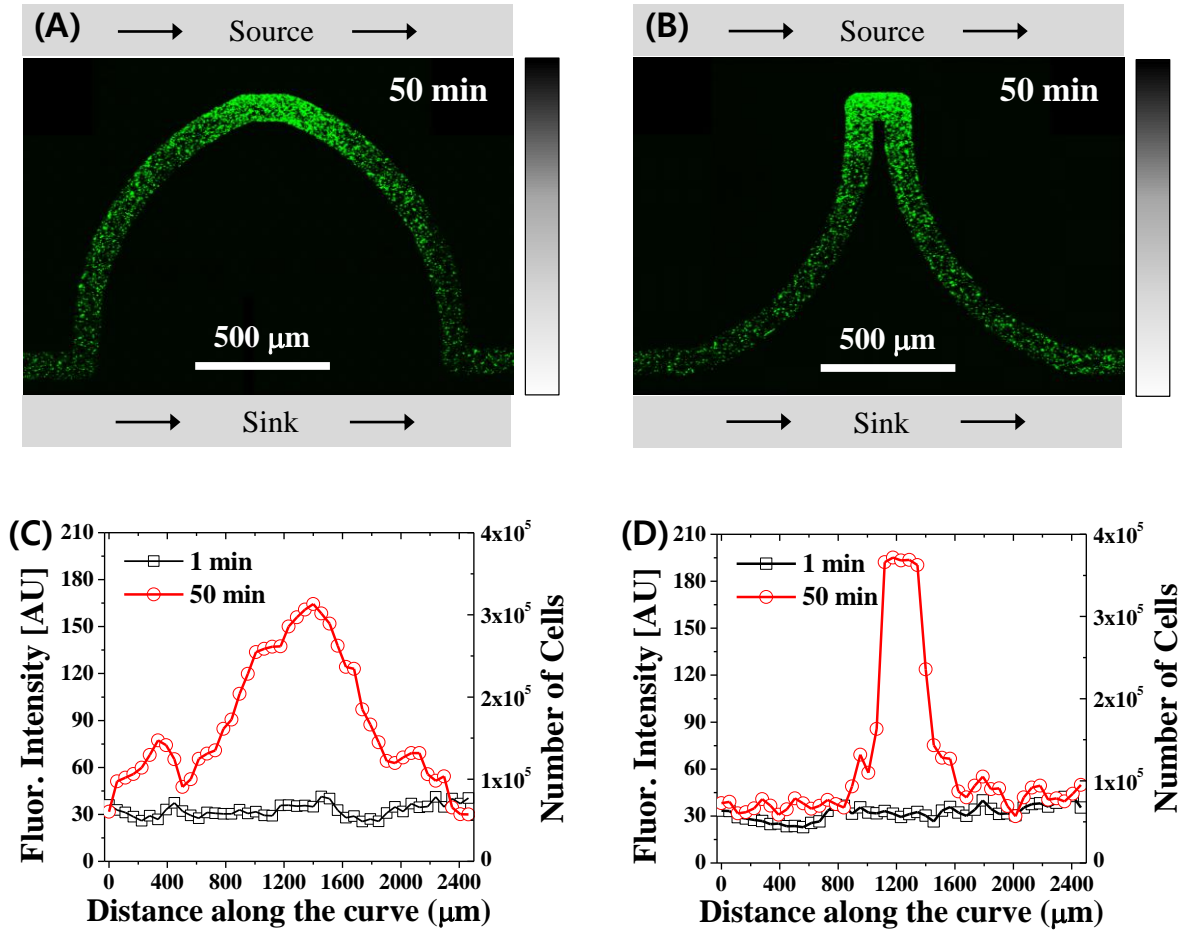


**Figure 3–6.** Chemotaxis assays in the convex and concave test channels. (A) Convex-like nonlinear concentration gradients caused the cells to migrate toward the highest concentrations region, forming a slightly wide population band. (B) Concave-like nonlinear concentration gradients caused more cells to be attracted to the highest concentration region, thus forming a narrow, focused population band. (C)–(D) Quantification of the fluorescent intensities along the test channels from left to right, respectively.

### Conclusions

The combination of hydrogel and PDMS prevents dehydration of the hydrogel and directs the diffusion/transport of chemoattractant molecules so that various concentration gradients are rapidly produced and accurately controlled without inducing convection flow. Such a device would be more appropriate for conducting chemotaxis assays of motile bacterial cells. In addition, the design concept and advantages of the PSH device over CHB devices were well validated by carrying out numerical

simulations. Both the linear and nonlinear concentration gradients were tested by *E. coli* cells that showed a positive chemotaxis toward a chemoattractant by using not only source and sink channels to produce a global, linear concentration gradient between the ends of a hydrogel layer but also a test channel in the hydrogel layer to produce a local, nonlinear concentration gradient. Hence, we believe that the PSH device developed in this work can be widely applied to chemotaxis assays for not only motile microorganisms but also numerous mammalian cells for species screening, drug screening and/or quantitative biological assays because it more quickly and accurately produces a broader range of concentration gradients that are more versatile, linear, durable, and controllable than those produced using CHB devices.

## Chapter 4. Self-integration of Nanoporous Membranes in Microfluidic Devices:

### Electrokinetic Preconcentration of Biosamples

#### *Introduction*

In nature, nanoporous membranes are widely found because biological and engineering systems such as cytoplasmic membranes, neuron synapses, fuel cells, and water purification systems need to meet the common purpose of regulating ion and mass transports at the molecular levels<sup>68</sup>. Owing to these essential roles of nanoporous membranes (NPMs), there have been attempts for integrating many natural or engineered NPMs, or miniaturizing them for use with microfluidic systems for filtration<sup>69</sup>, sensing<sup>70</sup>, analysis<sup>71</sup>, and selective delivery<sup>56, 72</sup> of various biomolecules. For example, an artificial membrane consisting of an cylindrical gold nanotube array was fabricated to manipulate molecular transport by applying tunable charge on the tube<sup>69</sup> and a stochastic sensor concept was suggested that has two outputs depending on whether the pore is occupied by analytes; current flow through the pore showed different magnitudes<sup>70a</sup>. Furthermore, nanoporous hydrogels were integrated into microfluidic channels for temporally and spatially controlling a chemical environment<sup>72</sup>.

In general, several critical membrane properties seem to be important for the successful application of NPMs to microfluidic systems. Membrane thickness affects physical strength and hydraulic resistance; pore-morphology such as pore size, pore-size distribution, and porosity determine flux and hydraulic resistance; and surface properties control permselectivity, chemical stability, biocompatibility, bio-fouling, etc. In particular, electrokinetic properties such as zeta-potential ( $\zeta$ ) of NPMs appear to be more important from the viewpoint of micro/nanofluidic pre-concentration devices because bio-samples are more often manipulated by electrical potentials than mechanical pressure<sup>73</sup>. Additionally, the electrokinetic properties of NPMs govern the pre-concentration efficiency and trapping mechanism of biomolecules<sup>74</sup>. For example, if the pore size is comparable to the thickness of the Debye layer, the nanopores allow permselective ion transport, extruding co-ion and absorbing counter-ion of the surface charge<sup>6</sup>. Conversely, NPMs with relatively large pores are insufficient to cause the Debye layer to overlap, showing no significant permselective effects<sup>6</sup>. The pore size explains why permselective NPMs are widely used for ion concentration polarization (ICP) in biomolecule pre-concentration.

Recently, many attempts were made to microfabricate NPMs in microfluidic devices for the pre-concentration of biomolecules. Nanoslits (nanochannels)<sup>75</sup> and nanopores by silica beads<sup>75a</sup> were nanofabricated between glass microchannels, but the nanofabrication processes seem to be expensive and labor-intensive. Non-lithographic nanochannels were made of polydimethylsiloxane (PDMS) polymers, which have elastomeric properties such as reversibly bonded nanogap<sup>76</sup> and cracked nanowrinkle<sup>19</sup>. Additionally, NPMs have been made from non-crosslinked mesoporous materials<sup>77</sup>, hydrogels<sup>14, 78</sup>, and charge-selective polymers<sup>79</sup>. However, these NPMs still have some drawbacks

such as complex nanofabrication processes, difficult shapes and dimension control in microfluidic devices, and the lack of methods for characterizing the electrokinetic properties in a microfluidic device format. Although it seems more or less challenging to address the drawbacks, it is still needed to develop a microfluidic platform that self-integrates various nanoporous materials between two microchannels with pre-determined cross-sectional areas for ion and mass transport. In addition, if the microfluidic platform can facilitate characterization and comparison of the physicochemical properties of NPMs, the NPMs can potentially be used for the pre-concentration or accumulation of bio-samples on a microfluidic device in a more efficient and more optimal manner.

For this reason, in this paper, we describe simple and robust methods for microfabricating various NPMs between two microchannels. Because the methods enable us to easily and rapidly pattern many precursor solutions such as photo-curable materials and thermally curable hydrogels, it is possible to adjust surface charges and pore sizes ( $2 \text{ nm} < d_p < 100 \text{ nm}$ ) of membranes for purpose-built applications in microfluidic devices. Using the methods, we demonstrate that four precursor solutions can be fabricated as NPMs in a microfluidic device and compare their electrokinetic properties because it is possible to fabricate membranes with same dimensions. In addition, we demonstrate that the device can actively control the effective ion transport area, pore size, and permselectivity by adjusting the microchannel geometries and blending precursor solutions with functional reagents. Lastly, we not only pre-concentrate biomolecules for ICP applications on the anodic side of the NPMs but also accumulate nanobeads and microorganisms for electrophoretic pre-concentration applications on the cathodic side.

### ***Methods and Materials***

**Chemical Reagents.** Phosphate-buffered saline (PBS, pH = 7.4) and potassium chloride (KCl, pH = 7.4) solutions were used as buffer solutions and, if necessary, were diluted with desalted water to a working concentration such as 1 mM and 5 mM, respectively. Fluorescein isothiocyanate (FITC) labeled bovine serum albumin (BSA) was diluted with the buffer solution and used for biomolecule pre-concentration experiments. In addition, biotinylated nanobeads of 1  $\mu\text{m}$  in diameter (solid 2 wt.%, Invitrogen, Korea) were suspended and then diluted up to 100 times with 1 mM of the PBS buffer for electrophoretic pre-concentration experiments. For bacterial pre-concentration experiments, *E. coli* MG-1655, which constitutively expresses green fluorescent protein genes (GFP), was grown overnight on LB agar solid medium plates with 100  $\mu\text{g/ml}$  of ampicillin at 32  $^{\circ}\text{C}$ . A single colony was used for inoculating 5 mL of tryptone broth (TB, 3% tryptone and 0.5% NaCl) media. Then, the *E. coli* cells were grown in a rotary shaking incubator (32  $^{\circ}\text{C}$ , 200 rpm) to a mid-log phase and required about 12 h for the optical density at a wavelength of 600 nm ( $\text{OD}_{600}$ ) to reach 2.0; the grown bacteria were then centrifuged at 5000 rpm for 5 min, based on our previous procedures<sup>56, 80</sup>. The cells were diluted to the final concentration of  $\text{OD}_{600} = 0.02$  in 1 mM of PBS for cell pre-concentration

experiments.

Four NPM precursors were tested in this work. First, Nafion solution (DuPont, Korea) including an ion-exchange resin (5 wt.%) was used as delivered. Second, 2-hydroxyethyl methacrylate (HEMA) and acrylic acid (AA) were mixed in a 5:1 ratio and referred to as (poly-)HEMA-AA. Third, HEMA and 2-(dimethylamino)-ethyl methacrylate (DMAEMA) were mixed in a 5:1 ratio and referred to as (poly-)HEMA-DMAEMA. 1 wt.% 2,2-dimethoxy-2-phenyl-acetophenone (DMPA) and 1 wt.% ethylene glycol dimethacrylate (EGDMA) were added to the HEMA-AA and HEMA-DMAEMA precursor mixtures as a photo-initiator and cross-linking agent, respectively. Lastly, agarose hydrogel (1.5 wt.%) was used. All chemical reagents used for membrane fabrication were purchased from Sigma-Aldrich and used as delivered, unless noted otherwise.

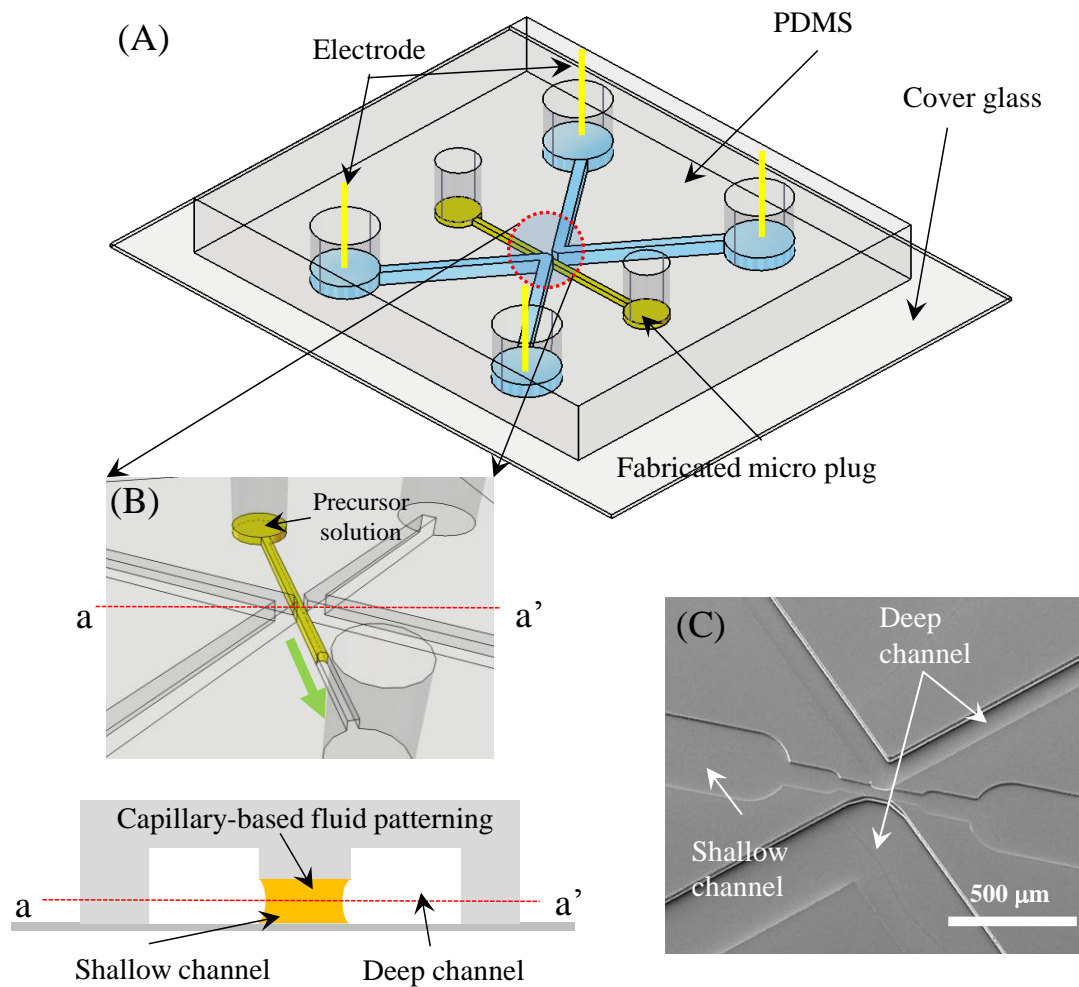


**Figure 4-1.** Schematic illustration of bio-sample pre-concentrator integrated with tunable ion-transport membranes. (A) The device consists of two deep microchannels for loading bio-samples and buffer solutions and one shallow microchannel at the center for integrating the membranes. (B) Zoomed-out view of the junction shows that the two deep channels are connected by a shallow channel, along which precursor solutions flow, guided by capillary forces. The precursor solutions are cured into a leakage-free, ion-transport-tunable membrane. (C) Scanning electron microscope (SEM) image of the PDMS device with dual-level depth microchannels.

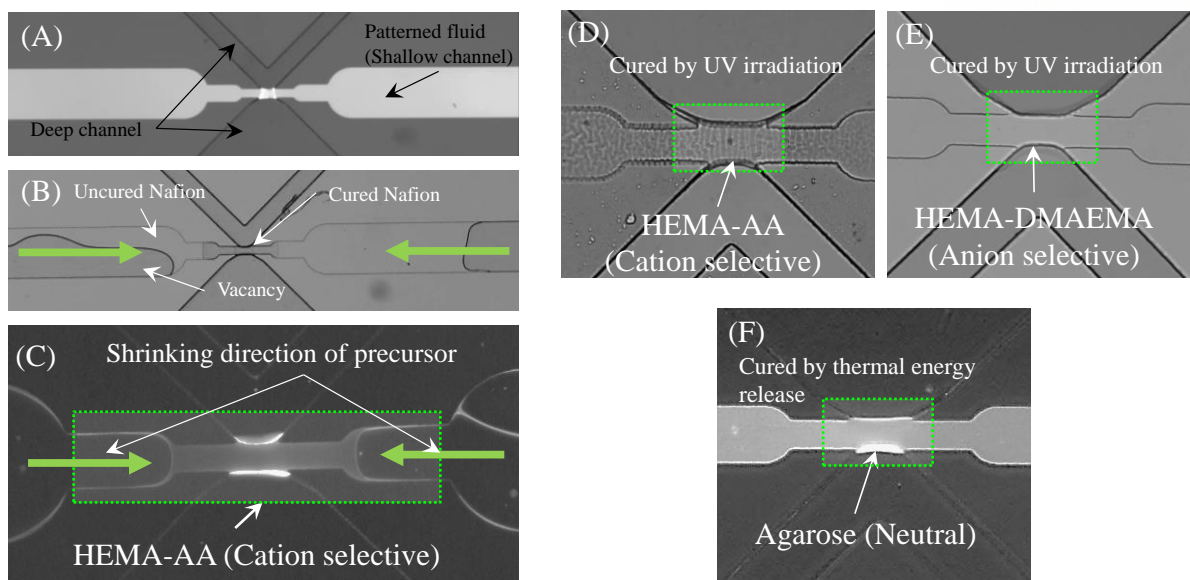


**Figure 4–2.** Fabrication process and various types of nanoporous membranes. (A) The shallow microchannel is filled with Nafion precursor solution owing to the capillary force, and the solution is cured on a hot plate (120 °C). (B) Because the solvent evaporates and escapes from the junction through the open, deep microchannels, the solution starts to solidify from the center of the junction; the resulting volume shrinkage is compensated for by extra solution from the shallow channel. (C) Nafion membrane is effectively self-sealed and uniformly formed in every device. (D) Photo-cured HEMA and AA mixture polymer that allows cation permselectivity. (E) Photo-cured poly-HEMA modified by DMAEMA for anionic permselectivity. (F) An agarose hydrogel membrane with large pores and weak surface charge density compared with the other materials.

**Design of Microfluidic Channel and Nanoporous Membranes.** The microfluidic device with dual-level depths was fabricated using standard soft-lithography technologies. Briefly, SU-8 (Microchem 2025, Newton, MA, USA) was spin-coated, baked, and then exposed to UV light using the first photo-mask (MA6, Sussmicrotec, Germany) for creating a shallow microchannel (15  $\mu\text{m}$  in thickness). Thereafter, the same set of procedures was repeated using another photo-mask for creating a deep microchannel network (30  $\mu\text{m}$  in thickness). The double coating, double exposure processes were followed by a single developing step, resulting in a dual-level depth master with 15- $\mu\text{m}$ -shallow and 30- $\mu\text{m}$ -deep microfluidic channel networks. Subsequently, the master was silanized using trichloro(3,3,3-trifluoropropyl)silane (Sigma-Aldrich, Korea) and then PDMS devices were prepared in the same manner as in other papers<sup>56, 80</sup>. The PDMS devices were directly bonded to a glass substrate with oxygen plasma treatment under 50 sccm of  $\text{O}_2$  and 50 W for 4~7 s (Cute-MP, Femto Science, Korea). This treatment was essential for precursor solutions to flow easily along the shallow channel; power and exposure time of the oxygen plasma were optimized because NPM formation depends on the viscosity and volatility of the precursor solutions. After self-integration of NPMs, all microchannels and glass surfaces were coated with a pluronic surfactant (F-127, 0.02%, Sigma-Aldrich) to minimize any nonspecific binding between the biomolecules and the glass surfaces by

flushing 200  $\mu\text{l}$  of the pluronic solution for 2 h. After surface treatment, the residue was rinsed with the buffer solution for 2 h.

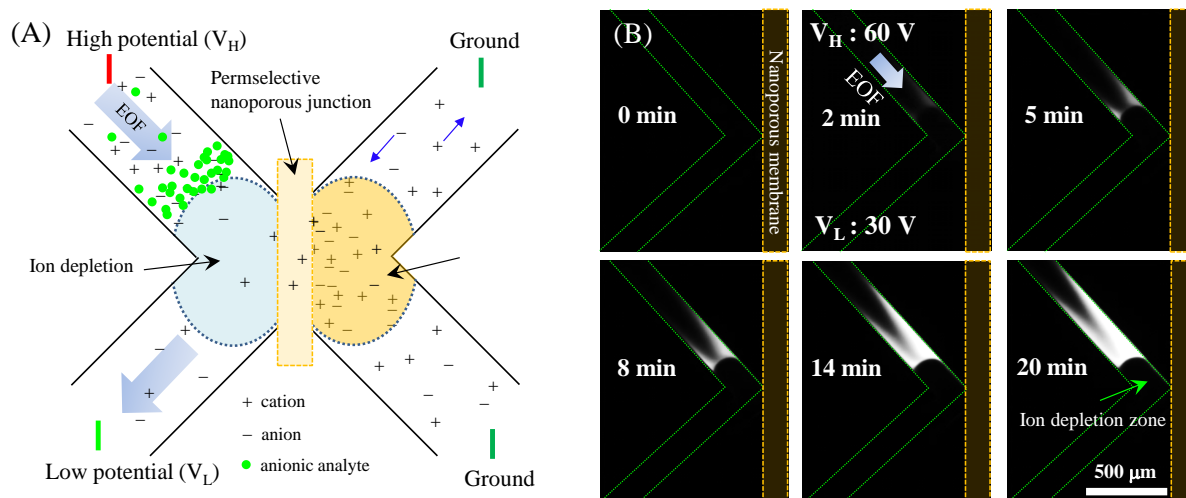


**Figure 4-3.** Schematic description of ion concentration polarization (ICP) and time-sequential fluorescent images of biomolecule pre-concentration. (A) Illustration of the ICP principle shows the movement direction of cations, anions, and negatively charged biomolecules. The left microchannel is filled with a buffer solution containing biomolecules, and electric potentials are applied to continuously deliver the biomolecule analytes using electroosmosis flow. The right channel is filled only with buffer and is connected to an electrical ground. (B) A time-lapse image sequence of fluorescently labeled BSA with an initial concentration of 100 nM in a 5 mM PBS buffer solution under an electrical potential of  $V_H = 60\text{ V}$  and  $V_L = 30\text{ V}$ .

**Fabrication of Nanoporous Membranes.** Each precursor solution was introduced for self-integration of NPMs in a shallow microchannel that is laterally open for connecting two deep microchannels, as shown in Fig. 4-1. When the solution approached to the junction, it kept flowing along the shallow channel but did not enter the deep channels. This is because surface tension in the shallow channel keeps the precursor solution along the shallow channel and prevents it from crossing over the adjacent deep channels<sup>81</sup>; the surface tension withstands the pressure difference between the shallow and deep channel. This is called the capillary-driven flow-patterning method<sup>81</sup> and is used for filling the shallow channel with Nafion, HEMA-AA, HEMA-DMAEMA, and agarose hydrogel. However, they have completely different solidification mechanisms, which are the focus of this work (refer to Results and Discussion).

## Results and Discussion

**Fabrication of Nanoporous Membranes.** First, the Nafion precursor solution was introduced along the shallow channel (Fig. 4-2(A)) and then solidified by evaporating the solvents in the precursor solution on a 95  $^{\circ}\text{C}$  hotplate for 10 min. Because the Nafion solution was exposed to air on the deep microchannel sides, solvent evaporation initiated at the center of the junction and caused

volume contraction of the solution during solidification. However, the contracted volume was replenished with extra solution in the shallow channel, resulting in the fabrication of a tightly sealed, robust Nafion membrane that caused no flow leakage during the electrokinetic pre-concentration of biomolecules, as shown in Fig. 4–2(B). Additional Nafion precursor supply was important during the fabrication; therefore, the shallow channel was designed with a cross section that increased from the junction to the reservoir for continuous replenishment. Fig. 4–2(C) shows a fully solidified Nafion membrane at the junction, whereas the wide shallow channel is seen to be empty because of the replenishment.

Second, poly-HEMA membranes were fabricated in a manner similar to the fabrication of a Nafion membrane (Fig. 4–2 (D) and (E)). For a cation-selective transport membrane (CSTM), the poly-HEMA was mixed with AA, whereas for an anion-selective transport membrane (ASTM), the poly-HEMA was mixed with DMAEMA; the details pertaining to mixing ratio and concentration are listed in Table 4–1. Basically, oxygen is known to affect the cross-linking of poly-HEMA<sup>82</sup>. In addition, PDMS is known to contain oxygen and be highly gas permeable. Hence, oxygen was eliminated during the polymerization process by placing both the poly-HEMA solution and the PDMS device in a homemade nitrogen box, in which nitrogen was continuously flowed for 2 h so that oxygen was completely extracted from the poly-HEMA solution and PDMS device. After introducing the mixture along the shallow channel, UV light from a 200 W mercury bulb was focused on the junction for 30 s using a fluorescent microscope without any optical filter cubes; a 40x lens was used to focus the UV light. Notably, the UV light was focused on only the junction to allow the precursor solution in the side channels, which were not yet cross-linked, to flow toward the junction where cross-linking was in process. This helped avoid fluid leakage that is typically caused by volume contraction during the photo-induced cross-linking process, as described for Nafion. As a control experiment, we tested the polymerization of poly-HEMA by irradiating a UV light in the flood mode. In this case, photopolymerization started everywhere, causing the precursor solution in the junction to flow toward the larger channels and resulting in unsuccessful membrane fabrication.

Lastly, agarose hydrogel (1.5 wt.%) was employed to form a hydrogel membrane that has relatively large pore sizes but no permselectivity. An agarose solution that was stored in a water bath at constant temperature (65 °C) was introduced into the microfluidic device on a 55 °C hotplate so that the agarose solution was maintained in a liquid state during the entire filling process. As soon as the device was removed from the hotplate to a workbench at room temperature (24 °C), the agarose solution cooled and solidified into hydrogel without any fluid leakage across the deep microchannels.

We summarized properties of the NPMs in Table 4–1. The Nafion membrane has pores that are a few nanometers in size and highly negatively charged owing to the presence of dense sulfate group<sup>83</sup>. The poly-HEMA mixtures have small pore sizes, which are in the same range as those of Nafion, but were much easier to tune the surface charge condition by simply mixing them with differently charged

compounds such as AA and DMAEMA<sup>14</sup>. Lastly, in case of the agarose hydrogel, it was possible to manipulate the surface charge density and the pore size by mixing charged molecules and by adjusting the chemical composition in the pre-hydrogel solution, respectively<sup>84</sup>. However, changing the chemical composition substantially influenced the viscosity, which is the most important parameter in dual-level depth based fluid patterning. In this experiment, the agarose concentration was set to 1.5 wt.% in an aqueous solution that has relatively large pore sizes (~120 nm)<sup>85</sup> and a weak surface charge density compared to other materials used. Notably, there was no fluid leakage in the solidification mechanisms of each NPM, although their relative mechanical robustness varied. We divided the degree of fabrication availability, membrane robustness, ICP strength, ion transport tunability, and chemical compatibility of the membranes into four relative grades for convenient comparison. For example, the Nafion and poly-HEMA membranes lasted over a few ten days in an atmospheric environment, whereas the agarose hydrogel needed to be kept in an aqueous environment for later use because it dehydrated easily and caused fluid leakage when rehydrated. Therefore, the Nafion and poly-HEMA obtained two plus symbols meaning “very good” whereas the agarose did one plus symbol meaning “good”.

	<b>Nafion</b>	<b>HEMA-AA (CSTM)</b>	<b>HEMA- DMAEMA (ASTM)</b>	<b>Agarose</b>
Composition	5% Nafion solution	HEMA(5), AA(1),	HEMA (5) DMAEMA (1)	1% Agarose
Surface charge property	Negative charge	Negative charge	Positive charge	Neutral
Nanopore size	2~5 nm	2~5 nm	2~5 nm	100 nm [ref]
Solidification method	Solvent evaporation	Photo curing	Photo curing	Temperature based curing
ICP strength <sup>a</sup>	++	+	—	—
Device robustness <sup>b</sup>	++	++	++	—
Chemical compatability <sup>c</sup>	++	—	—	++
Ion transport tunability <sup>d</sup>	—	++	++	+
Fabrication availability <sup>e</sup>	+	—	—	++

**Table 4-1.** Properties of self-integrated nanoporous membranes. <sup>a</sup>This denotes success rates of membrane fabrication and degree of easiness of material and curing equipment handling. <sup>b</sup>This denotes robustness of the membranes in the presence of high pressures and high electric fields, which is associated with fluid leakage. <sup>c</sup>This denotes ICP capability in the KCl buffer characterized with anionic analytes. <sup>d</sup>This denotes ion transport tunability through the membranes that is related with pore size, porosity, and zeta-potential. <sup>e</sup>This denotes chemical stability of the membranes in buffer solutions. ++: very good, +: good, -: poor, —: very poor

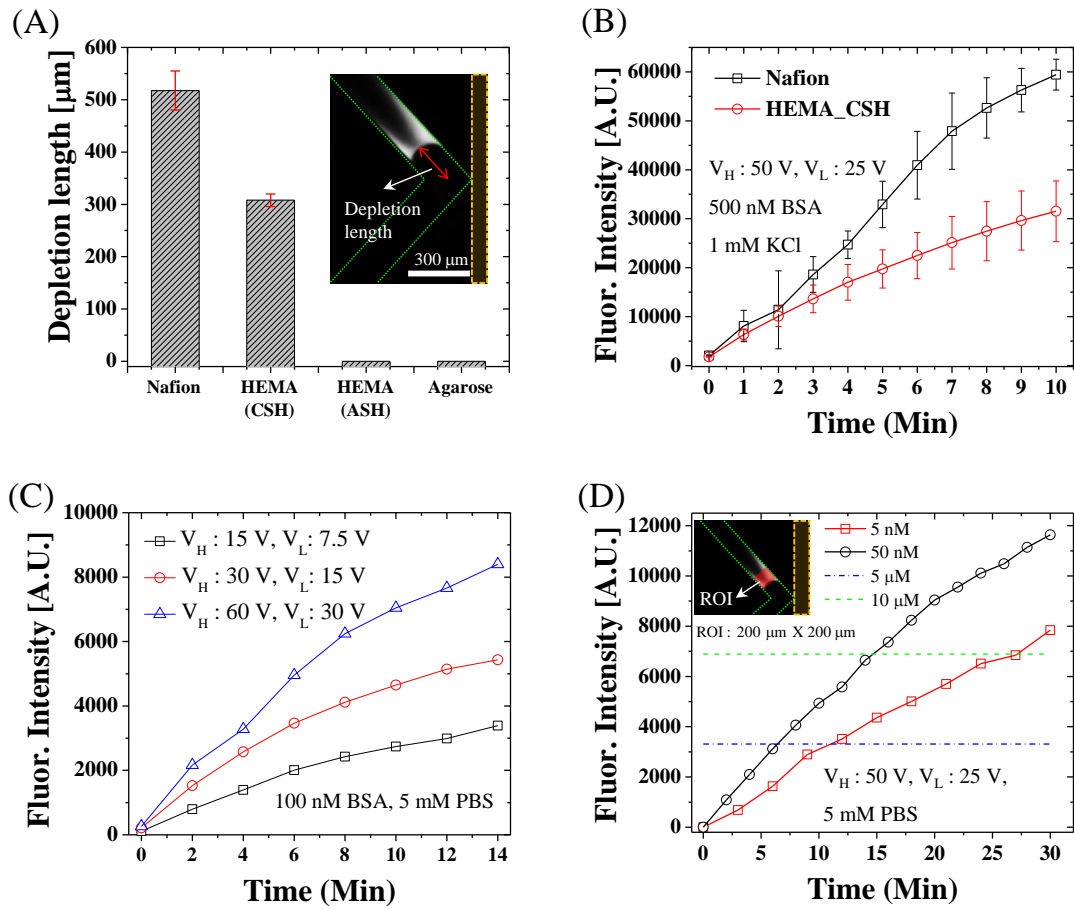


**Figure 4-4.** Comparison of electrokinetic properties. (A) Measurement of ion-depletion length that implies the permselective ion transport capability of the membranes. The Nafion membrane shows the best performance, followed by the HEMA-AA membrane, whereas the HEMA-DMAEA and agarose hydrogel membranes do not generate ICP. (B) Characterization of concentration enrichment factors under a continuous concentration condition. In a manner similar to the ion-depletion length, the Nafion membrane has the fastest concentration rate, showing a good consistency with (B). (C) and (D) show a pre-concentration of fluorescently labeled BSA of 100 nM under different electrical configurations and initial sample concentrations. The amount of biomolecules delivered by the EOF and the strength of ICP-induced pre-concentration increases with electrical potential.

**Ion Concentration Polarization by NPMs.** Typically, permselective membranes have a high potential for use in protein pre-concentration. The cation-permselective NPMs break local electric neutrality around the junction by selectively transporting cations in the buffer solution through the membranes. As shown in Fig. 4-3(A), the CSTMs allow counter ions of the surface charge (cations) to transport, but prevent co-ions (anions) from penetrating through the membrane pores. This unbalanced ionic transport is induced by Debye layer overlapping and anomalous rapid ion transport phenomena through the Nafion membrane in the presence of electric potentials<sup>3</sup>. Because this rapid transport causes local cation depletion at the anodic side (left) of the membrane and local cation accumulation at the cathodic side (right), owing to the electrical neutrality, anions are also depleted

and accumulated according to the cation concentration. This is known as ICP<sup>86</sup>. As the ICP (ion depletion) is induced in the anodic channel (left), a local electric field near the CSTMs has a steep gradient resulting from the local conductance change such that the analyte solution make an electrokinetic balance; the net analyte mobility becomes zero<sup>87</sup>. Therefore, negatively charged biomolecules are continuously delivered by bulk electroosmosis flow (EOF) from the sample reservoirs and are accumulated near the ion-depletion region.

As shown in Fig 4–3(B), we introduced a buffer solution with BSA into the anodic side (left) and filled the cathodic side (right) with only the buffer solution. The anodes were prepared to have a certain electrical potential to generate EOF along the direction of the applied electric field;  $V_H = 60$  V and  $V_L = 30$  V were applied to the high-potential and low-potential reservoirs, respectively, resulting in an electric field of 15 V/cm. On the other hand, both cathodes were connected to an electrical ground such that the permselective ion transport and current flow were allowed, but bulk flow was inhibited. A time-lapse image sequence shows electrokinetic pre-concentration of the anionic protein (BSA) using Nafion (CSTM). A 100 nM BSA solution in 5 mM PBS initially filled the sample channel, and pressure-driven flow (PDF) was minimized by balancing the hydraulic heads in both sample reservoirs. This is why fluorescent signals of the sample channel were not detected at the initial stage ( $t < 2$  min). However, the sample was continuously enriched and fluorescence intensities increased over time until they were clearly detected ( $t = 20$  min). The ion-depletion region was quantified to be 150- $\mu$ m long, 100- $\mu$ m wide, and 30- $\mu$ m deep, resulting in a depletion volume of  $4.5 \times 10^5 \mu\text{m}^3$  ( $150 \times 100 \times 30 \mu\text{m}$ ).

**Electrokinetic Properties of NPMs.** Self-integration methods for NPMs in the microfluidic channel can provide a standardized microfluidic platform that can be used for characterizing and comparing the electrokinetic properties of various membrane materials because it is possible to fabricate membranes with the same dimension. That is, the cross-sectional area of the membranes can be controlled by the geometry of the channel network, thus making it easy to fabricate NPMs with the same cross-sectional area. To expand on the electrokinetic properties of the NPMs, we measured ion-depletion areas that seemed to be directly proportional to cation transport flux through the membrane, which can be a good quantitative index for relative comparisons of the pre-concentration rates of the NPMs. As shown in Fig. 4–4(A), the Nafion membrane has the largest depletion area (see the inset), followed by HEMA-AA, whereas both the HEMA-DMAEMA and agarose hydrogel membranes could not generate ion depletion areas under the same buffer concentration and electric field strength. This is because only the Nafion and the HEMA-AA are cation-permselective. As shown in Fig. 4–4(B), the Nafion membrane allowed for twice the amount of pre-concentration of BSA than HEMA-AA, which is in good agreement with the quantification of ion-depletion areas in Fig. 4–4(A). On the other hand, the HEMA-DMAEMA is anion-permselective, and no ion-depletion area was observed in the anodic channel. The agarose hydrogel showed no significant ion permselectivity because the

surface charge density of the nanopores is weak and the pore size (~120 nm) is too large to allow for Debye layer overlapping ( $\lambda_d = \sim 10$  nm for 1 mM of KCl<sup>88</sup>). Therefore, neither permselectivity nor an ion-depletion area was observed in the agarose hydrogel membrane.

Because the Nafion membrane showed the best performance in the protein pre-concentration in Fig. 4-4(B), we further investigated the influence of electric field strength by calculating pre-concentration enhancement factors. As shown in Fig. 4-4(C), the strength of the bulk EOF generated in the anodic channel increases with the difference in the electric fields of the analyte reservoirs (top and bottom at the left side). The stronger the electric field between the anodes and the cathodes, the stronger is the permselective ion transport flux produced, implying that a larger ion-depletion area is formed. Three different combinations of electric potentials were tested; when  $V_H = 15$  V and  $V_L = 7.5$  V, the electric field between the two anodes was 3.25 V/cm. As the electric field strength was doubled, the fluorescence intensities doubled as well, because a twice-as-fast EOF delivers twice-as-more analytes. Although a high electric potential difference through the membrane resulted in the formation of a stronger ion-depletion area and a faster pre-concentration rate, the electric potential difference was limited to 15 V/cm to avoid several potential side effects such as sample damage, Joule heating, electrolyte dissociation, pressure build-up in the reservoir, and unstable nonlinear electrokinetic phenomena near the membrane<sup>89</sup>. As shown in Fig. 4-4(D), we concentrated 5 nM and 50 nM analytes in a 5 mM PBS buffer with an electric field of 12.5 V/cm for 30 min. The dashed lines indicate the calibrated fluorescence intensities of 5 and 10  $\mu$ M for the same analyte as reference concentrations. For instance, it was demonstrated that the 5 nM analyte was concentrated up to 5  $\mu$ M within 10 min, showing around  $10^3$ -fold pre-concentration. The effect of PDF on pre-concentration at the anodic side could to be tested because the membrane was tightly fabricated without any fluid leakage.

In addition to the ICP strength, the ability to tune ion transport through the membranes could be another important characteristic because the ion-transport flux is associated with the pre-concentration rate. For the poly-HEMA and agarose hydrogel, it was simple to tune the electrokinetic properties by mixing them with chemical agents at certain ratios<sup>14</sup>. Different mixing ratios of the poly-HEMA with other chemical agents may require different setups and UV exposure times. However, for the Nafion membrane, it was not easy to tune the ion-transport flux or permselectivity, and the transport mobilities of protons or other cations through the Nafion membrane under an electric field seem to remain undetermined<sup>3</sup>. Furthermore, the chemical compatibility of NPMs is worthy of discussion, and is summarized in Table 4-1. As is evident, the Nafion membrane was more stable than the other membranes because it worked in both PBS and KCl buffers. However, the poly-HEMA mixtures showed unstable behaviour in the PBS solution because they reacted with the PBS and, as a result, unwanted polymer by-products were formed. Therefore, it was impossible to use poly-HEMA as tightly sealed membranes in PBS, whereas they worked fine with a KCl buffer solution. In addition,

the HEMA-DMAEMA has a membrane degradation problem, whereby negatively charged protein samples clogged the nanopores in the membrane surface, causing a biochemical compatibility issue. On the other hand, the agarose hydrogel showed the most stable and compatible behaviour in both the buffer solutions; however, this membrane could melt at electric fields higher than 200 V/cm owing to Joule heating and be weakened by a high pressure build-up. Notably, these fabrication methods provide a microfluidic platform to directly compare the electrokinetic properties and biocompatibility of the NPMs in a controllable manner and under the same experimental conditions.

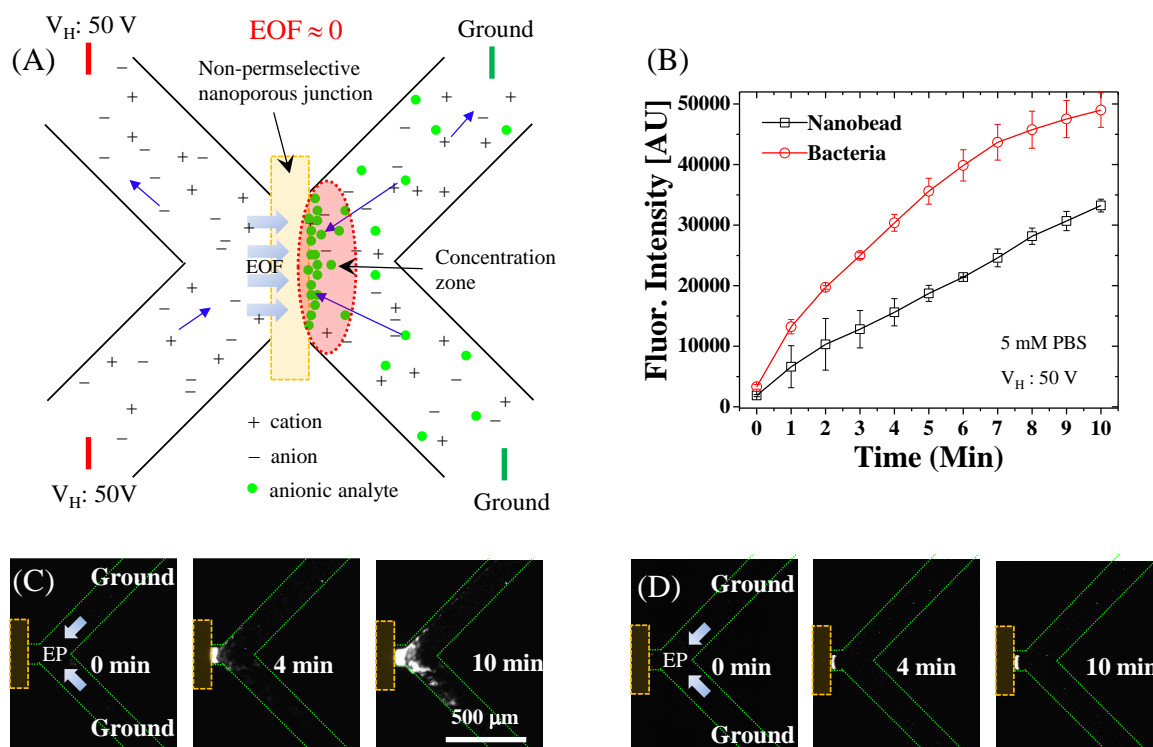


**Figure 4-5.** Electrophoretic concentrations of nanobeads and bacterial cells using a non-permeable agarose hydrogel membrane. (A) Schematic illustration of working principle for bio-sample concentration. Electrophoresis at the cathodic side of the agarose hydrogel membrane acts as a physical barrier for concentrating the bio-samples. (B) Quantification of the fluorescent intensities of nanobeads and bacterial cells. (C) Time-lapse image sequence of nanobead concentration (0.01 wt.% of solid). (D) GFP-expressing bacterial cells ( $10^7$  cells/mL) over time.

**Electrokinetic Properties of NPMs.** The ICP phenomena were used to concentrate biomolecules at the anodic side, but they were not allowed at the cathodic side, largely because of EOF (negative  $\zeta$  of glass and PDMS surfaces). Based on the characterized electrokinetic properties of the NPMs, we can see that HEMA-DAMEMA and the agarose hydrogel are inappropriate for generating ICP in the anodic channel. Although the HEMA-DAMEMA membrane possesses a clogging and degradation problem with negatively charged analytes, the agarose hydrogel membrane seems very useful for concentrating bio-samples at the cathodic side because electrophoresis-based pre-concentration of negatively charged bio-samples is possible, as illustrated in Fig 4-5(A). That is, because both EOF

and PDF are not allowed to penetrate through the agarose hydrogel membrane, net mobility ( $\bar{\mu}_{net}$ ) can be determined as follows

$$\bar{\mu}_{net} = \bar{\mu}_{EP} + \bar{\mu}_{EOF} + \bar{\mu}_{PDF} \quad \text{Eq. 4-1}$$

where  $\bar{\mu}_{EP}$ ,  $\bar{\mu}_{EOF}$ , and  $\bar{\mu}_{PDF}$  are the mobilities of electrophoresis, EOF, and PDF, respectively. Because PDF mobility is caused by its counterpart, i.e., EOF, fluid continuity should be satisfied

$$\bar{\mu}_{EOF} + \bar{\mu}_{PDF} = 0 \quad \text{Eq. 4-2}$$

Therefore, in the presence of an electric field, net mobility is only governed by electrophoresis; therefore, the cathodic channel can be used for electrophoretic pre-concentration. Most biological samples are negatively charged in physiological buffer solutions; thus, these samples migrate from the cathode to the anode. Using this mechanism, we concentrated fluorescently labeled nanobeads (1  $\mu\text{m}$  in diameter, Fig. 4-5(C)) and bacterial cells constitutively expressing GFP (2~3  $\mu\text{m}$  in length, Fig. 4-5(D)) at the cathodic side using 5 mM PBS buffer and an electric field of 25 V/cm. The nanobeads and bacterial cells were continuously accumulated over time, and quantitative analysis yielded a consistent result, as shown in Fig. 4-5(B).

## Conclusions

In this work, we developed several useful methods for self-integrating various NPMs into a microfluidic device with dual-level channel depths. The methods guaranteed the fabrication of leakage-free, ion-transport-tunable membranes using four nanoporous precursor materials, i.e., Nafion, HEMA-AA, HEMA-DMAEMA, and agarose hydrogel. All precursor materials were introduced into the shallow microchannel in liquid state and then solidified by using an optimized solidification process such as solvent evaporation, UV-assisted cross-linking, and temperature treatment, depending on the material. Each NPM was characterized and compared with each other in terms of their physicochemical properties such as fabrication availability, membrane robustness, ICP strength, ion transport tunability, and chemical compatibility. As an example of applications, we concentrated bio-samples such as protein, nanobeads, and microorganisms on either the cathodic or the anodic side of the membrane. Furthermore, we demonstrated that the membranes endured high pressure without any fluid leakage; therefore, it was possible to enhance biomolecule pre-concentration factors by combining EOF with PDF, because doing so helps deliver a larger amount of analytes to the junction. Because the methods allowed for the fabrication of various NPMs with the same dimensions and facilitated the characterization and comparison of ion transport capability, we believe that these

methods would extend the applications of NPMs to many microfluidic devices.

## Chapter 5. Continuous Concentration and Separation of Target Analytes by Using Aptamer Functionalized Microtubules and Hydrogel Sieving Structures

### *Introduction*

Most physiological samples contain diverse biomarkers that can be used as biological indicators in a wide range of clinical diagnostics. However, the large dynamic range of biological samples with highly variable concentrations has been a hurdle for detecting specific target biomolecules/biomarkers in a highly sensitive and highly selective manner<sup>90</sup>. To overcome limitations of detection, pre-concentration of target biomolecules followed by proper separation techniques such as capillary electrophoresis<sup>76</sup> and selective complementary binding<sup>91</sup> are crucial biochemical steps. For more than two decades, numerous techniques for amplifying initial bio-sample concentrations in microfluidics, such as affinity gradient focusing<sup>92</sup>, isoelectric focusing<sup>93</sup>, bipolar electrode focusing<sup>94</sup>, temperature gradient focusing<sup>92</sup>, electrophoresis based accumulation<sup>14</sup>, and ion concentration polarization-based biomolecule trapping<sup>7,65</sup> have been reported. However, the concentrated biomolecules are exposed to relatively harsh environments because these methods involve the use of spatially steep and temporally rapid environmental changes, such as changes in ion concentration (buffer strength)<sup>65, 77a</sup>, electric field<sup>95</sup>, non-linear vortex<sup>89a</sup>, and temperature<sup>96</sup>, which appear to be unfavorable towards some bio-samples. Importantly, most electrokinetic pre-concentration devices cannot selectively extract target analytes from a mixture of complex analytes for off-chip post-analysis<sup>14, 65, 76-77, 92, 94-95, 97</sup>.

To overcome the limitations of micro/nanofluidic sample pre-concentration devices, we developed a highly selective and sensitive method for detecting and concentrating target analytes by using aptamer-functionalized microtubules (AFMT) and a nanoporous hydrogel membrane (NHM) to selectively filter target analytes. Microtubules (MTs) are long, hollow cylinders (25 nm in diameter and a few tens of  $\mu\text{m}$  in length) composed of polymerized  $\alpha$ - and  $\beta$ -tubulin and nanoscale tubulins (approximately 8 nm) that provide numerous biomolecule binding sites (1600 sites per unit micrometer)<sup>98</sup>. A similar device utilizing MTs and a nanoscale sieving structure was used in our previous study<sup>98</sup>; however, in the present study, we significantly improved the sensitivity and selectivity of the method by replacing not only antibody-based binding sites with aptamer-based sites but also the glass nanoslit based sieving structure with an NHM, reducing the cost, time, and labor necessary for micro-/nano-fabrication.

Aptamers are high-affinity molecules derived from ribonucleic or deoxyribonucleic acids, which can be used for highly selective detection using affinity-based extraction of target analytes<sup>99</sup>. Compared to conventional affinity reagents such as antibodies or enzymes, aptamer-based biosensors possess distinct advantages. For example, these biosensors are chemically stable, cost-effective, and applicable for any given target, ranging from small molecules to large proteins as well as cells. Furthermore, aptamers offer remarkable flexibility and convenience in the design of their structures,

which has led to the development of novel biosensors with high sensitivity<sup>100</sup>. Thus, using aptamers rather than antibodies increases the capture efficiency and selectivity for target analytes. To concentrate or separate functionalized MTs, the NHM is integrated into a microfluidic channel network as a mechanical filter by using surface tension based patterning of precursor solutions<sup>101</sup>. Compared to the nanoslit-based sieve structure, constructing the NHM is both cost- and time-effective and the nanopores in the NHM can be manipulated by adjusting the chemical composition of the precursor solution.

To utilize the combination of MTs, aptamers, and NHM as a biosensor, we developed a protocol for functionalizing MTs with aptamers based on streptavidin and biotin binding, and optimizing the nanopore size of the NHM to selectively filter only target-analyte-bound-MTs (TABMTs). These TABMTs are continuously concentrated by the NHM, while non-target biomolecules are allowed to penetrate the NHM. Furthermore, we characterized factors that increase the concentration of target analytes and the limitation of detection. Separation and concentration were carried out simultaneously and continuously; these steps are typically performed sequentially when using other electrokinetic devices. Finally, we compared the sensitivity of our AFMT-based detection method with that of a conventional nanobead-based detection method that is commercially available.

### Theory

Charged biomolecules and ions in a microfluidic channel are driven in the presence of an electric field. The net mobility of these molecules is determined not only by the electrophoresis (EP) but also by viscous drag forces induced by bulk flow such as pressure-driven flow (PDF) and electroosmotic flow (EOF)<sup>101</sup>. Therefore, net mobility ( $\vec{\mu}_{net}$ ) can be calculated as follows:

$$\vec{\mu}_{net} = \vec{\mu}_{EP} + \vec{\mu}_{EOF} + \vec{\mu}_{PDF} \quad \text{Eq. 5-1}$$

where,  $\vec{\mu}_{EP}$ ,  $\vec{\mu}_{EOF}$ , and  $\vec{\mu}_{PDF}$  represent the motility of EP, EOF, and PDF, respectively. As illustrated in Fig. 5-1, our microfluidic device consisted of three parts: a cathodic microchannel filled with a mixture of complex analytes, an anodic microchannel filled with buffer media, and an NHM (~100 nm pore size)<sup>85</sup> that served as a junction of the two microchannels. Since the microchannel was constructed from glass and PDMS, surfaces that are known to have a negative surface charge density (approximately  $2000 \text{ e}^-/\mu\text{m}^2$ ), EOF was generated from the anode to the cathode. However, the NHM exhibits extremely high hydraulic resistance due to the presence of nanopores, which reduce the cross-sectional area such that no flow across the NHM is allowed. Therefore, Eq. 5-1 can be simplified to represent only electrophoretic mobility; bulk flow should be zero to satisfy the continuity of a fluid ( $\vec{\mu}_{EOF} + \vec{\mu}_{PDF} = 0$ ). Moreover, nonlinear electrokinetic phenomena which induce vortex flow near the anodic side of the NHM were not observed because the zeta-potential of the NHM (agarose hydrogel)

is much lower, generating permselective ion transport and an electric potential that is not focused across the NHM<sup>101</sup>; permselective ion transport is induced in a few tens of nanometers at conventional buffer concentrations<sup>88</sup>. We designed approximately 100 nm nanopores in the NHM to effectively suppress bulk flow and nonlinear electrokinetic flow by increasing hydraulic resistance but decreasing the zeta-potential.

### ***Methods and Materials***

**Reagents and materials.** BRB-80 (Cytoskeleton Inc., Denver, CO, USA) was primarily used for all electrokinetic experiments as a buffer (pH 6.8). Taxol (10  $\mu$ M, Cytoskeleton Inc.) was added to the buffer solution to stabilize polymerized MTs. As a target analyte, epidermal growth factor receptor (EGFR, R&D systems, Korea) was used and aptamers were designed from a nucleic acid library to capture the target analyte according to the manufacturer's protocol (5'-Cy3-EGFR aptamer-biotin-3', Aptamer Sciences Inc., Korea); 20 pM nucleic acids were dissolved in 1 $\times$  HEPES (pH 7.5, Sigma-Aldrich, Korea) at 95°C for 5 min and the mixture was incubated at room temperature (24°C) until the solution had cooled. The EGFR aptamer was purchased from Aptamer Sciences; its full sequence was AGTTCAGCCCCGG66A6ACGG6C6CA6GCC6G6GCG666AACC6AGACCA, in which 6 denotes 5-(N-naphthylcarboxamide)-2'-deoxyuridine. Streptavidin (STV, Sigma-Aldrich) was used to conjugate biotinylated MTs and aptamers. For polymerization of MTs, tubulins, tetramethylrhodamine isothiocyanate (TRITC)-labeled tubulins, and biotinylated tubulins (all from Cytoskeleton, Inc.) were used. Biotinylated nanobeads 200 nm in diameter (Invitrogen) were used for conventional nanobead-based detection of target analytes. To visualize the selective capture of target analytes and the separation of non-target analytes, fluorescein-isothiocyanate (FITC)-labeled bovine serum albumin (BSA, Sigma-Aldrich) was used.

**MT polymerization.** Tubulins were polymerized using the protocol recommended by the provider and previous studies<sup>102</sup>. For polymerization of biotinylated MTs, tubulins and biotinylated tubulins were mixed in an equal ratio and then suspended in 4  $\mu$ L polymerization buffer (2 $\times$  BRB-80 solution containing 10% dimethyl sulfoxide and 2 mM guanosine triphosphate) on ice, followed by incubation at 37°C for 20 min. After incubation, polymerized MTs were stabilized in 100  $\mu$ L of 1 $\times$  BRB-80 containing 10  $\mu$ M Taxol. To visualize polymerized MTs, TRITC-labeled tubulins were polymerized using the same protocol as was used for biotinylated MTs. The average length of MTs was measured to be approximately 15  $\mu$ m such that the working concentration of MTs was approximately 25 pM, which was estimated based on tubulin concentrations (Fig. 5–2(A)).

Polymerized MTs were sequentially functionalized with STV and aptamer to capture aptamer-conjugated target analytes at room temperature. First, STV (10  $\mu$ L) was added to the biotinylated MTs and the mixture was incubated for 10 min. This step allowed STV to bind with biotinylated MTs so that the surfaces of the MTs were functionalized with STV; this complex was referred to as an STV-

functionalized MT (SFMT) (Fig. 5–2(B)). Second, the SFMT was mixed with aptamers and then incubated for 20 min. This step enabled the SFMT surfaces to be further functionalized with for selective analyte capture, which was referred to as an aptamer-functionalized MT (AFMT) (Fig. 5–2(C)). Finally, aptamer-conjugated target analytes (EGFR) were mixed with Cy3-labeled aptamers to prepare EGFR-aptamer conjugates, which in turn were added to the SFMT and incubated for 20 min. This target analyte-bound SFMT was referred to as TABMT as illustrated in Fig. 5–2(D). Polymerization and functionalization steps were confirmed by fluorescence measurements. For example, polymerized MTs were visualized using TRITC-labeled tubulin. SFMT, AFMT, and TABMT were visualized using the TRITC-labeled STV, Cy3-labeled aptamer, and Cy3-labeled aptamer-EGFR conjugate, respectively (see the bottom images of Fig. 5–2). In this manner, a mixture of TABMTs and non-target analytes was prepared but the target analytes (EGFR) were not directly labeled; instead, aptamers were labeled with Cy3 for visualization. The same functionalization processes were used to visualize functionalized nanobeads.

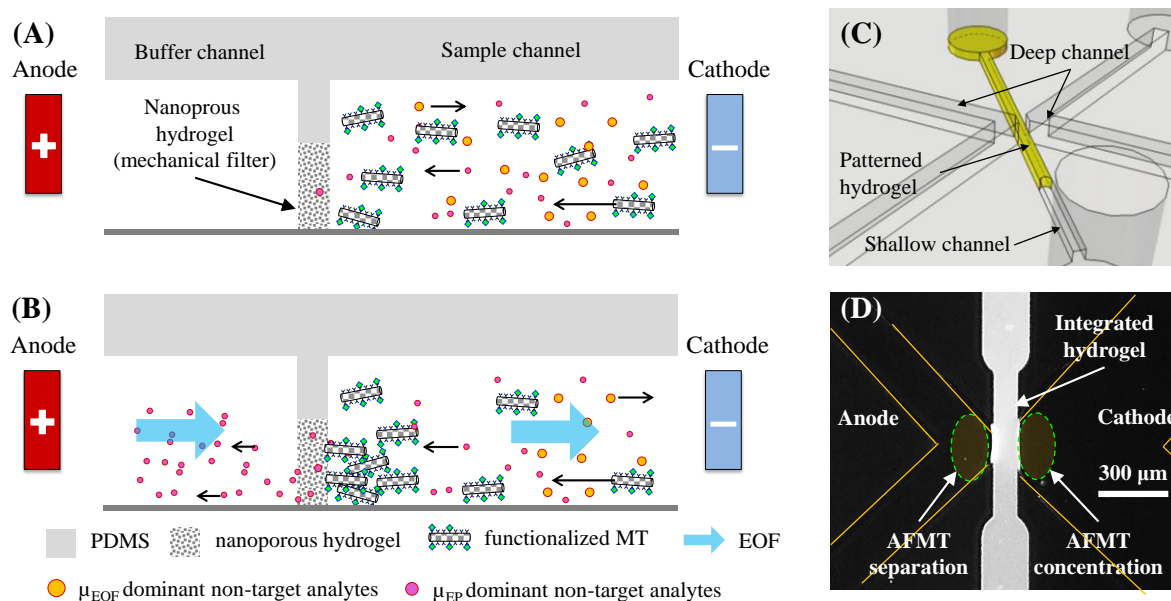


**Figure 5–1.** Working mechanism of the microfluidic device. (A) The device consists of three parts: a cathodic microchannel, an anodic microchannel, and a NHM (~100 nm) as a junction of the two microchannels. In the cathodic channel, an analyte mixture solution including specific target molecules, non-target molecules, and AFMTs is introduced, whereas only buffer solution is loaded into the anodic channel. (B) When an electric field is applied between the microchannels, the AFMTs with high electrophoretic mobility are drawn toward the anode and filtered by the NHM, while non-target analytes penetrate through the NHM regardless of their net mobility. (C) An agarose solution is patterned using a dual-level microfluidic channel network for fabricating the NHM. The surface tension facilitates the movement of the agarose solution along the shallow microchannel but prevents the solution from spreading over the deep microchannels. (D) The NHM fabricated between the two microchannels filters the AFMTs but allows the penetration of non-target biomolecules in the presence of an electric field.

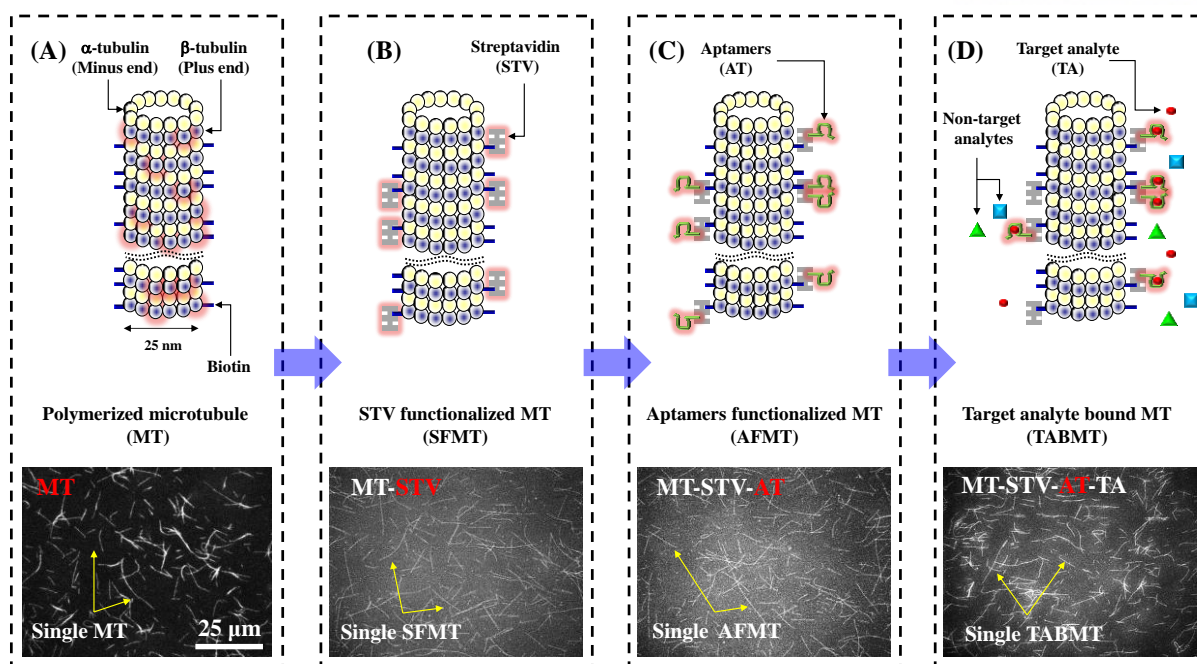


**Figure 5-2.** Polymerization and functionalization of MTs. (A) Unlabeled tubulins were polymerized as MTs, which had an average length of approximately 15  $\mu\text{m}$ . TRITC-labeled tubules were incorporated into plain tubulins to visualize individual polymerized MTs. (B) Biotinylated, unlabeled tubulins were polymerized and then functionalized with STVs to produce SFMTs. TRITC-labeled STVs were used to visualize SFMTs. (C) Biotinylated MTs were functionalized with unlabeled STVs, which were in turn conjugated with aptamers possessing biotin molecules at their 3' site to produce AFMTs from SFMTs. Cy3-labeled aptamers were used to visualize AFMTs. (D) Target analytes, EGFR, were conjugated by AFMTs that had been labeled with Cy3 for visualization. The abbreviations in the microimages such as MT, STV, and AT in red indicate that the molecules were fluorescently labeled.

**Design and fabrication of the microfluidic device.** The microfluidic device was designed to have microchannels with dual-level depths (30  $\mu\text{m}$  and 15  $\mu\text{m}$ ) for integration of an NHM using the capillary-based fluid patterning method<sup>101</sup>. The anodic channel was 100  $\mu\text{m}$  wide and the cathodic channel was 200  $\mu\text{m}$  wide to supply target analytes easily and to reduce hydraulic and electric resistance. The microfluidic device was fabricated using standard soft-lithography technology as described in our previous study. Briefly, SU-8 (2025, Microchem, Corp., Newton, MA, USA) was spin-coated, baked, and exposed to UV light using a first photo-mask (MA6, Suss MicroTec, Garching, Germany) to create a shallow microchannel. Next, the same process was repeated using the second photomask to create a deep microchannel. The double spin coating and double exposure processes were followed by a single developing process, resulting in a dual-level depth master. Subsequently, the master was silanized using trichloro(3,3,3-trifluoropropyl)silane (Sigma-Aldrich) and then PDMS replica devices were prepared. PDMS devices were directly bonded to a glass substrate by oxygen plasma treatment under 50 sccm of  $\text{O}_2$  and 50 W for 4 sec (Cute-MP, Femto Science, Gyeonggi, Korea). This treatment was essential for precursor solutions to flow easily along

the shallow channel; power and exposure time of the oxygen plasma were optimized because nanoporous hydrogel construction depends on the viscosity and volatility of the agarose hydrogel solutions. After self-integration of the agarose hydrogel, all microchannels and glass surfaces were coated with a Pluronic surfactant (F-127, 0.02%, Sigma-Aldrich) to minimize nonspecific binding between biomolecules and glass surfaces. The residue was rinsed with buffer solution.

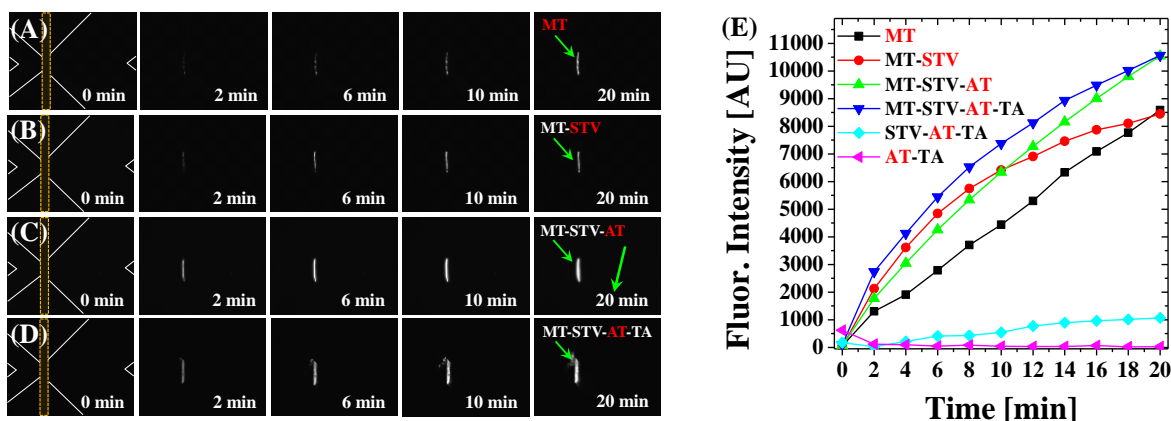


**Figure 5–3.** Time-lapse fluorescent images of functionalized MTs filtered by an NHM. (A) MT (TRITC-labeled). (B) SFMT in which STVs were TRITC-labeled. (C) AFMT in which aptamers were labeled with Cy3. (D) TABMT in which aptamers were Cy3-labeled. (E) Quantification of the fluorescent signals from differentially labeled and functionalized MTs in the presence of an electric field (25 V/cm). The signals continuously increased in the presence of MTs, whereas no signals were detected in the absence of MTs. MT, STV, and AT in red denote that the molecules were fluorescently labeled.

**Experimental setup and data analysis.** An inverted fluorescence microscope (Ti-U, Nikon, Tokyo, Japan) equipped with a CCD camera (ORCA R2, Hamamatsu Photonics, Hamamatsu, Japan) and 10× and 20× lenses was used to measure the fluorescence intensities of the samples. Two pairs of 0.25 mm diameter platinum wires (Huntingdon, U.K.) were used as electrodes to apply electric potentials to the microfluidic device. Electric potentials were generated and monitored using a source meter (Model No. 2635A, Keithley Instruments, Solon, OH, USA). For data analysis and image processing, Image J (NIH, Bethesda, MD, USA), and OriginPro 8 (OriginLab, Northampton, MA, USA) were used when necessary.

## Results

**Concentration of MTs and target analytes.** We tested the concentration of functionalized MTs using an NHM as shown in Fig. 5–3. We loaded TRITC-labeled MTs into the cathodic channel, while buffer solution was loaded into the anodic channel. Since the initial concentration of the MTs was too low for detection, no fluorescent signals were detected near the NHM ( $t = 0$  min). However, when an electric field of 25 V/cm was applied between the two microchannels across the NHM, fluorescent

signals from the MTs were detected at the cathodic side and these signals increased over time. Because the EP of MTs is much more dominant than electroosmosis<sup>98, 103</sup>, the MTs were transported from the cathode to the anode and then filtered by the nanopores in the NHM. In the same manner, we also tested TRITC-labeled SFMT and Cy3-labeled AFMT. As shown in Fig. 5–3(B) and (C), functionalized MTs were successfully concentrated, confirming that no significant change in electrophoretic mobility occurred due to functionalization with STV and aptamer. Thus, TRITC-labeled MTs, TRITC-labeled SFMT, and Cy3-labeled AFMT were successfully filtered by the NHM. Finally, Cy3-labeled AFMT-EGFR was filtered and concentrated by the NHM (Fig. 5–3(D)). As a control, we synthesized Cy3-labeled-aptamer conjugated EGFR and STV-Cy3-labeled-aptamer conjugated EGFR complexes, respectively, and repeated the same experiment. The complexes appeared to penetrate the NHM so that no fluorescent signal was detected near the NHM. Based on this result, we concluded that both MTs and the NHM have a key role in concentrating target analytes.

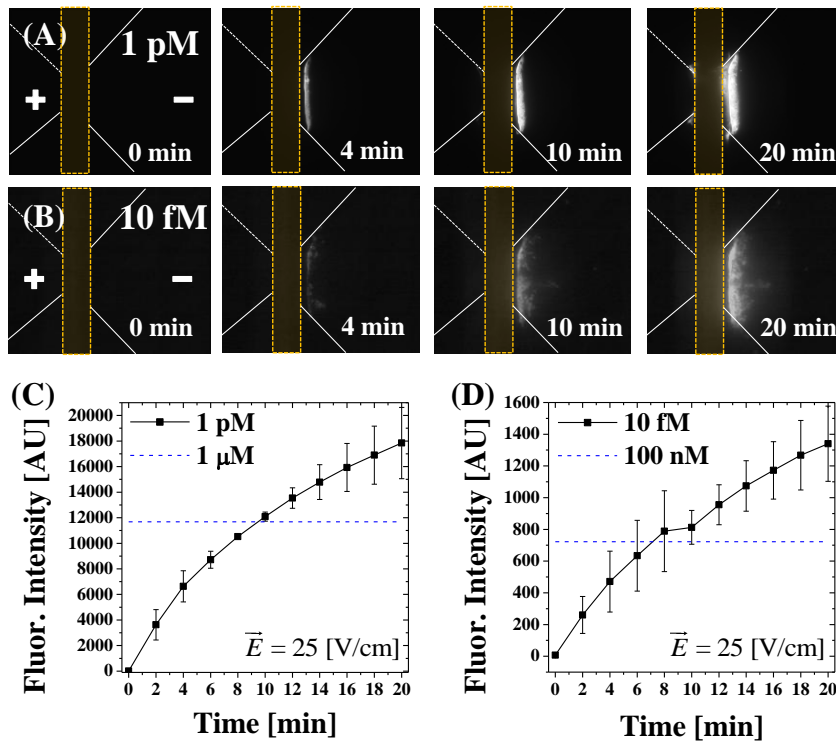


**Figure 5–4.** Characterization of concentration enhancement factors and detection limit. Cy3-labeled aptamers of (A) 1 pM and (B) 10 fM were continuously concentrated using the SFMT. Quantitative results of the fluorescent intensities: (C) 1 pM and (D) 10 fM. The aptamers were concentrated to over 1  $\mu$ M from 1 pM and 100 nM from 10 fM, respectively, achieving  $10^6$  to  $10^7$ -fold pre-concentrations within 10 min using the functionalized MTs.

**Characterization of concentration enhancement factors.** Using the method described in our previous study, we quantified the fluorescent intensities of concentrated biomolecules to determine the concentration enhancement factors. We aimed to capture and concentrate Cy3-labeled-aptamer conjugated EGFR as target analytes so that the complexes were diluted to a working concentration

before mixing with SFMTs. We calibrated fluorescent intensities using reference concentrations of the Cy3-labeled-aptamer conjugated EGFR such as 1  $\mu\text{M}$  and 100 nM. From the known reference concentrations and their intensities, we characterized the concentration of enhancement factors. As shown in time-lapse images in Fig. 5–4, we loaded 1 pM and 10 fM Cy3-labeled-aptamer conjugated EGFR samples into the cathodic channel and the buffer solution into the anodic channel, respectively. An electric field of 25 V/cm was applied to the microchannels. The device concentrated the target analytes from 1 pM to 1  $\mu\text{M}$  and from 10 fM to 100 nM within approximately 10 min and 7 min, respectively. Thus, it is possible to achieve a concentration of approximately  $10^6$ – $10^7$  of enhancement factors within 10 min and the detection limit was as low as 10 fM. The range of the concentration of enhancement factors obtained in this study were better or comparable to those obtained using other microfluidic devices<sup>77a</sup>.

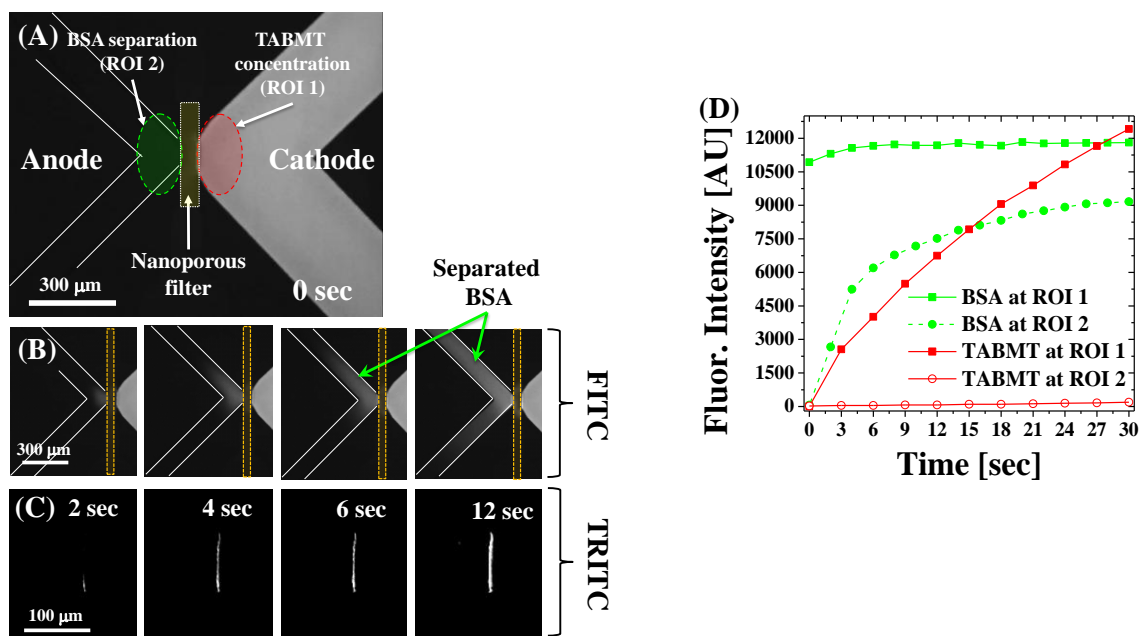


**Figure 5–5.** Selective concentration of target analyte conjugates (Cy3-labeled-aptamer conjugated EGFR) and separation of non-target analytes (FITC-labeled BSA) (A) A solution containing a mixture of target analyte conjugates (Cy3-labeled-aptamer conjugated EGFR) and non-target analytes (FITC-labeled BSA). The target analyte conjugates did not show fluorescence when a TRITC filter cube was used because their initial concentration was below the detection limit. In contrast, non-target analytes showed fluorescence because their initial concentration was sufficiently high to be detected using a FITC filter cube. (B) For the FITC filter cube, fluorescent intensities at ROI 2 increased until they reached the same value as those at ROI 1, indicating that non-target analytes continuously penetrated the NHM in the presence of an electric field of 25 V/cm. (C) For the TRITC filter cube, fluorescence intensities were only detected at ROI 1, indicating that target analyte conjugates were continuously filtered and concentrated. (D) Quantification of fluorescence intensities over time, confirming the continuous concentration of target analyte conjugates and simultaneous separation of non-target analytes.

**Separation of target analytes from non-target analytes.** To achieve the simultaneous separation

of target analytes from non-target analytes, a mixture solution was prepared that contained 25 pM SFTMs, 1 nM Cy3-labeled-aptamer conjugated EGFR as target analytes, and 100 nM FITC-labeled BSA as non-target analytes. After the mixture was loaded into the device and before an electric field was applied, the non-target analytes in the cathodic channel appeared to be bright, while the anodic channel appeared dark as shown in Fig. 5–5(A). This is because non-target analytes remained in the cathodic channel. However, as shown in Fig. 5–5(B), an electric field of 25 V/cm was applied, and the penetration of non-target analytes (BSA) was observed and quantified by measuring the fluorescence intensity at region of interest (ROI) 2. The fluorescent intensities at ROI 2 were very close to those at the ROI 1 in several seconds, meaning that the non-target analytes are neither filtered nor concentrated by the NHM. However, target analytes were not observed in the cathodic channel for the TRITC-filter cube before and immediately after the electric field was applied because the initial concentration was below the detection limit. However, the fluorescence intensities of target analytes at ROI 1 gradually increased over time, indicating that TABMT (Cy3-labeled-aptamer conjugated EGFR captured by the SFMTs) were continuously filtered and concentrated by the NHM. As a control, when the mixture solution contained no functionalized MTs (SFMTs), no fluorescent signal was detected; both target and non-target analytes were observed to pass through the NPH. Therefore, functionalized MTs can selectively capture target analytes while simultaneously removing non-target analytes from the concentration region (ROI 1).

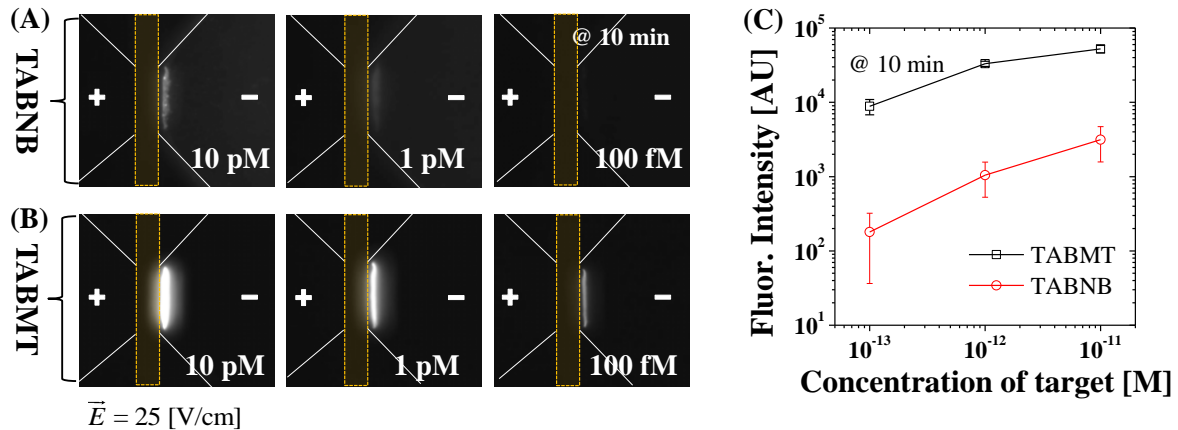


**Figure 5–6.** Comparison of the sensitivity of a nanobead-based detection method (TABNB) and of an MT-based detection (TABMT). Detection of 10 pM, 1 pM, and 100 fM of Cy3-labeled-aptamer conjugated EGFR using (A) the functionalized nanobeads and (B) MTs for 10 min. (C) Quantification of fluorescence intensities. The MT-based detection method showed sensitivity that was 1–2 orders of magnitude higher than that of conventional nanobead-based detection.

**Comparison of MT-based detection and conventional nanobead-based detection.** To demonstrate the superior sensitivity of the MT-based detection method over a conventional nanobead-based detection method, we compared the detection limits of both methods. Biotinylated nanobeads that were 200 nm in diameter were functionalized with the same aptamers using the same STV-biotin

conjugates as used for AFMT. To quantify the detection limit, SFMTs and STV-functionalized nanobeads (SFNB) were individually mixed with various concentrations of target analytes conjugates (Cy3-labeled aptamer-conjugated EGFR), including 10 pM, 1 pM, and 100 fM. SFMT and the SFNB were incubated in buffer solution for 20 min to allow STV to bind with target analyte conjugates. We then introduced the incubated mixture solutions into the cathodic microchannel and applied the same electric field (25 V/cm) for all comparison experiments. As shown in Fig. 5–6, TABMTs showed higher fluorescent intensities than target-analyte-bound-nanobeads (TABNB) for all concentrations of the target analytes. For example, the TABMTs showed 16.6-fold higher fluorescent intensities compared to that of TABNBs at 10 pM and 31.6- and 49.4-fold higher for 1 pM and 100 fM, respectively. Furthermore, for the 100 fM target concentration, the TABNB signal (179 AU in average) was close to the background noise level such that it was difficult to detect/identify the target analyte. Another interesting feature of the comparison was that the TABMTs showed low run-to-run variation; the average operating variation was 14.3% for TABMTs, while this value was 60.2% for TABNBs. Moreover, the magnitude of the variation for TABNBs was significantly higher to 80.3% at a low concentration of target conjugates (100 fM), while TABMTs showed reasonably low variation. This can be attributed to the difference in the number of binding sites, which appears to be related to the surface-to-volume ratio between MTs and nanobeads. The abundant binding sites appeared to allow SFMTs to capture a larger number of target analyte conjugates, rapidly increasing the fluorescent signal.

## Discussion

Biomolecules such as DNA and proteins that have lengths in the nanometer range freely penetrated through the NHM<sup>104</sup>, whereas MTs, SFMTs, AFMTs, and TABMTs were physically filtered and then continuously accumulated over time due to the micrometer-scale length of the MTs. Furthermore, non-target analytes were automatically separated regardless of their net mobility. Both EP-dominant analytes that are driven toward the anode ( $|\mu_{EP}| > |\mu_{EOF}|$ ) and EOF-dominant analytes ( $|\mu_{EP}| < |\mu_{EOF}|$ ) that are driven toward the cathode can penetrate through the NHM without binding to the AFMTs. Therefore, only target analytes conjugated to AFMT were concentrated on the cathodic side of the NHM. Although the dominance between EP and EO may depend on the electrokinetic properties of the microchannel and analytes, the method described in this study could be used to simultaneously separate and concentrate only target analytes by taking advantage of the strong biochemical affinity between aptamers and target analytes. Notably, the use of most microfluidic pre-concentration devices must involve an additional separation step on a chip to identify target analytes, which appears to be time- and labor-inefficient.

The NHM shows much lower electric resistance than glass nanoslits due to the increased effective cross-sectional area, making it much easier to eliminate side effects induced by the high strength of

electric fields such as Joule heating, hydrolysis, and sample damage<sup>105</sup>. To facilitate the transport of biomolecules, a 50  $\mu\text{m}$  NHM was fabricated, with no fluid leakage or damage observed during the experiment. Interestingly, TABMTs trapped by the NHM were easily removed when an opposite electric field was applied. This feature will be useful for selectively extracting concentrated target analytes from the microfluidic device for additional post-analysis.

### ***Conclusions***

We developed an NHM integrated microfluidic device and syndissertation protocols for functionalizing MTs with aptamers to detect aptamer-conjugated target analytes in continuous concentration and simultaneous separation manners. We demonstrated that aptamer-conjugated target analytes (EGFR) were selectively and highly concentrated, with concentration enhancement factors ranging from 6 to 7 orders of magnitudes from initial concentrations of 1 pM and 10 fM within 10 min. This was possible because the NHM continuously filtered and concentrated only target analytes that were repeatedly captured by the functionalized MTs. Additionally, non-target analytes were easily removed from the concentrated target analytes because they were not filtered by the NHM, enabling simultaneous separation of target analytes from non-target analytes without contamination. These steps are typically performed sequentially when using other electrokinetic devices. In addition, we compared the sensitivity of the device with that of other nanobead-based detection methods and found that the sensitivity and detection limit of our method was 1–2 orders of magnitude higher in the fluorescent signal amplification than other methods. Furthermore, aptamer-MT based detection showed several-fold lower run-to-run variation in the fluorescent signals. Thus, aptamer-functionalized MTs with the NHM integrated microfluidic device is a powerful and useful means to facilitate ultra-selective and ultra-sensitive analyte detection, capture, and concentration, which are required in biochemical analysis systems.

## Chapter 6. Ion Concentration Polarization in A Single and Open Microchannel Induced by A Surface-patterned Perm-selective Film

### *Introduction*

Ionic and molecular transport phenomena in nanoscale channels and nanopore clusters have been an intriguing research area for biomolecule concentration<sup>98, 106</sup>, filtration<sup>107</sup>, and separation applications<sup>24</sup>, and for even more intricate applications such as nanofluidic diodes<sup>108</sup>, transistors<sup>109</sup>, and energy convertors<sup>110</sup>. In particular, ion concentration polarization (ICP)<sup>7, 86</sup> or the exclusion enrichment effect<sup>111</sup> induced by the biased transport between co-ions and counter-ions caused by charged channel surfaces (zeta-potentials) has been widely utilized in biomolecule pre-concentration<sup>88</sup>, which is subsequently followed by a proper separation technique such as capillary electrophoresis<sup>76, 112</sup>. Such a pre-concentration method increases the concentration of biomolecule analytes by more than million-fold and enables the ultra-sensitive detection of biomolecules<sup>75a, 112</sup>. In principle, most ICP devices have similar micro- and nanofluidic channel networks in which the nanofluidic channels physically connect two microfluidic channels and play a common role in selectively transporting either the cations or anions. Various nanojunctions, such as a glass nanosheet<sup>75a, 86</sup>, porous hydrogel<sup>113</sup>, nanoscale polymer gap<sup>76</sup>, and Nafion strip,<sup>77a</sup> have been employed recently, and these devices are referred to as dual-channel ICP (DC-ICP) devices in this work. Most DC-ICP devices rely on complicated nanofabrication processes that connect the two microchannels with a nanofluidic channel or nanoporous material. These devices also require both microfluidic and nanofluidic channel networks in which an ionic sink channel is considered as an essential element for connection with an electric ground. Therefore, at least four electrodes are required, which is somewhat unfavorable for integration with other microfluidic elements<sup>114</sup>.

To address the issues in DC-ICP devices, we present not only a novel and simple ICP generation mechanism but also a single-channel based ICP (SC-ICP) device that consists of single, open microchannels and only two electrodes. As an example of perm-selective, nanoporous materials, Nafion was employed in the SC-ICP device because recently it was reported that nanofluidic channels that have critical pore sizes of a few nanometers and the high zeta-potential of walls can transport ions in an uncharacteristically rapid manner by means of electromigration<sup>3</sup> while the diffusivity can be reduced by a confined-diffusion region<sup>115</sup>. In addition, Nafion has high-selective and high transport capability for cations owing to its cluster network of pores with a few nanometer diameter and the high charge density of the sulfate group ( $-0.5 \text{ C/m}^2$ )<sup>83, 116</sup>. Although these characteristics of Nafion have led to its use as an uncharacteristic cation selective transporter in many DC-ICP devices<sup>75a, 77a, 79, 86, 117</sup>, in this paper, we innovatively simplify the micro- and nanofluidic channel network and the fabrication processes. For this reason, two distinct differences are noted; first, since the superior perm-selectivity and rapid ion transport capability of Nafion give rise to an ICP phenomenon in single

microchannels, only a pair of electrodes is required for experimental setup. Second, the SC-ICP device produces an ICP phenomenon in an open microchannel so that it holds several advantages over the DC-ICP devices in that it delivers ions/molecules in a high throughput manner and allows massive parallel processes on a chip because not only a nano-junction but also a common electrical ground are unnecessary. Moreover, the SC-ICP device is free from leakage, Joule heating, and membrane permselectivity breakdown caused by high electrical potentials to which the application of DC-ICP devices seems to be limited.

The mechanism of the SC-ICP phenomenon is illustrated in Fig. 6–1. Since cations are rapidly absorbed, transported, and then discharged through the Nafion film, an ion depletion zone (IDZ) seems to be formed, resulting in the SC-ICP phenomenon. This is because the surface-patterned Nafion film has a selectively transport cations from the anodic side to the cathodic side through the nanopore clusters<sup>116</sup>. Here, the flux of cations transported by the Nafion film is hypothesized to be much higher than that by the electroosmotic (EO) bulk flow and electrophoresis (EP) as demonstrated in 2 nm of nanochannels<sup>3</sup> and in the similar fashion as fast electron transport in bipolar electrodes<sup>94, 118</sup>. On the other hand, anions are unlikely to be transported by the Nafion film but transported by EP and also affected by the EO bulk flow. However, they should be depleted from the Nafion film in the same manner as the cations (microscopically) because of electroneutrality<sup>119</sup> although electroneutrality can be locally and nanoscopically broken near the Nafion film and the glass/PDMS channel surfaces. As a result, this mechanism generates an IDZ near and above the Nafion film, resulting in the creation of SC-ICP. In this work, we not only investigate the SC-ICP generation mechanism by using differently charged fluorescence dyes and monitoring currents along the channel but also characterize it by manipulating Nafion film compositions, electric field strengths, buffer conditions and so on. Lastly, we demonstrate that the SC-ICP device is applied to massive, parallel pre-concentration of biomolecules and simultaneous bacterial cell concentration and lysis on a chip.

### ***Methods and Materials***

**Chemical reagents.** A 100 mM phosphate buffered saline (PBS; pH 7.4) solution was diluted with desalted water for working concentrations of 100  $\mu$ M, 1 mM, 5 mM, and 10 mM. As a based buffer we used 5 mM PBS for all experiments otherwise noted. Fluorescein isothiocyanate (FITC)-labeled bovine serum albumin (BSA) was diluted with the buffer solution for pre-concentration experiments. 5 wt.% and 20 wt.% solutions of Nafion ion-exchange resin in lower aliphatic alcohols containing 34% of water were used as delivered. In addition, fluorescently labeled polyethylene microparticles of 1  $\mu$ m in diameter (solid 2 wt.%, Invitrogen) were suspended and then diluted up to 100 times with 1 mM of the PBS buffer for bead concentration and vortex visualization. All chemical reagents such as FITC, Rhodamine 6G, and Rhodamine 110 dye were purchased from Sigma-Aldrich and used as delivered, unless noted otherwise.

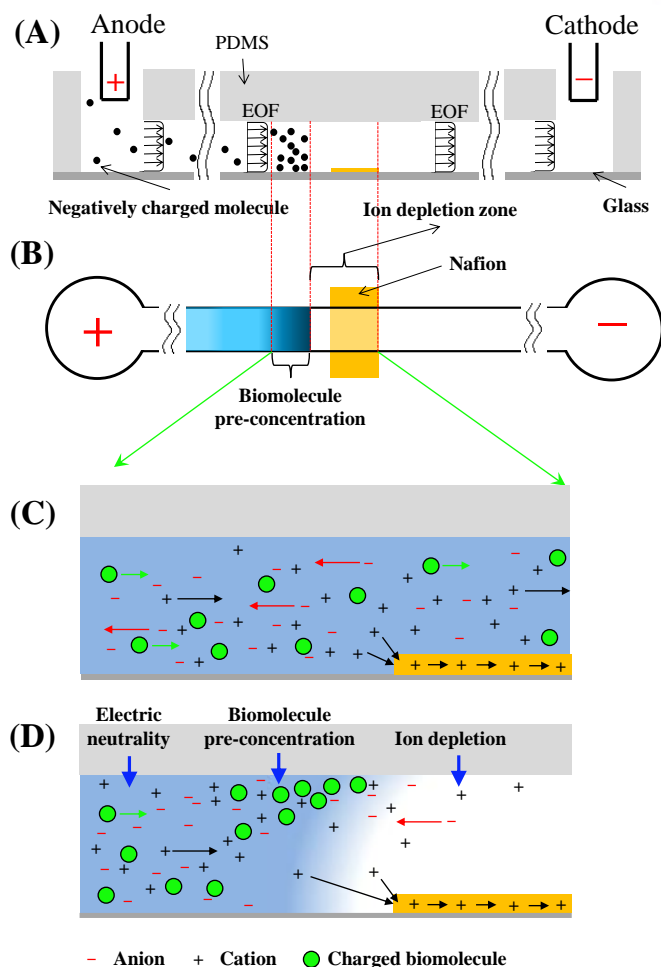


**Figure 6-1.** (A) Side view of an open, SC-ICP device in which a Nafion film is patterned at the center of the microchannel surface. (B) The surface-patterned Nafion film acts as an ultra-rapid and ultra-selective ion transporter in the presence of an electric-field, so an ion depletion zone (IDZ) develops near and above the Nafion film (top view). (C)–(D) Illustration of the ICP phenomenon by the Nafion film that rapidly and selectively absorbs, transports, and discharges cations from the anodic side to the cathodic side, resulting in the local formation of the IDZ.

**Cell culture.** For bacterial pre-concentration and bacterial cell lysis experiments, *E. coli* MG-1655, which constitutively expresses green fluorescent protein genes (GFP), was grown overnight on LB agar solid medium plates with 100  $\mu\text{g/ml}$  of ampicillin at 32  $^{\circ}\text{C}$ . A single colony was used for inoculating 5 mL of tryptone broth (TB, 3% tryptone and 0.5% NaCl) media. Then, the *E. coli* cells were grown in a rotary shaking incubator (32  $^{\circ}\text{C}$ , 200 rpm) to a mid-log phase and required about 12 h for the optical density at a wavelength of 600 nm ( $\text{OD}_{600}$ ) to reach 2.0; the grown bacteria were then centrifuged at 5000 rpm for 5 min, based on our previous procedures<sup>56, 80</sup>.

**Patterning of perm-selective materials.** We patterned a Nafion film on a glass substrate by using the microchannel flow-based patterning method. The solvent in the Nafion solution was removed by using a hotplate (95 $^{\circ}\text{C}$  for 10 min) for evaporation, and then, it was cured and brought into the solid

state. The thickness of the patterned and cured Nafion film was measured using a surface profiler (Alpha-Step) and ranged from 2  $\mu\text{m}$  to 14  $\mu\text{m}$ . The film has two evident peaks in both the side edges because of the side-wall effect during the patterning and curing process. The vertical peaks perpendicular to the flow direction were beneficial to the SC-ICP because they contributed towards a higher ion transport flux that was caused by the large effective surface area. Note that this method can be applied to patterning other perm-selective materials dissolved in precursor solutions.

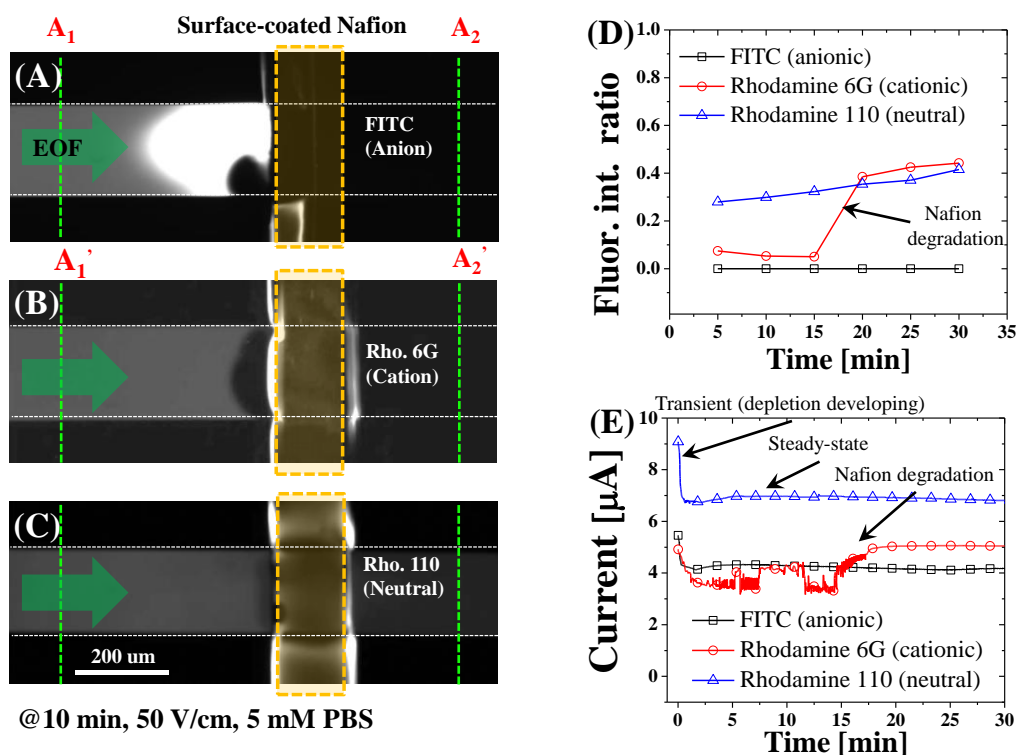


**Figure 6–2.** (A) Negatively charged dye molecules, FITC, in 5 mM PBS buffer cannot penetrate the IDZ that is produced by the Nafion film in the presence of an electric field (50 V/cm). (B) Positively charged dye molecules, Rhodamine 6G in the same buffer, is initially blocked by the IDZ but the ratio suddenly increases up to the same level of the neutral dye owing to the Nafion degradation by the surface clogging of cationic dye. (C) More than 30% of the neutral dye molecules, Rhodamine 110, pass over the Nafion film including the IDZ. (D) The quantified flux ratio of fluorescent intensities obtained from the cathodic side (A2–A2') to those from the anodic size (A1–A1') shows a good agreement with the qualitative results. (E) Current monitoring reveals that the SC-ICP develops within 1 min and that steady states are maintained for anionic and neutral dyes, while the fluctuation of the increase in the current for cationic dyes seem to be caused by electrostatic binding/clogging of the dye molecules to/at the nanopores of the Nafion film.

**Device design and fabrication.** We designed a single microfluidic microchannel with a width of 200  $\mu\text{m}$  and height of 20  $\mu\text{m}$ , 50  $\mu\text{m}$ , and 100  $\mu\text{m}$ . The microfluidic device was fabricated by using the standard soft-lithography technology as employed in other work<sup>56, 80</sup>. Briefly, an SU-8 master (Microchem 2025, Newton, MA, USA) was fabricated using standard photolithography processes. The surface was silanized using trichloro(3,3,3-trifluoropropyl)silane (Sigma-Aldrich) in a vacuum jar

for 1 h. Polydimethylsiloxane (PDMS) was then cast, cured, and peeled off. After punch holes were made, the microfluidic devices were prepared. The PDMS devices were directly bonded to a glass substrate containing a Nafion film with oxygen plasma treatment under 50 *sccm* of O<sub>2</sub> and 50 W for 30 s (Cute-MP, Femto Science, Korea). The PDMS microchannel was fluid leakage-tight. It is noted that the fabrication process of the device is much simpler and more cost and time effective than other DC-ICP devices. 50  $\mu\text{m}$  deep microchannels were used for confocal experiments while 20  $\mu\text{m}$  deep microchannels were mainly used for all other experiments otherwise noted; the experimental results quantified in Table 6–1 used 20  $\mu\text{m}$ , 50  $\mu\text{m}$ , and 100  $\mu\text{m}$  deep microchannels, respectively.

**Experimental setup and data analysis.** All microchannels were coated with a Pluronic surfactant (F-127, 0.01%, Sigma-Aldrich) to minimize any nonspecific binding between the biomolecule and the glass surface by pouring 200  $\mu\text{l}$  of the Pluronic surfactant over 2 h. After surface treatment, the residue was subsequently rinsed with a working concentration of the PBS buffer over 2 h. The fluorescence dye and protein concentration were monitored by inverted fluorescence microscopy (Ti-U, Nikon, Japan) and a CCD camera (ORCA R2, Hamamatsu, Japan) using 10x and 20x lenses and two filter cubes for detecting GFP (B-2E/C, Nikon) and red fluorescent protein (RFP, Y-2E/C, Nikon) fluorescent signals, respectively. Vortex flows were measured by using a high speed fluorescence camera (Neo sCMOS Camera, ANDOR Technology, UK) and fluorescent microparticles. Multi-focal depth *z*-stack images were obtained by confocal microscopy (LSM 700, Carl Zeiss, German). Except confocal images, all other images were obtained by using the inverted fluorescence microscope by focusing the center of the microchannel (the focal depth was about 8.5  $\mu\text{m}$  for 10 $\times$  objective lens). Electric potentials were applied between two ends of the microfluidic channel, which produce electroosmotic flow (EOF) by dipping two platinum wires with a 0.25 mm diameter (Huntingdon, U.K.) in each reservoir. A source meter (Model No. 2635A, Keithley, Ohio, USA) was used to not only supply an electric potential but also monitor the current flow simultaneously. The source meter was connected with a PC controlled by using the LabVIEW (National Instruments, USA). For data analysis and post processing, MATLAB (Mathworks, Natick, MA, USA), Image J (NIH, USA), and Origin 7.1 (OriginLab, Northampton, NC, USA) were used when required.

Nafion mixing ratio	Nafion film thickness ( $t_N$ )	The ratio of fluorescent intensity: ( $A_2 - A_2'$ ) / ( $A_1 - A_1'$ )		
		$d_C = 20 \mu\text{m}$	$d_C = 50 \mu\text{m}$	$d_C = 100 \mu\text{m}$
5%	2–3 $\mu\text{m}$	0.0	0.096	0.349
20%	8–14 $\mu\text{m}$	0.0	0.029	0.055

**Table 6–1.** Effects of the Nafion film thickness on the SC-ICP.

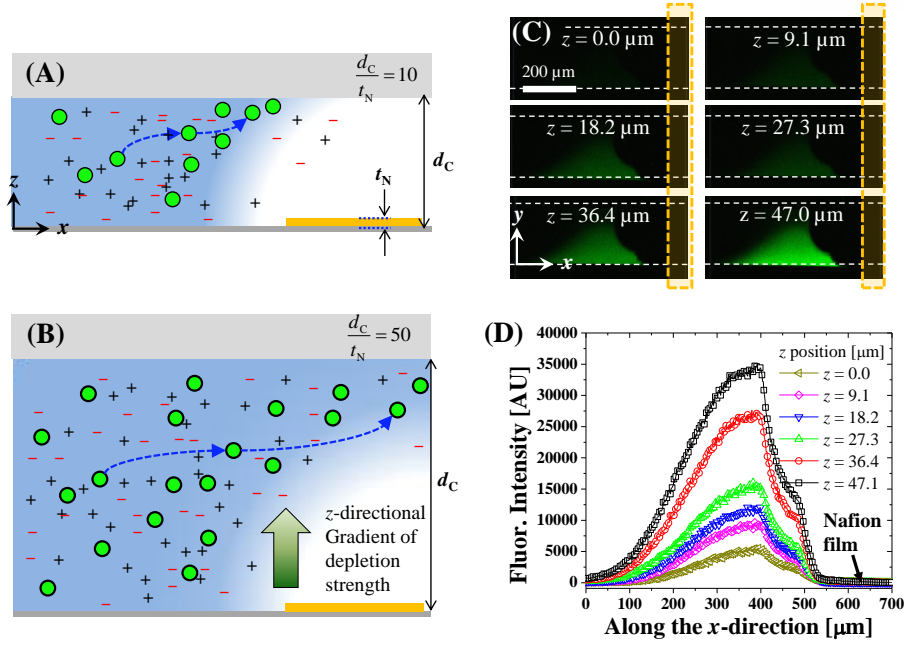


**Figure 6-3.** Schematic illustrations of the IDZ (SC-ICP) for a (A) low and (B) high ratio of the channel depth ( $d_c$ ) to the Nafion thickness ( $t_N$ ). The stronger the IDZ near the Nafion film, the farther is the SC-ICP phenomenon it induces. (C) Confocal images of fluorescent intensities of FITC molecules in PBS 0.5 mM obtained 10 min after an electric field of 25 V/cm was applied in a 50- $\mu\text{m}$  deep microchannel along the  $z$ -direction (upward from the Nafion film,  $d_c/t_N = 25$ ). (D) Quantified fluorescent intensities of the images in (C) along the  $x$ -axis show gradual increases along the  $z$ -axis, implying that more FITC molecules are concentrated at the top side of the microchannel.

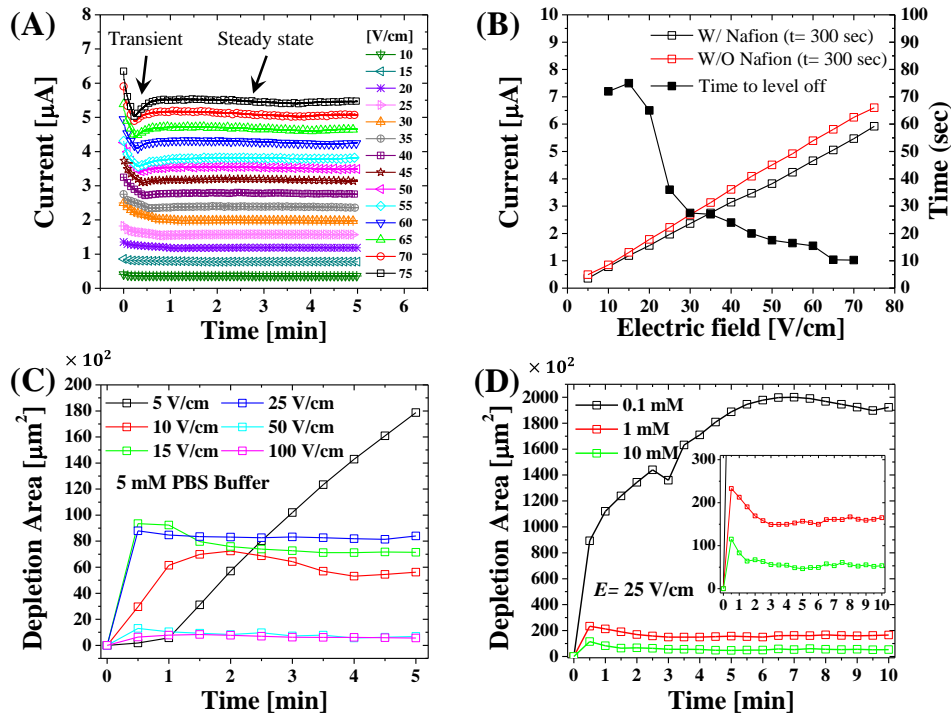


**Figure 6-4.** (A) Monitoring of current over time in various electric fields shows a stable and linear relationship between the current and the potential. (B) Electric resistance measurement with and

without the Nafion film in a microchannel in the steady states ( $t = 300$  s). (C) Quantification of ion depletion areas in various electric fields (ionic strength of 5 mM was used in (A), (B) and (C)). (D) The same quantification as in (C) at three different ionic strengths and the inset graph zoom in 1 mM and 10 mM data.

## ***Results and Discussion***

**Characterization of charged molecule transport.** We conducted experiments using the SC-ICP device in which a 200  $\mu\text{m}$  wide and 1 cm long Nafion film was patterned on the glass surface and a PDMS microchannel was put on top of the Nafion film. To investigate the SC-ICP phenomenon, we utilized differently charged fluorescent dyes: negatively charged dye (fluorescein isothiocyanate, FITC), positively charged dye (Rhodamine 6G) and neutral dye (Rhodamine 110) in 5 mM PBS buffer (all from Sigma Aldrich). All these dyes flow in the same direction as the EOF in the absence of the Nafion film. However, in the presence of the Nafion film, the migration behavior of the dyes in the IDZ was different and useful to understand the SC-ICP phenomenon. As shown in Figs. 6–2 (A)–(C), FITC continuously accumulates in front of the Nafion film because it is perfectly blocked by the IDZ where local depletion of ions results in the increase of electric fields along the channel, while Rhodamine 6G does not penetrate through the IDZ initially. However, Rhodamine 6G starts to penetrate through the IDZ in about 15 min and fluorescent signals are observed over the Nafion film. This can be attributed to the electrostatic clogging of the nanopores of the Nafion film. That is, positively charged Rhodamine 6G molecules appear to gradually bind with and block the nanopores electrostatically. However, the neutral dye, Rhodamine 110, appeared to penetrate through the IDZ because electrically neutral ones are not influenced by the IDZ. Interestingly, some neutral dye molecules were observed to be accumulated by the IDZ. This can be attributed to the fact that electrically impure dyes might be accumulated and bound to the Nafion film. In addition, nonlinear vortex flow may be helpful for the accumulation of the neutral dyes as reported in the literature<sup>89a</sup>.

The ratio of fluorescent intensities of the cathodic side of the Nafion film ( $A_2-A_2'$ ) to those of the anodic side ( $A_1-A_1'$ ) across the microchannel quantifies the flux of dyes/ions as shown in Fig. 6–2(D). The Nafion film almost completely blocks the passage of the anionic dyes (the ratio is almost zero), while the neutral dye passes over the Nafion film (the ratio is higher than 30%). Interestingly, the cationic dyes are initially blocked completely by the IDZ but the ratio suddenly rises up to 0.4. This can be attributed to the electrostatic binding/clogging of the cationic dyes to/at the nanopores of the Nafion film. This phenomenon was confirmed by monitoring the current through the microchannel as shown in Fig. 6–2(E). For anionic and neutral dyes, the current drops initially as the SC-ICP progresses ( $< 1$  min), whereas for the cationic dyes, the current drops in the similar fashion as the cations and remains constant at the early stage, increases at the intermediate stage, and results in a saturated current flow, showing a good agreement with the qualitative results. The SC-ICP strength at the late stage seems weaker than that at the early stage. This can be attributed to electrostatic clogging

of the nanopores ( $\sim 2$  nm) of the Nafion film by Rhodamine 6G dye ( $r_g = 1.6$  nm)<sup>120</sup>; the reduced surface area of the Nafion film causes the ion transport capability to deteriorate over time.

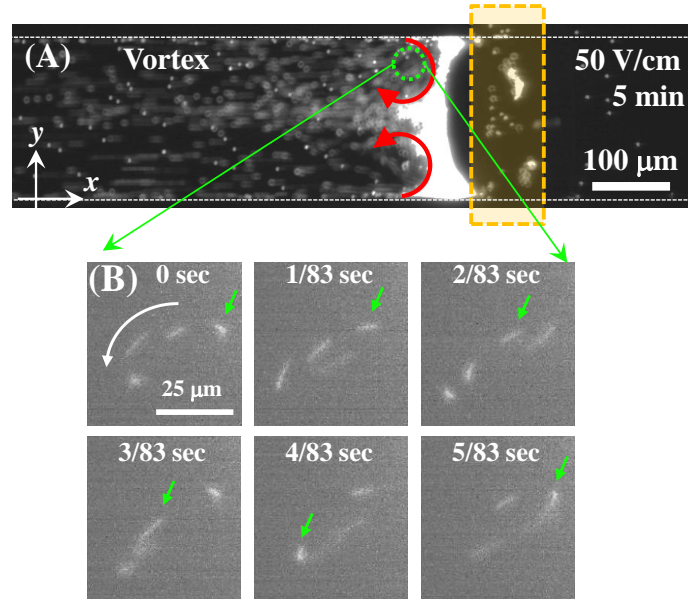


**Figure 6–5.** Visualization of vortex flows. (A) FITC-labeled microparticles of 1  $\mu\text{m}$  diameter are concentrated near the Nafion film and follow the vortex flow as indicated with two arrows in red. (B) Zoomed-in view shows a streamline of a small vortex flow that seems to be caused by the non-uniform patterning of the Nafion film along the y-axis.

**Effects of the Nafion film on SC-ICP.** Since SC-ICP is governed by ion transport of the Nafion film, we tested the thicknesses of the Nafion films that were fabricated by using 5% and 20% Nafion mixtures (w/v %) as listed in Table 6–1. Then, the Nafion films were irreversibly bonded with 200- $\mu\text{m}$  wide PDMS microchannels that were 20  $\mu\text{m}$ , 50  $\mu\text{m}$ , and 100  $\mu\text{m}$  in depth ( $d_c$ ). The effect of Nafion thickness on the SC-ICP was quantified by comparing the fluorescent intensities of FITC obtained along  $A_1$ – $A_1'$  and  $A_2$ – $A_2'$  in the same manner as in Fig. 6–2(D). For example, for a thin Nafion film ( $t_N = 2$ –3  $\mu\text{m}$ , 5% Nafion solution) in a 20  $\mu\text{m}$  deep microchannel, the FITC flux by the bulk flow (25 V/cm) was completely blocked, whereas the FITC flux was not completely blocked in 50  $\mu\text{m}$  (9.6% penetration) and 100  $\mu\text{m}$  (34.9% penetration) deep microchannels. On the other hand, for a thick Nafion film (8–14  $\mu\text{m}$ , 20% Nafion solution), the FITC flux decreased significantly, unlike the case of the thin film. The thick Nafion film seems to transport more cations (high transport flux), so more anions accumulate in front of the film, leading to a stronger IDZ. The stronger the IDZ, the farther is the SC-ICP phenomenon it induces.

Since cation transport is allowed mainly through the Nafion film at the bottom of the microchannel, it is hypothesized that the closer to the Nafion film the stronger is an IDZ produced. As illustrated in Figs. 6–3 (A)–(B), the Nafion film seems to have a certain limited capability to produce a 3 dimensional IDZ so that we imaged the spatial distribution of the fluorescent intensities of FITC from

the bottom to the top by using a confocal microscope. As shown in Fig. 6–3(C), no distinct fluorescent intensities are detected near the glass surface but they get stronger as the focal plane moves upwards to the top side of the PDMS channel. Asymmetrical distribution of fluorescent intensities along the y-axis seems to be caused by the non-uniform patterning of the Nafion film that may affect the local strength of the IDZ and the local electric field strength. Fig. 6–3(D) shows the fluorescent intensities measured from the confocal microscope along the x-axis, showing a good agreement with Fig. 6–3(C).

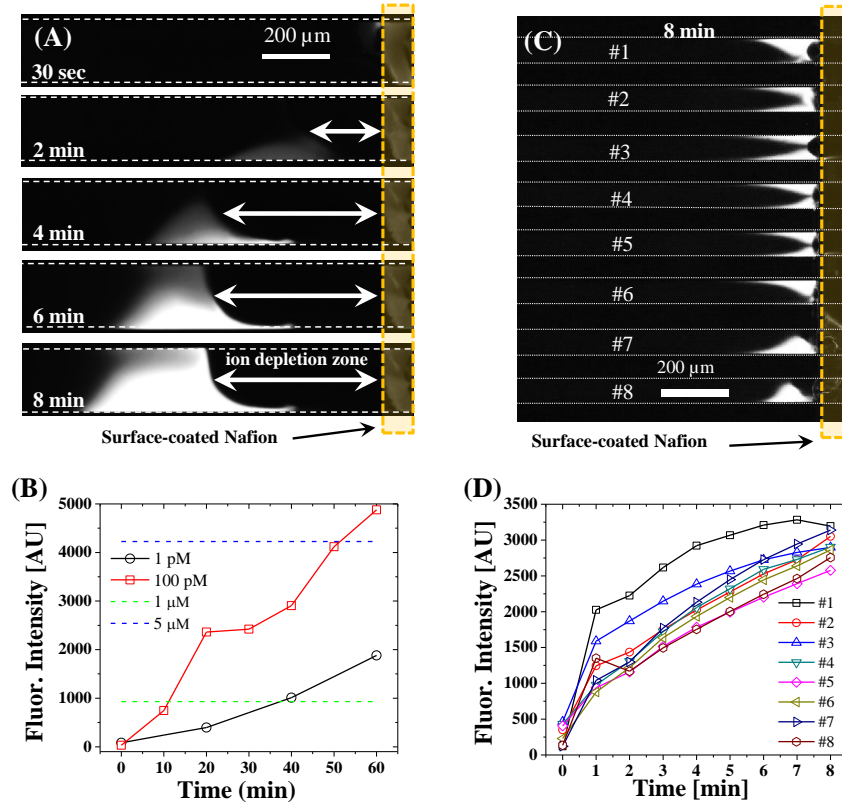


**Figure 6–6.** (A) Image sequence of 3  $\mu\text{M}$  FITC-labeled BSA pre-concentration over time (25 V/cm). (B) 1 pM and 100 pM FITC-BSA samples are concentrated up to  $10^5$  to  $10^6$  folds within 1 h. (C) and (D) The ICP allows the pre-concentration of the same BSA in multiple microchannels in parallel by using a single Nafion film and two electrodes.

**Effects of experimental conditions on SC-ICP: current monitoring across the IDZ.** In addition to the Nafion film thickness, the strength of the SC-ICP (the cation transport flux by the Nafion film) can be determined by electric field strengths. We chose a microchannel (20  $\mu\text{m}$  deep and 200  $\mu\text{m}$  wide) with a thin Nafion film (5% solution) on the surface and then monitored currents over time by applying various electric fields as shown in Fig. 6–4(A). For high electric fields ( $>50$  V/cm), as soon as the electric field was applied, the current dropped before the EOF fully developed and it then leveled off in a minute. In contrast, for low electric fields ( $<20$  V/cm) current variation appeared small. From the results, we calculated the electric resistances of the microchannel in steady state, which were determined 300 s after an electric field was applied. The currents in both the presence and the absence

of the Nafion film on the surface are linearly proportional to the potentials (constant resistances), but it can be inferred that the ICP phenomenon appears to slightly increase the resistance. This is because the ionic current (conductivity) is affected by the ICP phenomenon. Fig. 6–4(B) shows a plot of the time taken for the current to level off, indicating the fast development of the ICP phenomenon. Time is inversely proportional to the electric field; the stronger the applied electric field, the shorter it takes for the ICP to fully develop.

As reported in previous literature, the strength of the ICP was indirectly quantified by visualizing the FITC (cation) depletion area<sup>86</sup>. Fig. 6–4(C) shows the depletion area of the FITC in the presence of various electric fields. For all electric potentials, the depletion area initially increases with time and then levels off within a minute; achieving 5 V/cm takes much longer and it eventually levels off as well. For 50 V/cm, since the Nafion film causes, at most, a 5% difference in electrical resistance (current) as compared to the same plain microchannel that has no Nafion film, the SC-ICP allows an ion flux as high as an open-microchannel bulk flow but does not cause significant Joule heating, and breakdown membrane perm-selectivity; the maximum electric potential is however limited by Joule heating near nano-junctions in most DC-ICP devices. Therefore, it was demonstrated that the SC-ICP device has a unique advantage over the DC-ICP device, although the local electric field appears to increase, level off and then decrease over the IDZ and vortex flows are observed to be produced near the Nafion film, which will be discussed later. Since the net ion flux is affected by ion strengths, we further measured ion depletion areas by changing ionic strengths of a buffer solution as shown in Fig. 6–4(D). For a low ionic strength (100  $\mu$ M PBS), the transport flux of the Nafion film is higher than that of the bulk flow, so the depletion area continues to increase and then it levels off in about 10 min. On the other hand, the depletion area for 1 mM and 10 mM PBS is much smaller than that for 100  $\mu$ M PBS, implying that the transport capability of the Nafion film seems to be limited to a certain value.

**Vortex flows in SC-ICP.** Lastly, the generation of vortex flows is worthy of discussion. Near the Nafion film, many properties of the buffer solution appear to change such as local conductivity, buffer strength, etc, whereas flow rate should be conserved at any cross-sections along the x-axis according to fluid continuity. However, near the Nafion film, the decrease of buffer strength may cause a local increase of the zeta-potential of the surfaces so that the local net flow rate increases because the slip velocity given by the *Helmholtz-Smoluchowski* formula is linearly proportional to the zeta-potential<sup>121</sup>. Owing to the continuity, back flows should be generated as visualized in the Fig. 6–5(A). Interestingly, small vortex flows were also observed and seemed to be produced by the non-uniform patterning of the Nafion film along the y-axis (Fig. 6–5(B)). Although the current measurement was unable to generate the distinct Ohmic, limiting, and overlimiting regime, which can be attributed to the low resolution of the source meter used in this work, the observation of vortex flows verifies that the SC-ICP devices involve the limiting and over-limiting regime because it was reported that vortex flows occur at the overlimiting conditions caused by electrokinetic instabilities<sup>122</sup>. However, we note again

that the SC-ICP devices facilitate more stable and rapid pre-concentrations than DC-ICP devices because they allow higher electric fields.

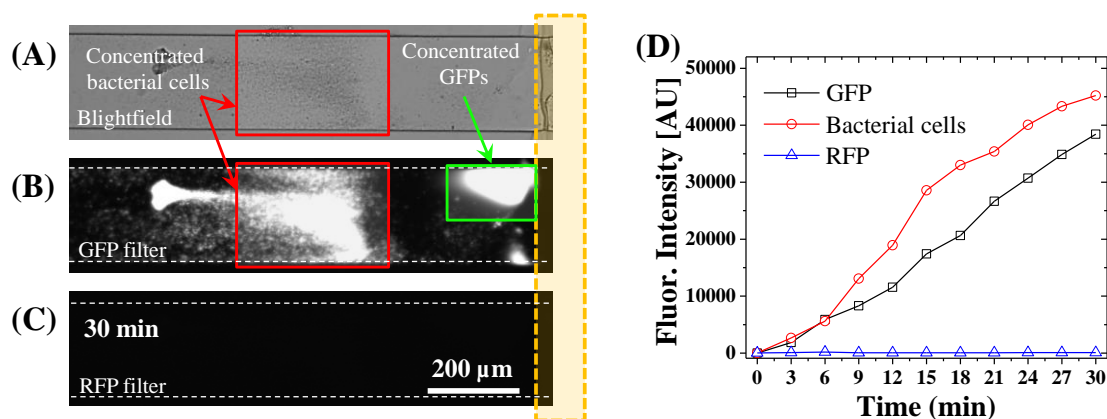


**Figure 6–7.** Concentration and lysis of bacterial cells using the SC-ICP. (A) Bacterial cells are migrated by EOF and then concentrated by the IDZ (50 V/cm, bright field image). (B) A fluorescent image obtained by using a GFP filter shows GFP-expressing cells at the same region as (A) and also shows strong fluorescent signals in front of the Nafion film where no bacterial cells were accumulated. (C) No fluorescent signals are detected through a RFP filter, confirming that the fluorescent signals originate from the GFP in the cells. (D) The fluorescent intensities are measured from the concentrated cells (300  $\mu\text{m}$  by 200  $\mu\text{m}$  rectangle in red) and the concentrated GFPs (200  $\mu\text{m}$  by 100  $\mu\text{m}$  rectangle in green) and then they are plotted over time.

**Applications of SC-ICP devices.** The SC-ICP device has a high potential in protein pre-concentration so that we demonstrated the applicability of the SC-ICP device by pre-concentrating FITC-labeled BSA. Fig. 6–6(A) shows the pre-concentration of 3  $\mu\text{M}$  of FITC- labeled BSA in 1 mM PBS buffer in a single, open, and straight microchannel, while Fig. 6–6(C) and (D) show a similar pre-concentration in 8 microchannels in parallel. Notably, only two electrodes were used in both the experiments and the pre-concentrated sample plug and the depletion area remained stable and constant. Fig. 6–6(B) shows the quantification of the pre-concentration enhancement factors. For doing this, we calibrated the microscope by filling a 20  $\mu\text{m}$  deep microchannel with known FITC-labeled BSA concentrations of 1  $\mu\text{M}$  and 5  $\mu\text{M}$  and then pre-concentrated 1 pM and 100 pM samples for 1 h. Here, 20  $\mu\text{m}$   $\times$  20  $\mu\text{m}$  squares that have the strongest fluorescent intensities were chosen from the pre-concentrated sample plugs and then compared with the calibration data. As a result, it was found that the pre-concentration enhancement factors obtained using the SC-ICP phenomenon ranged from  $10^4$  to  $10^6$  folds for samples ranging from 1 pM to 100 pM<sup>77a</sup>. In fact, the parallel microchannels have somewhat variations in the concentration factors that seem to be caused by the non-uniformity of the surface-patterned Nafion film. However, these variations can be eliminated by improving the microchannel flow-based patterning method employed in this work. For example, the restricting flow method can be a good candidate to enhance the chip-to-chip and microchannel-to-microchannel reproducibility<sup>81</sup>.

As another application of the SC-ICP device, we attempted to concentrate and lyse *E. coli* cells that expressed GFP constitutively. As shown in Fig. 6–7(A), the bacterial cells were driven by EOF toward the Nafion film from the anodic reservoir and then concentrated near the border line of the IDZ in the presence of a 50 V/cm electric field. Simultaneously, the bacterial cells lysed so that GFPs within the cells were extracted, separated from the concentrated cells and then formed a concentrated GFP plug in the right front of the Nafion film as shown in Fig. 6–7(B); they migrated further and closer to the Nafion film. We confirmed the concentrated cells and the GFP plug by measuring the fluorescent intensities through a RFP filter cube as shown in Fig. 6–7(C) in which no fluorescent signals were detected. The cell lysis seems to take place because of osmotic pressure between the cell and buffer solution at a low buffer strength<sup>123</sup> and the separation of the GFPs from the concentrated cells appears to be caused by the different net mobility of the cells and the GFPs. Fig. 6–7(D) shows the fluorescent intensities that were measured from the concentrated cells in the red rectangle (300  $\mu\text{m}$  by 200  $\mu\text{m}$ ) and the concentrated GFPs in the green rectangle (200  $\mu\text{m}$  by 100  $\mu\text{m}$  rectangle) in Fig. 6–7(B) over time. It can be inferred that both the concentration and lysis of the bacterial cells continuously and simultaneously occurred on a chip.

## Conclusions

We have demonstrated that rapid and stable ICP can be induced in single, open microchannels by using a surface-patterned Nafion film as an uncharacteristic fast ionic transporter. We quantified transport flux of negatively charged, positively charged, and neutral fluorescent dyes to investigate the SC-ICP phenomenon. We also found that the SC-ICP phenomenon is affected by Nafion film thicknesses, strengths of applied electric fields, and ionic strengths of buffer solutions. As a result, it was proved that SC-ICP devices have several advantages over DC-ICP devices: easy and simple fabrication processes, inherently leak-tight, stable and robust ICP induced rapidly, low electrical resistances to avoid Joule heating, and membrane perm-selectivity breakdown but allowing for as high bulk flux of analytes as an open, plain microchannel. We demonstrated that the SC-ICP devices were very useful for the pre-concentration of proteins and concentration enhancement factors we achieved ranged from  $10^4$  to  $10^6$  folds for samples ranging from 1 pM to 100 pM. We also demonstrated that the SC-ICP devices enabled the accumulation and lysis of bacterial cells. That is, proteins like GFPs within the cells were extracted and separated from the concentrated cells near the border line of an IDZ. Then, the proteins were removed further and closer to the Nafion film to form a concentrated protein plug. This process occurred simultaneously and continuously. Hence, we believe that the SC-ICP not only has high potential in massively parallel microchannels that require only one pair of electrodes but also holds higher possibilities of being easily integrated with traditional microfluidic systems to facilitate analytical, biotechnological applications on a chip.

## Chapter 7. Microfabricated Ratchet Structures for Amplifying Chemotactic Responses of Motile Bacterial Cells

### *Introduction*

Microfluidic devices have been widely used to study chemotaxis of bacterial cells because they can generate various concentration gradients by mixing, splitting, and injecting fluid flows that contain diffusible chemoeffectors.<sup>13, 35a, 35c, 124</sup> In particular, a flow-based, Y-shaped channel is very useful because it is easy to make two flows confront but not directly mix, allowing the soluble molecules from one flow stream to diffuse into the other to generate concentration gradients across the channel. As the motile cells are loaded into one stream and a soluble chemoattractant into the other, the cells migrate toward a high concentration of the chemoattractant, called chemotaxis.<sup>48</sup> This mechanism plays a key role in investigating the chemotaxis of various motile bacterial cells.<sup>39c, 125</sup> Many efforts have been made to resolve the problem of varying concentration gradients along the channel by employing novel microfluidic channel networks<sup>35b, 36, 124b, 126</sup> Even pure diffusion-based concentration gradient generation devices have been introduced to facilitate the chemotaxis assays in the absence of convection flows.<sup>13, 39b, 56, 127</sup> However, these devices still seem to hold limitations in analyzing chemotactic responses with high resolution and investigating the sensitivity of chemoreceptors of cells toward various chemoeffectors.

To address the current limitations of microfluidic devices developed for chemotaxis assays, we present a novel microfluidic device that consists of three main parts, as shown in Fig. 7–1. The first part is the typical Y-shaped microchannel, which generates concentration gradients of carbon sources across the channel to attract cells from the middle stream to a side stream. The second is the concentrator array beside the main microchannel at every 2 mm from the junction, which accumulates cells on the basis of their chemotactic responses and the sensitivities of chemoreceptors. The third is the arrowhead-shaped ratchet structure that is integrated with each concentrator to trap and unidirectionally relocate cells from the entrance to the centers of the concentrators. The arrowhead-shaped ratchet structures were recently used by Hulme et al.<sup>128</sup> to fractionate *E. coli* cells by length, and by Galajda et al. to selectively relocate bacterial cells from one side to the other and form spatial pattern on a surface.<sup>129</sup> In this work, the microfabricated ratchet structures not only guide and accumulate cells but also prevent cells from escaping from the concentrator. Similar microfabricated ratchet structures have been characterized in detail and employed in our previous work.<sup>130</sup>

In this study, we demonstrate that the presented device can not only identify the preferential chemotactic responses of cells toward various carbon sources, but also make the resolution of typical devices much higher. This is possible because the number of accumulated cells in the array of concentrators continuously increases with time, resulting in the amplification of chemotactic responses. In addition, we demonstrate that the device can analyze the relative sensitivity of

chemoeffectors toward five different carbon sources by comparing the number of cells in the concentrators at different locations. Because of the simple fabrication processes and the high resolution, we believe that the device has a high potential to be widely used in chemotaxis assays and the characterization of chemoreceptors, which may be impossible for previous microfluidics devices.

### Methods and Materials

**Preparation of bacterial cells.** We used three different *E. coli* K-12 strains. MG1655 was used as motile cells, while strain DH10B, as immotile. In addition, BW25113 with knockout in a chemoreceptor gene *trg* (JW1417) from Keio collection was used as a control. To compare their chemotactic sensitivity, each strain was transformed with pLtetO-1+GFP+term plasmids expressing green fluorescent protein from the PLtetO promoter for quantitative analysis of chemotactic response. For cultivation, a single colony of each *E. coli* grown on a Luria–Broth (LB) solid medium plate was inoculated into 5 mL of tryptone broth (TB, 1% tryptone and 0.5% NaCl) media.<sup>15</sup> The *E. coli* cells were then grown at 25°C in a rotary shaking incubator at 200 rpm to mid-log phase ( $OD_{600}=0.4$ ). Before the cell motility was observed, cells were centrifuged at 5000 rpm for 2 min, the supernatant liquid was poured off, and the pelleted cells were resuspended in M9 media.

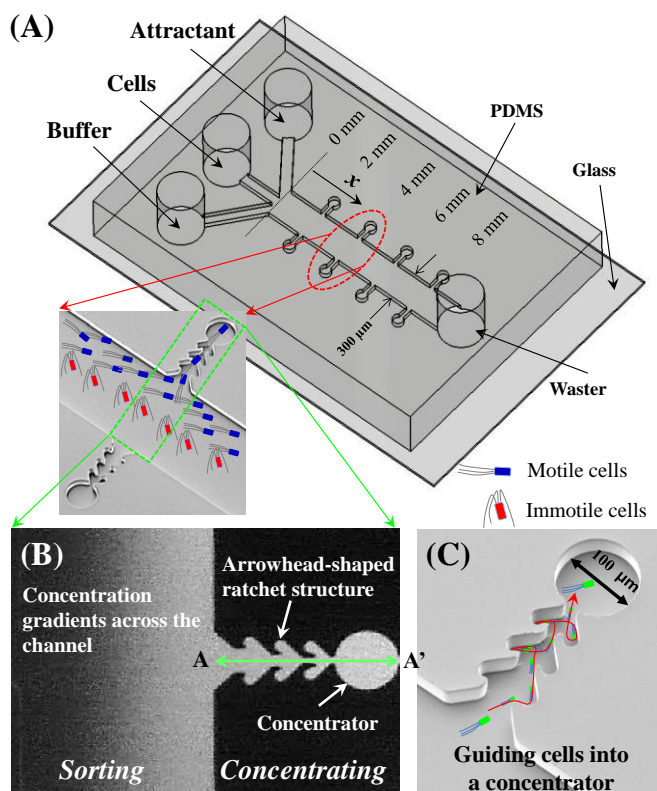


**Figure 7–2.** (A) Schematic of the device that can sort and concentrate motile bacterial cells. (B) The fluorescence image of the concentration gradient of FITC (50  $\mu$ M) across the channel and a concentrator connected with arrowhead-shaped ratchet structures. (C) SEM image of the ratchet structure that can uni-directionally relocate cells from the entrance to the center of the concentrator.

**Design and fabrication of devices.** As shown in Fig. 7–1, the main microchannel is 300  $\mu\text{m}$  wide, 20  $\mu\text{m}$  deep, and 8 mm long and the concentrator array is located at every 2 mm from the junction. The devices were fabricated using standard soft-lithography techniques (SU-8 molds and PDMS) as described in our previous work.<sup>127a, 131</sup>

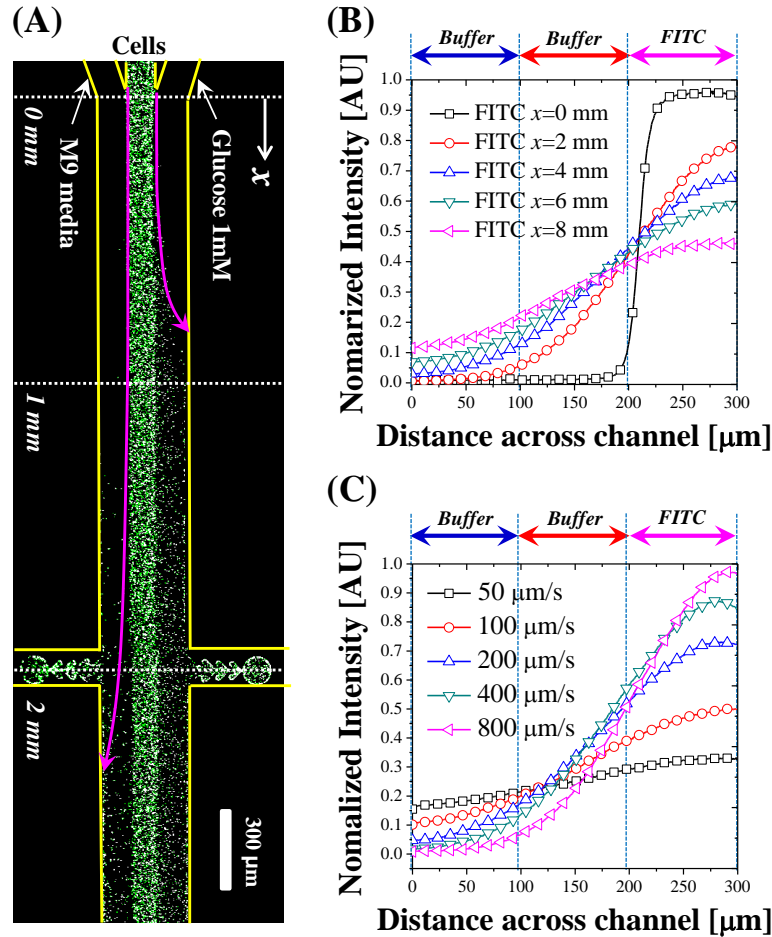


**Figure 7–2.** (A) Motile cells show chemotaxis toward a carbon source (glucose) but no chemotactic response toward buffer media containing no carbon sources (flow is 400  $\mu\text{m}/\text{s}$ ). (B) 50  $\mu\text{M}$  FITC was loaded to characterize concentration gradients of carbon sources at different locations (400  $\mu\text{m}/\text{s}$ ). (C) Characterization of the concentration gradients under various flow velocities ( $x=4$  mm).

**Experimental procedure and data analysis.** All microchannels were rinsed with the motility buffer solution (TB, 1% tryptone and 0.5% NaCl) and then coated with Pluronic surfactant (F-127, 0.01%) to minimize nonspecific binding between the cells and glass surfaces. The remaining surfactant was subsequently rinsed with the TB. The concentration gradients were characterized by quantifying the fluorescent intensities of 50  $\mu\text{M}$  fluorescein isothiocyanate (FITC). Five chemoeffectors (carbon sources) were tested and their molecular weights were found to be very similar to each other so that their diffusion coefficients seemed very close (glucose=180.16, galactose=180.16, mannose=180.16, arabinose=150.13, and xylose=150.13, Sigma–Aldrich). All colorless fluorescent microimages were obtained with an inverted epi-fluorescent microscope (Nikon,

Ti-S, Japan) and a CCD camera (Nikon, DS-Qi1, Japan) equipped with a digital image recorder (Digital Sight DS-U2, Nikon, Japan). Also, colorful microscopic images were obtained using a confocal microscope operated (Zeiss, LSM700, Japan) by the ZEN 2009 software. All images were analyzed by using Image J. (NIH, USA).

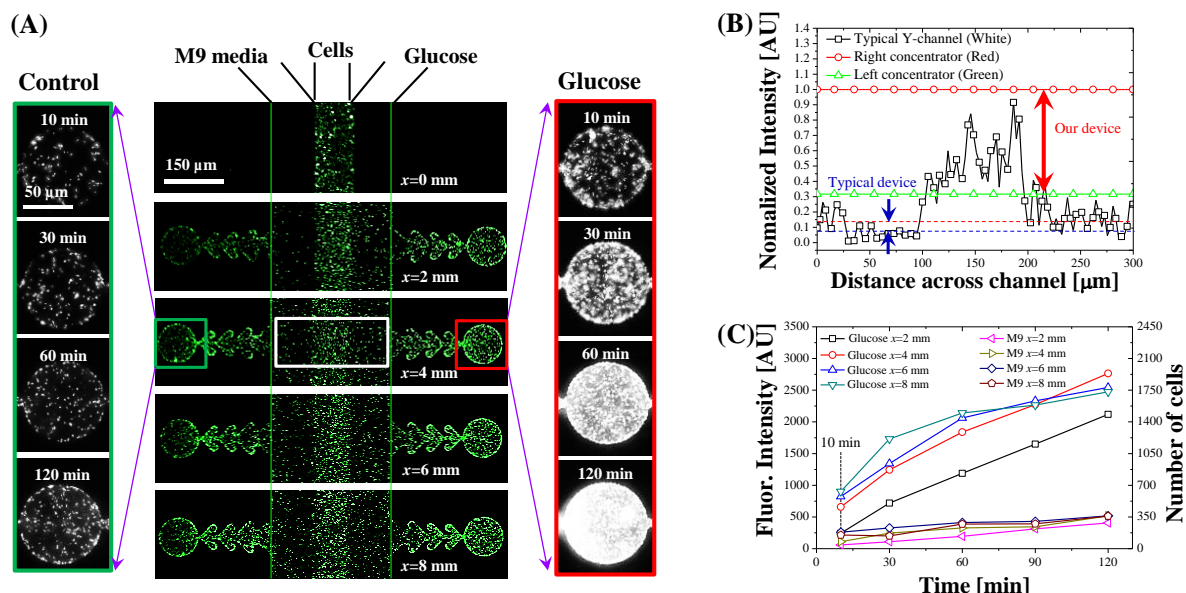


**Figure 7-3.** (A) A sorting and concentrating device. The white rectangle indicates the region where chemotaxis is observed in typical microfluidic devices utilizing Y-shaped channels, whereas the green and red rectangles indicate concentrators that can amplify chemotactic responses with respect to time by accumulating cells. (B) The fluorescent intensity profile obtained from a confocal microscope across the middle channel shows a slight difference (2–3 AU) between the left and right stream while that between the left and right concentrator shows about 10 AU. (C) The difference in the fluorescent intensity repeatedly obtained from an epi-fluorescence microscope between the left and right concentrator continuously increases, implying that the chemotactic response of cells is highly amplified with time.

## Results and Discussion

**Typical Y-shaped channels for chemotaxis.** We have attempted to identify the preferential chemotactic responses of bacterial cells toward five carbon sources using a typical Y-shaped channel. We flowed a buffer solution containing no carbon sources in the left channel, the same buffer solution with cells expressing GFP in the middle, and a solution containing a carbon source (glucose) in the right channel, as shown in Fig. 7-2(A). Chemotactic responses to glucose appear distinct (GFP signals), while no responses are observed in the other stream containing no carbon sources. Additional experiments were conducted and quantified, showing that the approach using typical Y-shaped channels was unable to provide sufficient resolution to identify the carbon source most preferred by the cells, showing the limitation of the current microfluidic devices for chemotaxis assay. Moreover, it seems impossible to investigate the relative sensitivity of chemoreceptors toward carbon sources.

Hence, we were encouraged to employ a microfluidic sorting and concentrating device that can amplify bacterial chemotactic responses by accumulating cells in the concentrators.

In fact, the cells are easily attracted from the middle stream to the right stream thanks to their chemotactic behavior but they are not easily concentrated at the concentrator located to the side of the main channel. Here, the arrowhead-shaped ratchet structures play a key role in trapping and guiding the cells into the concentrator as demonstrated in our previous work.<sup>130</sup> In addition, a range of flow rates was tested because under very high flow rates, the cells cannot swim out (escape) from shear stress, while under very low flow rates, the cells can migrate randomly and seem irrelevant to chemotactic responses. Furthermore, the concentration gradients across and along the channel were well adjusted by controlling the flow velocity from 50 to 800  $\mu\text{m/s}$ . For 400  $\mu\text{m/s}$ , cells in the middle stream started to show a chemotactic response toward glucose at  $x=0.5$  mm whereas no cells are observed to be moving toward the left buffer solution. However, at  $x=2$  mm, the cells migrate toward the buffer stream because glucose diffuses over the middle to the left. Fig. 7-2(B) quantifies concentration gradients across the channel at  $x=0, 2, 4, 6,$  and  $8$  mm, and Fig. 7-2(C) shows concentration gradients at  $x=4$  mm under different flow velocities. Since the concentration gradient is almost linear across the entire channel at  $x=4$  mm and at the flow velocity of 400  $\mu\text{m/s}$ , we used this distance and flow velocity for all experiments unless otherwise noted. We experimentally confirmed that no concentration gradients are generated from the entrance to the center of the concentrator.

**Amplification of chemotactic responses.** As shown in Fig. 7-3(A), we used the same experimental conditions as before and measured the fluorescent intensities across the main channel and those at the concentrators to analyze the chemotactic response of cells toward various carbon sources. In the same manner, we observed that cells showed chemotactic migration toward glucose and then started to be accumulated in the concentrator on the right side. On the other hand, cells did not show chemotactic migration toward the M9 buffer without carbon source; therefore no accumulation of cells in the concentrator on the left side.

For quantitative comparison between the typical Y-channel channel device and our device, we obtained fluorescent intensities with time from the middle channel (white rectangle), which is exactly the same as the typical Y-shaped channel device, those from the right concentrator (red rectangle), and those from the left concentrator (green rectangle). As shown in Fig. 7-3(B), the fluorescent intensity profile obtained by ensemble averaging 150  $\mu\text{m}$  across the main channel is slightly biased to the right stream, meaning that cells migrate toward glucose due to chemotaxis. However, the difference in the fluorescent intensity between the right glucose and the left M9 buffer appears to be about 2–3 AU, which is not enough to conclude preferential chemotaxis toward carbon sources. However, the difference in the fluorescence intensity between the right (glucose) and left concentrator (M9 as control) is gradually amplified and shows about ten times higher resolution (22 AU for a confocal microscope) than the typical approach in 60 min because cells are continuously accumulated into the

concentrator; no cells can exit from the concentrator due to the arrowhead-shaped structures. We further quantified the fluorescent intensities of both the right and left concentrators using a fluorescent microscope, as shown in Fig. 7–3(C). Since the experiment is performed at a steady state the chemotactic responses can be additionally amplified and are linearly proportional to time. On the other hand, the control concentrator shows very low intensities with time. This can be easily described by a simple diffusion analysis. Since the average flow velocity was about 400  $\mu\text{m/s}$ , it took about 10 s from the junction to  $x=4$  mm. Therefore, for 10 s, the diffusion length of glucose can be approximated to be 160  $\mu\text{m}$  ( $\delta \sim (2D_{\text{glu}} \times 20\text{s})^{1/2}$ , where  $D_{\text{glu}} = 7 \times 10^{-10} \text{ m}^2/\text{s}$  is the diffusion coefficient of glucose<sup>49</sup>) so that the concentration of glucose on the left stream appears insufficient to attract the cells. This is why all concentrators on the left show almost negligible increase in fluorescent signals, while those on the right show gradual and continuous increase in the number of fluorescent cells (up to 2000 cells).

Additionally, the number of cells at the concentrator at  $x=2$  mm is less than that at other concentrators. This can be attributed to the fact that chemoreceptors of cells are not completely activated to show chemotaxis because of the limited diffusion of glucose and short migration time of cells.

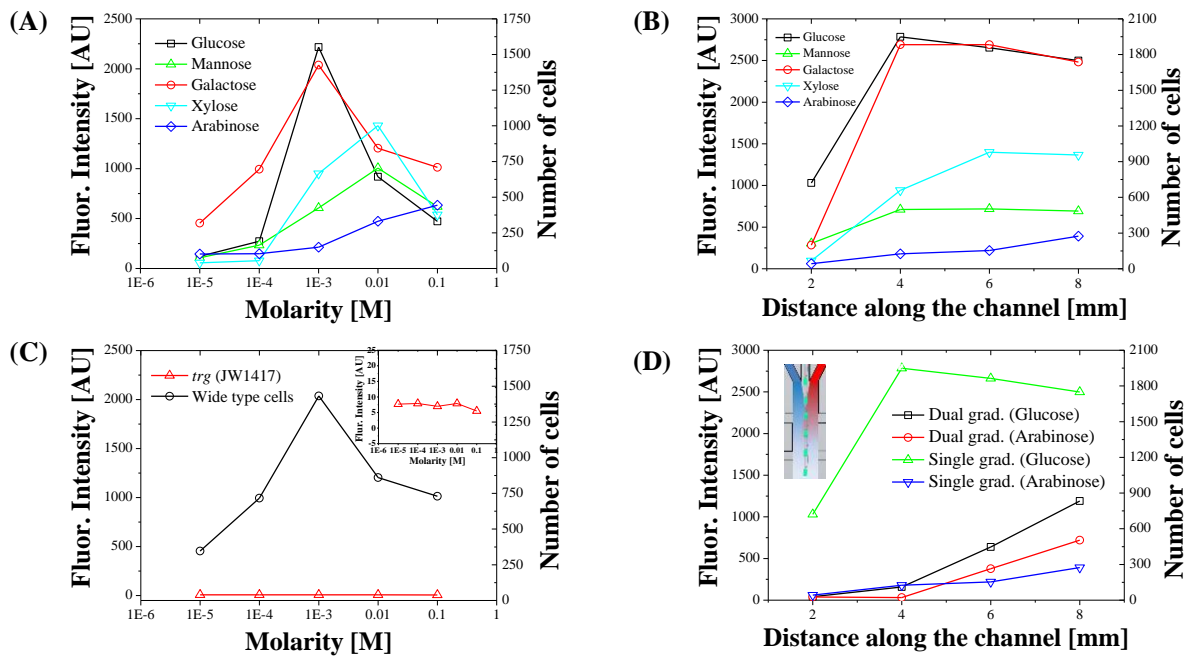


**Figure 7–4.** All fluorescent intensities were obtained from cells accumulated at the concentrator located at  $x=4\text{mm}$  and 60 min. (A) Chemotactic responses toward different concentrations and types of carbon sources. (B) At 1 mM concentration of carbon sources, fluorescent intensities from the concentrators located at  $x=2, 4, 6,$  and  $8$  mm in 60 min. (C) Comparison of the fluorescent intensities of wild type to those of mutant cells whose chemoreceptors are knocked out. (D) Chemotactic responses of cells in the presence of single (buffer and glucose or buffer and arabinose) and dual gradients (glucose and arabinose).

### **Preferential chemotaxis and relative sensitivity of chemoreceptors toward carbon sources.**

We applied the device to identify preferential chemotaxis of cells toward five carbon sources. As shown in Fig. 7–4(A), experiments were repeated with five different concentrations ranging from 10  $\mu$ M to 100 mM with a 10-fold interval. For glucose and galactose, the strongest chemotactic responses were found in the presence of 1 mM concentration gradients. On the other hand, for mannose, xylose, and arabinose, the same phenomena were observed at 10 mM. The different chemotactic responses can be attributed to the fact that *E. coli* cells not only have various chemoreceptors on their membranes, with most being more sensitive to glucose than other carbon sources, but are also known to express the enzymes for glucose metabolism consistently.<sup>131</sup> This result is well matched with other literature reporting that *E. coli* cells prefer glucose, galactose and mannose, in this order, to arabinose and xylose when they are exposed to 1–100 mM concentrations of these carbon sources.<sup>131</sup>

Furthermore, the device can characterize the sensitivity of the chemoreceptors of the cells toward carbon sources by analyzing the number of cells in the concentrators with respect to the distances from the junction under 1 mM concentrations of carbon sources (Fig. 7–4(B)). For glucose and galactose, the cells start getting concentrated at the first concentrator ( $x=2$  mm) and are saturated in the second concentrator ( $x=4$  mm). However, the chemotactic responses to other carbon sources gradually increase from the first to the fourth concentrator, although the difference between the diffusion coefficients for these carbon sources would be negligible because their molecular weights are similar.<sup>131</sup> This result suggests that chemoreceptors specific to a certain carbon source have different sensitivities or the number of chemoreceptors on the cell membrane differ in activating a chemotaxis signal pathway.<sup>53</sup> Cells are more sensitive to glucose and galactose than mannose, xylose and arabinose. This phenomenon also shows good agreement with other literature reporting that cells hold different threshold concentrations for different carbon sources at which chemotactic responses occurs.<sup>48, 56</sup>

As a control experiment, a knockout mutant of the *trg* gene that encodes a galactose chemoreceptor was used, and it showed significantly reduced chemotactic responses compared to wild type cells as shown in Fig. 7–4(C). This result confirms that chemotaxis is caused by the attachment of small chemoattractant molecules to the chemoreceptors on the cell membrane.<sup>53</sup> This can be further supported by the dual-gradient experiments as shown in Fig. 7–4(D). Using the device, we can easily generate a glucose gradient (1 mM) on the right and an arabinose (1 mM) on the left simultaneously. Cells are loaded in the middle channel. The fluorescent intensities gradually increase along the channel, meaning that chemotactic responses to glucose are significantly delayed. This is because the chemoreceptors of the cells can be activated by both the gradients and so that their chemotactic responses are delayed until one signal pathway is more strongly induced. In other words, the cells are induced to show chemotaxis toward glucose and arabinose simultaneously, and it takes time for them

to be additionally biased toward glucose, making their chemotactic activity much lower; the cells have no responses before the second concentrator ( $x=4$  mm), whereas the cells show chemotactic response to arabinose slightly earlier than the single arabinose gradient. This phenomenon can be attributed to the early activation of the chemoreceptors by glucose that helps to respond to the arabinose gradient faster. This observation can be supported by the mechanism of the amplification of chemotactic signals by the chemoreceptor array.<sup>132</sup>

### ***Conclusions***

We demonstrated a microfluidic device capable of analyzing the chemotactic responses of bacterial cells with about 10 times the resolution of devices that employ typical Y-shaped microfluidic channel networks. This was achieved by unidirectional relocation and continuous concentration of cells showing chemotaxis in a concentrator array connected with arrowhead-shaped ratchet structures. As a result, the device made it possible to identify not only the preferential chemotaxis but also the sensitivity of chemoreceptors of *E. coli* toward five carbon sources: the resulting preference was glucose and galactose over mannose, xylose, and arabinose. Since the fabrication processes are very simple and the resolution for chemotaxis assays and the characterization of the sensitivity of chemoreceptors are enhanced, the device could be further applied to or integrated with many other biotechnological microsystems for high-throughput screening, sorting, and concentration of bacterial cells.

## Chapter 8. Microfluidic Chemostat Device for Sensitive Microbial Biosensor to Detect Heavy Metal Ions

### *Introduction*

Detection of toxic compounds and heavy metals is important. In particular, heavy metals such as cadmium, mercury, and lead are found in many industrial wastes, including vehicle emissions, lead-acid batteries, and chemical fertilizers, and they are generally denser than iron. Heavy metals are toxic to cells mostly via oxidative stress<sup>133</sup> and also can accumulate over time in animal bodies, causing lung cancer<sup>134</sup>, brain dysfunction<sup>135</sup>, softening of bones<sup>136</sup>, and kidney disease<sup>137</sup>. Generally, detection of heavy metal ions (HMIs) using conventional methods requires skilled operation and methods requiring expensive instruments such as atomic absorption spectroscopy<sup>138</sup> and coupled plasma-atomic emission/mass spectroscopy<sup>139</sup>, in addition to complex configuration of electrochemical instruments<sup>140</sup>. To overcome the limitations of the conventional methods, microbial biosensors, which utilize pre-engineered genetic circuits of live microbes, have been generated with the rapid growth of synthetic biology<sup>141</sup>. The microbial biosensors offer considerable advantages: they provide inexpensive and facile detection without complex equipment and provide flexibility for various analyses, and pre- and/or post- processes such as purification and separation are not required. For example, microbial fluorescence-based<sup>142</sup> and luminescence-based biosensors<sup>143</sup> utilize the expression of reporter genes that can be specifically switched on by biochemical interaction events between cellular receptors and inducer molecules (i.e., HMIs). The optical or fluorescent signals produced by the microbes can be directly quantified during incubation of the microbes with test solutions, thereby enabling detection of target analytes with unknown concentrations.

Recently, bioreactor systems have been miniaturized to not only shorten diffusion distances and enhance reaction kinetics but also to reduce the labor involved and sample consumption. For example, Gu *et al.* introduced a milliliter-scale bioreactor (58 mL working volume) that can be operated in a continuous and repeatable manner for testing toxic compounds in an aqueous solution. They found that higher growth rates and/or dilution rates enhanced the performance of microbial biosensors<sup>144</sup>. Additionally, Charrier *et al.* reported a bioreactor system with multiple wells that had a diameter of several millimeters and were connected in series. They immobilized microbial biosensors in the multiple wells and then applied a sample solution containing several heavy metals to utilize the biosensors to express bioluminescence in response to the target analytes<sup>145</sup>. For further miniaturization, several research groups developed microfluidic devices and combined them with microbial biosensors for detecting toxic compounds and HMIs. For instance, Rothert *et al.* used a microbial whole-cell biosensor in a centrifugal microfluidic device to detect six different conditions of HMIs such as arsenite and antimonite by generating selective fluorescence signals from the biosensors<sup>146</sup>. In addition, Garcia-Alonso *et al.* prepared a microfluidic device that had several microchannels in

parallel and could screen multiple toxic compounds or a single compound at different concentrations on a chip by using chemical gradients and recombinant yeast cells<sup>147</sup>. These approaches combining a microbial biosensor and a miniaturized device/system provided many advantages, including small sample volume consumption and short analysis time<sup>146-147</sup>, high throughput<sup>145-147</sup>, and enhanced sensitivity and selectivity, compared to conventional methods<sup>144, 146</sup>. However, most of these approaches appeared to rely on conventional batch-mode culture environments. Basically, the batch-type mixing of microbes and target analytes in a confined solution not only limits the maximum cell growth because of depletion of nutrients but also gradually reduces the number of target analytes available for additional induction over time. In contrast, it is advantageous to provide a continuous nutrient environment for microbes to enable high cell growth rates in a microchamber on a chip<sup>148</sup>. For this reason, a continuous culture and induction environment is essential to enhance detection sensitivity because continuous feeding of nutrients and target analytes (target HMIs) helps enhance the gene expression in the microbial biosensor.

In this study, we developed a microfluidic device that not only concentrates motile microbes in a compartmentalized microchamber array using microfabricated ratchet structures but also grows the concentrated microbes in a continuous-feed mode. This novel device enabled the feeding of nutrients and various concentrations of HMIs (e.g.,  $\text{Pb}^{2+}$  and  $\text{Cd}^{2+}$ ) in the compartmentalized microchambers in a continuous manner, thereby introducing a simple and convenient chemostat-like culture environment. Using the combination of the chemostat-like culture environment and synthetically engineered microbial biosensors, we characterized the sensitivity and selectivity of the microbial biosensors for detecting HMIs and then compared the result with that obtained using conventional batch-type methods.

### ***Methods and Materials***

**Reagents and materials.** For visualization and quantification of the microfluidic channels, green, red, and yellow dyes and 50 mM fluorescein isothiocyanate (FITC) were mixed with deionized water, respectively. As the target HMI,  $\text{Pb}^{2+}$  and  $\text{Cd}^{2+}$  were prepared in a cell culture solution (tryptone broth (TB), 1% tryptone, and 0.5% NaCl) with ampicillin (75  $\mu\text{g}/\text{mL}$ ). A Luria broth (LB) agar plate was prepared by mixing agar (1% w/v) for colony formation. For detection of HMIs, analyte solutions of  $\text{PbCl}_2$  (Cat. No. 203572) and  $\text{CdCl}_2$  (Cat. No. 439800) were purchased from Sigma-Aldrich and diluted into autoclaved distilled water to the desired concentrations when necessary.

**Preparation of bacterial cells.** We used two *Escherichia coli* K-12 strains (MG1655 and DH5) as platform cells to develop microbial sensors. The MG1655 strain harboring pTKU4-2 plasmid that constitutively expresses green fluorescent protein (GFP) was used for testing cell growth in the chemostat-like microfluidic device. DH5 $\alpha$  cells harboring plasmids pHK194 and pHK200 were used

for detecting  $\text{Pb}^{2+}$  and  $\text{Cd}^{2+}$  and named as the HK621 and HK622 strains, respectively<sup>149</sup>. For continuous induction testing in the microfluidic device, a single colony of the *E. coli* on an LB agar plate was grown in 5 mL in LB broth in a test tube that was rigorously agitated in a rotary shaking incubator (37°C and 200 rpm) overnight. The cells were then introduced into the microfluidic device. For batch-type detection in test tubes, the cells were grown to mid-log phase in 5 mL of LB broth until the optical density at a wavelength of 600 nm reached  $\text{OD}_{600} = 0.5$  and various concentrations of the HMI were added for induction of fluorescent reporter gene expression followed by incubation at 37°C and 200 rpm overnight. For a fair, reasonable comparison of the batch-type biosensing method with the chemostat-like biosensing method, the cell density of the batch-type method was intentionally enhanced by centrifugation (Combi 514R, Han-Il Instrument, Incheon, Republic of Korea) at 3000 rpm for 10 min at 25°C.

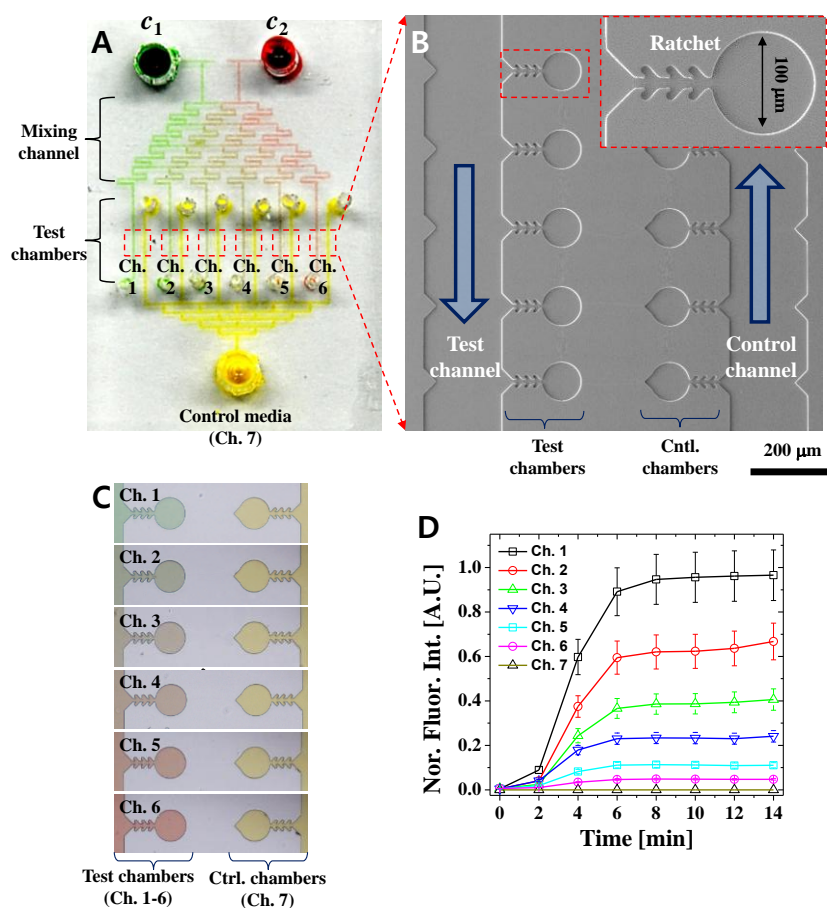


**Figure 8-1.** A microfluidic device for microbial biosensors for detecting HMIs ( $\text{Pb}^{2+}$  and  $\text{Cd}^{2+}$ ). (A) Microscopic image shows the microfluidic channels consisting of a concentration gradient generator and a microbe culture chamber array. (B) SEM image shows one set of test channels and control channels. Chambers are connected to the main channel with ratchet structures that enable chemicals and molecules to be transported but prevent motile cells in the chamber from escaping to the main channel. (C) Microscopic images to visualize concentration gradients in the test chambers and the control chambers. (D) Quantification of concentration gradients by using fluorescence intensity (50  $\mu\text{M}$  FITC solution).

**Design and fabrication of the microfluidic device.** The microfluidic device was fabricated and its channel feature was 200  $\mu\text{m}$  wide and 10  $\mu\text{m}$  deep. The microfluidic device consisted of a mixing channel network and a microchamber array for compartmentalized cell culture on a chip as used in our previous study<sup>150</sup>. The microchamber array was integrated with ratchet structures to physically isolate the microbes from the main channel but chemically allow the transport of nutrients and small molecules to and from the main channel<sup>59a, 150-151</sup>. The microfluidic device was fabricated using standard soft lithography as used in our previous work. Briefly, an SU-8 (Microchem 2025, Newton, MA, USA) master (approximately 10  $\mu\text{m}$  thick) was fabricated using standard photolithographic procedures. The surface was silanized using trichloro(3,3,3-trifluoropropyl)silane (Sigma Aldrich, Korea) in a vacuum jar for 1 h. Polydimethylsiloxane (PDMS) was then cast, cured, and peeled off to prepare the microfluidic devices. The PDMS devices were treated with oxygen plasma under 50 sccm of  $\text{O}_2$  and 50 W for 30 s (Cute-MP, Femto Science, Korea) prior to the experiments. This treatment was performed to make the surfaces of the PDMS channel hydrophilic so that the solutions flowed along the channel easily and no bubbles were trapped.

**Experimental setup and data analysis.** An inverted fluorescence microscope (Ti-U, Nikon, Tokyo, Japan) equipped with a CCD camera (ORCA R2, Hamamatsu Photonics, Hamamatsu, Japan) and a 10 $\times$  lens was used to measure the fluorescence from the FITC and *E. coli*. For data analysis and image processing, Image J (NIH, Bethesda, MD, USA) and OriginPro 8 (OriginLab, Northampton, MA, USA) were used when necessary.

## Results and Discussion

**Generation of concentration gradients and culture chambers with ratchet structures.** Fig. 8–1A shows the microfluidic device consisting of a mixing channel network<sup>150</sup> and a test microchamber array. The device has 6 sets of control and test channels and each set has five cell-culture chambers in a column to minimize uncertainty in measuring fluorescent and optical signals from microbial biosensors. Fig. 8–1B shows a scanning electron microscope (SEM) image from Ch. 6. Each microchamber is connected to the main channel through ratchet structures that not only guide and accumulate motile microbes from the main channel but also prevent the trapped microbes from escaping to the main channel. In addition, the ratchet structures offer a chemostat-like culture environment for the microbes to grow in a continuous-feed mode that continuously supplies fresh nutrients and inducer molecules (HMI) from the main channel to the chambers and, at the same time, washes away secreted metabolites from the chamber to the main channel. These aspects were well characterized in our previous work<sup>151</sup>. To test the mixing channels, a solution with green food dye was loaded in the top-left reservoir ( $c_1$ ) whereas a solution with red food dye was applied in the top-right reservoir ( $c_2$ ). The solutions flowed along the mixing channels and mixed together, resulting in the generation of concentration gradients from Ch. 1 to Ch. 6. The control channels (Ch. 7) were

positioned in parallel with each test channel for direct comparison. Fig. 8–1C shows that each set of test and control chambers exhibited different colors. Therefore, we confirmed that the mixing channels generate concentration gradients, suggesting utility for high-throughput assays. The concentration gradients of HMI were indirectly characterized by application of a buffer solution with fluorescein (50  $\mu$ M FITC) and then quantified as shown in Fig. 8–1D. As designed and expected, each test channel showed different fluorescence intensities, corresponding to the following concentrations: 100% (50  $\mu$ M), 63 (31.5  $\mu$ M), 39 (19.5  $\mu$ M), 23 (11.5  $\mu$ M), 10 (5  $\mu$ M), 5 (2.5  $\mu$ M), and 0% (buffer only) from Ch. 1 through Ch. 7. Because HMIs are much smaller than FITC and thus have higher diffusivity than FITC, the concentrations of HMIs in the microfluidic device are likely the same as the quantified concentration of FITC.

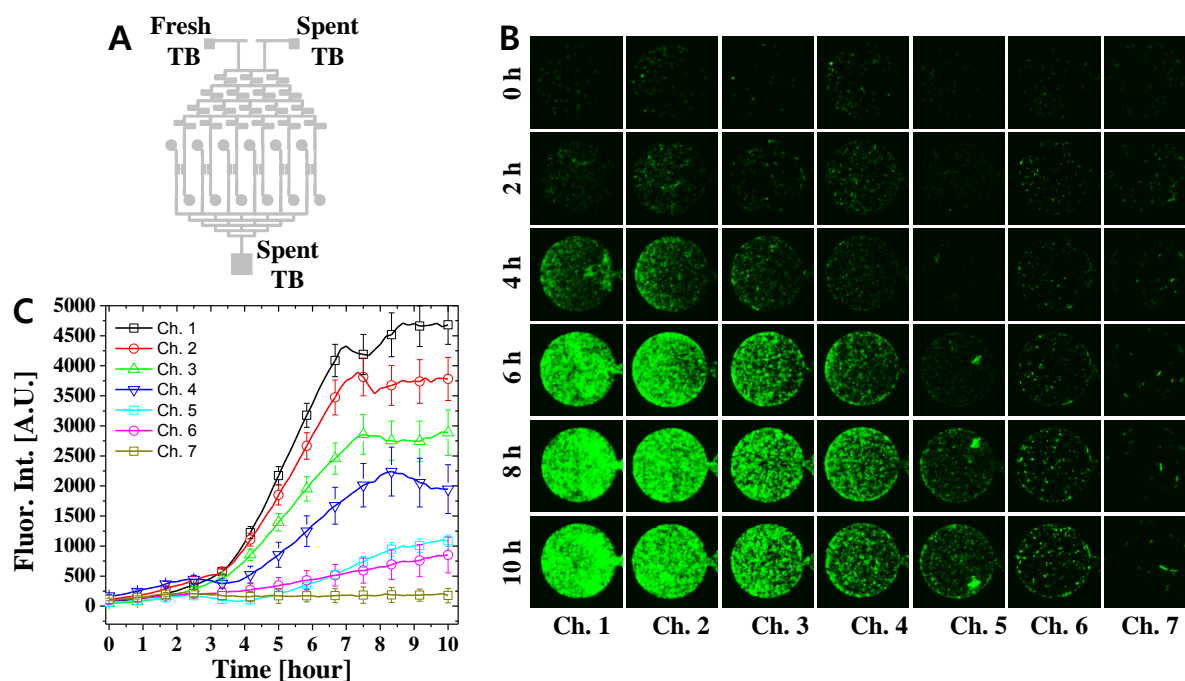


**Figure 8–2.** Bacterial cell growth (*E. coli*) in continuous-feed and batch modes. (A) A microimage showing experimental conditions in which concentration gradients of fresh TB media and spent TB media are produced at the same time from left to right and vice versa. (B) Fluorescent time-lapse images show cell growth in various nutrient-feeding conditions. Ch. 1 represents a continuous-feed mode (100% fresh TB), whereas Ch. 7 (control) represents a batch-type mode (100% spent TB). (C) Quantification of GFP signals of the cells in the chambers reveal various growth rates determined by the mixing ratios (concentrations) of the fresh and used TB.

**Bacterial cell growth in a chemostat-like culture environment.** We tested *E. coli* cell growth by using fresh and spent TB medium as shown in Fig. 8–2A to determine whether cellular growth was affected by continuous feeding generated using ratcheting structure. Because the microfluidic device can generate various concentration gradients as designed, a single experiment provided six different culture conditions plus a control on a chip. To determine whether cellular growth properly increases in

microchambers as nutrients are supplied, we monitored the growth of *E. coli* cells that constitutively express green fluorescent protein (GFP) using a fluorescent microscope, as shown in Fig. 8–2B. Fig. 8–2C shows the quantified fluorescence intensities corresponding to the cell growth results presented in Fig. 8–2B. At  $t = 0$  h, the number of fluorescent *E. coli* cells in each microchamber appeared to be unbiased. However, the fluorescence intensities, although they only indirectly represent the growth rate of the cells in each chamber, significantly changed over time in every chamber. For Ch. 1, in which 100% fresh medium was added (continuous feed mode), the fluorescent intensities showed an exponential increase between 3 h and 7 h, which is likely to be proportional to the increase in the number of fluorescent cells. In contrast, for Ch. 7, in which 100% spent TB medium was added (similar to the batch-type mode), the fluorescent intensities did not increase and remained almost constant over time. For other various intermediate conditions, the growth rates appeared to be precisely proportional to the nutrient gradients.

Even though fully grown fluorescent cells, after overnight incubation in a test tube, were injected into the device, we observed further cell growth in the microchambers as nutrients were supplied. Additionally, the fluorescent cells were not able to escape from the microchambers with the ratchet structures, but nutrients and metabolites could freely diffuse into and out of the microchambers. We confirmed that the chemostat-like cell culture environment dramatically increased the cell density on the chip, which in turn was helpful to improve the performance of microbial HMI detection compared to conventional cell culture environments such as test tubes and microplate instruments that only allow a batch-type culture environment. This remarkable rise of cell growth may play a key role in increasing the biosensing sensitivity because intense fluorescence signals were measured in response to target HMIs continuously delivered in the microchambers.

**Characterization of gene expression level to detect HMIs.** We employed two types of microbial whole-cell biosensors that harbored artificially engineered plasmids for detection of  $\text{Pb}^{2+}$  or  $\text{Cd}^{2+}$  in solution. The detection mechanism was based on the negative control of the GFP reporter gene mediated by CadC-type transcriptional repressors, which bind to  $\text{Pb}^{2+}$  or  $\text{Cd}^{2+}$  divalent ions and derepress the GFP reporter promoters. Two *cadC* transcriptional modules were cloned from the genome of *Bacillus oceanisediminis* 2691<sup>149</sup>. These microbial biosensors were integrated into the ratchet structure-integrated microfluidic device to provide a chemostat-like environment for improving the sensitivity of the sensors. We characterized the microbial biosensors HK621 for  $\text{Pb}^{2+}$  ions and HK622 for  $\text{Cd}^{2+}$  ions using the microfluidic device. HMI dissolved in TB medium (20  $\mu\text{M}$ ) was introduced to the left-top reservoirs and only TB media was introduced to the right-top and right-bottom control reservoirs. As shown in Figs. 8–3A, C, each microfluidic device was used for seven different detection experiments on a chip with various concentrations of  $\text{Pb}^{2+}$ . After five hours of cell culture, the fluorescent intensities showed a linear dependency on the concentration of the  $\text{Pb}^{2+}$  ion; a higher concentration was associated with stronger fluorescence intensity. After 10 h, the differences

among the normalized fluorescence intensities from Ch. 1 to Ch. 6 appeared to decrease. This effect was attributed to the continuous supplementation with  $\text{Pb}^{2+}$  ions, which activated microbial transcription to over-express the biosensor construct and trigger the accumulation of GFP within the cells. For  $\text{Cd}^{2+}$  ion detection, we found that the fluorescence intensities showed a nonlinear dependency on the concentration of  $\text{Cd}^{2+}$  as shown in Figs. 8–3B, D. The plasmid activity and cell growth appeared to be affected by high concentrations of  $\text{Cd}^{2+}$  in the solution. However, the continuous-feed culture enabled by the microfluidic device showed increased fluorescence intensity, especially with low concentrations of metal ions. It could therefore be speculated that  $\text{Cd}^{2+}$  ions gradually accumulate in cells up to a concentration sufficient to turn on the reporter gene without interfering with cellular growth. Therefore, the combination of the microfluidic device and the microbial biosensors improved the sensitivity and the dynamic range for HMI detection.

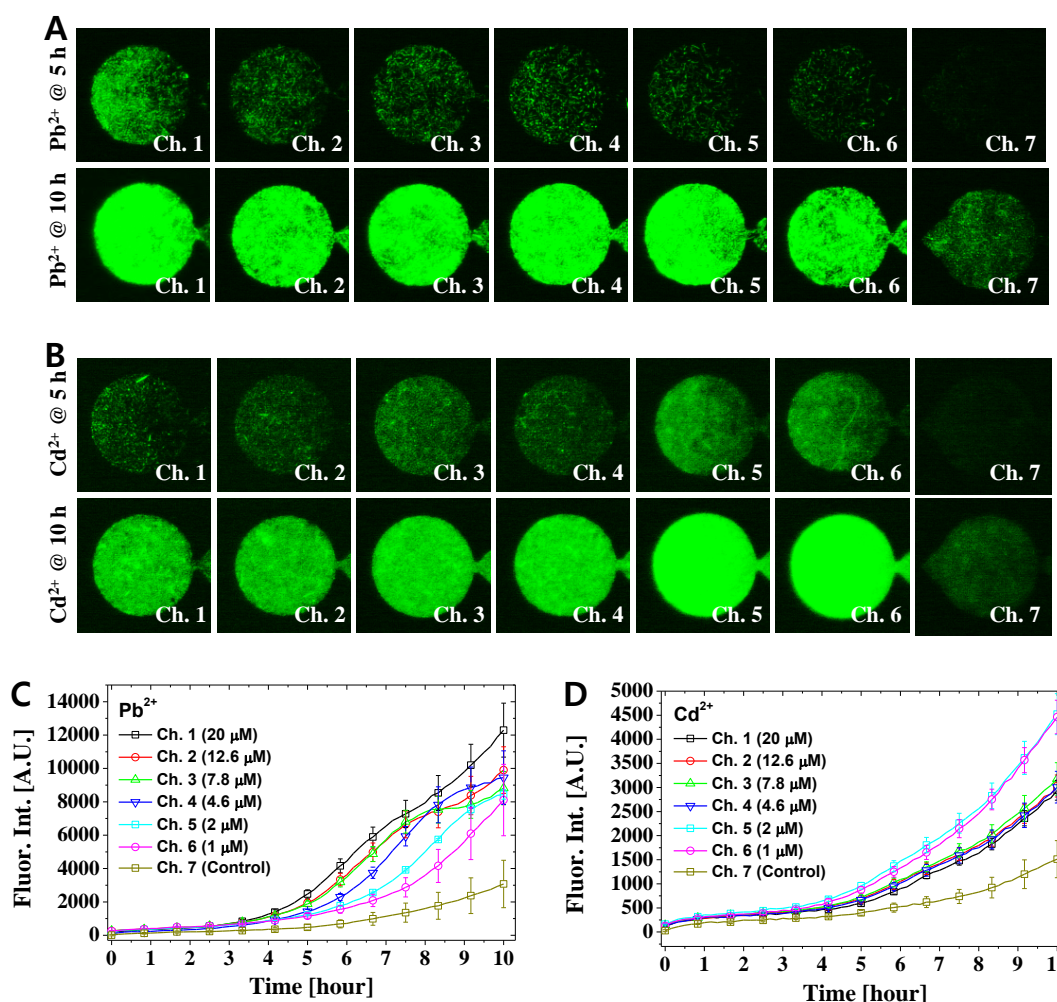


**Figure 8–3.** Detection of HMIs by the microfluidic device and the microbial biosensors. (A) and (C) Detection of  $\text{Pb}^{2+}$  ions using *E. coli* HK621 cells at various concentrations ranging from 20  $\mu\text{M}$  to 0  $\mu\text{M}$  (control). (B) and (D) Detection of  $\text{Cd}^{2+}$  ions using *E. coli* HK622 cells at various concentrations ranging from 20  $\mu\text{M}$  to 0  $\mu\text{M}$  (control). The fluorescent intensities depended on the concentrations of HMIs over time.

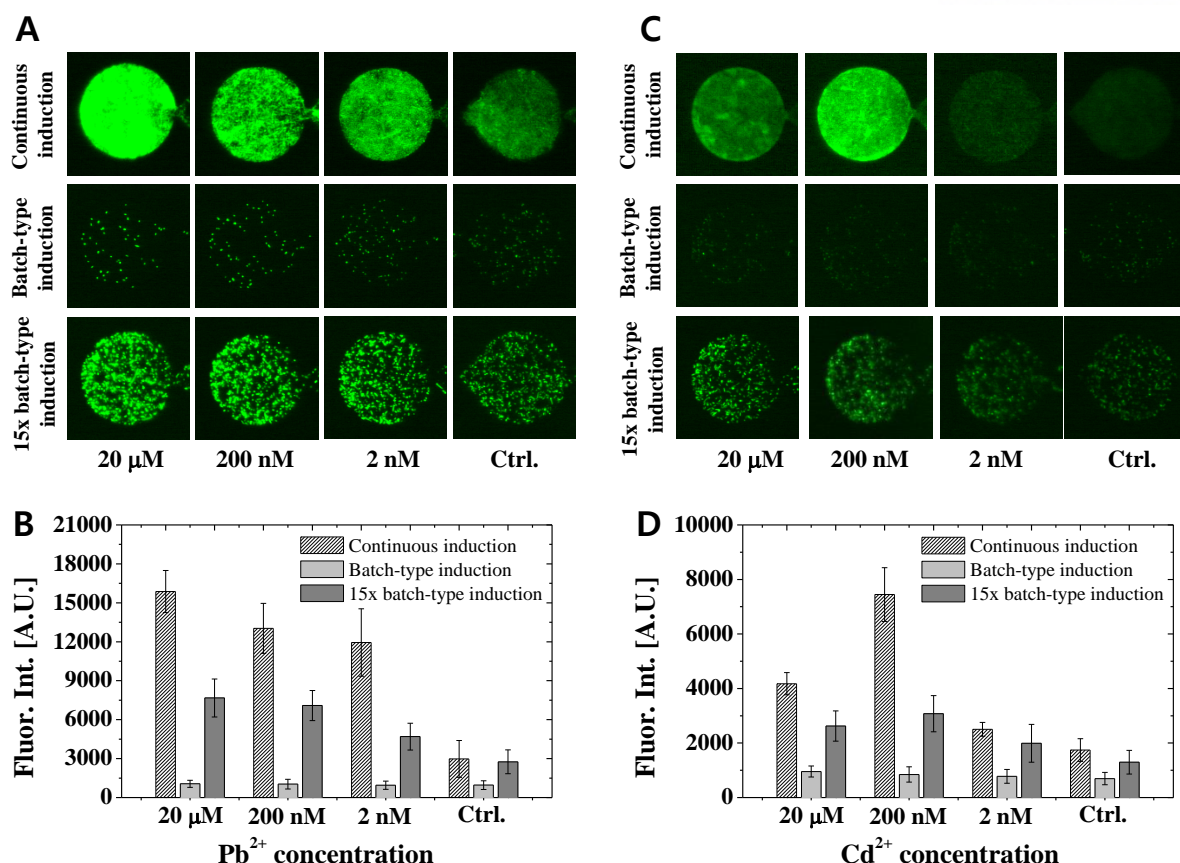


**Figure 8–4.** Comparison between continuous and batch-type induction of microbial biosensors. (A) and (B) Continuous and batch-type induction of *E. coli* HK621 cells in various concentrations of  $Pb^{2+}$  ions such as 20  $\mu M$ , 200 nM, 2 nM, and 0 nM as a control. In continuous induction, the microbial cells were grown and treated with inducer molecules ( $Pb^{2+}$  ions) in the chemostat-like microfluidic device for 10 h. The batch-type induction and 15x accumulated batch-type induction were performed in conventional batch-type culture tubes for 10 h, and then the induced microbial cells were loaded into the microfluidic device for immediate fluorescent measurements. The 15x concentration enhancement was achieved by using a centrifuge immediately before loading into the microfluidic device. (C) and (D) Induction of *E. coli* HK622 cells in various concentrations of  $Cd^{2+}$  ions. All fluorescence images were obtained under the same microscopic configurations.

**Comparison of continuous induction and batch-type induction for HMI detection.** The detection performance for HMIs using the microfluidic device was compared to that of the conventional detection method using batch culture under the same microscopic image acquisition conditions. First, we obtained the fluorescent intensities from the microbial biosensors for different concentrations of  $Pb^{2+}$  ions (20  $\mu M$ , 200 nM, and 2 nM; none as a negative control) after 10 h of incubation in the chemostat-like environment as shown in Figs. 8–4A, B. Because the device enabled continuous supplementation of nutrients and maintained  $Pb^{2+}$  ions in their initial state in the detection chamber, a signal increase of approximately 4–5 fold was obtained when compared with the control experiment (without HMI) even at low concentrations such as 200 nM and 2 nM. However, the batch-

type induction did not produce sufficient fluorescence signal to enable differentiation from the control signal because of the lower cell density and limited supplementation of  $\text{Pb}^{2+}$  ions. An alternative method of increasing the signal difference in the batch-type induction method was demonstrated by increasing the cell density by a factor of 15 using an external centrifuge as described in EXPERIMENTAL section. However, the fluorescence signals in the 15x batch-type induction were still much lower than those in continuous induction. Moreover, this method required an additional cell-concentrating step with increasing sample consumption and labor. Similar to the findings during  $\text{Pb}^{2+}$  detection,  $\text{Cd}^{2+}$  ions showed a higher signal-to-noise ratio in the continuous induction method than in the batch-induction method, as shown in Fig 8–4C, D. Therefore, the microbial biosensors with a continuous chemostat-like environment improved the sensitivity and dynamic range of the microbial biosensors by approximately three orders of magnitude compared to the conventional batch-induction method for detecting HMIs<sup>152</sup>. The enhanced performance can be attributed to the continuous expression of the engineered genes and the larger number of cells in the detection chamber. Even with a low concentration of HMI (e.g., 2 nM), the genes appeared to continuously activated over time by continuous supplementation and/or intracellular accumulation of the target HMI, resulting in over-expression of GFP in the cells<sup>153</sup>.

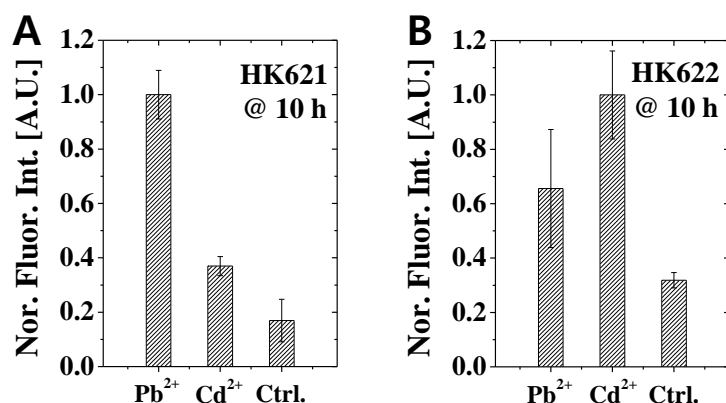


**Figure 8–5.** High-throughput characterization of the selectivity and cross-talk of the two microbial biosensor cells, HK621 and HK622, respectively, using the microfluidic device. (A) Induction of the HK621 biosensor in a solution containing both 20  $\mu\text{M}$   $\text{Pb}^{2+}$  and 20  $\mu\text{M}$   $\text{Cd}^{2+}$  ions after 10 h. (B) Induction of the HK622 biosensor in the same solution after 10 h. The fluorescence intensities measured under the same microscopic conditions were normalized by the maximum fluorescence intensity value.

**Characterization of the selectivity of the microbial biosensors.** The microfluidic device enables diverse characterizations of microbial biosensors in various HMI conditions. For example, to confirm the selectivity of the microbial biosensor, we tested each type of microbial cells with a non-target HMI; the microbial sensor cells that were designed for  $\text{Pb}^{2+}$  detection were exposed to a solution containing both 20  $\mu\text{M}$   $\text{Pb}^{2+}$  and 20  $\mu\text{M}$   $\text{Cd}^{2+}$  and vice versa. As described in Fig. 8–5, the microbial

biosensors showed the maximum fluorescent intensity in the target HMI conditions, indicating heavy metal selectivity. Although the results with the non-target HMI showed a low amount of fluorescence intensity caused by leaky expression or non-specific removal of the repressor on the *cadC* gene in the engineered microbes, the microfluidic device provides a quantitative platform with remarkable potential to characterize the whole-cell-based biosensing system in various HMI conditions with a considerably decreased response time and reduced sample consumption. We also note that the microfluidic device is simple and operated by only using static hydraulic heads, thus showing high potential as a portable biosensor.

### ***Conclusions***

We developed a microfluidic platform that consisted of a micromixer to generate concentration gradients of HMIs and a microchamber array with ratchet structures to concentrate and compartmentalize motile microbial whole-cell biosensors. The microfluidic platform provided a chemostat-like culture environment with the microbial biosensors such that an extremely high cell population (density) in each microchamber was achieved because the microbes grew well in a continuous feed mode. In addition, the culture environment enabled higher reporter gene expression in the microbes, enhancing the sensitivity and dynamic range by three to four orders of magnitude for detection of  $\text{Pb}^{2+}$  and  $\text{Cd}^{2+}$  when compared to conventional batch-type feeding and induction methods. This increase was achieved because the microfluidic platform not only provided fresh solutions containing nutrients and HMIs to the compartmentalized microbial biosensors but also simultaneously removed secreted metabolites. Notably, the total amount of the solutions used was much lower than that with other conventional methods (e.g., only 200  $\mu\text{L}$  was required for 6 experiments on a chip basis, compared to one sample in a 5 mL tube in conventional experiment). Moreover, the combination of the chemostat-like microfluidic platform and synthetic microbial biosensors offered remarkable advantages compared to conventional biosensors for detecting HMIs: 1) cost-effective and time-reduced detection without complex equipment, 2) flexibility for multiplex detection in a high-throughput manner, and 3) direct and convenient measurement without pre- or post-treatment of sample solutions.

## Chapter 9. Cracking-assisted Photolithography for Mixed-scale Patterning and Nanofluidics

### *Introduction*

Standard photolithography techniques produce various micropatterns but are limited to a feature size of approximately a micron<sup>154</sup>. To overcome this limitation, conventional nanolithography techniques such as electron-beam lithography and focused ion-beam are commonly employed<sup>155</sup>. Often, the standard photolithography and nanolithography techniques are used together to create mixed-scale patterns. However, the nanolithography and/or the combination of the two multi-scale lithography techniques show weaknesses in throughput and cost caused by the direct-writing-based nanofabrication processes and scale-up or scale-down lithography processes in-series<sup>155-156</sup>. Cracks as one of material failures have never been welcome in micro-/nanofabrication processes but active manipulation of cracking phenomena made it possible to produce various micro- and nanoscale patterns, showing remarkable potential for a novel unconventional patterning technique<sup>16-17, 157</sup>. However, the cracking-based micro- and nanopatterns show several weaknesses and limitations: only 1-D or limited 2-D patterns because of the direction of applied stresses<sup>16-17, 157a-c</sup> and the crystallinity of a substrate<sup>157e</sup>, respectively; the insufficient controllability of the geometric dimension (e.g. width, depth, and length) of cracks/patterns caused by the incapability of manipulating the stress strength<sup>16b, 157a, 157b, 157d-h</sup>; low success rates in patterning because of unwanted crack formation<sup>17, 157c, 157e</sup>; low throughput in fabrication because of sequential and multiple fabrication processes<sup>157e, 157h</sup>; incompatibility with other microfabrication processes<sup>16a, 157a, 157b, 157d</sup>; and low reproducibility by micromoulding and/or soft lithography<sup>157d-f</sup>. The most relevant alternatives for cracking-based patterning appear to partially or individually address the weaknesses and limitations<sup>16b, 17, 157c, 157e</sup>. Therefore, an innovative technique that can comprehensively and fully address all the weaknesses and overcome the crucial limitations is strongly required for the practical applications of crack-based patterns.

Here, we describe an innovative crack-assisted photolithography technique that utilizes a non-crystallized, monolithic, and organic material (e.g. SU-8 photoresist) for the first time and relies only on a standard photolithography process. This innovative technique can produce any desired nanopatterns on the surface of a micropatterned photoresist over large areas, with a high-throughput, and with no need for any specific nanofabrication techniques and equipment. Furthermore, the technique allows accurate control of the geometric dimensions of the nanopatterns, thereby resolving the limitations that previous cracking-based techniques were confronted by. As an example of practical application, we demonstrate a nanofluidic device with 1000 pairs of microchambers that are individually interconnected by a crack-assisted nanochannel; it appears to be impossible to produce the same nanofluidic device by using either the conventional or the unconventional fabrication

techniques because of throughput and controllability limits, respectively. However, the technique proposed in this work can produce such a complex nanofluidic device in single batch process with high reproducibility by soft lithography and with positioning of both the microchannels and nanochannels on the same surface, which is essential for a broad range of nanofluidic applications. Therefore, the “crack-photolithography” technique will provide an unprecedented nanofabrication technique for various nanopatterns and numerous nanofluidic applications.

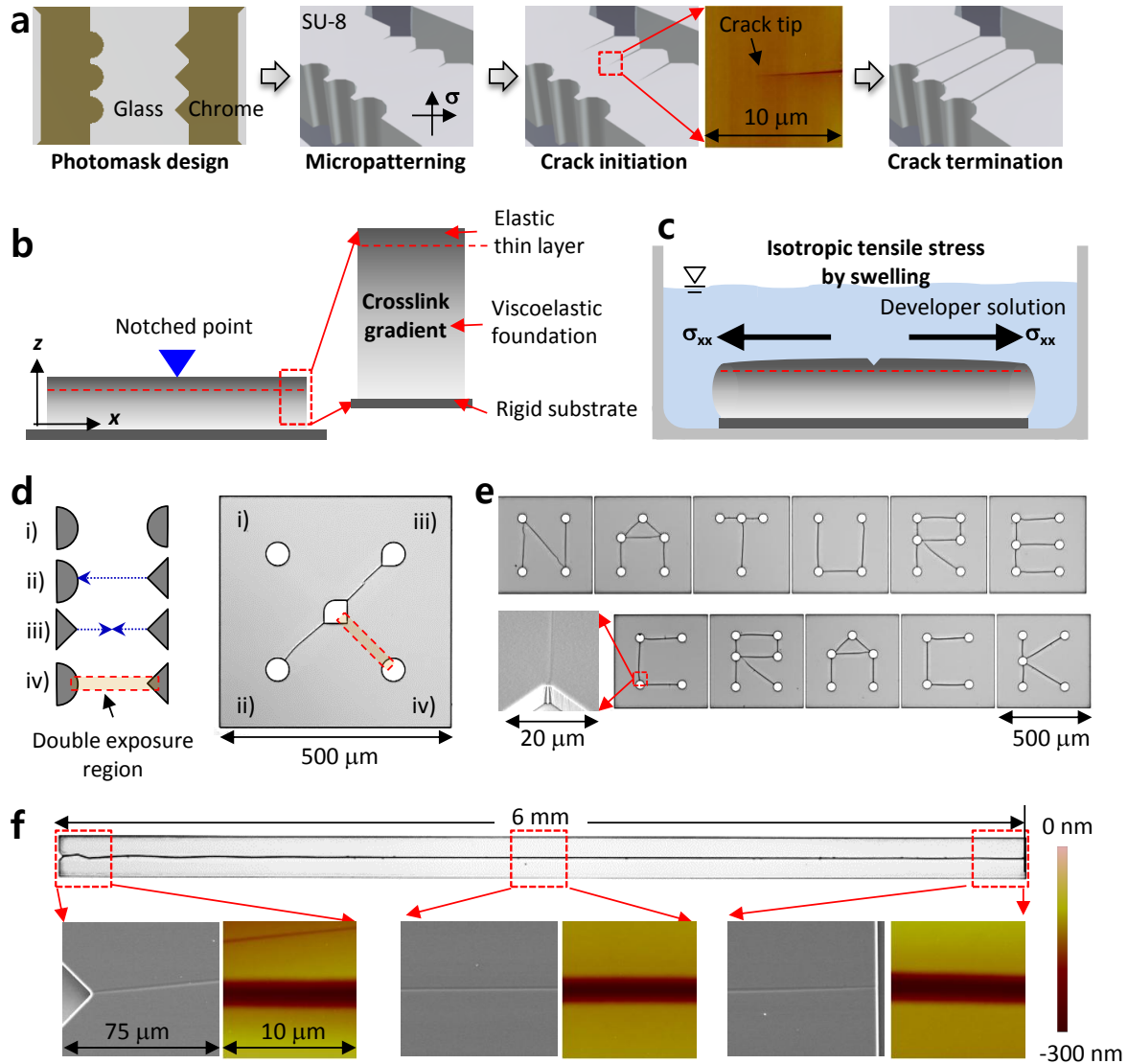


**Figure 9–1.** Cracking-assisted photolithography. a, Schematic diagram describing the process, from designing a photomask to fabricating nanopatterns on the surface of micropatterned photoresist. Cracking is initiated and terminated at the previously designed micro-notch structures. The inset is an AFM image showing a propagating crack tip. b, The UV-exposed photoresist consists of an elastic thin layer onto a viscoelastic layer on a silicon substrate and exhibits a gradient in cross-linking density along the direction normal to the substrate. c, The viscoelastic layer swells during the development process, causing the occurrence of tensile stresses in the elastic layer. This two-layered thin film in the presence of tensile stresses generates cracking at the notch, where stresses are more concentrated. d, The images reveal that not only the shapes of the micropatterns but also the exposure energy can be used to precisely control the initiation and termination of cracking. e, Controlling the

cracking mechanism permits the creation of various nanopatterns, including the words “NATURE” and “CRACK”, produced by connecting the nodes with cracking-assisted nanopatterns. f, SEM and AFM images of 6 mm long, 2  $\mu\text{m}$  wide and 170 nm deep straight nanopattern. The uniformity of the width and depth throughout the nanopattern is revealed.

### ***Methods and Materials***

**Crack-assisted photolithography process.** SU-8 (2010, MicroChem, USA) was spin-coated on a silicon wafer at 3000 rpm for 30 seconds to obtain a 10  $\mu\text{m}$  thick photoresist film. After soft-baking on a hotplate (95° C) for 3 minutes, the SU-8 was exposed to UV light using the first photomask and a mask aligner (MA6, Suss MicroTec, Germany). No optical filters were used in order to create a cross-linking gradient in the direction normal to the substrate. Then, the SU-8 was post-exposure baked on a hotplate (95° C) for 3 minutes before developing. For a single exposure (photomask) process, the SU-8 was maintained in fresh SU-8 developer solution (MicroChem, USA) for more time than required by the specifications, with the process time depending on the crack length and varying between 2.5 and 120 minutes. For a double exposure (photomask) process, the SU-8 was firstly developed for 2.5 minutes and then removed from the developer solution and rinsed thoroughly. Then, the SU-8 micropatterns were exposed again to UV light using the second photomask, baked as above, and developed for long as necessary. The first photomask was used to produce micropatterns with notch structures, while the second one was optionally used, not only to prevent unwanted cracking but also to guide precisely the crack propagation. Both photomasks were 7" soda-lime photomasks guaranteeing a minimum feature size of 5  $\mu\text{m}$  with 0.5  $\mu\text{m}$  tolerance and 2  $\mu\text{m}$  position accuracy.

**Replication of SU-8 pattern.** SU-8 micropatterns with cracking-assisted nanopatterns were replicated by using polyurethane acrylate (PUA, MINS-311RM, Minuta Tech., Osan, Korea) and polyethylene terephthalate (PET) film (Minuta Tech., Osan, Korea). The PUA solution was spin-coated at 1000 rpm and cured using a handy-type UV lamp (365 nm, 4W, UVL-21, Fisher Scientific Inc.) in a nitrogen environment for 2 min to minimise oxygen inhibition during photocuring. Both processed SU-8 pattern/mould and PUA are hydrophobic so that the micro-/nanogap of the SU-8 pattern was easily filled with PUA by surface adhesion/affinity<sup>166</sup>. Then the additional PUA solution was poured and covered by a PET film, followed by photocuring to make the two PUA layers monolithic. After being peeled off from the SU-8 master, the PUA patterns were again used as moulds for polydimethylsiloxane (PDMS, Sylgard 184 silicone elastomer kit, Dow Corning, USA) replica devices.

**Fabrication and handling of micro/nanofluidic device.** The roof-collapse problem of regular PDMS nanochannels on a glass substrate was resolved by using hard-PDMS (h-PDMS) with a relatively higher modulus ( $\sim 9 \text{ N mm}^{-2}$ ), which consists of VDT-731 (3.4 g, JSI Silicone, Seongnam, Korea), a Pt catalyst (18  $\mu\text{l}$ , JSI silicone, Seongnam, Korea), and 2,4,6,8-

tetramethyltetravinylcyclotetrasiloxane (4  $\mu\text{L}$ , Sigma-Aldrich, Korea)<sup>167</sup>. The h-PDMS was spin-coated at 1000 rpm on the PUA mould and cured in a hot oven (65  $^{\circ}\text{C}$ ) for 30 min. Then, additional regular PDMS was poured onto the h-PDMS-coated mould, followed by curing in a hot oven (65  $^{\circ}\text{C}$ ) for more than 4 hrs. It is noted that when a positive PUA mould was replicated with the h-PDMS, the h-PDMS precursor solution was well degased in a vacuum jar approximately for an hour to avoid bubble generation. In addition, air bubbles trapped between the PUA (bottom) and the h-PDMS (top) surfaces during soft lithography floated up and disappeared while the h-PDMS and regular PDMS cured. Subsequently, the h-PDMS surfaces and a glass substrate were treated with oxygen plasma under 50 sccm of  $\text{O}_2$  and 50 W for 30 s (Cute-MP, Femto Science, Korea) to make the surface hydrophilic and for strong irreversible bonding between them. Since the hybrid channel became hydrophilic, the micro-/nanochannels could be automatically filled with aqueous solution (e.g. water) by capillary forces as shown in Fig. 9–5f. The plasma treatment made the PDMS devices irreversibly bonded to the glass substrate, resulting in the tight seal of the micro-/nanochannels. The treatment also made all the channel surfaces hydrophilic so that aqueous solutions were flowed along the main microchannels easily and then toward the nanochannels. Air trapped in the nanochannels was easily eliminated by squeezing pressure driven by capillary forces and the high gas permeability of PDMS ( $5.2 \times 10^{-6} - 3.4 \times 10^{-5} \text{ cm}^2 \text{ s}^{-1}$ )<sup>168</sup>. As a result, no air bubbles were formed in the device.

**Experimental setup and data analysis.** A UV intensity meter (SUSS MicroTec, Germany) was used to measure the exposure energy during the photolithography process. The thickness of the SU-8 film was measured using a surface profiler (P-6, KLA Tencor, USA). AFM (D3100, Veeco, USA) and SEM (Quanta200, FEI, USA) were used for imaging and quantifying cracks. An inverted fluorescence microscope (Ti-U, Nikon, Japan) equipped with a charge-couple device (CCD) camera (ORCA R2, Hamamatsu Photonics, Japan) was used to obtain the optical microscopic and fluorescent images. FITC (Sigma-Aldrich, Korea) and fluorescently labelled microbeads (Invitrogen, USA) were used for visualising and quantifying mass transport through nanochannels. Two pairs of 0.25-mm-diameter platinum wires (Huntingdon, U.K.) were used as electrodes to apply electric potentials, which were generated and monitored via a source meter (Model No. 2635A, Keithley Instruments, USA). For data analysis and image processing, Image J (NIH, USA), and OriginPro 8 (OriginLab, USA) were used.

## ***Results and Discussion***

**Mechanism for creating cracking-assisted nanopatterns.** Fig. 9–1a shows a schematic diagram of the proposed nanofabrication process. Micropatterns with feature sizes of about 5  $\mu\text{m}$  are typically fabricated by using standard photolithography<sup>154</sup>, and using specific stress-concentrating and/or stress-releasing structures in conjunction, one can control the initiation, propagation, and termination of cracking to create the desired nanopatterns. For example, a sharp notch tends to concentrate stresses more effectively than a blunt one, and causes formation of cracks. In general, cracks are initiated

when a stiff and thin elastic layer placed on a viscoelastic underlying layer is subjected to tensile stresses higher than its fracture strength<sup>158</sup>. In the present work, the elastic and viscoelastic layers were formed by exposing the same spin-coated photoresist (10  $\mu\text{m}$  thick) to UV light without using the i-line filters recommended by the manufacturer to enable uniform cross-linking throughout the thickness<sup>159</sup>. This delicate process produced a relatively stiff and elastic layer onto a viscoelastic layer with a cross-linking gradient along the direction normal to the substrate, namely a silicon wafer (Fig. 9–1b). Tensile stresses occur naturally in the elastic layer during the development process, causing the viscoelastic layer to swell (Fig. 9–1c)<sup>160</sup>. When the coarsely cross-linked viscoelastic layer absorbs the solvent molecules, it swells isotropically, and consequently, the thin elastic layer above is subjected to an isotropic tensile stress. Once cracking is initiated, it keeps propagating until it reaches a termination structure, whereupon the concentrated stresses are finally released. Thus, a nanoscale crack is successfully created between the initiating notch and the termination structure, as planned during the design stage.

Cracking can be easily controlled either by the shape of the micropattern (decided during mask design), which determines the concentrated stress near notches or crack tips ( $\sigma_c$ ) or the amount of exposure energy (during fabrication), which influences material properties, including fracture strength ( $\sigma_f$ ). For example, in cases i) and iv) of Fig. 9–1d, cracking was not initiated because stresses were insufficiently concentrated, since the used structure had a rounded shape ( $\sigma_c < \sigma_f$ ) and, additionally, the high exposure energy caused a strong cross-linking in the photoresist, further increasing the fracture strength ( $\sigma_c < \sigma_f$ ). Conversely, in cases ii) and iii), cracks initiated and propagated in straight lines until terminated by a structure with a rounded shape or until in contact with other cracks. Additionally, we demonstrated that the cracking-assisted nanofabrication technique is capable of creating various nanopatterns with arbitrary trajectories, including words like “NATURE” and “CRACK” (Fig. 9–1e) or long, straight nanochannels (6  $\mu\text{m}$ ) with a uniform width (2  $\mu\text{m}$ ) and depth (170 nm) (Fig. 9–1f).

**Control of cracking for mixed-scale patterns.** We investigated the control of initiation, propagation, and termination of cracking by testing various stress-concentrating and stress-releasing microstructures. The experimental results are categorised into three cases: multiple cracks originating from acute notches ( $\theta_N < 90^\circ$ ,  $\sigma_c \gg \sigma_f$ ), single cracks originating from obtuse notches ( $90^\circ < \theta_N < 148^\circ$ ,  $\sigma_c > \sigma_f$ ), and no crack formation around circular notches ( $\theta_N > 148^\circ$ ,  $\sigma_c < \sigma_f$ ) (Fig. 9–2a). It is evident that the acute angles of the isosceles-triangle-shaped notch concentrate stresses more effectively than the obtuse ones. When concentrated stresses are higher than the fracture strength of the photoresist, cracking initiates and propagates until the concentrated stresses at the crack tip are comparable to or lower than the fracture strength. Fig. 9–2b shows that cracking can be initiated everywhere and its propagation trajectories may be oriented in any direction because of the

amorphous nature of the photoresist and the isotropic tensile stresses. Interestingly, crack tips are redirected and affected by the notch spacing and boundary conditions that are also important factors determining cracking behaviour.

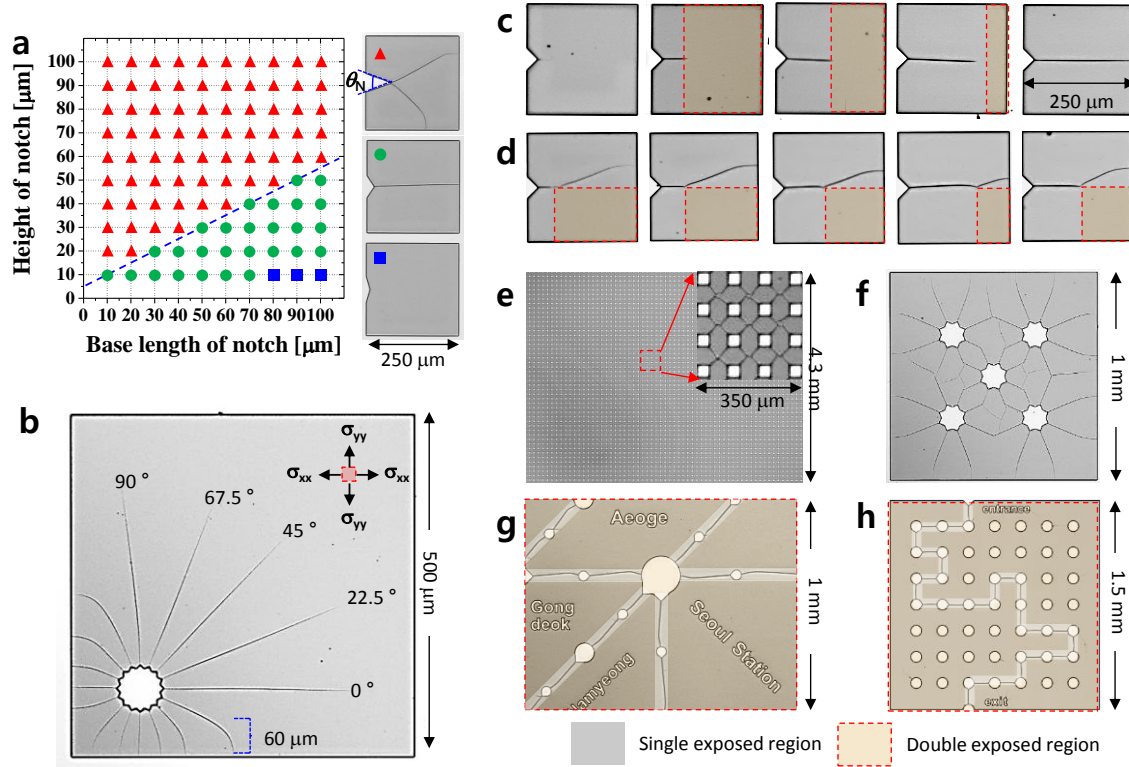


**Figure 9-2.** Control of cracking for nanopatterns with arbitrary trajectories. a, Effect of the notch shape on the initiation of cracking. Acute angles tend to initiate more than two cracks, while obtuse angles result in one crack. The blue dashed line indicates the critical angle (90°). The microscope images on the right show representative types of crack initiation. b, Isotropic propagation and redirection behaviour of crack tips. c, d, Prevention and termination of cracking by adjusting the exposure energy. The red dashed boxes indicate the double exposed areas in which no cracking is observed. e, f, The single exposure process allows production of complex, well-organised, and short nanopatterns ( $l_p < 1$  mm). g, h, The double exposure process allows production of precisely determined, long nanopatterns such as the Seoul subway map in which micropatterned stations are connected with cracking-assisted nanopatterns ( $l_p > 1$  mm). More than 400 stations and about 330 km long railway were miniaturised in an area of 4 cm<sup>2</sup>.

Fig. 9-2c shows that the exposure energy affects cracking because the local fracture strength of the double exposed region (ca. 250 mJ cm<sup>-2</sup>) is higher than that of the single one (ca. 125 mJ cm<sup>-2</sup>). Overall, there are three ways to stop the propagation of cracking: first, crack-terminating structures (local relaxation of  $\sigma_c$ ), second, spatially increased exposure energy (local enhancement of  $\sigma_f$ ), and last, removing the photoresist from the developer (throughout stress removal). The first two methods are useful to selectively terminate cracking, while the last one is used for the immediate termination of all propagating cracks. Also, a propagating crack tip can be redirected by forming spatially non-

uniform fracture strength which can be achieved by using different amounts of exposure energy, resulting in that the crack tip cannot propagate straight, instead detouring to the open boundary (Fig. 9–2d). It is worth noticing that single exposure is appropriate to generate complex but well-organised, short nanopatterns throughout micropatterns (propagation length,  $l_p < 1$  mm) (Figs. 9–2e,f), while double exposure allows selective and precise formation of long nanopatterns along the desired paths ( $l_p > 1$  mm) (Figs. 9–2g,h). This is because the single exposed photoresist is more vulnerable to molecular level defects that can act as notches to initiate unwanted cracking, whereas the double exposed photoresist enables the formation of cracking onto the single exposed region only, preventing the occurrence of unwanted cracking. All these characteristics allow the production of nanopatterns that could not be achieved using either conventional techniques showing low throughput and requiring high cost or unconventional techniques depending on a crystallised substance<sup>157e</sup> and/or applied anisotropic tensile stresses<sup>16–17, 157c</sup>.

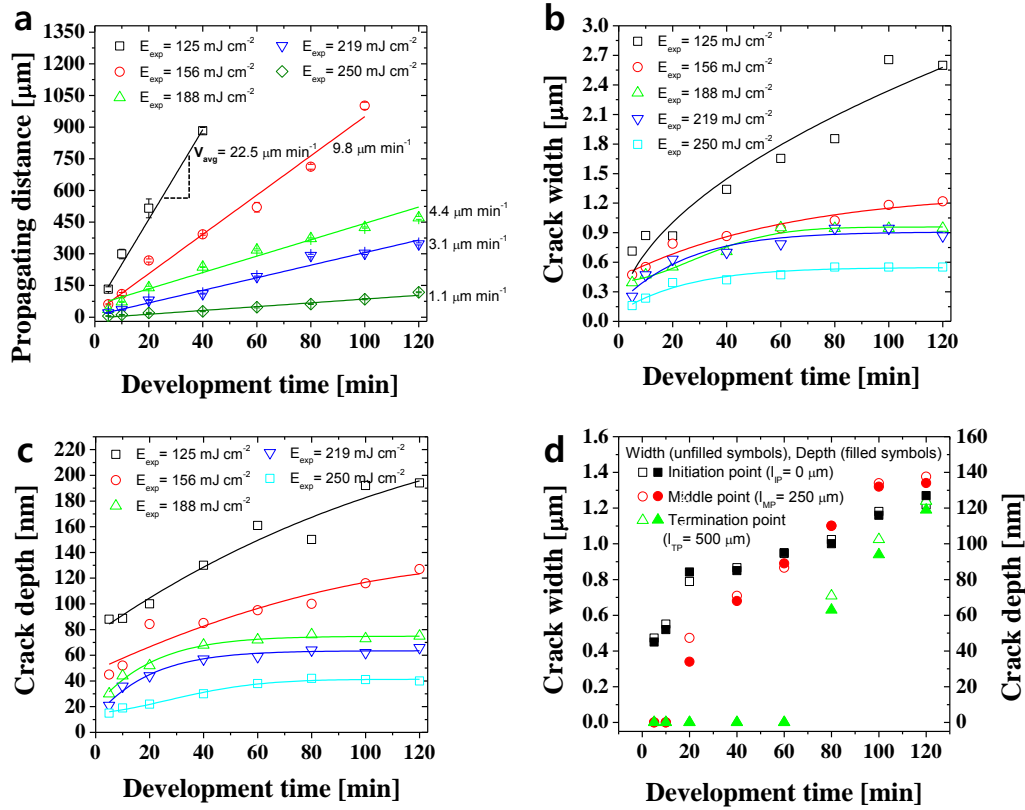


**Figure 9–3.** Characterisation of cracking behaviour and geometry of cracks. a, The propagation distances and velocities (slopes) were measured using microscope images of the cracks produced on single exposure photoresist micropatterns. The error bars correspond to the standard deviations of 10 different cracks on a single wafer. The measurement of the distances was limited to 1 mm to avoid the unwanted initiation of cracking. The data points are fitted using a linear approximation. b, c, Width and depth of the cracks. The data points are fitted using asymptotic functions ( $y = a + b \cdot c^x$ , where  $a$ ,  $b$  and  $c$  are constants). d, Width (unfilled symbols) to depth (filled symbols) ratio along the crack propagating direction. The width and depth of the cracks propagating for up to 500  $\mu\text{m}$  were measured as a function of the development time in three regions of interest, including the initiation point ( $l_{\text{IP}} = 0$

$\mu\text{m}$ ), a middle point ( $l_{\text{MP}} = 250 \mu\text{m}$ ), and a termination point ( $l_{\text{TP}} = 500 \mu\text{m}$ ), resulting in a ratio of 10. All the data were obtained from AFM images for high accuracy.

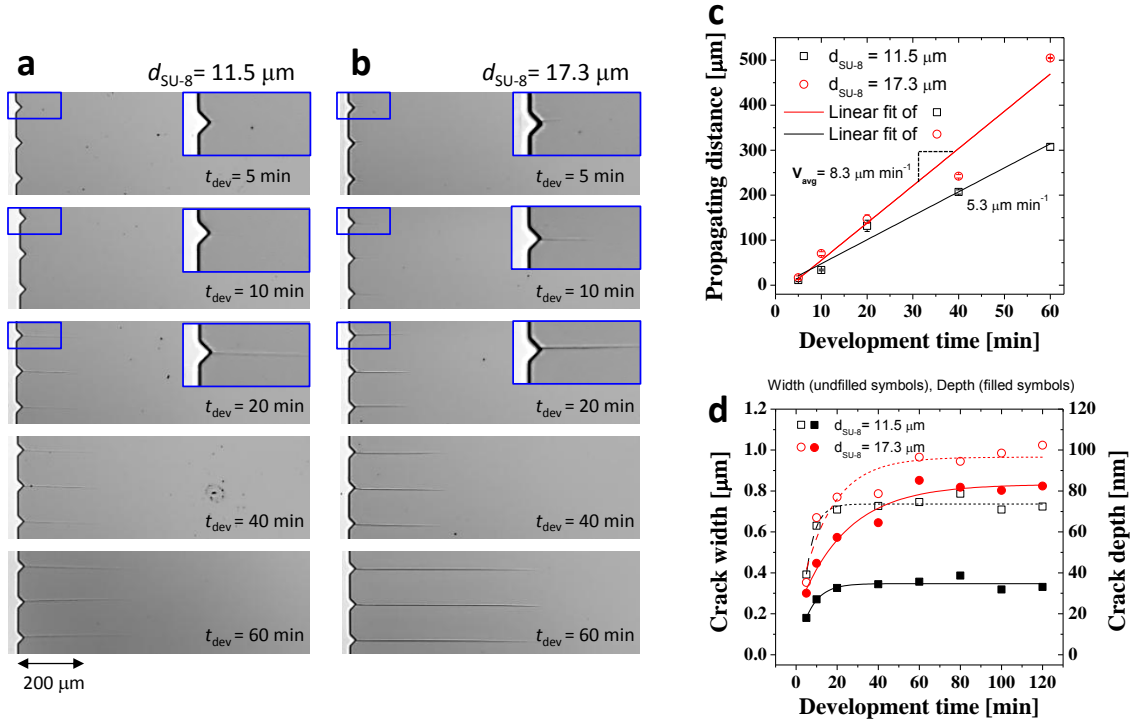


**Figure 9-4.** Effect of film thickness on cracking behaviour. a,b, Microscopic images of cracks created on the surface of micropatterned photoresist with film thicknesses ( $d_{\text{SU-8}}$ ) of  $11.5 \mu\text{m}$  and  $17.3 \mu\text{m}$ , respectively. c, Quantification of propagation distances and corresponding velocities. The linear guide lines were obtained by using a least-square method. d, Quantification of the width and depth of the cracks as a function of development time. The data points were fitted using asymptotic functions ( $y = a + b \cdot c^x$ , where  $a$ ,  $b$  and  $c$  are constants).

**Control of propagation velocity and crack dimension.** The cracking behaviour was characterised from the viewpoint of propagating distances/velocities and geometric dimensions of cracks under various photolithography conditions. First of all, the propagating distances are proportional to the development time and decrease with increasing exposure energy (Fig. 9-3a). This is because an increased exposure energy causes an increase of the material failure strength thanks to stronger cross-linking<sup>161</sup>. We note that the maximum crack length may not be limited but the UV expose time needs to increase to reduce the crack width and depth, resulting in the increase of development time. Therefore, the development time can be a limiting factor for long cracks. Surprisingly, the propagating velocities were substantially slower ( $1\text{--}22 \mu\text{m min}^{-1}$ ) than those reported in previous studies<sup>17-18, 157e</sup>, enabling us to precisely control the length of cracks. In addition, the width of the fully formed cracks varied between  $0.5 \mu\text{m}$  and  $2.7 \mu\text{m}$ , their depth between  $40 \text{ nm}$  and  $190 \text{ nm}$ . Both dimensions are inversely proportional to the exposure energy (Figs. 9-3b,c) because the volume expansion due to swelling decreases as the cross-linking density increases<sup>160</sup>. We also found that the

cracks tend to reach a constant width-to-depth ratio of about 10 (e.g. 130 nm deep and 1.3  $\mu\text{m}$  wide) (Fig. 9–3d). This means that the crack surface in the photoresist is suitable for the fabrication of uniform nanoslit structures commonly found in nanofluidic applications<sup>162</sup>. Furthermore, not unexpectedly, it is very important to investigate the effect of film thicknesses on cracking behaviour and crack dimension. As shown in Fig. 9–4, the thinner ( $d_{\text{SU-8}} = 11.5 \mu\text{m}$ ) film shows slower propagation velocities and smaller aspect ratios than the thicker one ( $d_{\text{SU-8}} = 17.3 \mu\text{m}$ ) under the same photolithography conditions. This can be attributed to the fact that the thinner film can be more densely cross-linked than the thicker film under the same exposure energy ( $E_{\text{exp}} = 188 \text{ mJ cm}^{-2}$ ). Additionally, the thicker (more coarsely cross-linked) film may cause stronger tensile stresses by absorbing more solvent molecules than the thinner film. In this context, it is noted that a wide range of aspect ratios of cracks can be obtained by manipulating different combinations of the film thickness and the exposure energy, showing high potential for producing various nanopatterns in conjunction with micropatterns simultaneously.

**Fabrication of master moulds for nanofluidics.** As an application of the proposed technique, we developed a nanofluidic device consisting of 1000 nanochannels (132 nm deep, 1.4  $\mu\text{m}$  wide and 200  $\mu\text{m}$  long), each one connecting two microchambers (Figs. 9–5a–f). The negatively patterned SU-8 mould was replicated using PUA for a positive mould, which in turn was replicated using PDMS. The success rate of the crack-assisted nanochannel fabrication was an astonishing 99.9%. It is worth noticing that an SU-8 mould can be used for several tens of PUA replications, and each PUA mould can be used for several hundreds of PDMS replications<sup>163</sup>. This shows the unique capability of the proposed technique to form nanopatterns with high-throughput over large-areas and to provide an extremely reproducible fabrication method for soft lithography<sup>164</sup>. Using the PDMS replica devices, we demonstrated that the transport of fluorescein isothiocyanate (FITC) is freely diffused from one microchamber to the opposite one, although 1  $\mu\text{m}$  fluorescent particles could not penetrate the nanochannel (Fig. 9–5g). This is very important because accurate control of the transport of small molecules in nanofluidic devices is crucial for various biological and physicochemical assays and applications<sup>165</sup>. An applied electric potential was also used to test the rapid electrokinetic migration of FITC, and we demonstrated that the nanochannel was very robust and reliable even under oscillating electric potentials (Figs. 9–5h,i). Because of the high hydraulic resistance of the nanochannel, pressure-driven flow was negligible, thus demonstrating that the nanochannel could not only play a key role in nanofluidic devices but also replace nanoporous membranes widely used in micro- and nanofluidic devices<sup>165b</sup>. Given that a nanochannel array can be easily integrated with other microfluidic components on the same layer, single-layered, membrane-free micro- and nanofluidic devices may potentially be developed using cracking-assisted photolithography.

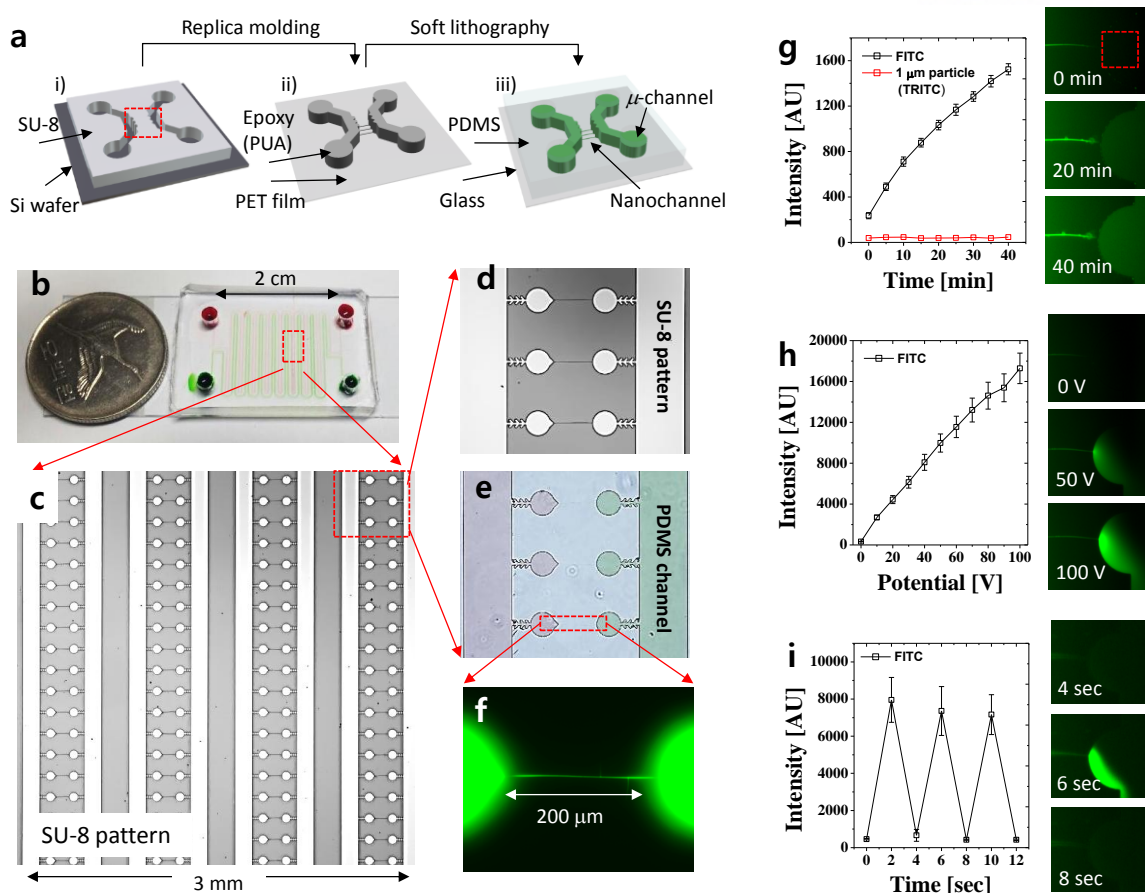


**Figure 9-5.** Nanofluidic application of cracking-assisted nanopatterns. a, Fabrication processes: negative micropatterns with cracks are replicated with PUA for a positive mould, which is in turn replicated with PDMS for a single-layered, nanochannel-integrated nanofluidic device. b, The nanofluidic device has 1000 pairs of microchambers connected through nanochannels for the transport of small molecules. c, Microscope image of an SU-8 mould. d, Details of micropatterns for chambers and cracks for nanochannels. e, Microscope image of a PDMS replica device filled with solutions of green (right) and red (left) dyes. f, Fluorescent image showing mass transport by diffusion from left to right along a nanochannel. g–i, Quantitative and qualitative characterisation of mass transport: transient diffusion, electrokinetic migration, and oscillatory control of the migration of small molecules by electric potentials throughout a nanochannel. The average values and error bars were obtained from triplicate experiments.

## Conclusions

The proposed technique appears to be the simplest and most controllable methodology among the fabrication techniques based on materials failure<sup>162</sup> and presents many advantages such as cost reduction, time optimization, suitability for large areas, and simultaneous production of micropatterns and nanopatterns. In addition, the technique affords: a wide range of nanochannel dimensions, with depths varying between 40 and 190 nm, widths between 0.5 and 2.7  $\mu\text{m}$ , and lengths between 10 and 10000  $\mu\text{m}$ ; perfect compatibility with conventional photolithography without any need for additional nanolithography processes and equipment; and practical applications such as mixed-scale master

moulds for micro- and nanofluidic devices. Furthermore, the technique can be distinguished from the most relevant alternatives<sup>16b, 17, 157c, 157e</sup> from the view point of perfect 2-D nanopatterning; accurately manipulated isotropic stresses; simultaneous micro-/nanopatterning in a monolithic material; complete suppression of unwanted cracking; whole and complete controllability of crack dimension, termination and redirection; and a versatile experimental platform for studying the fundamental physics and mechanics of materials failure<sup>158b</sup>. Hence, the proposed “crack-photolithography” will not only open new opportunities for advancement of nanopatterning technologies but also revolutionize the development of novel micro- and nanofluidic devices.

## Chapter 9. Crack-photolithography for Membrane-free Diffusion-based

### Micro/nanofluidic Devices

#### *Introduction*

Spatiotemporal control of biomolecular transport in micro/nanofluidic systems has resulted in increasingly sophisticated and massively parallelized bioassays on a chip<sup>169</sup>. These small but highly integrated fluidic networks enable more accurate and faster bioassays than conventional bioprocesses using bench-top equipment because fluidic motions of a microdomain are well-ordered (have a low Reynolds number) and adapt rapidly to a given environment because the volume is small. Physicochemical microenvironments (e.g., temperature and concentration) for cellular or biomolecular assays can be engineered to meet the demands of end users by simply controlling fluid flows. Generally, convective (laminar flow)<sup>35b, 170</sup> and/or diffusive<sup>56-57, 127b</sup> transport is employed for accurate transport control in most microfluidic devices. The convection-flow-based microfluidic devices rapidly change extracellular chemical environments by switching flow streams in a programmed manner. However, shear stress induced by viscous flows often limits applicable cell types to only adhesive cells<sup>35b, 170a</sup> because flows can damage cells and sweep away cell-secreted biomolecules and even cells. Therefore, diffusion-based microfluidic devices are preferred for non-adhesive or swimming cells such as *Escherichia coli* (*E. coli*) to avoid shear stress-induced damages<sup>34</sup> and provide compartmentalized cellular environments for long-term observation.

In general, nanoporous membranes or hydrogels have been integrated with microfluidic devices as diffusion-permitting and convection-preventing structures. For example, a nanoporous membrane made of polyethylene or polycarbonate was sandwiched between top and bottom polydimethylsiloxane (PDMS) microchannels and functioned as a diffusion layer to minimize the convective transport of biomolecules<sup>12, 39c, 171</sup>. As an alternative, agarose and alginate hydrogels were also sandwiched between two PDMS layers to incorporate a nonporous membrane<sup>13, 62</sup>. Instead of the sandwich-type fabrication methods, hydrogels, nanomaterials, and nanobeads were directly loaded into multi-level microchannels using the capillary effect, resulting in the formation of a plug-shaped nanoporous microstructure<sup>56, 172</sup>. These membrane-integrated microfluidic devices minimize unwanted convective flow but allow the required diffusion on a chip. However, they seem to have inherent weaknesses: 1) fluid leakage (requiring a skillful bonding technique), 2) somewhat large fabrication-to-fabrication variation, 3) interference with microscopic observation due to opaque membranes, 4) degradability and deformability of nanoporous structures during long-term experiments, and 5) low throughput in fabrication.

For these reasons, a nanochannel array was suggested as an alternative to overcome the aforementioned limitations because that nanochannel array can accurately control the mass transport of small molecules *via* diffusion by controlling nanochannel dimensions and numbers. However, it has

been difficult to fabricate such a nanochannel array using conventional nanofabrication techniques that utilize high-energy beam sources<sup>173</sup> such as electron, ion, or laser beams because of the fabrication cost, time, and throughput. In particular, the high cost and low throughput issues become more critical when both the microfabrication and the nanofabrication techniques need to be used in series to create mixed-scale micro/nanofluidic devices. Therefore, an innovative fabrication technique can be a breakthrough to address not only the current weaknesses of the membrane-integrated microfluidic devices but also the conventional nanofabrication techniques. As a promising candidate, our group has developed the so-called ‘crack-photolithography’ technique that enables the simultaneous fabrication of mixed-scale micro-nanopatterns by using nanoscale cracking phenomena (nanofabrication) during the standard photolithography process (microfabrication) in a cost-, time-, and throughput-effective manner<sup>174</sup>. In addition, the crack-photolithography technique not only produces a dimension-controllable nanochannel array at any position without limitations in patterning direction but also provides perfect integration compatibility with microchannel networks from the designing step. Furthermore, a number of mixed-scale master molds for soft lithography are easily fabricated in a single batch-fabrication process up to a wafer scale (e.g., 6 inches) so that the technique seems to be most suitable for replicating novel mixed-scale micro/nanofluidic devices.

In this work, we adapted the crack-photolithography technique for the first time to develop single-layered, membrane-free, and diffusion-based micro/nanofluidic devices and then demonstrated that a nanochannel array functions successfully as a membrane for accurate control of mass transport. First, we optimized the fabrication parameters of the crack-photolithography to be suitable for controlling the transport of small molecules by increasing the critical crack dimension (height) to several hundred nanometers. Then, we characterized the geometrical uniformity of nanocracks (a nanochannel array) in various configurations of microchambers and the rate of diffusion by adjusting their number (control of transport rate) and length (control of transport timing). As an application of such a membrane-free micro/nanofluidic device, we performed genetic induction assays with synthetic bacterial cells. Because the genetic induction experiments require chemically well-controlled diffusion environments, we attempted to apply the devices for high-throughput and versatile analyses of gene expression of synthetic bacterial cells under various induction conditions including direct exposure to different inducer concentrations and neighboring to inducer-secreting cells and exposure to two inducers with concentration gradients.

## ***Methods and Materials***

**Reagents and materials.** A Sylgard 184 silicone elastomer kit (Dow Corning, Midland, MI, USA) was used for PDMS soft lithography. A polyurethane acrylate (PUA) solution, MINS-311RM, and a polyethylene terephthalate (PET) film (Minuta Tech., Osan, Gyeonggi, Korea) were used for replication of the SU-8 master. Fluorescein isothiocyanate (FITC, Sigma-Aldrich, Yongin, Gyeonggi,

Korea) was dissolved in phosphate buffered saline (PBS, Sigma-Aldrich, Yongin, Gyeonggi, Korea) and used for visualizing and quantifying mass transport through nanochannels.

**Crack-photolithography for simultaneous micro-/nanopatterning.** A negative photoresist, SU-8 (SU-8 2010, MicroChem, Newton, MA, USA), was employed for micropatterning and the crack-photolithography process using two photomasks (Microimage, Ansan, Gyeonggi, Korea). The first photomask was used to generate SU-8 micropatterns including crack initiation and termination patterns, while the second photomask was used to selectively strengthen the SU-8 for the complete suppression of unwanted cracking. The detailed crack-photolithography process is described in our previous work<sup>174</sup>. Briefly, SU-8 was spin-coated on an Si wafer of 10- $\mu\text{m}$  thickness, followed by soft baking on a hotplate (95 °C) for 3 min. Then, the SU-8 film was UV-exposed under the first photomask using a mask aligner (MA6, Suss MicroTec AG, Schleissheimer, Garching, Germany) without any UV filters that cut off the light of wavelengths shorter than 350 nm. The short wavelength contributes to making the top side of the SU-8 stiffer than the bottom side, consequently resulting in a crosslinking gradient being formed in the direction of the thickness. The UV-exposure energy (110  $\text{mJ}/\text{cm}^2$ ) used in this work was reduced slightly to make relatively larger cracks than the standard protocol (125  $\text{mJ}/\text{cm}^2$ ) provided by the manufacturer and our previous work. After post-exposure baking (PEB) on a hotplate (95 °C) for 3 min, the SU-8 film was developed for 2 min to fabricate microchannels; no nanopatterns were created. The SU-8 film was additionally UV-exposed under the second photomask, followed by the second PEB. The relatively insufficient exposure energy in the first exposure process may cause weak material properties such as adhesion problems of the SU-8. However, most regions were further strengthened during the second UV treatment. Thus, no delamination and adhesion problems were observed. Lastly, the SU-8 film was additionally developed for a relatively longer period of time than the standard development time to generate the necessary nanocracks. Cracking occurred only in single-UV-exposed regions; no cracking was allowed in double-UV-exposed regions. We have comprehensively characterized the UV exposure energy and development time governing the dimensions and propagating speed of nanocracks in our previous work<sup>174</sup>, determining that nanochannels of various dimensions could be obtained in a controllable manner.

**Preparation of bacterial cells.** We used recombinant *E. coli* MG1655, a motile bacterial strain, to characterize engineered genetic circuits of the intercellular plasmids by using various induction environments. The MG1655 strain was transformed with plasmid k084012 and named ‘sender’ cells (SCs) in this work because this plasmid produces an inducer molecule, acyl homoserine lactones (AHL)<sup>150</sup>. In parallel, the same strain was transformed with plasmid t9002 and named ‘receiver’ cells (RCs) because RCs express green fluorescent proteins (GFPs) when they receive and then are activated by AHL<sup>172c</sup>. For a dual induction study, the same strain was transformed with plasmid

pZBRG producing both red fluorescent proteins (RFPs) and GFPs in the presence of 40 mM arabinose and 10  $\mu$ M tetracycline as inducer molecules for RFP and GFP expression<sup>175</sup>, respectively. The same culture and preparation protocols as those used in our previous protocols<sup>56, 176</sup> were used for the bacterial cells. A single colony grown on a Luria Broth (LB) agar plate was inoculated in 5 ml of M9 medium (Sigma-Aldrich, Yongin, Gyeonggi, Korea) with 1% glucose and 1% tryptone (TB, Sigma-Aldrich, Yongin, Gyeonggi, Korea) for preparation of the SC and RC. Then, the colony was incubated overnight in a rotary shaker (200 rpm, 36 °C), resulting in the OD<sub>600</sub> value marked 0.4. For the pZBRG cells, the cells were incubated in 1% LB media until the OD<sub>600</sub> value marked 1.0. We note that all the cells were carefully handled and incubated with antibiotics such as ampicillin (for the SCs and RCs) and chloramphenicol (for the pZBRG cells) to protect against contamination.

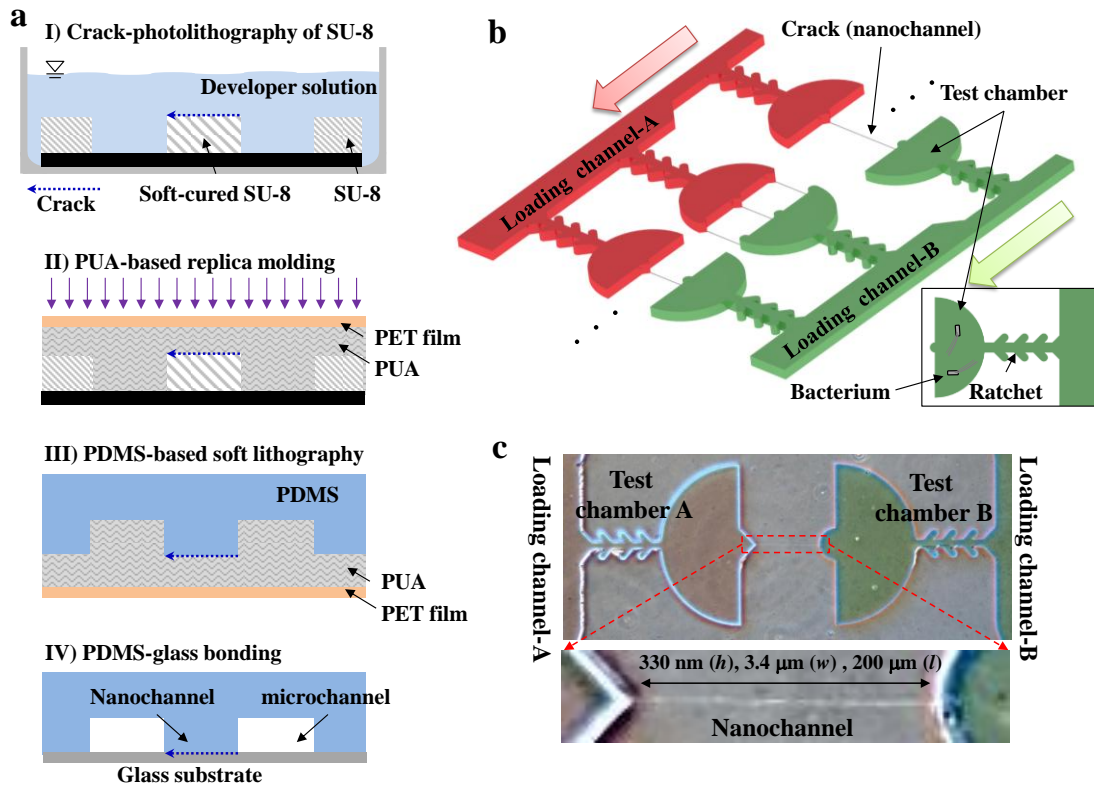


**Figure 10–1.** Fabrication processes of crack-photolithography for a diffusion-based micro/nanofluidic device. a, Schematic illustrations show how to generate nanocracks (I, standard photolithography). The nanocracks are produced only at pre-designed cracking points on soft-cured SU-8 micropatterns. Then, the negative micropattern (microchannel) and nanocrack (nanochannel) are demolded into a positive PUA mold (II, PUA-molding). Subsequently, the micro-/nanopatterned PUA mold is replicated with PDMS (III, soft lithography). Finally, the PDMS replica is bonded to a glass substrate. b, A micro/nanofluidic channel network for accurate diffusion control using nanochannels. Test chambers beside the loading channels A and B are connected with each other through nanochannels, of which the number and length are designed and fabricated differently. All the test chambers employed an arrowhead-shaped ratchet structure to guide the motile bacteria into the chambers. c, Microscopic images showing a micro/nanofluidic device with channels filled with food dyes.

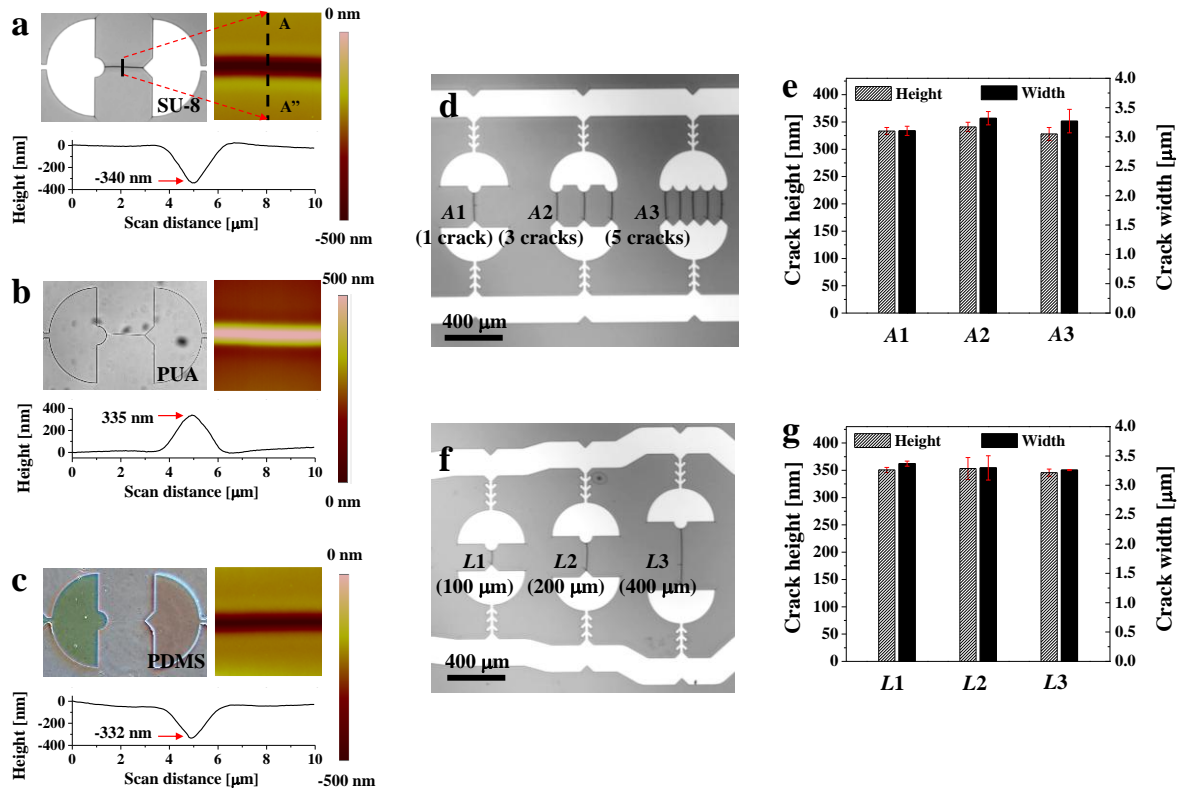


**Figure 10–2.** Surface morphology and dimension analysis of nanocracks during the replication processes. a, b, c, Microscopic and AFM images of SU-8, PUA, and PDMS micro-/nanopatterns (nanochannels). The surface profiles show the width and height of each nanopattern. d, e, Microscopic image of PDMS micro-/nanopatterns and their quantified uniformity. Three micro-nanopatterns with the different number of cracks indicated with A1, A2, and A3 showing a high degree of uniformity in width and height. f, g, Microscopic image of PDMS micro-/nanopatterns with different lengths such as 100, 200 and 400 μm show a high degree of uniformity in height and width.

**Experimental setup and data analysis.** A UV intensity meter (SUSS MicroTec AG, Schleissheimer, Garching, Germany) was used to measure the exposure energy during the photolithography process. The thickness of the SU-8 film was measured using a surface profiler (P-6, KLA Tencor, Milpitas, CA, USA). AFM (D3100, Veeco Instruments, Plainview, NY, USA) was used for imaging and quantifying crack dimensions. A handy-type UV lamp (365 nm, 4 W, UVL-21, Thermo Fisher Scientific, Inc., USA) was used for curing PUA solutions. Oxygen plasma equipment (Cute-MP, Femto Science, Hwseong, Gyeonggi, Korea) was used under 50 sccm of oxygen and 70 W for 10 s for bonding a PDMS channel and a glass substrate. An inverted fluorescence microscope (Ti-U, Nikon, Minato-ku, Tokyo, Japan) equipped with a charge-coupled device (CCD) camera (ORCA R2, Hamamatsu Photonics, Hamamatsu, Shizuoka, Japan) was used to obtain the optical microscopic and fluorescent images. All microscopic images were processed and quantified by using Image J (NIH, Bethesda, MD, USA) and OriginPro 8 (OriginLab, Wheeling, IL, USA).

## Results and Discussion

**Fabrication of mixed-scale micro/nanofluidic devices.** Fig. 10–1a illustrates the overall standard microfabrication processes to fabricate mixed-scale micro/nanofluidic devices. First, SU-8 micropatterns including crack-initiation and termination patterns are fabricated using the standard photolithography process. Because the crack-initiation and termination patterns create nanopatterns as designed during the developing process, micropatterns and nanopatterns are obtained simultaneously without any nanofabrication techniques. This unconventional mixed-scale fabrication technique is the so-called crack-photolithography (I). Then, the micro-/nanopatterns are replicated by using a PUA solution and a PET film (II). A PUA solution with relatively lower viscosity (168 cP) was chosen to facilitate the replication of the SU-8 molds for PDMS-based soft lithography because the selected PUA showed high durability at room temperature and even after a hundred replications. This durability can be attributed to the high Young’s modulus of the PUA (300~1500 MPa)<sup>177</sup>. The PUA solution is poured and then covered by the PET film, followed by solidification of the PUA using a UV lamp in a custom-made nitrogen chamber (3 cm (*h*) × 15 cm (*w*) × 15 cm (*l*)) for 2 min. The oxygen-free inert environment minimizes oxygen inhibition during the photocuring of the PUA solution<sup>178</sup>, ensuring the perfect replication of the micro-/nanoscale SU-8 molds without significant volume reduction. After being peeled from the SU-8 molds, the PUA patterns are again used as molds for PDMS-based soft lithography (III). Then, the PDMS nanochannel (*h* = approximately 330 nm) is additionally incubated in a 160 °C oven overnight to increase the Young’s modulus of the PDMS, which helps alleviate the roof-collapse problem<sup>179</sup>. We recommend the use of h-PDMS for the thinner PDMS nanochannels than 300 nm<sup>167</sup>. Otherwise, the roof-collapse problem may not be resolved easily. Subsequently, the PDMS surface and a glass substrate are treated with oxygen plasma to make the surface hydrophilic and for strong irreversible bonding between them (IV).

Figs. 10–1b shows the mixed-scale micro/nanofluidic device that consists of two separated microchannels, which are named ‘loading channel-A’ and ‘loading channel-B’ and used to individually introduce cells and chemical solutions without cross contamination and a crack (nanochannel) array, which connects each pair of microchambers with various spacing distances (nanochannel lengths) and different numbers. The test chambers employed a ratchet microstructure to not only guide motile bacterial cells in the loading channel into the test chamber but also to prevent the trapped cells from escaping from the test chamber. The mechanisms and functions of the ratchet microstructure have been studied intensively in our previous work<sup>150, 176</sup>. Therefore, the trapped cells can be isolated physically from the loading channel and continuously incubated by providing nutrients from the loading channel to the test chamber through the ratchet microstructure. At the same time, it is possible to flow a solution containing inducers along the other loading channel without any interference with the cell loading. Fig. 10–1c shows a pair of microchambers in a PDMS replica device, which are filled with red and green food dyes. The two microchambers are connected with a nanochannel approximately 330 nm deep, 3.4 μm wide and 200 μm long. We need to consider the

tradeoff strategies in engineering the nanochannel dimensions because the nanochannel should be small enough to keep convection flow negligible and large enough to secure the necessary rate of diffusion. Generally, a proper characteristic length of nanochannel for bacterial assays in microfluidic devices is regarded to be approximately several hundred nanometers<sup>148</sup> because the critical dimension can compartmentalize bacterial cells that are approximately 2  $\mu\text{m}$  long and 1  $\mu\text{m}$  thick with continuous supplements of chemicals. In addition the convective flow driven by a pressure gradient seems to be negligible because of the high hydraulic resistance of the nanochannel. Notably, the nanoslit-like crack produced by the crack-photolithography seems to be advantageous for the higher rate of diffusion than a nanochannel with a square cross-section. Basically, the nanoslit array used in this work has a cross-sectional area that is approximately 10 times larger than the cross-sectional area of a rectangular nanochannel (330 nm wide and 330 nm deep).

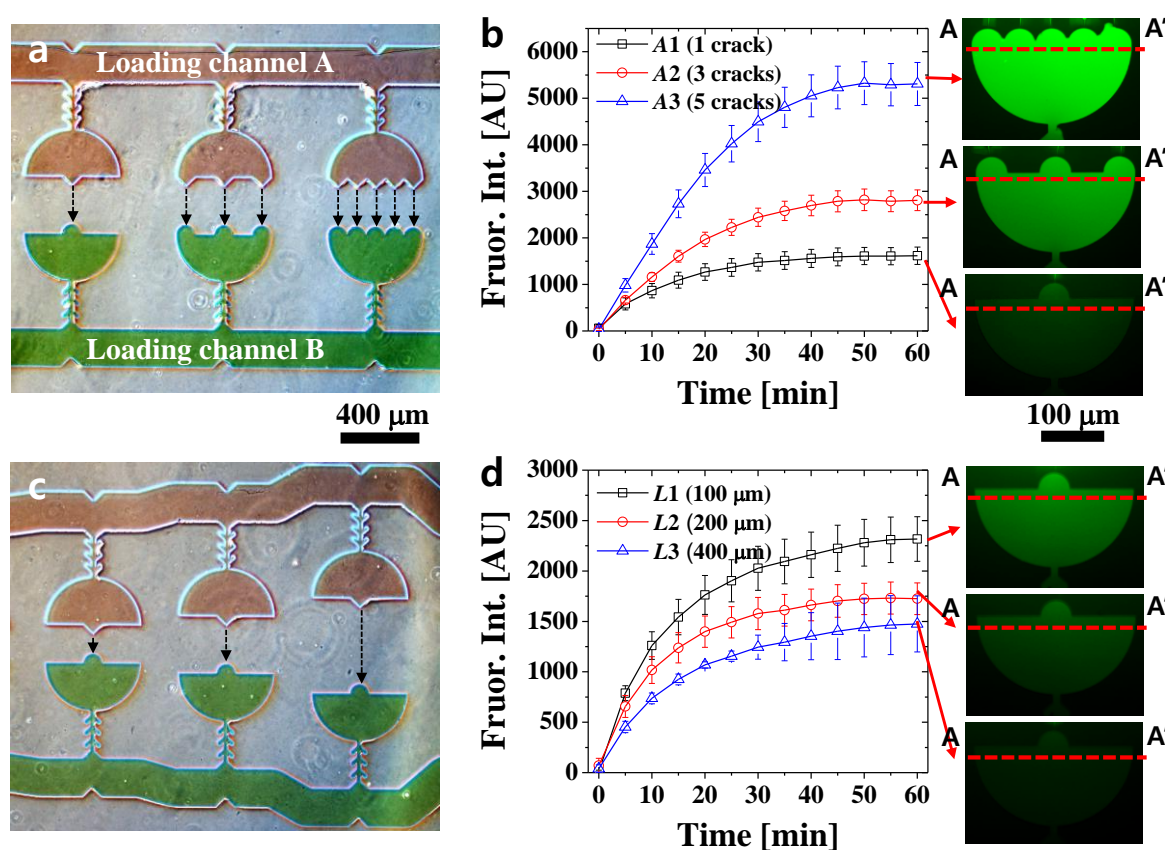


**Figure 10-3.** Visualization and characterization of the rate of diffusion through nanochannel arrays. a, c, Microscopic images show micro/nanofluidic PDMS devices used to characterize the rate of diffusion in case of the different numbers and lengths of nanochannel arrays. b, d, Graphs show the quantified rate of diffusion of 100  $\mu\text{M}$  FITC dye passing across the A–A' dashed line that is located at the interface between the nanochannel array and the microchamber.

**Characterization of nanocrack dimension during the replication processes.** As briefly mentioned previously, for the accurate transport control of small molecules through a nanochannel array, the surface morphology and dimension of nanocracks should be well controlled and optimized.

Using the relationship between the UV-exposure dose and crack dimensions characterized in our previous work, we fabricated nanocracks and analyzed their surface morphology and dimension by using the AFM images shown in Fig. 10–2. The negative SU-8 micro-/nanopatterns were fabricated (Fig. 10–2a) and then replicated into the positive PUA patterns *via* the replicate molding process (Fig. 10–2b). The micro-/nanopatterns in the SU-8 were well conserved after the peeling-off process because of the high Young’s modulus of SU-8 (60 MPa) and low surface energy of the PUA (23 dyn/cm)<sup>177</sup>, meaning that a SU-8 master can replicate PUA patterns over multiple times, approximately a few tens of replication. The Young’s modulus of the PUA (40 MPa) is as much high as that of the SU-8, so that the micro-/nanopattern in the PUA was transferred into the PDMS device repeatedly *via* soft lithography (Fig. 10–2c). Given that a PUA mold can be used for several hundred times of replications<sup>177</sup>, a SU-8 mold produces the PDMS device almost infinitely without changing in shapes and dimensions. The surface profile data show that the nanocrack is like a nanoslit with an aspect ratio of approximately 10 (e.g., 3.4  $\mu\text{m}$  to 340 nm in SU-8). The PDMS replica shows 2% reduced channel height compared to the SU-8. The variation in the height appeared during the successive replication processes of which the PUA and PDMS undergo phase transition from liquid precursors to solid substrate, apparently negligible. In addition, we note that the replication processes show several advantages over the standard photolithography processes. First, the replication processes guarantee the same geometry of the nanochannel without fabrication-to-fabrication variation. Second, the replication processes do not require specialized facilities such as a yellow room and a mask aligner. Third, the replication is much cheaper and simpler to repeat than the photolithography process in a cleanroom.

To further characterize the dimensions of nanochannels, we fabricated two types of PDMS replica devices that consist of microchambers and nanochannels. The first device has three pairs of identical microchambers connected with different numbers of nanochannels as shown in Fig. 10–2d ( $A1 = 1$  crack,  $A2 = 3$  cracks and  $A3 = 5$  cracks). Similarly, the second device has three pairs of identical microchambers, which are connected with different lengths of nanochannels as shown in Fig. 10–2f (100  $\mu\text{m}$ , 200  $\mu\text{m}$ , and 400  $\mu\text{m}$ ). The measured width and height of the nanochannels were almost identical regardless of the crack numbers produced, which was demonstrated in triplicate characterizations using three different crack samples in a wafer (Fig. 10–2e). In addition, the cracking dimensions were confirmed not to depend on the length of the cracks (Fig. 10–2 g). Therefore, we can conclude that the crack-photolithography technique and the replication processes guarantee highly uniform nanochannel arrays, indicating that the rate of diffusion through nanochannel arrays can be controlled directly by regulating the dimension and number of cracks (cross-sectional area for diffusion), although the maximal crack length and crack number in a confined area seem to be limited by the crack-photolithography process<sup>174</sup>.

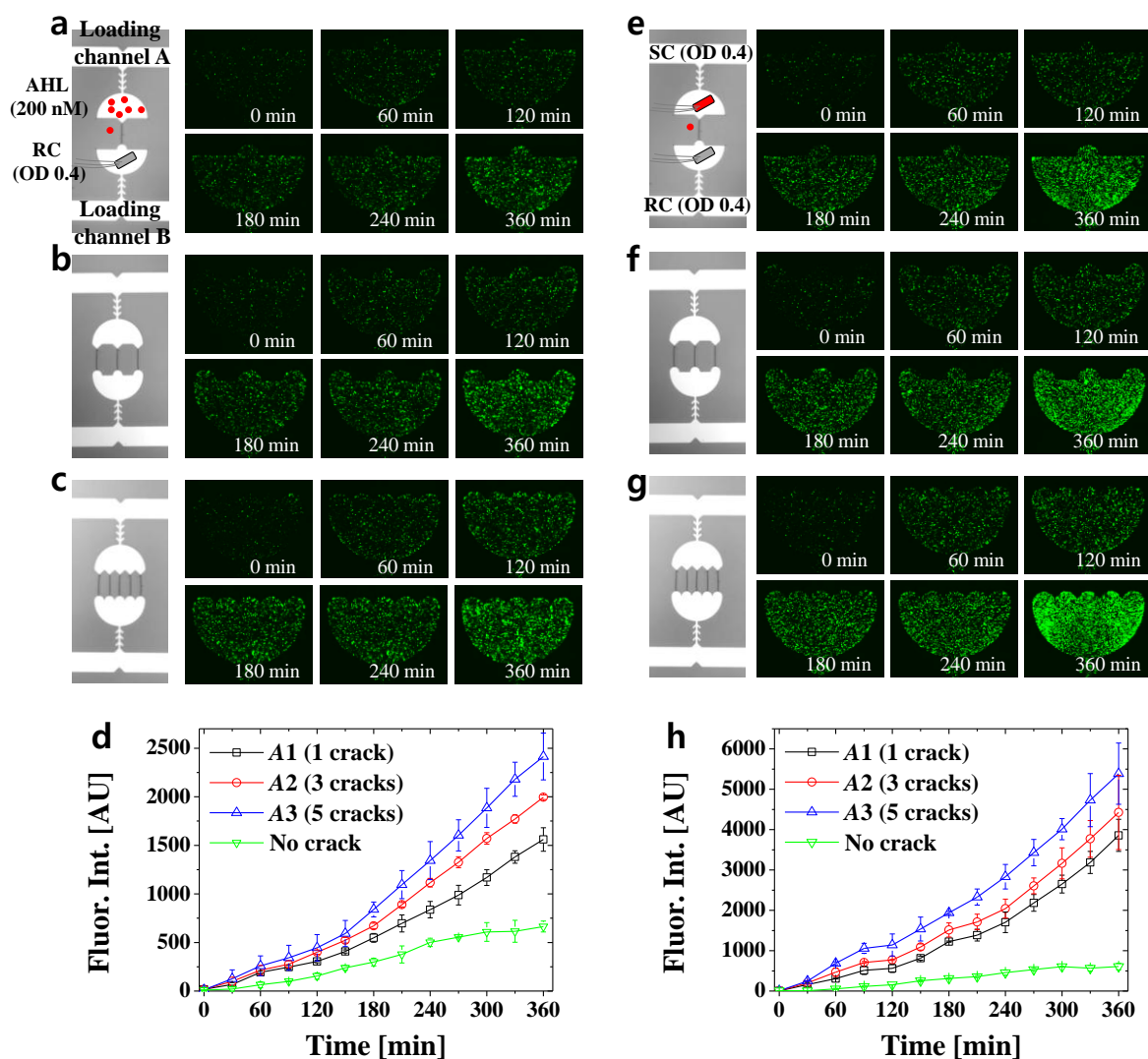


**Figure 10-4.** Application of the diffusion-based micro/nanofluidic device to genetic induction assays of synthetic bacterial cells. a–c, Fluorescent time-lapse images show GFP expression levels of the RCs induced by AHL that are transported from loading channel-A to loading channel-B through the nanochannel arrays: a (one nanochannel), b (three nanochannels) and c (five nanochannels) as shown in left microscopic images. d, Quantification results of the fluorescent intensities in a–c and those of a control experiment in the absence of a nanochannel array (No crack). e–g, Fluorescent time-lapse images show GFP expression levels of the RCs induced by the neighboring SCs in the loading channel-A. AHLs are secreted by the SC and then transported to the RCs in the loading channel-B through the nanochannel arrays. h, Quantification results of the fluorescent intensities in e–g and those of a control experiment in the absence of a nanochannel array (no crack).

**Quantification of the rate of diffusion through a nanochannel array.** We visualized and characterized the rate of diffusion in various configurations of microchannels and a nanochannel array. As shown in Fig. 10-3a, the loading channels A and B that were filled with red and green food dyes were physically separated from each other but interconnected with a nanochannel array where the transport of small molecules occurs. The food dye solutions were continuously flushed, but no

noticeable convective mixing was observed over time because the very high hydraulic resistance of the nanochannel array hindered convection flows. For quantitative measurements of the rate of diffusion, we introduced 100  $\mu\text{M}$  FITC molecules dissolved in a PBS solution to loading channel-A and a pure PBS buffer to loading channel-B. The concentration difference of the FITC between the two loading channels drives diffusion transport through nanochannels; the diffusion transport can be quantified by measuring fluorescent intensities along the A–A' line over time. As shown in Fig. 10–3b, all the fluorescent intensities were saturated in 40 min and almost linearly proportional to the number of cracks, demonstrating that the rate of diffusion can be linearly controlled by adjusting the number of nanochannels that determine the cross-sectional area ( $A$ ) in Fick's law ( $J = -DA\nabla c \approx DA\Delta c(\Delta L)^{-1}$ , where  $J$  is the rate of diffusion,  $D$  is the diffusion coefficient, and  $c$  is the concentration).

In the same manner, we characterized the effects of the nanochannel length ( $L$ ) on the rate of diffusion as shown in Fig. 10–3c and d. As the nanochannel length increases, the rate of diffusion decreases because the concentration gradient becomes milder. This result also follows Fick's law. Therefore, we came to the conclusion that adjusting the nanochannel number is more straightforward than changing the nanochannel length because the former is based on a linear control, while the latter is based on a nonlinear control. In addition, for the latter case, the concentrations at the boundaries may be affected by the nanochannel length, varying over time. Furthermore, absorption of small molecules at the surface of the PDMS channel<sup>180</sup> can become significant by increasing the nanochannel length and may reduce the effective concentrations of samples. For this reason, we fixed the nanochannel length at 200  $\mu\text{m}$  and adjusted the nanochannel number for precise control of the rate of diffusion between two neighboring microchambers, which were used for diffusion-based genetic induction assays.

**Diffusion-based genetic induction assay of bacterial cells.** As an application of the membrane-free and diffusion-controllable microfluidic device, we performed genetic induction experiments with synthetic bacterial cells. As shown in microscopic images in Fig. 10–4 a–c, GFP expression levels of the RCs were quantified for three different induction conditions. The RCs were trapped into the test chamber by loading a cell suspension solution ( $\text{OD}_{600} = 0.4$ ) into the empty loading channel-B by a capillary flow in a few minutes without trapped bubbles. The remaining cells in the channel were then flushed with a fresh medium. Subsequently, a PBS buffer solution containing 200 nM AHL was loaded into loading channel-A to maintain the concentration constant. Right after AHL was flown, fluorescent intensities (GFP) from the RCs in the test chambers were measured every hour and observed to increase gradually over time. As expected, the fluorescent intensities became stronger as the number of nanochannels increased (one in Fig. 10–4a, two in Fig. 10–4b, and three in Fig. 10–4c), indicating that the rate of diffusion of the AHL is proportional to the number of nanochannels, resulting in high GFP production by the RCs. Fig. 10–4d shows quantified fluorescent intensities from

the time-lapse fluorescent images, supporting the precise control of the diffusion transport of AHL by the number of nanochannels. Therefore, the rate of diffusion of small molecules through nanochannels can be manipulated in an even easier and simpler manner compared to conventional membranes. The RCs are known to be very sensitive to the concentration of AHL (1 nM) in expressing GFP<sup>181</sup>, and even in the absence of nanochannels (no AHL diffusion), fluorescent intensities were measured and were attributed to the leaky expression<sup>182</sup>. Obviously, no bacterial cells were observed to pass through the nanochannel array.

As another induction experiment, the SCs and the RCs were introduced to loading channels A and B, respectively and then co-cultured over time without cross contaminations; the cells were physically separated but chemically connected with each other via the nanochannel array. Physically isolated but chemically connected cellular environments seem to be very important because many bacterial species use a quorum sensing mechanism to regulate gene expression according to the concentration of the signaling molecules<sup>183</sup>. As shown in Fig. 10–4 e–h, the SC and RC were introduced with the same cell density ( $OD_{600} = 0.4$ ), and the GFP signals gradually increased over time for every nanochannel configuration. The increased GFP expression was caused mainly by both cell growth and genetic induction. The effect of cell growth seems to be almost equal in every case because a cell-culturing chamber employed a ratcheting microstructure that can prevent bacterial cells escaping from the test chambers and allow for continuous supplements of nutrients<sup>176</sup>. The GFP expression due to the genetic induction varied with the nanochannel numbers. From this experiment, we confirmed that the nanochannel array manipulates the net rate of diffusion of AHL precisely. Furthermore, because the microchambers with the ratchet structure function as a chemostat-like bioreactor and the nanochannel array substitutes for nanoporous membranes, the micro/nanofluidic device developed in this work could facilitate various cell-to-cell communication assays on a chip, thereby showing many advantages over conventional batch-type assays<sup>176</sup>. Recently, precise characterization of synthetically engineered genetic circuits in bacterial cells has been an intriguing research field because it is important to understand fundamental metabolic and genetic regulation mechanisms for better and increased production of useful bio-refineries<sup>184</sup>.

**High-throughput induction assay with concentration gradients of two inducers.** One of the major advantages of the crack-photolithography is that any functional microfluidic elements such as pumps, valves, and mixers can easily be integrated with the nanochannel arrays without limitations in the numbers and positions. For example, as shown in Fig. 10–5a and b, we integrated a Christmas-tree-like micromixer in the loading channel-A (blue color) with the cell culture chambers and nanochannel arrays in the loading channel-B (gray color). For the dual induction assay, we loaded 40 mM arabinose into the left reservoir and 10  $\mu$ M tetracycline into the right reservoir for the generation of linear concentration gradients of the two inducers. As a result, the left-most channel (Ch. 1) contained 100% arabinose and no tetracycline, while the right-most channel (Ch. 6) contained 100%

tetracycline and no arabinose, thereby showing two extreme cases. Because similar micromixer designs have frequently been used in our previous work protocols<sup>176</sup>, the concentration gradients were not repeatedly characterized in this work. However, the cells in Ch. 1 and those in Ch. 6 were confirmed to express only RFP and GFP, respectively, as shown in Fig. 10–5c. For the intermediate conditions from Ch. 2 to Ch. 5, the expression of RFP and GFP appeared to be simultaneous, and the expression levels were proportional to the concentration of each inducer. Therefore, arabinose and tetracycline were demonstrated to induce each promoter in a selective manner without significant crosstalk because the plasmid can be tightly regulated by the inducer concentrations given<sup>175</sup>.

In addition, the normalized expression levels of both GFP and RFP exhibited similar time-dependent behaviors as shown in the quantitative results in Fig. 10–5d and e. For example, remarkable increases in the fluorescent intensity appeared 2 hours after the initial loading, and then, the signals approached a plateau in 4 hours. The delay of the gene expressions may be attributed to the lag-phase of bacterial growth, which is basically required for adapting to a new chemical environment. After 4 hours, not only did the initially loaded bacterial cells ( $OD_{600} = 1.0$ ) fully fill the test chamber (100  $\mu\text{m}$  in diameter) without a remaining space for further cell proliferation, but most of the bacterial cells also produced as many fluorescent proteins as they could. Thus, the fluorescent signals seem to be fully saturated. In the high-throughput experiment, the proposed membrane-free microfluidic device showed superior compatibility with other microfluidic elements. In addition, the parallelized genetic induction assay with different chemical environments could be further expanded by increasing the channel numbers with a proper design of microchannels and nanochannels. Notably, crack-photolithography does not require additional time and cost to fabricate the nanochannel array with the micropatterns.

It is worthwhile to discuss the advantages of the diffusion-based micro/nanofluidic devices fabricated by using the crack-photolithography over the conventional, membrane-based microfluidic devices. First, the devices proposed in this work are even less sensitive to a pressure difference between the two loading microchannels, so that the effect of convention flows seems to be substantially eliminated. Additionally, the rate of diffusion of the small molecules is linearly controlled by the number of nanochannels, resulting in more accurate analyses. However, the conventional membrane-based devices are difficult to control the rate of diffusion accurately because commercial nanoporous membranes have pre-determined pore sizes and limited membrane thicknesses. Second, the device can easily be integrated with other microfluidic components from the early designing step. However, it does not seem to be easy to incorporate other microfluidic components with most membrane-based devices (e.g., interference with integrated membranes). Lastly, the crack-photolithography technique can produce several tens of micro/nanofluidic devices by using a single batch process *via* replica molding and soft lithography, thereby guaranteeing high reproducibility and low device-to-device variation. This feature of our method can be the most unique

compared to the previous membrane-based fabrication methods because the membrane-integration processes involve somewhat uncontrollable variation and show a low fabrication throughput. Therefore, our method shows excellent reproducibility and precision in experiments due to minimized run-to-run variations.

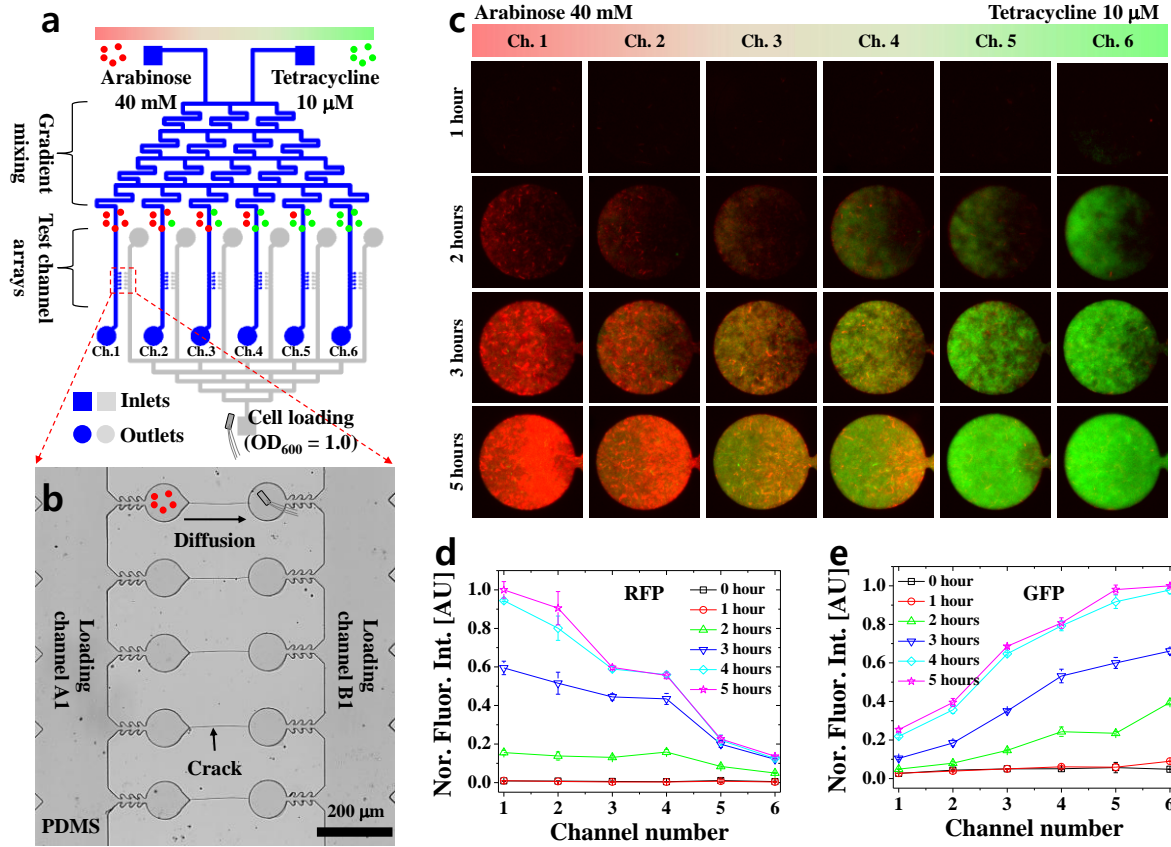


**Figure 10-5.** High-throughput induction assays of dual-inducible cells (pZBRG) with a concentration gradient of two inducers. a, A schematic image shows a microfluidic channel design and its experimental setup. The device consists of six cell loading channels and a concentration gradient generator. The inducer concentrations of each chamber are controlled by the nanochannel array connected to the concentration gradient generator. b, A microscopic image of the PDMS device showing a unit chamber array in which each inducer-loading chamber is individually connected to each cell-loading chamber by a single nanochannel. c, Time-lapse fluorescent images showing gene expression of the dual-inducible cells by different concentrations of tetracycline (10  $\mu$ M) and arabinose (40 mM), respectively. Two linear concentration gradients seem to form simultaneously by the concentration gradient generator (from Ch. 1 to Ch. 6, an increasing concentration gradient of tetracycline with a decreasing concentration gradient of arabinose). d, e, The normalized fluorescent signals of GFP and RFP show the quantitative gene expression results over five hours and appear to depend on the concentrations of the corresponding inducer.

## Conclusions

We successfully demonstrated that the ‘crack-photolithography’ technique produces a single-

layered, membrane-free and diffusion-based micro/nanofluidic device in a batch-processing and high-throughput manner. Not only does the crack-photolithography rely only on the standard photolithography without additional nanofabrication processes and equipment, but it also provides a number of master molds that can be almost infinitely duplicable *via* replica molding and soft lithography. The micro/nanofluidic device developed in this work enabled us to control mass transport of small molecules by adjusting the number and length of nanochannel arrays that are directly related to the diffusive rate and time. Given that accurate control of the diffusive rate and time can easily be manipulated at will by designing and fabricating nanochannel arrays, the crack-photolithography-based micro/nanofluidic devices seem to be advantageous compared to conventional membrane-integrated devices. Therefore, crack-photolithography shows remarkable potential for developing novel diffusion-based micro/nanofluidic devices. In this work, we applied the devices to conducting genetic induction assays of synthetic bacterial cells. Because nanochannel arrays act as a membrane in microfluidic devices, the nanochannel arrays played a key role in allowing chemical communication between inducers and cells but prohibiting physical mixing of cells, being further applied to cell-to-cell communication assays. In addition, it was very convenient to incorporate a concentration gradient generator into the device at the same processed layer without additional microfabrication processes, so that genetic induction assays in various extracellular microenvironments were easily performed in a run and in a high-throughput manner. In this context, the membrane-free, diffusion-based micro/nanofluidic device could be fabricated in a time- and cost-effective and high-throughput manner with high repeatability, making the replacement of previous membrane-integrated microfluidic devices with nanochannel array-based ones possible.

## Chapter 11. Summary and Future Outlook

In this dissertation, four fundamental strategies were used for fabrication of mixed-scale micro/nanofluidic devices to control molecular transports in an accurate and active manner. First, nanoporous hydrogels were integrated into microfluidic devices as microscale membranes (microplug) and played a key role to prevent convective flows but allow diffusive transports of biomolecules. The convection-free and diffusion-controlled microenvironments (pure diffusion) were advantageous to chemically stimulate non-adhesive swimming cells such as *E. coli* without any convective interference. Thus, the hydrogel-integrated devices were applied to characterize chemotaxis of swimming bacterial cells in a variety of chemical types and concentration-gradient profiles (Chapter 2 and 3).

Second, the hydrogel-integrating methods were directly expanded toward the integration of ion selective membranes (ISMs) in microfluidic devices, forming mixed-scale micro/nanofluidic networks with the capability of permselective ion transports. That is, the ISMs allowed transports of counter-ions having the opposite polarity to the ISMs and hindered co-ionic transport, resulting in breaking down electrical neutrality near the junction of nanoporous ISMs and microchannels. Such unique phenomena occurring at micro/nanofluidic interfaces were developed to continuously concentrate charged biomolecules and particles including bacterial cells. In addition to the concentration processes, the ISM-integrated devices also performed separation of biomolecules according to their electrokinetic mobilities. Consequently, the continuous enrichment processes made the low abundant concentration of biomolecules to be detectable (enhancement of sensitivity), and the simultaneous separation process minimized the false-positive signals by eliminating noise molecules (enhancement of selectivity), resulting in a highly-sensitive and selective detection/analysis of target analytes (Chapter 4–6).

Third, arrowhead-shaped ratchet microstructures were fabricated with a resolution of a few microns to generate pure diffusion microenvironments, which has the same function of the hydrogel-integrated devices. The ratchet structure guided bacterial motion to be unidirectional, so that micron-sized bacterial cells were trapped inside of a confined microchamber with continuous supplements of chemicals *via* diffusive transports from the connected ratcheting microchannel. It means that the ratchet structure physically isolates and chemically connects motile bacterial cells to a neighboring microchannel for continuous supplements of nutrients and elimination of metabolites without loss in cell population, providing chemostat-like cellular environments. Using the diffusion-controllable chemostat-like devices, microbial biosensors that can express fluorescent proteins by genetic induction were applied to detect heavy metal ions such as lead and cadmium (Chapter 7 and 8).

Last, a number of microfluidic devices with nanochannel arrays were easily fabricated by the crack-photolithography that can simultaneously produce well-controlled microchannels and

nanochannels in any desired shapes with a variety of geometric dimensions by only using a standard photolithography process. Using the multi-scale fabrication technique, various mixed-scale micro/nanofluidic devices were fabricated in a high-throughput and reproducible manner, and used for accurately manipulating chemical environments *via* pure diffusion or pure electrophoresis. Such pure transport controls were possible because the nanochannel minimized unwanted convective flows driven by pressure (PDF) or potential gradients (EOF), due to the extremely high hydraulic resistances of the nanochannel. As an application, the pure diffusion-based microfluidic devices were used to conduct accurate genetic induction assays of various synthetically engineered bacterial cells to understand fundamental principles that regulate genetic expression. The pure electrophoretic-based microfluidic devices enabled active manipulation of molecular transports by adjusting an applied electric field in a controllable manner (Chapter 9 and 10).

Henceforward the nanoporous-hydrogel-integrated microfluidic devices can be further applied to a variety of diffusion-based bioassays including genetic studies, biochemical detections, cellular signaling studies, which basically requires accurate manipulation of chemical species and concentration. The ISMs can be also widely used in purification of waste/non-drinkable water, and electrochemical devices such as Li-ion batteries and glucose sensors. Thus, the ISM-integrated microfluidic devices have high potential to be used for environmental and electrochemical applications such as water treatment (purification and desalinization), biochemical sensing, and even portable power generation. Furthermore, the membrane-integrated micro/nanofluidic devices developed in this work are distinguished to the conventional membrane-based devices employing sandwiching or UV-curing methods: 1) single-layered device, 2) no membrane interferences in observation, 3) relatively high controllability in mass transports due to small and confined transport regions, 4) no residual precursor solutions in microchannel. Also, the membrane-free micro/nanofluidic devices, such as ratchetting-based and cracking-assisted ones, have the similar functionality and advantages with the membrane-integrated devices, but they exhibit higher capability to be integrated with other existing micro/nanofluidic elements due to the simple fabrication and high flexibility in designing the devices. Consequently, the membrane-integrated and membrane-free micro/nanofluidic devices introduced in this dissertation would be a step forward to realize fully-integrated total analysis systems for various biological and chemical applications.

## References

1. Zhang, C.; Jiang, K.; Liu, F.; Doyle, P. S.; van Kan, J. A.; van der Maarel, J. R. C., A nanofluidic device for single molecule studies with in situ control of environmental solution conditions. *Lab Chip* **2013**, *13* (14), 2821-2826.
2. Karnik, R.; Castelino, K.; Duan, C. H.; Majumdar, A., Diffusion-limited patterning of molecules in nanofluidic channels. *Nano Lett* **2006**, *6* (8), 1735-1740.
3. Duan, C. H.; Majumdar, A., Anomalous ion transport in 2-nm hydrophilic nanochannels. *Nat Nanotechnol* **2010**, *5* (12), 848-852.
4. van der Heyden, F. H. J.; Bonthuis, D. J.; Stein, D.; Meyer, C.; Dekker, C., Power generation by pressure-driven transport of ions in nanofluidic channels. *Nano Lett* **2007**, *7* (4), 1022-1025.
5. Karnik, R.; Fan, R.; Yue, M.; Li, D. Y.; Yang, P. D.; Majumdar, A., Electrostatic control of ions and molecules in nanofluidic transistors. *Nano Lett* **2005**, *5* (5), 943-948.
6. Sparreboom, W.; van den Berg, A.; Eijkel, J. C. T., Principles and applications of nanofluidic transport. *Nat Nanotechnol* **2009**, *4* (11), 713-720.
7. Zangle, T. A.; Mani, A.; Santiago, J. G., Theory and experiments of concentration polarization and ion focusing at microchannel and nanochannel interfaces. *Chem Soc Rev* **2010**, *39* (3), 1014-1035.
8. Duan, C. H.; Wang, W.; Xie, Q., Review article: Fabrication of nanofluidic devices. *Biomicrofluidics* **2013**, *7* (2).
9. Haneveld, J.; Jansen, H.; Berenschot, E.; Tas, N.; Elwenspoek, M., Wet anisotropic etching for fluidic 1D nanochannels. *J Micromech Microeng* **2003**, *13* (4), S62-S66.
10. Kim, W. S.; Lee, J.; Ruoff, R. S., Nanofluidic channel fabrication and characterization by micromachining. *ASME Conference Proceedings* **2003**, 841-846.
11. Stern, M. B.; Geis, M. W.; Curtin, J. E., Nanochannel fabrication for chemical sensors. *J Vac Sci Technol B* **1997**, *15* (6), 2887-2891.
12. Chueh, B. H.; Huh, D.; Kyrtos, C. R.; Houssin, T.; Futai, N.; Takayama, S., Leakage-free bonding of porous membranes into layered microfluidic array systems. *Anal Chem* **2007**, *79* (9), 3504-3508.
13. Ahmed, T.; Shimizu, T. S.; Stocker, R., Bacterial chemotaxis in linear and nonlinear steady microfluidic gradients. *Nano Lett* **2010**, *10* (9), 3379-3385.
14. Dhopeswarkar, R.; Li, S. A.; Crooks, R. M., Electrokinetic concentration enrichment within a microfluidic device using a hydrogel microplug. *Lab Chip* **2005**, *5* (10), 1148-1154.
15. Efimenko, K.; Rackaitis, M.; Manias, E.; Vaziri, A.; Mahadevan, L.; Genzer, J., Nested self-similar wrinkling patterns in skins. *Nat Mater* **2005**, *4* (4), 293-297.
16. (a) Zhu, X. Y.; Mills, K. L.; Peters, P. R.; Bahng, J. H.; Liu, E. H.; Shim, J.; Naruse, K.; Csete, M. E.; Thouless, M. D.; Takayama, S., Fabrication of reconfigurable protein matrices by cracking. *Nat Mater* **2005**, *4* (5), 403-406; (b) Adelung, R.; Aktas, O. C.; Franc, J.; Biswas, A.; Kunz, R.; Elbahri, M.; Kanzow, J.; Schurmann, U.; Faupel, F., Strain-controlled growth of

- nanowires within thin-film cracks. *Nat Mater* **2004**, 3 (6), 375-379.
17. Huh, D.; Mills, K. L.; Zhu, X. Y.; Burns, M. A.; Thouless, M. D.; Takayama, S., Tuneable elastomeric nanochannels for nanofluidic manipulation. *Nat Mater* **2007**, 6 (6), 424-428.
  18. Livne, A.; Bouchbinder, E.; Svetlizky, I.; Fineberg, J., The near-tip fields of fast cracks. *Science* **2010**, 327 (5971), 1359-1363.
  19. Chung, S.; Lee, J. H.; Moon, M. W.; Han, J.; Kamm, R. D., Non-lithographic wrinkle nanochannels for protein preconcentration. *Adv Mater* **2008**, 20 (16), 3011-3016.
  20. Li, B.; Cao, Y. P.; Feng, X. Q.; Gao, H. J., Mechanics of morphological instabilities and surface wrinkling in soft materials: A review. *Soft Matter* **2012**, 8 (21), 5728-5745.
  21. Fu, J. P.; Schoch, R. B.; Stevens, A. L.; Tannenbaum, S. R.; Han, J. Y., A patterned anisotropic nanofluidic sieving structure for continuous-flow separation of DNA and proteins. *Nat Nanotechnol* **2007**, 2 (2), 121-128.
  22. Liang, X. G.; Chou, S. Y., Nanogap detector inside nanofluidic channel for fast real-time label-free DNA analysis. *Nano Lett* **2008**, 8 (5), 1472-1476.
  23. Song, Y. A.; Melik, R.; Rabie, A. N.; Ibrahim, A. M. S.; Moses, D.; Tan, A.; Han, J.; Lin, S. J., Electrochemical activation and inhibition of neuromuscular systems through modulation of ion concentrations with ion-selective membranes. *Nat Mater* **2011**, 10 (12), 980-986.
  24. Han, J.; Craighead, H. G., Separation of long DNA molecules in a microfabricated entropic trap array. *Science* **2000**, 288 (5468), 1026-1029.
  25. Song, Y. A.; Ibrahim, A. M. S.; Rabie, A. N.; Han, J.; Lin, S. J., Microfabricated nerve-electrode interfaces in neural prosthetics and neural engineering. *Biotechnol Genet Eng* **2013**, 29 (2), 113-134.
  26. Zhang, G. S.; Du, W.; Liu, B. F.; Hisamoto, H.; Terabe, S., Characterization of electrokinetic gating valve in microfluidic channels. *Anal Chim Acta* **2007**, 584 (1), 129-135.
  27. Lee, S.; An, R.; Hunt, A. J., Liquid glass electrodes for nanofluidics. *Nat Nanotechnol* **2010**, 5 (6), 412-416.
  28. Kim, D.; Raj, A.; Zhu, L.; Masel, R. I.; Shannon, M. A., Non-equilibrium electrokinetic micro/nanofluidic mixer. *Lab Chip* **2008**, 8 (4), 625-628.
  29. Kim, S. J.; Ko, S. H.; Kang, K. H.; Han, J., Direct seawater desalination by ion concentration polarization (vol 5, pg 297, 2010). *Nat Nanotechnol* **2013**, 8 (8), 609-609.
  30. (a) Irimia, D.; Toner, M., Spontaneous migration of cancer cells under conditions of mechanical confinement. *Integrative Biology* **2009**, 1 (8-9), 506-512; (b) Nie, F. Q.; Yamada, M.; Kobayashi, J.; Yamato, M.; Kikuchi, A.; Okano, T., On-chip cell migration assay using microfluidic channels. *Biomaterials* **2007**, 28 (27), 4017-4022.
  31. Chung, S.; Sudo, R.; Zervantonakis, I. K.; Rimchala, T.; Kamm, R. D., Surface-treatment-induced three-dimensional capillary morphogenesis in a microfluidic platform. *Adv Mater* **2009**, 21 (47), 4863-4867.
  32. Chung, S.; Sudo, R.; Vickerman, V.; Zervantonakis, I. K.; Kamm, R. D., Microfluidic platforms

- for studies of angiogenesis, cell Migration, and cell-cell Interactions. *Ann Biomed Eng* **2010**, 38 (3), 1164-1177.
33. (a) Boedicker, J. Q.; Vincent, M. E.; Ismagilov, R. F., Microfluidic confinement of single cells of bacteria in small volumes initiates high-density behavior of quorum sensing and growth and reveals its variability. *Angew Chem, Int Ed* **2009**, 48 (32), 5908-5911; (b) Cheng, W. C.; Hardwick, J. M., A quorum on bacterial programmed cell death. *Mol Cell* **2007**, 28 (4), 515-517.
  34. Kim, T.; Pinelis, M.; Maharbiz, M. M., Generating steep, shear-free gradients of small molecules for cell culture. *Biomed Microdevices* **2009**, 11 (1), 65-73.
  35. (a) Irimia, D.; Liu, S. Y.; Tharp, W. G.; Samadani, A.; Toner, M.; Poznansky, M. C., Microfluidic system for measuring neutrophil migratory responses to fast switches of chemical gradients. *Lab Chip* **2006**, 6 (2), 191-198; (b) Jeon, N. L.; Baskaran, H.; Dertinger, S. K. W.; Whitesides, G. M.; Van de Water, L.; Toner, M., Neutrophil chemotaxis in linear and complex gradients of interleukin-8 formed in a microfabricated device. *Nat Biotechnol* **2002**, 20 (8), 826-830; (c) Mao, H. B.; Cremer, P. S.; Manson, M. D., A sensitive, versatile microfluidic assay for bacterial chemotaxis. *Proc Natl Acad Sci USA* **2003**, 100 (9), 5449-5454.
  36. Amarie, D.; Glazier, J. A.; Jacobson, S. C., Compact microfluidic structures for generating spatial and temporal gradients. *Anal Chem* **2007**, 79 (24), 9471-9477.
  37. Howard, J., Mechanics of motor proteins and the cytoskeleton. *Sindauer, Sunderland, MA*. **2001**.
  38. Chueh, B. H.; Huh, D. G.; Kyrtos, C. R.; Houssin, T.; Futai, N.; Takayama, S., Leakage-free bonding of porous membranes into layered microfluidic array systems. *Anal Chem* **2007**, 79 (9), 3504-3508.
  39. (a) Ling, Y.; Rubin, J.; Deng, Y.; Huang, C.; Demirci, U.; Karp, J. M.; Khademhosseini, A., A cell-laden microfluidic hydrogel. *Lab Chip* **2007**, 7 (6), 756-762; (b) Cheng, S. Y.; Heilman, S.; Wasserman, M.; Archer, S.; Shuler, M. L.; Wu, M. M., A hydrogel-based microfluidic device for the studies of directed cell migration. *Lab Chip* **2007**, 7 (6), 763-769; (c) Diao, J. P.; Young, L.; Kim, S.; Fogarty, E. A.; Heilman, S. M.; Zhou, P.; Shuler, M. L.; Wu, M. M.; DeLisa, M. P., A three-channel microfluidic device for generating static linear gradients and its application to the quantitative analysis of bacterial chemotaxis. *Lab Chip* **2006**, 6 (3), 381-388.
  40. Celani, A.; Vergassola, M., Bacterial strategies for chemotaxis response. *Proc Natl Acad Sci USA* **2010**, 107 (4), 1391-1396.
  41. Herzmark, P.; Campbell, K.; Wang, F.; Wong, K.; El-Samad, H.; Groisman, A.; Bourne, H. R., Bound attractant at the leading vs. the trailing edge determines chemotactic prowess. *Proc Natl Acad Sci USA* **2007**, 104 (33), 13349-13354.
  42. Adler, J.; Templeto, B., Effect of environmental conditions on motility of Escherichia coli. *J Gen Microbiol* **1967**, 46, 175-184.
  43. Merrin, J.; Leibler, S.; Chuang, J. S., Printing multistrain bacterial patterns with a piezoelectric inkjet printer. *Plos One* **2007**, 2 (7), e663.
  44. Berg, H. C.; Brown, D. A., Chemotaxis in Escherichia-coli analyzed by 3-dimensional tracking. *Nature* **1972**, 239 (5374), 500-504.
  45. Gokarn, N. A.; Rajurkar, N. S., Diffusion of cesium ions labeled with Cs-134 in agar gel containing alkali metal iodides: Obstruction effect and activation energy. *J Solution Chem* **2006**,

- 35 (4), 507-517.
46. Rani, S. A.; Pitts, B.; Stewart, P. S., Rapid diffusion of fluorescent tracers into *Staphylococcus epidermidis* biofilms visualized by time lapse microscopy. *Antimicrob Agents Chemother* **2005**, 49 (2), 728-732.
  47. Adler, J.; Hazelbauer, G.; Dahl, M. M., Chemotaxis toward sugars in *Escherichia coli*. *J Bacteriol* **1973**, 115 (3), 824-847.
  48. Adler, J., Chemotaxis in bacteria. *Science* **1966**, 153 (3737), 708-716.
  49. Andersson, M.; Axelsson, A.; Zacchi, G., Diffusion of glucose and insulin in a swelling N-isopropylacrylamide gel. *Int J Pharm* **1997**, 157 (2), 199-208.
  50. Teixeira, A. I.; Ilkhanizadeh, S.; Wigenius, J. A.; Duckworth, J. K.; Inganas, O.; Hermanson, O., The promotion of neuronal maturation on soft substrates. *Biomaterials* **2009**, 30 (27), 4567-4572.
  51. Dos Santos, E.; Piovan, T.; Roberto, I. C.; Milagres, A. M. F., Kinetics of the solid state fermentation of sugarcane bagasse by *Thermoascus aurantiacus* for the production of xylanase. *Biotechnol Lett* **2003**, 25 (1), 13-16.
  52. Chao, Y. P.; Liao, J. C., Metabolic responses to substrate futile cycling in *Escherichia coli*. *J Biol Chem* **1994**, 269 (7), 5122-5126.
  53. Adler, J., Chemoreceptors in bacteria. *Science* **1969**, 166 (3913), 1588-1969.
  54. Ahmed, T.; Shimizu, T. S.; Stocker, R., Microfluidics for bacterial chemotaxis. *Integr Biol* **2010**, 2 (11-12), 604-629.
  55. Sahai, R.; Cecchini, M.; Klingauf, M.; Ferrari, A.; Martino, C.; Castrataro, P.; Lionetti, V.; Mencias, A.; Beltram, F., Microfluidic chip for spatially and temporally controlled biochemical gradient generation in standard cell-culture Petri dishes. *Microfluid Nanofluid* **2011**, 11 (6), 763-771.
  56. Kim, M.; Kim, T., Diffusion-based and long-range concentration gradients of multiple chemicals for bacterial chemotaxis assays. *Anal Chem* **2010**, 82 (22), 9401-9409.
  57. Si, G. W.; Yang, W.; Bi, S. Y.; Luo, C. X.; Ouyang, Q., A parallel diffusion-based microfluidic device for bacterial chemotaxis analysis. *Lab Chip* **2012**, 12 (7), 1389-1394.
  58. Choi, E.; Chang, H. K.; Lim, C. Y.; Kim, T.; Park, J., Concentration gradient generation of multiple chemicals using spatially controlled self-assembly of particles in microchannels. *Lab Chip* **2012**, 12 (20), 3968-3975.
  59. (a) Kim, M.; Kim, S. H.; Lee, S. K.; Kim, T., Microfluidic device for analyzing preferential chemotaxis and chemoreceptor sensitivity of bacterial cells toward carbon sources. *Analyst* **2011**, 136 (16), 3238-3243; (b) Gorman, B. R.; Wikswo, J. P., Characterization of transport in microfluidic gradient generators. *Microfluid Nanofluid* **2008**, 4 (4), 273-285; (c) Englert, D. L.; Manson, M. D.; Jayaraman, A., Investigation of bacterial chemotaxis in flow-based microfluidic devices. *Nat Protoc* **2010**, 5 (5), 864-872.
  60. Hill, J.; Kalkanci, O.; McMurtry, J. L.; Koser, H., Hydrodynamic surface interactions enable *Escherichia coli* to seek efficient routes to swim upstream. *Phys Rev Lett* **2007**, 98 (6), 068101.

61. Yeh, C. H.; Chen, C. H.; Lin, Y. C., Use of a gradient-generating microfluidic device to rapidly determine a suitable glucose concentration for cell viability test. *Microfluid Nanofluid* **2011**, *10* (5), 1011-1018.
62. Haessler, U.; Kalinin, Y.; Swartz, M. A.; Wu, M. W., An agarose-based microfluidic platform with a gradient buffer for 3D chemotaxis studies. *Biomed Microdevices* **2009**, *11* (4), 827-835.
63. Stock, A. M., A nonlinear stimulus-response relation in bacterial chemotaxis. *Proc Natl Acad Sci USA* **1999**, *96* (20), 10945-10947.
64. Qin, D.; Xia, Y. N.; Whitesides, G. M., Soft lithography for micro- and nanoscale patterning. *Nat Protoc* **2010**, *5* (3), 491-502.
65. Kim, M.; Jia, M.; Kim, T., Ion concentration polarization in a single and open microchannel induced by a surface-patterned perm-selective film. *Analyst* **2013**, *138* (5), 1370-1378.
66. Ellegood, J.; Hanstock, C. C.; Beaulieu, C., Trace apparent diffusion coefficients of metabolites in human brain using diffusion weighted magnetic resonance spectroscopy. *Magnet Reson Med* **2005**, *53* (5), 1025-1032.
67. Lebrun, L.; Junter, G. A., Diffusion of sucrose and dextran through agar-gel membranes. *Enzyme Microb Tech* **1993**, *15* (12), 1057-1062.
68. (a) Kowalczyk, S. W.; Blosser, T. R.; Dekker, C., Biomimetic nanopores: Learning from and about nature. *Trends Biotechnol* **2011**, *29* (12), 607-614; (b) Dekker, C., Solid-state nanopores. *Nat Nanotechnol* **2007**, *2* (4), 209-215.
69. Nishizawa, M.; Menon, V. P.; Martin, C. R., Metal nanotubule membranes with electrochemically switchable ion-transport selectivity. *Science* **1995**, *268* (5211), 700-702.
70. (a) Bayley, H.; Cremer, P. S., Stochastic sensors inspired by biology. *Nature* **2001**, *413* (6852), 226-230; (b) Yusko, E. C.; Johnson, J. M.; Majd, S.; Prangkio, P.; Rollings, R. C.; Li, J. L.; Yang, J.; Mayer, M., Controlling protein translocation through nanopores with bio-inspired fluid walls. *Nat Nanotechnol* **2011**, *6* (4), 253-260.
71. Kasianowicz, J. J.; Brandin, E.; Branton, D.; Deamer, D. W., Characterization of individual polynucleotide molecules using a membrane channel. *Proc Natl Acad Sci USA* **1996**, *93* (24), 13770-13773.
72. Choi, N. W.; Cabodi, M.; Held, B.; Gleghorn, J. P.; Bonassar, L. J.; Stroock, A. D., Microfluidic scaffolds for tissue engineering. *Nat Mater* **2007**, *6* (11), 908-915.
73. Razunguzwa, T. T.; Lenke, J.; Timperman, A. T., An electrokinetic/hydrodynamic flow microfluidic CE-ESI-MS interface utilizing a hydrodynamic flow restrictor for delivery of samples under low EOF conditions. *Lab Chip* **2005**, *5* (8), 851-855.
74. Stein, D.; Kruithof, M.; Dekker, C., Surface-charge-governed ion transport in nanofluidic channels. *Phys Rev Lett* **2004**, *93* (3).
75. (a) Foote, R. S.; Khandurina, J.; Jacobson, S. C.; Ramsey, J. M., Preconcentration of proteins on microfluidic devices using porous silica membranes. *Anal Chem* **2005**, *77* (1), 57-63; (b) Pu, Q. S.; Yun, J. S.; Temkin, H.; Liu, S. R., Ion-enrichment and ion-depletion effect of nanochannel structures. *Nano Lett* **2004**, *4* (6), 1099-1103; (c) Kim, T.; Meyhofer, E., Nanofluidic concentration of selectively extracted biomolecule analytes by microtubules. *Anal Chem* **2008**,

80 (14), 5383-5390.

76. Kim, S. M.; Burns, M. A.; Hasselbrink, E. F., Electrokinetic protein preconcentration using a simple glass/poly(dimethylsiloxane) microfluidic chip. *Anal Chem* **2006**, 78 (14), 4779-4785.
77. (a) Shen, M.; Yang, H.; Sivagnanam, V.; Gijss, M. A. M., Microfluidic protein preconcentrator using a microchannel-integrated nafion strip: Experiment and modeling. *Anal Chem* **2010**, 82 (24), 9989-9997; (b) Kim, S. J.; Han, J., Self-sealed vertical polymeric nanoporous-junctions for high-throughput nanofluidic applications (vol 80, pg 3507, 2008). *Anal Chem* **2008**, 80 (18), 7179-7179.
78. (a) Hatch, A. V.; Herr, A. E.; Throckmorton, D. J.; Brennan, J. S.; Singh, A. K., Integrated preconcentration SDS-PAGE of proteins in microchips using photopatterned cross-linked polyacrylamide gels. *Anal Chem* **2006**, 78 (14), 4976-4984; (b) Kim, P.; Kim, S. J.; Han, J.; Suh, K. Y., Stabilization of ion concentration polarization using a heterogeneous nanoporous junction. *Nano Lett* **2010**, 10 (1), 16-23.
79. Chun, H. G.; Chung, T. D.; Ramsey, J. M., High yield sample preconcentration using a highly ion-conductive charge-selective polymer. *Anal Chem* **2010**, 82 (14), 6287-6292.
80. Kim, M.; Lee, S. K.; Kim, S. H.; Kim, T., Microfluidic device for analyzing preferential chemotaxis and chemoreceptor sensitivity of bacterial cells toward carbon sources. *Analyst* **2011**, 136 (16), 3238-3243.
81. Lam, P.; Wynne, K. J.; Wnek, G. E., Surface-tension-confined microfluidics. *Langmuir* **2002**, 18 (3), 948-951.
82. O'Brien, A. K.; Bowman, C. N., Impact of oxygen on photopolymerization kinetics and polymer structure. *Macromolecules* **2006**, 39 (7), 2501-2506.
83. Mauritz, K. A.; Moore, R. B., State of understanding of Nafion. *Chem Rev* **2004**, 104 (10), 4535-4585.
84. Serwer, P., Agarose gels - Properties and use for electrophoresis. *Electrophoresis* **1983**, 4 (6), 375-382.
85. Ackers, G. K.; Steere, R. L., Restricted diffusion of macromolecules through agar-gel membranes. *Biochim Biophys Acta* **1962**, 59 (1), 137-149.
86. Kim, S. J.; Wang, Y. C.; Lee, J. H.; Jang, H.; Han, J., Concentration polarization and nonlinear electrokinetic flow near a nanofluidic channel. *Phys Rev Lett* **2007**, 99 (4), 044501.
87. Hlushkou, D.; Crooks, R. M.; Tallarek, U., Numerical simulation of electric field gradient focusing and separation of analytes in microchannels with embedded bipolar electrode. *High Performance Computing in Science and Engineering, Garching/Munich 2009* **2010**, 719-730.
88. Kirby, B. J.; Hasselbrink, E. F., Zeta potential of microfluidic substrates: 1. Theory, experimental techniques, and effects on separations. *Electrophoresis* **2004**, 25 (2), 187-202.
89. (a) Chang, H. C.; Yossifon, G.; Demekhin, E. A., Nanoscale electrokinetics and microvortices: How microhydrodynamics affects nanofluidic ion flux. *Annu Rev Fluid Mech* **2012**, 44, 401-426; (b) Leinweber, F. C.; Tallarek, U., Concentration polarization-based nonlinear electrokinetics in porous media: Induced-charge electroosmosis. *J Phys Chem B* **2005**, 109 (46), 21481-21485.

90. Anderson, N. L.; Valkirs, G., Protein arrays - A new option. *Sci Am* **2002**, 286 (2), 52-53.
91. He, M.; Herr, A. E., Polyacrylamide gel photopatterning enables automated protein immunoblotting in a two-dimensional microdevice. *J Am Chem Soc* **2010**, 132 (8), 2512- 2513.
92. Balss, K. M.; Ross, D.; Begley, H. C.; Olsen, K. G.; Tarlov, M. J., DNA hybridization assays using temperature gradient focusing and peptide nucleic acids. *J Am Chem Soc* **2004**, 126 (41), 13474-13479.
93. O'Neill, R. A.; Bhamidipati, A.; Bi, X. H.; Deb-Basu, D.; Cahill, L.; Ferrante, J.; Gentalen, E.; Glazer, M.; Gossett, J.; Hacker, K.; Kirby, C.; Knittle, J.; Loder, R.; Mastroieni, C.; MacLaren, M.; Mills, T.; Nguyen, U.; Parker, N.; Rice, A.; Roach, D.; Suich, D.; Voehringer, D.; Voss, K.; Yang, J.; Yang, T.; Vander Horn, P. B., Isoelectric focusing technology quantifies protein signaling in 25 cells. *Proc Natl Acad Sci USA* **2006**, 103 (44), 16153-16158.
94. Dhopeswarkar, R.; Hlushkou, D.; Nguyen, M.; Tallarek, U.; Crooks, R. M., Electrokinetics in microfluidic channels containing a floating electrode. *J Am Chem Soc* **2008**, 130 (32), 10480-+.
95. Hlushkou, D.; Perdue, R. K.; Dhopeswarkar, R.; Crooks, R. M.; Tallarek, U., Electric field gradient focusing in microchannels with embedded bipolar electrode. *Lab Chip* **2009**, 9 (13), 1903-1913.
96. Kim, S. M.; Sommer, G. J.; Burns, M. A.; Hasselbrink, E. F., Low-power concentration and separation using temperature gradient focusing via Joule heating. *Anal Chem* **2006**, 78 (23), 8028-8035.
97. Scarff, B.; Escobedo, C.; Sinton, D., Radial sample preconcentration. *Lab Chip* **2011**, 11 (6), 1102-1109.
98. Kim, T.; Meyhofer, E., Nanofluidic concentration of selectively extracted biomolecule anattes by microtubules. *Anal Chem* **2008**, 80 (14), 5383-5390.
99. (a) Wang, W. J.; Chen, C. L.; Qian, M. X.; Zhao, X. S., Aptamer biosensor for protein detection using gold nanoparticles. *Anal Biochem* **2008**, 373 (2), 213-219; (b) Strehlitz, B.; Nikolaus, N.; Stoltenburg, R., Protein detection with aptamer biosensors. *Sensors-Basel* **2008**, 8 (7), 4296-4307.
100. (a) Song, S. P.; Wang, L. H.; Li, J.; Zhao, J. L.; Fan, C. H., Aptamer-based biosensors. *Trac-Trend Anal Chem* **2008**, 27 (2), 108-117; (b) Lin, Q.; Nguyen, T., Aptamer-based microfluidic biosensors. *Ieee-Nano* **2009**, 812-814; (c) Srinivas, R. L.; Chapin, S. C.; Doyle, P. S., Aptamer-functionalized microgel particles for protein detection. *Anal Chem* **2011**, 83 (23), 9138-9145.
101. Kim, M.; Kim, T., Integration of nanoporous membranes in microfluidic devices: Electrokinetic bio-sample pre-concentration. *Analyst* **2013**, 138, 6007-6015.
102. Choi, D. S.; Byun, K. E.; Hong, S., Dual transport systems based on hybrid nanostructures of microtubules and actin filaments. *Small* **2011**, 7 (13), 1755-1760.
103. Kim, T.; Kao, M. T.; Hasselbrink, E. F.; Meyhofer, E., Nanomechanical model of microtubule translocation in the presence of electric fields. *Biophys J* **2008**, 94 (10), 3880-3892.
104. Southern, E. M., Detection of specific sequences among DNA fragments separated by gel-electrophoresis. *J Mol Biol* **1975**, 98 (3), 503-508.

105. Kim, T.; Kao, M. T.; Hasselbrink, E. F.; Meyhofer, E., Active alignment of microtubules with electric fields. *Nano Lett* **2007**, 7 (1), 211-217.
106. Senapati, S.; Basuray, S.; Slouka, Z.; Cheng, L. J.; Chang, H. C., A nanomembrane-based nucleic acid sensing platform for portable diagnostics. *Top Curr Chem* **2011**, 304, 153-169.
107. Striemer, C. C.; Gaborski, T. R.; McGrath, J. L.; Fauchet, P. M., Charge- and size-based separation of macromolecules using ultrathin silicon membranes. *Nature* **2007**, 445 (7129), 749-753.
108. Yan, R. X.; Liang, W. J.; Fan, R.; Yang, P. D., Nanofluidic diodes based on nanotube heterojunctions. *Nano Lett* **2009**, 9 (11), 3820-3825.
109. Daiguji, H.; Oka, Y.; Shirono, K., Nanofluidic diode and bipolar transistor. *Nano Lett* **2005**, 5 (11), 2274-2280.
110. Daiguji, H.; Yang, P. D.; Szeri, A. J.; Majumdar, A., Electrochemomechanical energy conversion in nanofluidic channels. *Nano Lett* **2004**, 4 (12), 2315-2321.
111. Plecis, A.; Schoch, R. B.; Renaud, P., Ionic transport phenomena in nanofluidics: Experimental and theoretical study of the exclusion-enrichment effect on a chip. *Nano Lett* **2005**, 5 (6), 1147-1155.
112. Wang, Y. C.; Stevens, A. L.; Han, J. Y., Million-fold preconcentration of proteins and peptides by nanofluidic filter. *Anal Chem* **2005**, 77 (14), 4293-4299.
113. Hlushkou, D.; Dhopeswarkar, R.; Crooks, R. M.; Tallarek, U., The influence of membrane ion-permeability on electrokinetic concentration enrichment in membrane-based preconcentration units. *Lab Chip* **2008**, 8 (7), 1153-1162.
114. (a) Wang, S. C.; Wei, H. H.; Chen, H. P.; Tsai, M. H.; Yu, C. C.; Chang, H. C., Dynamic superconcentration at critical-point double-layer gates of conducting nanoporous granules due to asymmetric tangential fluxes. *Biomicrofluidics* **2008**, 2 (1); (b) Mani, A.; Zangle, T. A.; Santiago, J. G., On the propagation of concentration polarization from microchannel-nanochannel interfaces Part I: Analytical model and characteristic analysis. *Langmuir* **2009**, 25 (6), 3898-3908; (c) Zangle, T. A.; Mani, A.; Santiago, J. G., On the propagation of concentration polarization from microchannel-nanochannel interfaces Part II: Numerical and experimental study. *Langmuir* **2009**, 25 (6), 3909-3916.
115. Mitchell, M. C.; Spikmans, V.; Bessoth, F.; Manz, A.; de Mello, A., Towards organic syndissertation in microfluidic devices: Multicomponent reactions for the construction of compound libraries. *Mesa Mg* **2000**, 463-465.
116. Colinart, T.; Didierjean, S.; Lottin, O.; Maranzana, G.; Moyne, C., Transport in PFSA membranes. *J Electrochem Soc* **2008**, 155 (3), B244-B257.
117. Sinton, D.; Scarff, B.; Escobedo, C., Radial sample preconcentration. *Lab Chip* **2011**, 11 (6), 1102-1109.
118. (a) Anand, R. K.; Sheridan, E.; Knust, K. N.; Crooks, R. M., Bipolar electrode focusing: Faradaic ion concentration polarization. *Anal Chem* **2011**, 83 (6), 2351-2358; (b) Laws, D. R.; Hlushkou, D.; Perdue, R. K.; Tallarek, U.; Crooks, R. M., Bipolar electrode focusing: Simultaneous concentration enrichment and separation in a microfluidic channel containing a bipolar electrode. *Anal Chem* **2009**, 81 (21), 8923-8929.

119. Rubinstein, I., Mechanism for an electrodiffusional instability in concentration polarization. *J Chem Soc Farad T 2* **1981**, 77, 1595-1609.
120. Tsunomori, F.; Ushiki, H., Pore size effect on diffusion coefficient of rhodamine B in PNIPA gel. *Phys Lett A* **1999**, 258 (2-3), 171-176.
121. Dutta, P.; Beskok, A., Analytical solution of combined electroosmotic/pressure driven flows in two-dimensional straight channels: Finite debye layer effects. *Anal Chem* **2001**, 73 (9), 1979-1986.
122. (a) Yossifon, G.; Chang, H. C., Selection of nonequilibrium overlimiting currents: Universal depletion layer formation dynamics and vortex instability. *Phys Rev Lett* **2008**, 101 (25); (b) Rubinstein, S. M.; Manukyan, G.; Staicu, A.; Rubinstein, I.; Zaltzman, B.; Lammertink, R. G. H.; Mugele, F.; Wessling, M., Direct observation of a nonequilibrium electro-osmotic instability. *Phys Rev Lett* **2008**, 101 (23).
123. Bien, D. C. S.; Mitchell, S. J. N.; Gamble, H. S., Characterisation of microfluidic devices. *ICMTS 2002: Proceedings of the 2002 International Conference on Microelectronic Test Structures* **2002**, 211-215.
124. (a) Weibel, D. B.; DiLuzio, W. R.; Whitesides, G. M., Microfabrication meets microbiology. *Nat Rev Microbiol* **2007**, 5 (3), 209-218; (b) Jeong, H. H.; Lee, S. H.; Kim, J. M.; Kim, H. E.; Kim, Y. G.; Yoo, J. Y.; Chang, W. S.; Lee, C. S., Microfluidic monitoring of *Pseudomonas aeruginosa* chemotaxis under the continuous chemical gradient. *Biosens Bioelectron* **2010**, 26 (2), 351-356; (c) Kalinin, Y.; Neumann, S.; Sourjik, V.; Wu, M. M., Responses of *Escherichia coli* bacteria to two opposing chemoattractant gradients depend on the chemoreceptor ratio. *J Bacteriol* **2010**, 192 (7), 1796-1800.
125. (a) Ismagilov, R. F.; Stroock, A. D.; Kenis, P. J. A.; Whitesides, G.; Stone, H. A., Experimental and theoretical scaling laws for transverse diffusive broadening in two-phase laminar flows in microchannels. *Appl Phys Lett* **2000**, 76 (17), 2376-2378; (b) Guo, X. Q.; Chen, K.; Wen, Y.; Li, R.; Li, S. P.; Jiang, J. D., Comparison of in-situ biodegrading abilities of *Pseudomonas putida* mutants: LeuB(-) auxotroph, fliC(-) non-motility, and cheA(-) non-chemotaxis. *Int Biodeter Biodegr* **2009**, 63 (5), 576-581.
126. (a) Campbell, K.; Groisman, A., Generation of complex concentration profiles in microchannels in a logarithmically small number of steps. *Lab Chip* **2007**, 7 (2), 264-272; (b) Dertinger, S. K. W.; Chiu, D. T.; Jeon, N. L.; Whitesides, G. M., Generation of gradients having complex shapes using microfluidic networks. *Anal Chem* **2001**, 73 (6), 1240-1246.
127. (a) Kim, T.; Pinelis, M.; Maharbiz, M. M., Generating steep shear-free gradients of small molecules for cell culture. *Biomed Microdevices* **2009**, 11 (1), 65-73; (b) Atencia, J.; Morrow, J.; Locascio, L. E., The microfluidic palette: a diffusive gradient generator with spatio-temporal control. *Lab Chip* **2009**, 9 (18), 2707-2714.
128. Hulme, S. E.; DiLuzio, W. R.; Shevkoplyas, S. S.; Turner, L.; Mayer, M.; Berg, H. C.; Whitesides, G. M., Using ratchets and sorters to fractionate motile cells of *Escherichia coli* by length. *Lab Chip* **2008**, 8 (11), 1888-1895.
129. Galajda, P.; Keymer, J.; Chaikin, P.; Austin, R., A wall of funnels concentrates swimming bacteria. *J Bacteriol* **2007**, 189 (23), 8704-8707.
130. Kim, S. Y.; Lee, E. S.; Lee, H. J.; Lee, S. Y.; Lee, S. K.; Kim, T., Microfabricated ratchet structures for concentrating and patterning motile bacterial cells. *J Micromech Microeng* **2010**,

20 (9), 095006.

131. Garvis, S.; Munder, A.; Ball, G.; de Bentzmann, S.; Wiehlmann, L.; Ewbank, J. J.; Tummler, B.; Filloux, A., *Caenorhabditis elegans* semi-automated liquid screen reveals a specialized role for the chemotaxis gene *cheB2* in *Pseudomonas aeruginosa* virulence. *Plos Pathog* **2009**, *5* (8), e1000540.
132. Gestwicki, J. E.; Kiessling, L. L., Inter-receptor communication through arrays of bacterial chemoreceptors. *Nature* **2002**, *415* (6867), 81-84.
133. (a) Cuypers, A.; Plusquin, M.; Remans, T.; Jozefczak, M.; Keunen, E.; Gielen, H.; Opdenakker, K.; Nair, A. R.; Munters, E.; Artois, T. J.; Nawrot, T.; Vangronsveld, J.; Smeets, K., Cadmium stress: An oxidative challenge. *Biometals* **2010**, *23* (5), 927-940; (b) Ercal, N.; Gurer-Orhan, H.; Aykin-Burns, N., Toxic metals and oxidative stress Part I: Mechanisms involved in metal-induced oxidative damage. *Curr Trends Med Chem* **2001**, *1* (6), 529-39.
134. Coen, N.; Mothersill, C.; Kadhim, M.; Wright, E. G., Heavy metals of relevance to human health induce genomic instability. *J Pathol* **2001**, *195* (3), 293-299.
135. Karri, S. K.; Saper, R. B.; Kales, S. N., Lead encephalopathy due to traditional medicines. *Current drug safety* **2008**, *3* (1), 54-9.
136. Duruibe, J. O.; Ogwuegbu, M. O. C.; Egwurugwu, J. N., Heavy metal pollution and human biotoxic effects. *Int J Phys Sci* **2007**, *2* (5), 112-118.
137. Roels, H. A.; Lauwerys, R. R.; Buchet, J. P.; Bernard, A. M.; Vos, A.; Oversteens, M., Health significance of cadmium induced renal dysfunction - A 5 year follow up. *Brit J Ind Med* **1989**, *46* (11), 755-764.
138. Jackson, K. W.; Chen, G. R., Atomic absorption, atomic emission, and flame emission spectrometry. *Anal Chem* **1996**, *68* (12), R231-R256.
139. Burlingame, A. L.; Boyd, R. K.; Gaskell, S. J., Mass spectrometry. *Anal Chem* **1996**, *68* (12), R599-R651.
140. Anderson, J. L.; Bowden, E. F.; Pickup, P. G., Dynamic electrochemistry: Methodology and application. *Anal Chem* **1996**, *68* (12), R379-R444.
141. (a) Lei, Y.; Chen, W.; Mulchandani, A., Microbial biosensors. *Anal Chim Acta* **2006**, *568* (1-2), 200-210; (b) Su, L. A.; Jia, W. Z.; Hou, C. J.; Lei, Y., Microbial biosensors: A review. *Biosens Bioelectron* **2011**, *26* (5), 1788-1799; (c) D'Souza, S. F., Microbial biosensors. *Biosens Bioelectron* **2001**, *16* (6), 337-353.
142. Castillo, J.; Gaspar, S.; Leth, S.; Niculescu, M.; Mortari, A.; Bontidean, I.; Soukharev, V.; Dorneanu, S. A.; Ryabov, A. D.; Csoregi, E., Biosensors for life quality - Design, development and applications. *Sensor Actuat B-Chem* **2004**, *102* (2), 179-194.
143. (a) Leth, S.; Maltoni, S.; Simkus, R.; Mattiasson, B.; Corbisier, P.; Klimant, I.; Wolfbeis, O. S.; Csoregi, E., Engineered bacteria based biosensors for monitoring bioavailable heavy metals. *Electroanal* **2002**, *14* (1), 35-42; (b) Shetty, R. S.; Deo, S. K.; Shah, P.; Sun, Y.; Rosen, B. P.; Daunert, S., Luminescence-based whole-cell-sensing systems for cadmium and lead using genetically engineered bacteria. *Anal Bioanal Chem* **2003**, *376* (1), 11-17.
144. Gu, M. B.; Dhurjati, P. S.; VanDyk, T. K.; LaRossa, R. A., A miniature bioreactor for sensing

- toxicity using recombinant bioluminescent *Escherichia coli* cells. *Biotechnol Progr* **1996**, *12* (3), 393-397.
145. Charrier, T.; Chapeau, C.; Bendria, L.; Picart, P.; Daniel, P.; Thouand, G., A multi-channel bioluminescent bacterial biosensor for the on-line detection of metals and toxicity. Part II: Technical development and proof of concept of the biosensor. *Anal Bioanal Chem* **2011**, *400* (4), 1061-1070.
  146. Rothert, A.; Deo, S. K.; Millner, L.; Puckett, L. G.; Madou, M. J.; Daunert, S., Whole-cell-reporter-gene-based biosensing systems on a compact disk microfluidics platform. *Anal Biochem* **2005**, *342* (1), 11-19.
  147. (a) Garcia-Alonso, J.; Fakhrullin, R. F.; Paunov, V. N.; Shen, Z.; Hardege, J. D.; Pamme, N.; Haswell, S. J.; Greenway, G. M., Microscreening toxicity system based on living magnetic yeast and gradient chips. *Anal Bioanal Chem* **2011**, *400* (4), 1009-1013; (b) Garcia-Alonso, J.; Greenway, G. M.; Hardege, J. D.; Haswell, S. J., A prototype microfluidic chip using fluorescent yeast for detection of toxic compounds. *Biosens Bioelectron* **2009**, *24* (5), 1508-1511.
  148. Groisman, A.; Lobo, C.; Cho, H. J.; Campbell, J. K.; Dufour, Y. S.; Stevens, A. M.; Levchenko, A., A microfluidic chemostat for experiments with bacterial and yeast cells. *Nat Methods* **2005**, *2* (9), 685-689.
  149. Kim, H. J.; Jeong, H.; Lee, Y. J.; Lee, D. W.; Lee, S. J., Insights into diversity and specificity of heavy metal resistance and efflux systems in *Bacillus oceanisediminis* 2691. *New Biotechnol.* **2014**, S154.
  150. Park, S.; Hong, X. Q.; Choi, W. S.; Kim, T., Microfabricated ratchet structure integrated concentrator arrays for synthetic bacterial cell-to-cell communication assays. *Lab Chip* **2012**, *12* (20), 3914-3922.
  151. Kim, S. Y.; Lee, E. S.; Lee, H. J.; Lee, S. Y.; Lee, S. K.; Kim, T., Microfabricated ratchet structures for concentrating and patterning motile bacterial cells. *J Micromech Microeng* **2010**, *31*, 095006.
  152. Corbisier, P.; van der Lelie, D.; Borremans, B.; Provoost, A.; de Lorenzo, V.; Brown, N. L.; Lloyd, J. R.; Hobman, J. L.; Csoregi, E.; Johansson, G.; Mattiasson, B., Whole cell- and protein-based biosensors for the detection of bioavailable heavy metals in environmental samples. *Anal Chim Acta* **1999**, *387* (3), 235-244.
  153. Andersen, J. B.; Sternberg, C.; Poulsen, L. K.; Bjorn, S. P.; Givskov, M.; Molin, S., New unstable variants of green fluorescent protein for studies of transient gene expression in bacteria. *Appl Environ Microb* **1998**, *64* (6), 2240-2246.
  154. Chiu, G. L. T.; Shaw, J. M., Optical lithography: Introduction. *Ibm J Res Dev* **1997**, *41* (1-2), 3-6.
  155. Koek, B. H.; Chisholm, T.; Vonrun, A. J.; Romijn, J.; Davey, J. P., An electron-beam lithography tool with a schottky emitter for wide-range applications. *Microelectron Eng* **1994**, *23* (1-4), 81-84.
  156. Gates, B. D.; Xu, Q. B.; Stewart, M.; Ryan, D.; Willson, C. G.; Whitesides, G. M., New approaches to nanofabrication: Molding, printing, and other techniques. *Chem Rev* **2005**, *105* (4), 1171-1196.

157. (a) Yuse, A.; Sano, M., Transition between Crack Patterns in Quenched Glass Plates. *Nature* **1993**, 362 (6418), 329-331; (b) Green, D. J.; Tandon, R.; Sglavo, V. M., Crack arrest and multiple cracking in glass through the use of designed residual stress profiles. *Science* **1999**, 283 (5406), 1295-1297; (c) Kim, B. C.; Matsuoka, T.; Moraes, C.; Huang, J. X.; Thouless, M. D.; Takayama, S., Guided fracture of films on soft substrates to create micro/nano-feature arrays with controlled periodicity. *Sci Rep* **2013**, 3, 3027; (d) Leung, K. T.; Jozsa, L.; Ravasz, M.; Neda, Z., Pattern formation - Spiral cracks without twisting. *Nature* **2001**, 410 (6825), 166-166; (e) Nam, K. H.; Park, I. H.; Ko, S. H., Patterning by controlled cracking. *Nature* **2012**, 485 (7397), 221-224; (f) Skjeltorp, A. T.; Meakin, P., Fracture in Microsphere Monolayers Studied by Experiment and Computer-Simulation. *Nature* **1988**, 335 (6189), 424-426; (g) Nakahara, A.; Matsuo, Y., Transition in the pattern of cracks resulting from memory effects in paste. *Phys Rev E* **2006**, 74 (4), 045102; (h) Alaca, B. E.; Sehitoglu, H.; Saif, T., Guided self-assembly of metallic nanowires and channels. *Appl Phys Lett* **2004**, 84 (23), 4669-4671.
158. (a) Huang, R.; Prevost, J. H.; Suo, Z., Loss of constraint on fracture in thin film structures due to creep. *Acta Mater* **2002**, 50 (16), 4137-4148; (b) Liang, J.; Huang, R.; Prevost, J. H.; Suo, Z., Thin film cracking modulated by underlayer creep. *Exp Mech* **2003**, 43 (3), 269-279.
159. Jamal, M.; Zarafshar, A. M.; Gracias, D. H., Differentially photo-crosslinked polymers enable self-assembling microfluidics. *Nat Commun* **2011**, 2, 527.
160. Zhou, Z.; Huang, Q. A.; Li, W. H.; Lu, W.; Zhu, Z.; Feng, M., The swelling effects during the development processes of deep UV lithography of SU-8 photoresists: Theoretical study, simulation and verification. *Ieee Sensor* **2007**, 1-3, 325-328.
161. Keller, S.; Blagoi, G.; Lillemose, M.; Haeftiger, D.; Boisen, A., Processing of thin SU-8 films. *J Micromech Microeng* **2008**, 18 (12), 125020.
162. Chantiwas, R.; Park, S.; Soper, S. A.; Kim, B. C.; Takayama, S.; Sunkara, V.; Hwang, H.; Cho, Y. K., Flexible fabrication and applications of polymer nanochannels and nanoslits. *Chem Soc Rev* **2011**, 40 (7), 3677-3702.
163. Choi, S. J.; Yoo, P. J.; Baek, S. J.; Kim, T. W.; Lee, H. H., An ultraviolet-curable mold for sub-100-nm lithography. *J Am Chem Soc* **2004**, 126 (25), 7744-7745.
164. Xia, Y. N.; Whitesides, G. M., Soft lithography. *Angew Chem Int Edit* **1998**, 37 (5), 551-575.
165. (a) Sparreboom, W.; van den Berg, A.; Eijkel, J. C. T., Principles and applications of nanofluidic transport. *Nat Nanotechnol* **2009**, 4 (11), 713-720; (b) Kim, H. J.; Boedicker, J. Q.; Choi, J. W.; Ismagilov, R. F., Defined spatial structure stabilizes a synthetic multispecies bacterial community. *Proc Natl Acad Sci USA* **2008**, 105 (47), 18188-18193.
166. Lee, S. E.; Lim, H. G.; Lee, S. S.; Choi, D. G.; Lee, D.; Hong, S. U., Embossed superhydrophobic polymer surfaces with topological variances. *Macromol Res* **2013**, 21 (8), 916-920.
167. Odom, T. W.; Love, J. C.; Wolfe, D. B.; Paul, K. E.; Whitesides, G. M., Improved pattern transfer in soft lithography using composite stamps. *Langmuir* **2002**, 18 (13), 5314-5320.
168. Merkel, T. C.; Bondar, V. I.; Nagai, K.; Freeman, B. D.; Pinnau, I., Gas sorption, diffusion, and permeation in poly(dimethylsiloxane). *J Polym Sci Pol Phys* **2000**, 38 (3), 415-434.
169. Mark, D.; Haeberle, S.; Roth, G.; von Stetten, F.; Zengerle, R., Microfluidic lab-on-a-chip platforms: Requirements, characteristics and applications. *Chem Soc Rev* **2010**, 39 (3), 1153-

1182.

170. (a) Takayama, S.; Ostuni, E.; LeDuc, P.; Naruse, K.; Ingber, D. E.; Whitesides, G. M., Laminar flows - Subcellular positioning of small molecules. *Nature* **2001**, *411* (6841), 1016-1016; (b) Hung, P. J.; Lee, P. J.; Sabounchi, P.; Lin, R.; Lee, L. P., Continuous perfusion microfluidic cell culture array for high-throughput cell-based assays. *Biotechnol Bioeng* **2005**, *89* (1), 1-8.
171. Abaci, H. E.; Gledhill, K.; Guo, Z. Y.; Christiano, A. M.; Shuler, M. L., Pumpless microfluidic platform for drug testing on human skin equivalents. *Lab Chip* **2015**, *15* (3), 882-888.
172. (a) Jeong, H. H.; Lee, S. H.; Lee, C. S., Pump-less static microfluidic device for analysis of chemotaxis of *Pseudomonas aeruginosa* using wetting and capillary action. *Biosens Bioelectron* **2013**, *47*, 278-284; (b) Gumuscu, B.; Bommer, J. G.; van den Berg, A.; Eijkel, J. C. T., Large scale patterning of hydrogel microarrays using capillary pinning. *Lab Chip* **2015**, *15* (3), 664-667; (c) Lee, S. H.; Heinz, A. J.; Shin, S.; Jung, Y. G.; Choi, S. E.; Park, W.; Roe, J. H.; Kwon, S., Capillary based patterning of cellular communities in laterally open channels. *Anal Chem* **2010**, *82* (7), 2900-2906; (d) Hong, J. W.; Song, S.; Shin, J. H., A novel microfluidic co-culture system for investigation of bacterial cancer targeting. *Lab Chip* **2013**, *13* (15), 3033-3040.
173. (a) Fouad, M.; Yavuz, M.; Cui, B., Nanofluidic channels fabricated by e-beam lithography and polymer reflow sealing. *J Vac Sci Technol B* **2010**, *28* (6), C6i11-C6i13; (b) Harnett, C. K.; Coates, G. W.; Craighead, H. G., Heat-depolymerizable polycarbonates as electron beam patternable sacrificial layers for nanofluidics. *J Vac Sci Technol B* **2001**, *19* (6), 2842-2845; (c) Wang, K.; Yue, S.; Wang, L.; Jin, A.; Gu, C.; Wang, P.; Wang, H.; Xu, X.; Wang, Y.; Niu, H., Nanofluidic channels fabrication and manipulation of DNA molecules. *Iee P-Nanobiotechnol* **2006**, *153* (1), 11-15.
174. Kim, M.; Ha, D.; Kim, T., Cracking-assisted photolithography for mixed-scale patterning and nanofluidic applications. *Nat Commun* **2015**, *6*, 6247.
175. Choi, W. S.; Kim, M.; Park, S.; Lee, S. K.; Kim, T., Patterning and transferring hydrogel-encapsulated bacterial cells for quantitative analysis of synthetically engineered genetic circuits. *Biomaterials* **2012**, *33* (2), 624-633.
176. Kim, M.; Lim, J. W.; Kim, H. J.; Lee, S. K.; Lee, S. J.; Kim, T., Chemostat-like microfluidic platform for highly sensitive detection of heavy metal ions using microbial biosensors. *Biosens Bioelectron* **2015**, *65*, 257-264.
177. Choi, S. J.; Yoo, P. J.; Baek, S. J.; Kim, T. W.; Lee, H. H., An ultraviolet-curable mold for sub-100-nm lithography. *J Am Chem Soc* **2004**, *126* (25), 7744-7745.
178. Jeong, H. E.; Suh, K. Y., On the role of oxygen in fabricating microfluidic channels with ultraviolet curable materials. *Lab Chip* **2008**, *8* (11), 1787-1792.
179. Huh, D.; Mills, K. L.; Zhu, X. Y.; Burns, M. A.; Thouless, M. D.; Takayama, S., Tuneable elastomeric nanochannels for nanofluidic manipulation. *Nat Mater* **2007**, *6* (6), 424-428.
180. Toepke, M. W.; Beebe, D. J., PDMS absorption of small molecules and consequences in microfluidic applications. *Lab Chip* **2006**, *6* (12), 1484-1486.
181. Andersen, J. B.; Heydorn, A.; Hentzer, M.; Eberl, L.; Geisenberger, O.; Christensen, B. B.; Molin, S.; Givskov, M., gfp-based N-acyl homoserine-lactone sensor systems for detection of bacterial communication. *Appl Environ Microb* **2001**, *67* (2), 575-585.

182. Kawe, M.; Horn, U.; Pluckthun, A., Facile promoter deletion in Escherichia coli in response to leaky expression of very robust and benign proteins from common expression vectors. *Microb Cell Fact* **2009**, 8, 8.
183. Kim, H. J.; Boedicker, J. Q.; Choi, J. W.; Ismagilov, R. F., Defined spatial structure stabilizes a synthetic multispecies bacterial community. *Proc Natl Acad Sci USA* **2008**, 105 (47), 18188-18193.
184. Choi, Y. J.; Lee, S. Y., Microbial production of short-chain alkanes. *Nature* **2013**, 502 (7472), 571-574.

## Acknowledgements

Prof. Taesung Kim, I would like to put his name on the first place of the acknowledgements. Without his valuable advices and endless encouragements, it would not be possible to achieve this much big growth in not only professionalism but also philosophy towards the life. I am forever in debt to him. I should expand my thanks to all committee members (Prof. Heungjoo Shin, Prof. Jaesung Jang, Prof. Sung Kuk Lee and Prof. Yun Seok Heo) for their generous and scrupulous advices on this dissertation. Thanks again for their valuable time and comments. Also, I keenly appreciate to faculty members who gave me informative and illuminating lectures in the Department of Mechanical Engineering at UNIST: Prof. Taesung Kim for Thermodynamics, Microfluidics, and BioMEMS, Prof. Heungjoo Shin for MEMS, Prof. Jaesung Jang for Heat Transfer, Prof. Hyungson Ki for Fluid Mechanics, Prof. Sung Youb Kim for Fracture Mechanics, and Prof. Chun Sang Yoo for Numerical Analysis.

My special thanks to go former and current  $\mu$ FNM laboratory members who became like family over the past five years. I shared many precious memories with Sungyong Park and Yoongwang Nam who were the lab mate as well as roommate. Mingie Jia was nice to me and we discussed a lot of things regarding electrokinetic phenomenon in micro/nanofluidics. Jiwon Lim helped me a lot to conduct my microbial experiments and he expanded my knowledge about the microbiology and synthetic biology. Dogyeong Ha and Jongwan Lee were always polite and diligent, so that I believe they will have big progresses to lead their research fields. Dong-joo Kim who recently joined the  $\mu$ FNM as a postdoc would well assimilate with the Lab's juniors due to his kind personality. I appreciate all aforementioned members, and other Lab members including hyunmoon Nam, Jungsik Park and undergraduate students. I will always look forward to hearing good messages (i.e., to publish a big paper, to have a girl friend – especially for Dogyeong and Jongwan, to get a nice job, and etc.) from you guys. Also, my life in UNIST was entertained thanks to my friends in other Labs of the same department. I could not call everyone here, but now there are several names popped up in my mind: Hyunmeong Kim, Jaehoon Kim, Sang-Ha Hwang, Youngjin Lim, Jeong-il Huh, Yoonjung Lee, Soon-dong Park, Insu Jo, and others.

Lastly but most importantly, I would like to thank my family. My mother and brother, Jumsook Park and Geunseok Kim, have supported my every aspiration with sincere love. They always were my driving force to do my best. Also, my father-in-law and mother-in-law have treated me with profound affection and even cared about me as if being their own son. Finally, I thank my wonderful and beautiful wife, Sunyoung Choi, to whom I dedicate this work and my life. The destiny we were connected each other is the greatest gift I could imagine.

---

**Minseok Kim, Ph. D.**

Department of Mechanical Engineering  
Ulsan National Institute of Science and Technology (UNIST)  
505, EB 1, 50 UNIST-gil, Ulsan 689-805, Republic of Korea  
E-mail: [mk\\_1985@naver.com](mailto:mk_1985@naver.com) or [prodeus1985@unist.ac.kr](mailto:prodeus1985@unist.ac.kr)  
Lab homepage: <http://www.ufnm.unist.ac.kr>

---

**PERSONAL**

Date of birth: July, 26<sup>th</sup>, 1985, Republic of Korea  
Gender: Male  
Marital status: Married

**EDUCATION**

- 03/2010 – Present Ulsan National Institute of Science and Technology (UNIST)**  
Combined M.S. & Ph. D. in Mechanical Engineering  
Advisor: Prof. Taesung Kim ([tskim@unist.ac.kr](mailto:tskim@unist.ac.kr))  
Dissertation: Membrane-Integrated and Membrane-Free Micro and Nanofluidics  
for Accurate Molecular Transport in Biological Assays
- 03/2004 – 02/2010 Chonnam National University (CNU)**  
B.S. in Mechanical Engineering

**HONORS AND AWARDS**

- 2015 **Excellent poster awards**, The 17<sup>th</sup> Korea MEMS Conference  
2015 **Best Ph. D Thesis Award**, Department of Mechanical Engineering, UNIST  
2015 **Samsung Human Tech Paper Award** (\$10,000, 1<sup>st</sup> ranked in M.E.), SAMSUNG  
2014 **Best paper award**, Korea Society of Mechanical Engineers (KSME)  
2013 **Excellent poster awards**, KSME Conference, Bioengineering Division  
2012–2015 **UNIST Elite Fellowship** (03/2012 – 02/2015, \$ 30,000/year), UNIST  
2012 **Global Ph. D. Fellowship**, National Research Foundation (Nominated as a recipient)  
2012 **Best paper award**, KSME Conference, Bioengineering Division  
2011 **Best poster award**, The 5th International Conference on Sensor, Asia sense (co-author)  
2011 **Excellent poster awards**, KSME Conference, Bioengineering Division, 2011 (co-author)  
2010 **Travel grant awards** (\$ 500), Micro-TAS 2010  
2010 **Excellent poster awards**, KSME Conference, Bioengineering Division (co-author)  
2007–2009 **NURI Scholarship**, Full or Partial-funding, Department of Mechanical Engineering, CNU  
2004–2005 **Brain Korea 21 Scholarship**, Full-funding, Department of Mechanical Engineering, CNU



## RESEARCH EXPERIENCE

**03/2010 – Present    Microfluidics and Nanomechanics Lab in UNIST (Adviser: Prof. Taesung Kim)**

*Graduate Student Researcher*

- **Development of unconventional fabrication techniques for mixed-scale micro-/nanofluidic devices**
  - For the first time, developed crack photolithography technique that can simultaneously fabricate micro-/nanoscale mixed patterns by controlling nanoscale cracking phenomena during a standard microfabrication process (photolithography). (Ref. M. Kim *et al.*, *Nat. Commun.*, 2015)
  - Developed several methods to integrate/assembly nanoporous materials such as hydrogels, Nafion, and nanoparticles into microfluidic channels to fabricate micro-/nanofluidic interfaces for manipulation of biomolecules and bacterial cells. (Ref. M. Kim and T. Kim, *Anal. Chem.*, 2010)
  - Fabricated multi-height microchannel networks using gray-scale photolithography for sorting microparticle and yeast cells (Ref. Y.-G. Nam *et al.*, *J. Micromech. and Microeng.*, 2013)
- **Electrokinetic concentration and separation of biomolecules and microbes**
  - Created a new experimental model for generating ion concentration polarization (ICP) in a single and open microfluidic channel with surface-patterned nanomaterials, which was applied for simultaneous concentration and lysis of bacterial cells in order to extract inter-cellular proteins. (Ref. M. Kim *et al.*, *Analyst*, 2013)
  - Integrated various nanoporous hydrogels and nanostructured membranes inside of microfluidic devices by using selective patterning of precursor solutions for electrokinetic concentration of protein and bacterial cells. (Ref. M. Kim *et al.*, *Analyst*, 2013)
  - Assisted and discussed on multi-physics simulation of the linear and/or nonlinear electrokinetic transport phenomena (e.g. vortex) by backing up theoretical data with experiments. (Ref. M. Jia and T. Kim, *Anal. Chem.*, 2014)
- **Development micro-bioreactors for analyzing synthetic bacterial cells**
  - Developed a micro-chemostat device that can program chemical environments and cell populations in compartmentalized microchamber arrays by using a mass-transport-tunable nanofluidic film formed between solid surfaces by lubrication. (Ref. manuscript in preparation)
  - Fabricated a membrane-free diffusion-based micro-/nanofluidic device by using crack-photolithography for analyzing gene expression of synthetic bacterial cells in a versatile and high-throughput manner. (Ref. M. Kim and T. Kim, *Anal. Chem.*, 2015)
- **Development of micro-/nanofluidic devices for bacterial chemotaxis assays**
  - Developed a diffusion-based and long-ranged concentration gradient generator to investigate preferential chemotaxis of bacterial cells for various carbon sources by using nanoporous-hydrogel-integrated microfluidic devices. (Ref. M. Kim and T. Kim, *Anal. Chem.*, 2010)
  - Developed a microfluidic device that can continuously sorting and concentrating motile bacterial cells based on their chemotactic sensitivity. (Ref. M. Kim *et al.*, *Analyst*, 2011)
  - Developed a PDMS-sealed and hydrogel-patterned microfluidic channels to generate user-definable concentration gradients for analyses of nonlinear chemotaxis of microbes (Ref. M. Kim *et al.*, *Microfluid. Nanofluid.*, 2014)
- **Fluorescent-based detection of heavy metal ions and biomolecules**
  - Created a new concept to selectively capture and actively transport target biomolecules bound on aptamers-functionalized microtubules by using electrokinetic manipulation and performed continuous and simultaneous concentration and separation of target biomarkers (e.g. EGFR) by

employing nanomechanical sieving structures. (Ref. M. Kim and T. Kim, *Sensor. Actuat. B-Chem.*, 2014)

- Developed chemostat-like microfluidic devices to enhance the efficiency of microbial biosensors for pM-level-detection of heavy metal ions (Ref. M. Kim *et al.*, *Biosens. Bioelecton.*, 2015)

## JOURNAL PUBLICATIONS

- [1] M. Kim, J.-W. Lim, S.-K. Lee\*, and T. Kim\*, "Microfluidic chemostat array for programming cell growth and high-throughput screening", *in preparation*
- [2] J. Lee<sup>†</sup>, M. Kim<sup>†</sup>, J.-Y Park, and T. Kim\*, "Microfluidic concentration of bacterial cells for in-situ genetic induction studies using self-assembled particle membranes", *in preparation*
- [3] M. Kim<sup>†</sup>, D. Kim<sup>†</sup> and T. Kim\*, "Crack lithography for micro/nanopatterns and their applications", *in preparation*
- [4] M. Kim and T. Kim\*, "Crack-photolithography for membrane-free diffusion-based micro/nanofluidic devices", *Anal. Chem.*, in press
- [5] M. Kim, D. Ha, and T. Kim\*, "Cracking-assisted photolithography for mixed-scale patterning and nanofluidic applications", *Nat. Commun.*, 6, 6247, 2015 (IF 10. 745) [This paper was highlighted in many news medias.](#)
- [6] M. Kim<sup>†</sup>, J.-W. Lim<sup>†</sup>, H.-J. Kim, S.-K. Lee, S.-J. Lee\*, and T. Kim\*, "Chemostat-like microfluidic platform for highly sensitive detection of heavy metal ions using microbial biosensors", *Biosens. Bioelecton.*, 65(15), 257-264, 2015 (IF 6.451, Top 5%, 0 cited)
- [7] M. Kim and T. Kim\*, "Aptamer-functionalized microtubules for continuous and selective concentration of target analytes", *Sensor. Actuat. B-Chem.*, 202, 1229-1236, 2014 (IF 3.840, Top 5%, 1 cited)
- [8] M. Kim, Jia, M, Kim, Y., and T. Kim\*, "Rapid and accurate generation of various concentration gradients using polydimethylsiloxane-sealed hydrogel device", *Microfluid. Nanofluid.*, 12, 1613-4982, 2014 (IF 2.665, Top 10%, 0 cited)
- [9] Y.-K. Nam, M. Kim, and T. Kim\*, "Pneumatically controlled multi-level microchannel for separation and extraction of microparticles", *Sensor. Actuat. B-Chem.*, 190, 86-92, 2014 (IF 3.840, Top 5%, 1 cited)
- [10] Y.-K. Nam, M. Kim, and T. Kim\*, "Fabricating a multi-level barrier-integrated microfluidic device using grey-scale photolithography", *J. Micromech. and Microeng.*, 23, 105015, 2013 (IF 1.725, Q2, 3 cited)
- [11] M. Kim and T. Kim\*, "Integration of nanoporous membranes into microfluidic devices: electrokinetic bio-sample pre-concentration", *Analyst*, 138, 6007-6015, 2013 (IF 3.906, Top 10%, 10 cited)
- [12] M. Kim, M. Jia, and T. Kim\*, "Ion concentration polarization in a single and open microchannel induced by a surface-patterned perm-selective film", *Analyst*, 138, 1370-1378, 2013 (IF 3.906, Top 10%, 14 cited). [This paper was selected as the inside front cover of the issue.](#)
- [13] W.-S. Choi, M. Kim, S. Park, S.-K. Lee and T. Kim\*, "Patterning and transferring hydrogel-encapsulated bacterial cells for quantitative analysis of synthetically engineered genetic circuits", *Biomaterials*, 33, 624-633, 2012 (IF 8.312, Top 5%, 6 cited)
- [14] P. Vinuselvi, S. Park, M. Kim, J.-M. Park, T. Kim\*, and S.-K. Lee\*, "Microfluidic technologies for

synthetic biology”, *Int. J. of Mol. Sci.*, 12, 3576-3593, 2011 (IF 2.339, Q2, 15 cited)

- [15] M. Kim, S.-H. Kim S.-K. Lee\*, and T. Kim\*, “Microfluidic device for analyzing preferential chemotaxis and chemoreceptor sensitivity of bacterial cells toward carbon sources”, *Analyst*, 136, 3238-3243, 2011 (IF 3.906, Top 10%, 13 cited) [This paper was selected as the front cover of the issue.](#)
- [16] M. Kim and T. Kim\*, “Diffusion-based and long-range concentration gradients of multi-chemicals for bacterial chemotaxis assays, *Anal. Chem.*, 82(22), 9401-9409, 2010 (IF 5.825, Top 5%, 43 cited). [This paper was highlighted as a news article in the American Chemical Society \(ACS C&EN\).](#)

\* and † denote correspondence and co-first authors, respectively.  
 The citation number is based on Google Scholar.

## CONFERENCE PROCEEDINGS

- [1] M. Kim and T. Kim, “Crack-photolithography for mixed-scale micro-/nanofluidic devices”, *MicroTAS 2015*, Gyeongju, Korea (accepted)
- [2] M. Kim and T. Kim\*, “Cracking-assisted photolithography for high-throughput nanopatterning and nanofluidic applications” *Transducer 2015*, Anchorage, Alaska, USA
- [3] M. Kim, and T. Kim\*, “Crack-photolithography for nanopatterning and nanofluidics, *Korea MEMS conference 2015*, Jeju, Korea ([excellent poster award](#))
- [4] J. Lee, M. Kim, and T. Kim\*, “Development of Microfluidic Device using Self-assembled Particle Membranes (SAPMs) for Pre-concentration and Post-analysis of Microbes, *Korea MEMS conference 2015*, Jeju, Korea
- [5] M. Kim, J.-W. Lim, and T. Kim\*, “Programming bacterial population and chemical environments in microchemostat array for high-throughput screening, *KSME 2014*, Gwangju, Korea ([oral presentation, best paper award](#))
- [6] Park, J. D. Ha, M. Kim, and T. Kim\*, KSME “Microfluidic platform with a hydrogel-encapsulated bioreactor array for long shelf-life microbial biosensors”, *KSME 2014*, Gwangju, Korea
- [7] J. Lee, M. Kim, and T. Kim\*, “Self-assembled particle membranes integrated microfluidic bioreactor for concentration and screening of microbes”, *KSME 2014*, Gwangju, Korea
- [8] M. Kim, J.-W. Lim, and T. Kim\*, “Chemostat-like microfluidic platform for highly Sensitive detection of heavy metal ions using microbial biosensors, *KSME 2014*, Gwangju, Korea ([oral presentation](#))
- [9] J. Lee, D. Ha, M. Kim, and T. Kim\*, “Temporally programmable cell culture environment using a membrane integrated microbioreactor”, *MicroTAS 2014*, San Antonio, Texas, USA
- [10] M. Jia, M. Kim, and T. Kim\*, “Multiphysics simulation of ion concentration polarization induced by nanoporous membranes in dual channel devices”, *MicroTAS 2014*, San Antonio, Texas, USA
- [11] M. Kim, J.-W. Lim, and T. Kim\*, “Nanoscale fluid film-based microbioreactor for modulating cell growth”, *KSME-Bioengineering division 2014*, Gyeongju, Korea
- [12] Y.-K. Nam, M. Kim, and T. Kim\*, “Fabrication of multi-level microchannel by using grey-scale photolithography for separation and extraction of microparticles”, *MicroTAS 2013*, Freiburg, Germany
- [13] M. Kim and T. Kim\*, “Aptamer-functionalized microtubule for continuous and selective capturing and filtering using a nanoporous hydrogel membrane”, *MicroTAS 2013*, Freiburg, Germany
- [14] M. Kim, M. Jia, and T. Kim\*, “A PDMS-sealed hydrogel device for rapid and accurate generation of various concentration gradients”, *MicroTAS 2013*, Freiburg, Germany
- [15] Y.-K. Nam-K., M. Kim, and T. Kim\*, “Separation and extraction of microparticles using multi-level

- microchannels fabricated by grey-scale photolithography”, **BAMM 2013**, Jeju, Korea
- [16] M. Jia, M. Kim, and T. Kim\*, “Numerical simulation of ion concentration polarization induced in an open and single microchannel device”, **BAMM 2013**, Jeju, Korea
- [17] M. Kim and T. Kim\*, “Continuous and selective concentration of target biomolecules captured by aptamer-functionalized microtubules”, **BAMM 2013**, Jeju, Korea ([oral presentation](#)).
- [18] T. Kim\*, Choi, W.-S., M. Kim, and S.-K. Lee, “Patterning and transferring hydrogel-encapsulated synthetic bacterial cells for quantification and biosensor-application of genetic circuits”, **MMB 2013**, LA, USA
- [19] Y.-K. Nam, M. Kim, and T. Kim\*, “Separation and extraction of microparticles using multi-level microchannels fabricated by gray-scale photolithography”, **KSME-Bioengineering division 2013**, Yeosu, Korea
- [20] M. Kim and T. Kim\*, “Continuous and selective capturing of biomolecules by combining aptamer-functionalized microtubules with a nanoporous membrane”, **KSME-Bioengineering division 2013**, Yeosu, Korea ([excellent poster awards](#))
- [21] M. Kim, M. Jia, and T. Kim\*, “Ion concentration polarization in a single and open microchannel using surface-patterned nafion: experimental and theoretical Study”, **MicroTAS 2012**, Okinawa, Japan
- [22] M. Kim and T. Kim\*, “Self-integration of ion transport tunable nanoporous microplugs in a microfluidic chip for electrokinetic bio-sample concentration”, **MicroTAS 2012**, Okinawa, Japan
- [23] M. Jia, M. Kim, and T. Kim\*, “Experimental and numerical investigation on ion concentration polarization in a single microchannel induced using surface-patterned nafion film”, **ISFMFE 2012**, Jeju, Korea ([oral presentation](#))
- [24] M. Kim, Hur, H.-Y., and T. Kim\*, “High-sensitive and high-selective electrokinetic detection of target bio-sample using aptamer-functionalized microtubules”, **KSME-Micro/Nano division 2012**, Daejeon (KIMM), Korea
- [25] Y.-K. Nam, M. Kim, and T. Kim\*, “Gray-scale photomasks and their application to microparticle separation”, **KSME-Micro/Nano division 2012**, Daejeon (KIMM), Korea
- [26] M. Kim, Kim, Y., and T. Kim\*, “Linear and non-linear concentration gradient generation on a PDMS-hydrogel hybrid device for bacterial chemotaxis assay”, **KSME-Bioengineering division 2012**, Gwangju (Chonnam Nat. Univ.), Korea ([best paper award](#))
- [27] Choi, W.-S., M. Kim, S. Park, and T. Kim\*, “Hydrogel-encapsulated bacterial cell patterning methods for whole cell based biosensor applications”, **Biochip 2011**, Ulsan (UNIST), Korea
- [28] M. Kim, and T. Kim\*, “Capillary-based microfabrication of nanoporous materials for various sample concentration”, **Biochip 2011**, Ulsan (UNIST), Korea
- [29] M. Kim and T. Kim\*, “Single-channel ion concentration polarization using nafion as anomalous rapid ion transporter”, **ASIASENSE 2011**, Jeju, Korea
- [30] Choi, W.-S., M. Kim, S. Park, and T. Kim\*, “Hydrogel-encapsulated bacterial cell patterning methods for whole cell based biosensor applications”, **ASIASENSE 2011**, Jeju, Korea ([best paper award](#))
- [31] S. Park, X. Hong, M. Kim, Choi, W.-S., and T. Kim\*, “Bacterial cell-to-cell communication assays in a micro-fabricated concentrator array device”, **MicroTAS 2011**, Seattle, USA ([oral presentation](#))
- [32] M. Kim, and T. Kim\*, “Single-channel ion concentration polarization using nafion as anomalous rapid ion transporter”, **KSME-Micro/Nano division 2011**, Pusan, Korea
- [33] S. Park, X. Hong, M. Kim, Choi, W.-S., and T. Kim\*, “Bacterial cell-to-cell communication assays in microfabricated concentrator array device”, **KSME-Bioengineering division 2011**, Pohang (Postech), Korea ([excellent paper awards](#))

- [34] M. Kim and T. Kim\*, "Single-channel ion concentration polarization using nafion as anomalous rapid ion transporter", **ISMM 2011**, Seoul, Korea
- [35] S. Park, X. Hong, M. Kim, Choi, W.-S., T. Kim\*, "Bacterial cell-to-cell communication assays in a micro-fabricated concentrator array device", **ISMM 2011**, Seoul, Korea
- [36] M. Kim, S.-H. Kim S.-K. Lee, and T. Kim\*, "Amplification of chemotactic responses of motile bacterial cells for characterizing preferential chemotaxis toward carbon sources", **Transducers 2011**, Beijing, China ([oral presentation](#))
- [37] M. Kim and T. Kim\*, "Long-range concentration gradients of multi-compounds for bacterial chemotaxis assay", MicroTAS 2010, Groningen, The Netherland
- [38] S.-H. Kim M. Kim, S.-K. Lee, and T. Kim\*, "Sorting and concentration of motile microbes for chemotaxis assay", **MicroTAS 2010**, Groningen, The Netherland
- [39] M. Kim and T. Kim\*, "A long-range concentration gradient generator of multi-compounds for bacterial chemotaxis assay", **Biochip 2010**, Seoul (Sogang Univ.), Korea
- [40] M. Kim and T. Kim\*, "A novel microfluidic device for generating multi-concentration gradients", **KSME-Bioengineering division 2010**, Jeju, Korea ([oral presentation](#))
- [41] S.-H. Kim M. Kim, S. Park, S.-K. Lee and T. Kim\*, "Characterizing food preference of E.coli for enhanced biofuel production", **KSME-Bioengineering division 2010**, Jeju, Korea ([excellent paper awards](#))

## **PATENTS**

- [1] T. Kim, M. Kim, and J.-W. Lim "Chemostat-like microfluidic platform for highly sensitive detection of heavy metal ions using microbial biosensors"  
**Application #:** KR 10-2014-0169737 (date: 2014. 12. 01)
- [2] T. Kim and M. Kim, "Method for manufacturing a mold for a fine channel, method for manufacturing a die for a fine channel, and method for manufacturing a block formed on which a fine channel is formed"  
**Application #:** KR 10-2014-0087653 (date: 2014. 07. 11)
- [3] T. Kim and M. Kim, "Cell culture device"  
**Application #:** PCT/KR 2014/004483 (date: 2014. 05. 20)
- [4] T. Kim, M. Kim, and D. Ha, "Nanoparticles generating device and generating method using the same"  
**Application #:** KR 10-2013-0089697 (date: 2013. 07. 29)
- [5] T. Kim and M. Kim, "Batch- and continuous-type bioreactor array using a nanoscale fluid film"  
**Application #:** KR 10-2013-0089699 (date: 2013. 07. 29) [This patent was highlighted in Ulsan Chamber of Commerce and Industry \(UCCI\) 2014 February Vol.125, pp. 7.](#)
- [6] T. Kim and M. Kim, "Method for making fine channel"  
**Application #:** KR 10-2013-0082739 (date: 2013. 07. 15)  
**Registration #:** KR 10-1390700 (date: 2014. 04. 24)
- [7] T. Kim and M. Kim, "Device for identifying the target using fine structure and the method thereby"  
**Application #:** KR 10-2013-0082074 (date: 2013. 07. 12)
- [8] T. Kim, Y.-K. Nam, and M. Kim, "Apparatus for separation and extraction of microparticles or microbes and using the same"  
**Application #:** KR 10-2013-0065874 (date: 2013. 06. 10)  
**Registration #:** KR 10-1430727 (date: 2014. 08. 08)
- [9] T. Kim and M. Kim, "Concentration gradient generating microfluidic device and method of manufacturing the same"  
**Application #:** KR 10-2012-0108006 (date: 2012. 09. 27)

**Registration #:** KR 10-1390665 (date: 2014. 04. 24)

- [10] T. Kim and M. Kim, "Method of single channel ion concentration polarization and bio molecule concentration device"  
**Application #:** KR 10-2011-0077877 (date: 2011. 08. 04)  
**Registration #:** KR 10-1290834 (date: 2012. 07. 23)
- [11] T. Kim and M. Kim, "Microfluidic Device for amplifying chemotactic responses of microbes and method thereof"  
**Application #:** KR 10-2011-0009890 (date: 2011. 02. 01)  
**Registration #:** KR 10-1181132 (date: 2012. 09. 03)
- [12] T. Kim and M. Kim, "Method for measuring concentration using chemotaxis of micro-organisms and microfluidic device thereof"  
**Application #:** KR 10-2010-0105363 (date: 2010. 10. 27)  
**Registration #:** KR 10-1211773 (date: 2012. 12. 06)
- [13] T. Kim and M. Kim, and S.-K. Lee, "Microfluidic screening device and method thereof"  
**Application #:** KR 10-2010-0031526 (date: 2010. 04. 06)  
**Registration #:** KR 10-1206619 (date: 2012. 11. 23)